Diffraction and Radiation of Linear Water Waves by a Vertical Compound Porous Cylinder of Various Configurations in Finite Ocean Depth

by

Abhijit Sarkar

DEPARTMENT OF MATHEMATICS
INDIAN INSTITUTE OF TECHNOLOGY
GUWAHATI
GUWAHATI-781039, INDIA
October, 2020

भारतीय प्रौद्योगिकी संस्थान गुवाहाटी
Indian Institute of Technology Guwahati

Diffraction and Radiation of Linear Water Waves by a Vertical Compound Porous Cylinder of Various Configurations in Finite Ocean Depth

A Thesis Submitted in Partial Fulfillment of the Requirements for the Degree of

Doctor of Philosophy

by

Abhijit Sarkar

(Roll No. - 156123013)

to the

DEPARTMENT OF MATHEMATICS
INDIAN INSTITUTE OF TECHNOLOGY GUWAHATI
GUWAHATI-781039, INDIA

October, 2020

भारतीय प्रौद्योगिकी संस्थान गुवाहाटी
Indian Institute of Technology Guwahati

Dedicated To My Parents

Shri Kamal Sarkar
&
Smt. Manashi Sarkar
and
To My Late Maternal Grandfather

Binoy Kumar Tarafder

भारतीय प्रौद्योगिकी संस्थान गुवाहाटी
Indian Institute of Technology Guwahati

Declaration

I do hereby declare that this thesis entitled **Diffraction and Radiation of Linear Water Waves by a Vertical Compound Porous Cylinder of Various Configurations in Finite Ocean Depth** is a presentation of my original research work carried out under the supervision of **Dr. Swaroop Nandan Bora**, Professor, Department of Mathematics, Indian Institute of Technology Guwahati for the award of the degree of Doctor of Philosophy and this work has not been submitted elsewhere for a degree.

October, 2020

Abhijit Sarkar
Roll No. 156123013
Department of Mathematics
Indian Institute of Technology Guwahati
Guwahati 781 039, Assam, India

भारतीय प्रौद्योगिकी संस्थान गुवाहाटी
Indian Institute of Technology Guwahati

Certificate

It is to certify that the work contained in this thesis entitled **Diffraction and Radiation of Linear Water Waves by a Vertical Compound Porous Cylinder of Various Configurations in Finite Ocean Depth** has been carried out by **Abhijit Sarkar**, a student in the Department of Mathematics, Indian Institute of Technology Guwahati, under my supervision for the award of the degree of Doctor of Philosophy and this work has not been submitted elsewhere for a degree.

October, 2020

Dr. Swaroop Nandan Bora
Professor
Department of Mathematics
Indian Institute of Technology Guwahati
Guwahati 781 039, Assam, India

भारतीय प्रौद्योगिकी संस्थान गुवाहाटी
Indian Institute of Technology Guwahati

Acknowledgements

A creation must require some inspiration. Mine is not any exception. But for some inspirers' constant encouragement, my study would have been in vain. It is their supporting roles that triggered me to acquire the right kind of wisdom, mental strength, perseverance and patience suitable for this kind of creation.

To the God Almighty, our Lord and Saviour, for giving the wisdom, strength, support and knowledge in exploring things; for the guidance in helping surpass all the trials that I encountered and for giving determination to pursue my study and to make it possible.

I am very grateful to my supervisor Prof. Swaroop Nandan Bora for his generous guidance throughout those years. I would also like to express my deep appreciation for his patience, understanding and support. He helped me to overcome many obstacles that emerged while working on several problems. In a good way, he always used to push for better results. He was deeply involved and helped me in every possible way. His continuous encouragement and advice made it possible for me to work on this thesis. I could not have imagined having a better advisor and mentor for my Ph.D study.

I would like to express my gratitude to my doctoral committee members, Prof. Durga Charan Dalal, Prof. Natesan Srinivasan and Prof. Rajen Kumar Sinha for their encouragement and precious comments which definitely resulted in improvement of my research work.

I am highly grateful to the Ministry of Education (earlier Ministry of Human Resource Development), Government of India for necessary financial support. I sincerely acknowledge Indian Institute of Technology Guwahati for providing a very conducive environment and all kinds of support for carrying out my research without any trouble. I am also grateful to all the staff members of the Department of Mathematics for their assistance in various ways during my research period.

I would like to thank my friends and colleagues Somnath, Shantiram, Ayan, Sumit, Rakesh, Sunil, Nilay, Gautam, Mohit, Bandita, Swarup Da, Sougata Da, Swapnendu Da, Sonjoy Da, Madhu Da, Devanand Da, Koyel Di, Avijit, Mrityunjoy, Shyam, Shamik and many others for all their encouragement and support during this period. My special appreciation goes to my close friends Somnath, Shantiram, Ayan, Sumit, Rakesh, Sunil, Rupak, Avijit, Mrityunjoy, Shyam, Shamik and Kanti with whom I have shared some of the best moments of my life. The space here is too limited to mention the names of all the people who were part of my life during these years, but still the quality time I spent with them is something which is stored deep inside my heart and I will cherish the memory for the rest of my life.

I am extremely grateful to my parents, my elder brother Chandan Sarkar and all other family members for their love, concern, care, encouragement and moral support throughout my life. I would like to express my deepest gratitude to them for standing besides me all the time with unconditional support. Finally, I would like to acknowledge

everybody who is important to the successful completion of the thesis as well as express my apology that I could not mention each of them individually.

At present, COVID19 has created a havoc all around the globe. I consider myself fortunate that I have been able to complete my assignment despite being in uncertainty and under tremendous stress and anxiety for most of the time. It has been a difficult time to complete the thesis by staying at home which deprived many of us the facilities and the environment of Indian Institute of Technology Guwahati. However, goodwill of my well-wishers along with my motivation resulted in my thesis seeing the light of the day.

October, 2020 **Abhijit Sarkar**

भारतीय प्रौद्योगिकी संस्थान गुवाहाटी
Indian Institute of Technology Guwahati

भारतीय प्रौद्योगिकी संस्थान गुवाहाटी
Indian Institute of Technology Guwahati

Abstract

Porous structures reduce the waveload and wave run-up on the structures as well as in the adjoining region. These structures are very flexible, reusable and can be used to develop low cost wave attenuation and protection systems. In general, vertical cylinders are used as coastal and offshore structures due to a variety of advantages. Some examples are floating airports, floating oil-drilling platform, semi-submersibles and wave power energy conversion system. Various porous structures are used to create oil rigs. Sea-cage culture is also based on porous structures. Further, Very Large Floating Structures (VLFS), such as floating airports, bridges, breakwaters, piers, docks etc. are constructed with the help of porous structures. The main objective of this thesis is to investigate the wave forces, wave run-up and hydrodynamic coefficients of various compound porous cylindrical structures in water of finite depth within the framework of linear water wave theory.

In the beginning of this study, we consider wave interaction with a bottom-mounted compound porous cylinder with a semi-porous single cylinder as a special case. The physical problem involving diffraction is reduced to a boundary value problem governed by the three-dimensional Laplace's equation. The method of solution is based on the separation of variables and matched eigenfunction expansion technique. In the study of porous structures, an eigenfunction expansion, along with matching technique, is widely used due to its considerable accuracy. By using these techniques, the analytical expressions for the diffracted potentials are presented, and by applying the appropriate matching conditions, which ensure the continuity of velocity and pressure along the virtual boundaries between two consecutive regions, we obtain a system of linear equations in each case which are solved for the unknown coefficients. We evaluate hydrodynamic force and wave run-up for different parameters such as radii, draft ratio, porous coefficient. In continuation, we also consider a floating compound porous cylinder. In this case also, we investigate hydrodynamic force and wave-run up. Next we attempt a diffraction problem in an ocean due to the presence of a specific type of cylinders for two configurations: (i) a floating surface-piercing truncated partial-porous cylinder, and (ii) a surface-piercing truncated

partial-porous cylinder placed at the bottom. In both cases, the configuration of the compound cylinder is such that it consists of an impermeable inner cylinder rising above the free surface and a coaxial truncated porous cylinder around the lower part of the inner cylinder with the top of the porous cylinder being impermeable. The next study explores the problem related to the diffraction of linear waves by a cylindrical storage tank, the inner part of which contains a cylindrical pile and the outer part contains a coaxial thin hollow porous cylinder in finite depth. The main aim is to construct a storage tank surrounding the cylindrical pile of the aerogenerators for aquaculture. Here we consider two cases: (i) an impermeable solid circular cylinder surrounded by an outer coaxial thin hollow porous cylinder of same height extending from free surface to sea-bed, (ii) a similar structure fully placed atop an impermeable solid circular cylinder of same radius. In the next problem, radiation problems pertaining to partial-porous compound cylinder is taken up and the associated hydrodynamic coefficients are evaluated. We primarily discuss the surge and heave motions for a floating partial-porous compound cylinder in finite depth. We also investigate the added mass and damping coefficient for different parameters by using the same technique for calculating the unknown coefficients.

Next we discuss the interaction of linear surface waves with a bottom-mounted compound partial-porous cylinder which consists of two coaxial cylinders with a hollow upper cylinder with a thin porous wall and a rigid lower cylinder placed on the sea-bed. Here also we evaluate hydrodynamic force and wave run-up for different parameters. Further, we describe the exciting forces for an arrangement of two coaxial vertical cylinders – a riding porous cylinder and a bottom-mounted solid rigid cylinder. We take up two cases: first we consider a hollow porous cylinder at the top and secondly a solid porous cylinder at the top, and for both the cases, there is a solid rigid cylinder at the bottom. We mainly focus on hydrodynamic forces and wave run-up for different parameters. We then consider two coaxial vertical cylinders – a riding porous cylinder and a bottom-mounted solid rigid cylinder. This is an extension of previous model. For these two cases, we first discuss the problem for a riding hollow porous cylinder and then for a riding solid porous cylinder. The translational motions in the x- and z-directions, i.e., surge and heave motions, are investigated. The added mass starts from nonzero values and becomes negative for increasing values of wavenumber. It is found that the added mass for surge motion takes higher values corresponding to decreasing values of porous coefficient. It is observed that added mass and damping coefficients due to surge motion for both a hollow porous cylinder and a solid porous cylinder, added mass takes lower values and damping coefficient takes higher values for the former case than those for the latter case.

In all cases, the results are validated by comparing them with available results in the literature and the successful validation points towards the effectiveness of the present model in investigation of such ocean engineering problems.

The outcome of this present study suggests the selection of appropriate values of various parameters to be used to get the maximum benefit when a specific type of structure

(breakwater) in the form of a compound porous cylinder undergoes diffraction and/or radiation. The attenuation of wave energy and control of wave-run are the major objectives which are expected to be immensely helpful in designing appropriate porous structures for various applications in coastal and offshore engineering.

भारतीय प्रौद्योगिकी संस्थान गुवाहाटी
Indian Institute of Technology Guwahati

Nomenclature

i	$= \sqrt{-1}$
a	Radius of the inner cylinder
b	Radius of the outer cylinder
h, h_j	Water depth measured from the free surface $j = 1, 2, 3$
l	Thickness of the porous wall
g	Acceleration due to gravity
H	Amplitude of the incident wave
ω	Angular wave frequency
Φ	Velocity potential
ϕ	Spatial component of velocity potential in (r, θ, z)
$\Psi^m_{\text{rad},j}$	Radiation potential in the m-th mode in the j-th region
k_0	Wavenumber of the incident wave
k_j	Wavenumber of the scattered wave, $j = 1, 2, \ldots$
λ_j	Wavenumber of the scattered wave, $j = 0, 1, 2, \ldots$
σ_j	Wavenumber of the scattered wave, $j = 0, 1, 2, \ldots$
μ_j	Wavenumber of the scattered wave, $j = 0, 1, 2, \ldots$
γ_j	Wavenumber of the scattered wave, $j = 0, 1, 2, \ldots$
ρ	Density of fluid
G	Complex porous effect parameter of the structure
γ	Porosity of the structure
R	Dimensionless impedance of the porous medium
f	Linearized friction factor
S	Inertial coefficient
P	Dynamic pressure
p	Spatial dynamic pressure
$J_m(.)$	Bessel function of first kind of order m
$I_m(.)$	Modified Bessel function of first kind of order m
$K_m(.)$	Modified Bessel function of second kind of order m

$H_m^{(1)}(.)$	Hankel function of first kind of order m
$H_m^{(2)}(.)$	Hankel function of second kind of order m
$J'_m(.)$	Derivative of Bessel function of first kind of order m
$I'_m(.)$	Derivative of Modified Bessel function of first kind of order m
$K'_m(.)$	Derivative of Modified Bessel function of second kind of order m
$H_m^{(1)'}(.)$	Derivative of Hankel function of first kind of order m
$H_m^{(2)'}(.)$	Derivative of Hankel function of second kind of order m
Re	Real part
η_j	Wave run-up, $j = 1, 2, 3$
ζ_j	Spatial component of wave run-up, $j = 1, 2, 3$
$\tilde{F}_x^j$	Horizontal hydrodynamic force, $j = 1, 2$
$\widehat{F}_x^j$	Horizontal hydrodynamic force, $j = 1, 2$
$\tilde{F}_z^j$	Vertical Hydrodynamic force, $j = 1, 2$
M_{y1}	Moments due to the horizontal force
M_{y2}	Moments due to vertical force
$\mathcal{A}_l$	Coefficients matrices
$\mathcal{H}_l$	Coefficients matrices
$\mathcal{T}_l$	Coefficients matrices
$\mathcal{X}_l$	Unknown column matrices
$\mathcal{B}_l$	The right hand vectors in matrix equation
$\mathcal{Y}_l$	The right hand vectors in matrix equation
χ_{jl}	Added mass, $l, j = 1, 2, 3, 4, 5, 6$
Λ_{jl}	Damping coefficient, $l, j = 1, 2, 3, 4, 5, 6$
$\vec{v}$	Structural velocity
$\vec{n}$	Outward normal to the cylindrical surface
S_s	Solid surface of cylinder
S_p	Porous surface of cylinder

Contents

List of Figures

List of Tables

भारतीय प्रौद्योगिकी संस्थान गुवाहाटी
Indian Institute of Technology Guwahati

CHAPTER 1

Introduction

1.1 Preamble

A fluid is a substance that deforms continuously under an applied shear stress or, equivalently, one that does not have a preferred shape. Fluid mechanics is the study of fluids either in motion (fluid dynamics) or at rest (fluid statics) and the subsequent effects of the fluid upon the boundaries, which may be either solid surfaces or interfaces with other fluids. Gases and liquids both are classified as fluids, and the number of engineering applications of fluids is enormous: breathing, blood flow, swimming, pumps, fans, turbines, airplanes, ships, rivers, windmills, pipes, missiles, icebergs, engines, filters, jets, and sprinklers, to name a few. When one thinks about it, almost everything on this planet is either a fluid or something that moves within or near a fluid. The analysis of the behaviour of fluids is based upon the fundamental laws of applied mechanics that relate to the conservation of mass, energy and momentum. One of the key concepts in defining the fluid properties like density, volume, temperature, pressure etc. is the continuum assumption. According to this assumption, fluids are continuous matter rather than being made up of particles so that the fluid properties can be defined at infinitesimally small points and they vary continuously from one point to another. When fluid meets any solid boundary, then the fluid velocity is equal to that of the solid boundary. Physically, one can think of the outermost molecules of fluid to be stuck to the surfaces past which it flows. Because the solution is prescribed at given locations, this is an example of a *Dirichlet boundary condition*. This type of boundary condition is known as *no-slip condition*. There are two different points of view in analysing problems in fluid mechanics. The first, known as the *Lagrangian type*, involves observing the trajectory of each individual fluid parcel as it moves from some initial location. The alternative is the *Eulerian type* of specification which corresponds to a coordinate system fixed in space, and in which fluid properties

are studied as functions of time as the flow passes through fixed spatial locations. The Lagrangian type of specification is useful in certain special contexts, but it leads to rather cumbersome analysis and in general is at a disadvantage in not giving directly the spatial gradients of velocity in the fluid and hence, an Eulerian specification is being employed in most of the cases. In the Eulerian description, three types of curves are commonly used to describe fluid motions - *streamlines*, *pathlines*, and *streaklines*. These curves are often valuable for understanding fluid motion and they form the basis for experimental techniques that track seed particles or dye filaments. A *streamline* is a curve that is instantaneously tangent to the fluid velocity throughout the flow field. A *streakline* is the curve obtained by connecting all the fluid particles that will pass or have passed through a fixed point in space. A *pathline* is the line traced by a given particle. Streamlines, pathlines, and streaklines all coincide when the flow is steady.

Viscosity is that fluid property by virtue of which a fluid offers resistance to shear stresses. In fluid mechanics, most theoretical investigations begin from the concept of an *ideal fluid* where two contacting layers experience no *tangential forces* (i.e., shearing stresses) but act on each other with *normal forces* (i.e., pressure) only. It means that no internal resistance exists in an ideal fluid. On the other hand, the inner layers of a *real fluid* experience tangential as well as normal stresses. These frictional tangential forces in a real fluid describe the existence of viscosity. Fluid flow can be categorized into different types in accordance with its various properties. If the density of a fluid changes significantly with changes in pressure and temperature, the flow is called a *compressible fluid flow*; and if the change in density is negligible, it is called an *incompressible fluid flow*. Specifically in aerodynamics, *Mach number* (the ratio of the speed of an object moving through a fluid to the local speed of sound) of the flow is utilized in order to determine compressible and incompressible flows. The flow is called *inviscid* or *non-viscous* if the viscosity (measure of resistance to gradual deformation) is negligible, otherwise it is called *viscous*. If the fluid properties do not change with respect to time, the flow is termed as *steady* flow but if the properties change in time, the flow is termed *unsteady*. Recirculation, swirl in the flow and randomness in the fluid make a flow *turbulent*. A fluid flow is called *laminar* if turbulence is not exhibited in the flow. Depending upon the mathematical relation between stress and strain, fluid is categorized into two types: *Newtonian* fluid (water, air etc.), which satisfies a very close linear relation between stress (internal force) and strain (normalized measure of deformation); *non-Newtonian* (blood, polymer, latex, honey etc.), which does not follow any linear relation between stress and strain. Fluid flow is also termed as *subsonic*, *transonic*, *supersonic* and *hypersonic* depending upon the velocity (*Mach number*) of the flow.

A flow field with a velocity vector $\vec{u}$ is said to be *irrotational* if curl $\vec{u} = 0$; otherwise, it is called *rotational*. The condition of irrotationality guarantees the existence of a scalar function ϕ, called the velocity potential. If the flow is both irrotational and incompressible, the Laplacian of the velocity potential must be zero - giving us the equation of continuity

for a potential flow.

In physics, mathematics and related fields, a wave is a disturbance (change of state from equilibrium position) of one or more fields such that the field values oscillate repeatedly about a stable equilibrium (resting) value. There are two types of waves, namely, *mechanical* wave and *electromagnetic* wave. In a mechanical wave, stress and strain fields oscillate about a mechanical equilibrium (water wave, sound wave etc.). In an electromagnetic wave, the electric and magnetic fields oscillate. A traveling electromagnetic wave (light) consists of a combination of variable electric and magnetic fields that propagates through space. Radio waves, infra-red radiation, visible light, ultraviolet radiation, X-rays and gamma rays etc. are some examples of electromagnetic wave.

In practical sense, a simple example of water waves is the one when we throw a stone into a pond and observe sinusoidal ripples around the point of impact and spreading in all directions. More instances are: when wind blows over water region (lake, ocean etc.) and creates ripples on the water surface; due to the motion of a ship in an ocean; flow over bottom undulation in a water region. These types of waves have small amplitudes of oscillation. But there also exist cases where the amplitude is not that much small but is significantly visible. Tidal waves, Rogue waves and Tsunami waves are such kind of waves where a huge amount of energy is carried through the waves which may create destruction in coastal areas, structures in ocean (e.g., petroleum extraction machinery) and floating objects (e.g., ships, submarines). For this reason, the topic of wave-structure interaction is a major branch of fluid mechanics and assumes special significance due to its wide range of applications in marine technology and ocean engineering.

In recent times, various types of porous breakwaters have been proposed by researchers for the protection of coastal regions and construction sites. Porous structures reduce the wave loads and wave run-up on them. These structures are also extensively used in the construction of floating airports, bridges, piers, docks, wave power conversion system etc. Vertical cylinders are found to be more appropriate for use in the construction of coastal and offshore structures. The objective is focussed on designing marine structures that will be able to resist various atmospheric conditions. Therefore, investigation in the area of hydrodynamics has laid special emphasis on developing an optimized system in order to find a way to avoid significant hydrodynamic impacts.

In water wave mechanics, when a physical problem is formulated, then water is usually considered in a region bounded by a free surface (in contact with the atmosphere) or a rigid surface or a porous surface or any other medium. Moreover, virtual boundaries are also incorporated for the sake of simplification and convenience. There is a parallel interest in analysing wave interaction with a large floating ice-sheet which can be modeled as a large floating elastic plate obeying the Euler- Bernoulli beam equation and is of significant importance in the marginal ice zone of the polar region. In many situations, the structures are considered flexible in nature and a precise hydroelastic analysis is required to analyse several hydrodynamic characteristics. Some of these structures have advantages

over the traditional rigid structure because they are reusable, environmental-friendly and cost-effective. As a result, a substantial growth of knowledge in the dynamics of ocean surface waves and their effects on ocean structures has been witnessed in the past few decades. Depending upon the physics of the problem, the wave motion within the water region follows either Laplace's or Helmholtz or modified Helmholtz equation along with boundary conditions of Dirichlet type (no derivative involved) or Neumann type (only derivative involved) or Robin type (mixture of derivative and non-derivative). There are a number of methods available for solving water wave problems such as Fourier analysis, complex function theory, Green's function techniques, the boundary integral equation method, the least square approximation method, the wide spacing approximation method, integral transform methods and the method of stationary phase. Analogous theory is also applicable for a porous structure.

The history of water waves is a few centuries old which can be found in the study of Craik [8] who has thoroughly penned down all aspects of water wave theory. Through his narration, we discuss briefly the development of water wave theory. Isaac Newton was the first one to attempt to present a theory of water waves. In Book II, Prop. XLV of *Principia* (1687), he proposed a dubious analogy with oscillations in a U-tube, correctly deducing that the frequency of deep water waves must be proportional to the inverse of the square root of the "breadth of the wave". Later, Newton's argument was also supported by many others such as Wilhelm-Jacob's Gravesande (1721) and the Charles Bossut (1786). After that, Joseph Louis Lagrange (1781, 1786), perhaps independently, derived the linearised governing equations for small-amplitude waves, and obtained the solution in the limiting case of long plane waves in shallow water. This is repeated almost exactly in '*Mechanique Analitique*' (1788). For shallow water waves, he found that "the speed of propagation of waves will be that which a heavy body would acquire in falling from ... half the height of the water in the canal" (Lagrange 1786); that is, $(gh)^{1/2}$, where g is gravitational acceleration and h the liquid depth. Before 1800, a few other works also discussed wave motion. Exceptional works were carried out by M. Flaugergues (1793) and Francois de la Coudraye (1796) and later summarized by Weber and Weber (1825).

Franz Joseph von Gerstner (1802) explained the first exact nonlinear solution for waves of finite amplitude for deep water. The Gerstner wave solution was long overlooked; even today it is usually regarded more as a curiosity rather than a result of practical importance because the motion is not irrotational. Its independent rediscovery was due to W. J. Macquorn Rankine (1863). In December 1813, the French *Academie des Sciences* announced a prize for a mathematical competition on surface wave propagation in liquid of indefinite depth. In July 1815, 25 year-old Augustin-Louis Cauchy submitted his entry, and, in August, Simeon D. Poisson, one of the judges, deposited a memoir of his own to record his independent work. Cauchy was awarded the prize in 1816, Poisson's memoir was published in 1818, and Cauchy's work eventually appeared in 1827, with an astonishing 188 pages of additional notes. Horace Lamb in *Hydrodynamics* (1895) gave

the Cauchy-Poisson analysis, but restricted it to two-dimensional disturbances. The first edition of his book is brief, incomplete and relegated it to small print, but he treated the subject more elaborately in the fourth edition in 1916. The Cauchy-Poisson analysis is now acknowledged as an important milestone in the mathematical theory of initial value problems. A very different work on waves was published in Leipzig: *Wellenlehre auf Experimente gegrundet* (1825) by the brothers Ernst Heinrich Weber and Wilhelm Eduard Weber. This book describes Weber's careful laboratory experiments in plane periodic wave trains in a channel, together with extracts from and comments on such theoretical work as was then available. In 1837, John Scott Russell and Sir John Robinson [44] provided a remarkable report on wave characteristics in sea, river and canals. These experiments are now well known for the discovery of nonlinear solitary waves. They had distinguished four types of waves: waves of translation, including their newly found solitary waves, tides, and bores; oscillatory waves, or periodic wave trains; capillary waves; and corpuscular waves, which are compressive sound waves propagating through water. Next year, George Green [17] gave an exemplary analysis of the effects of slow variations on the motion of waves in a variable canal of small depth and width, though limited to the long linear shallow water wave. In 1840, Philip Kelland [20] investigated long waves of small amplitude in canals with triangular cross sections, and correctly derived the result of the wave speed. The representation of a solitary wave by discontinuous expressions was taken up by Samuel Earnshaw [14] in 1847. He pointed out the conspicuous lack of success in obtaining general solutions to the equations of hydrodynamics, and he emphasized the need to limit theoretical studies to restricted classes of motions, based on hypotheses suggested by experiments. Later that year, a nonlinear theory attempted by him failed which George Gabriel Stokes [51] developed. In 1876, Bénard Rayleigh [43] derived the correct approximate solution, retaining both dispersion and nonlinearity, and he further observed that Earnshaw's solution was not irrotational. George Biddell Airy's long and influential article "Tides and Waves" was published in the *Encyclopaedia Metropolitana* in 1841. When it appeared, Airy's scientific reputation as mathematician and astronomer was already of very high standing. Airy's article has long been recognized as a major contribution to water wave theory.

For a variety of ocean engineering applications, the boundary value problems are set up in an appropriate coordinate system usually with Laplace's equation as the governing equation and sometimes with Helmholtz equation or modified Helmholtz equation. Depending on the problem, the available boundary conditions as well as matching conditions are applied to solve the problem. Subsequently, the required quantities, such as forces, moments, wave run-up and hydrodynamic coefficients can be computed and the same may be analysed with respect to various important parameters. In the following section, a brief description of the basic equations and conditions in linearised water wave theory for the case of constant depth are presented.

1.2 Relevant equations and conditions

In this section, we briefly describe the equations of motion inside the fluid domain in an ocean. Below we present some important definitions and description in connection with water waves which will be beneficial in understanding the basics of water wave theory.

With the help of linearised water wave theory, different boundary conditions are derived and discussed. We consider the fluid to be homogeneous, incompressible and inviscid, and the motion irrotational. The sea-bed is considered to be flat and impermeable. The

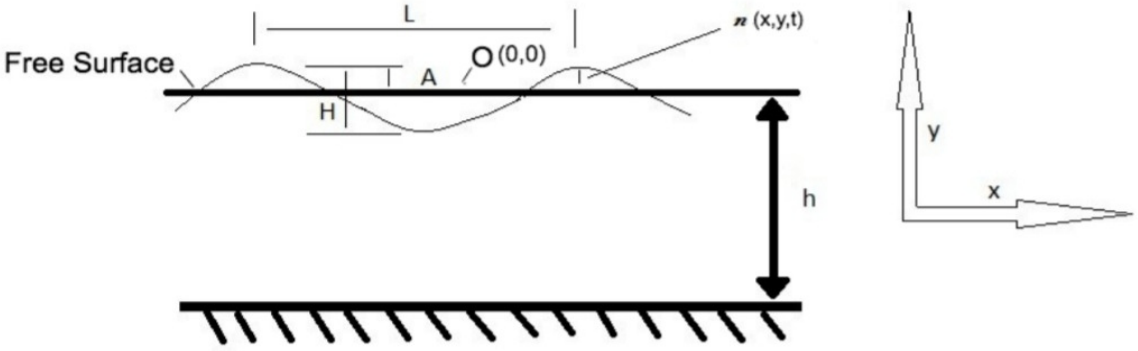

Figure 1.1: Schematic diagram of wave propagation

important parameters to describe waves are their length and height, and the water depth over which they propagate. All other parameters, such as wave-induced water velocities and accelerations, can be determined theoretically from these quantities. Figure 1.1 represents the two-dimensional schematic diagram of a wave propagating in the x-direction. A *crest* is a point on a surface wave where the displacement of the medium is at maximum. A *trough* is the opposite of a crest and so it is the minimum or lowest point in a wave cycle. The *wavelength* L is the horizontal distance between two successive wave crests or the highest points on a wave or alternatively, the distance between two consecutive wave troughs. The standard notations associated with a water wave are as follows:
h: water depth - from mean water level to the bottom of the sea,
$\eta(x, y, t)$: vertical displacement of water surface above mean water level,
$A = \dfrac{H}{2}$: wave amplitude,
H: wave height,
T: wave period,
$k = \dfrac{2\pi}{L}$: wavenumber,
$\omega = \dfrac{2\pi}{T}$: wave angular frequency.
Here a two-dimensional reference coordinate in x and y is considered.

Ocean waves are almost always seen as *irregular* or *random*. *Irregular waves* can be

viewed as the superposition of a number of regular waves (wave components) with different frequencies and amplitudes. A regular wave (wave component) has a single frequency (wavelength) and amplitude (height). *Wind waves*, *swells* are some examples of regular water waves. *Surf beats*, *harbour resonance*, *seiche* and *tsunamis* can be categorized into irregular wave. According to wavelength, there are two types of water waves that exist. One is called *deep water wave* and the other is called a *shallow water wave*. When the wavelength of water wave is much larger than the depth of water, it is called shallow water wave (or long wave). Tidal waves, Tsunami waves are some examples of shallow water wave. Then there are waves whose wavelengths are smaller compared to the depth of water and they are termed as deep water waves (or short waves). Rogue wave falls into this category. There are also waves which are neither shallow water waves nor deep water waves and they are known as *intermediate depth* water waves. If it is assumed that the amplitude of the wave is small compared to the wavelength, then the theory is called *linearised theory of water waves*. It may be noted that ocean waves are in general nonlinear. However, it has been found that for most of the engineering applications, experiments establish that there is only a very small margin of error if linear theory is employed instead of nonlinear theory. Therefore, the problems in water wave mechanics are usually modelled for small amplitude waves, i.e., by employing linear wave theory. In this thesis, linearised water wave theory is utilized to tackle all the problems taken up.

The equations for conservation of mass and momentum for inviscid incompressible fluid with velocity $\vec{u}$ are given by

$$\nabla.\vec{u} = 0, \tag{1.1}$$

$$\frac{\partial \vec{u}}{\partial t} + (\vec{u}.\nabla)\vec{u} = \vec{g} - \frac{1}{\rho}\nabla p, \tag{1.2}$$

where ρ is the density, $\vec{g}$ is the acceleration due to gravity and p is the pressure. Now consider that the flow is irrotational. Then we can find a potential function Φ such that

$$\vec{u} = -\nabla\Phi. \tag{1.3}$$

Now substituting (1.3) in (1.1), we get the **Laplace's equation**

$$\nabla^2\Phi = 0, \tag{1.4}$$

which is the equation of continuity for a potential flow. For time harmonic motions, a velocity potential in cartesian coordinates (x, y, z) can be expressed as

$$\Phi(x, y, z, t) = \mathrm{Re}[\phi(x, y, z)\exp(-\mathrm{i}\omega t)], \tag{1.5}$$

where $\phi(x, y, z)$ is the complex-valued potential, ω is the angular wave frequency and 'Re'

denotes the real part. If gravity acts in the negative z-direction, then we can write

$$\vec{g} = \nabla(-gz). \tag{1.6}$$

The momentum equation, therefore, becomes

$$\nabla\left[\frac{\partial\Phi}{\partial t} + \frac{1}{2}\nabla\Phi.\nabla\Phi + \frac{p}{\rho} + gz\right] = 0, \tag{1.7}$$

which, after integration, can be written as

$$\frac{\partial\Phi}{\partial t} + \frac{1}{2}\nabla\Phi.\nabla\Phi + \frac{p}{\rho} + gz = C(t), \tag{1.8}$$

for some function $C(t)$. However, we can take $C(t) = 0$ by using the simple transformation

$$\Phi = \Phi + \int_0^t C(s)ds,$$

which does not affect the velocity field. For this type of flow, we obtain **Bernoulli's equation** (dynamic boundary condition) as

$$\frac{\partial\Phi}{\partial t} + \frac{1}{2}\nabla\Phi.\nabla\Phi + \frac{p}{\rho} + gz = 0. \tag{1.9}$$

In the Cartesian coordinate system (x, y, z), x and y are measured in horizontal directions while z is measured vertically upward from the undisturbed water level. The water depth $h(x, y)$ is a varying function of x and y. On the free surface $z = \eta$, the kinematic boundary condition is given by

$$\frac{\partial\Phi}{\partial z} = \frac{\partial\eta}{\partial t} + \frac{\partial\eta}{\partial x}\frac{\partial\Phi}{\partial x} + \frac{\partial\eta}{\partial y}\frac{\partial\Phi}{\partial y}, \quad \text{at} \quad z = \eta(x, y, t). \tag{1.10}$$

Here by employing linear water wave theory, we have the following boundary value problem consisting of the governing equation

$$\nabla^2\Phi \;=\; 0, \tag{1.11}$$

subject to the linearised dynamic boundary condition

$$\frac{\partial\Phi}{\partial t} + \frac{p}{\rho} + g\eta = 0, \quad \text{at} \quad z = 0, \tag{1.12}$$

and the linearised kinematic condition

$$\frac{\partial\Phi}{\partial z} = \frac{\partial\eta}{\partial t} \quad \text{at} \quad z = 0. \tag{1.13}$$

Combining (1.12) and (1.13), we get the free surface condition at $z = 0$, by taking $\vec{p} = 0$, as

$$\frac{\partial \Phi}{\partial z} - \frac{\omega^2}{g}\Phi = 0. \tag{1.14}$$

If S is a boundary of an obstacle through which the fluid cannot pass, we define an impermeable boundary condition

$$\frac{\partial \Phi}{\partial n} = 0 \qquad \text{on } S, \tag{1.15}$$

where n is the outward normal drawn at the boundary S and $\frac{\partial}{\partial n}$ represents differentiation along the normal to the boundary S. In the case of an impermeable bottom boundary at a constant depth $z = -h$, the above condition reduces to

$$\frac{\partial \Phi}{\partial z} = 0 \quad \text{at} \quad z = -h. \tag{1.16}$$

Depending on the problem, different types of coordinate system, such as cylindrical or spherical may be considered. Accordingly, the equation will take an appropriate form.

1.3 A brief discussion on fluid flow through porous media

While discussing the theory of flow inside a porous material, first we will elaborate some concept about porous medium and its applications. Porous medium or a porous material is a medium or a material containing pores. The skeletal part of the medium is often called the "matrix" or "frame". The pores are typically filled with a fluid (liquid or gas). The skeletal part is usually a solid, but structures like foams are also often usefully analysed using concept of porous media. Many natural substances such as rocks and soil (e.g., aquifers, petroleum reservoirs), zeolites, biological tissues (e.g., bones, wood, cork), and man-made materials such as cements and ceramics can be considered as porous media. Many of their important properties can be rationalized only by considering them to be porous media. The idea of porous media is used in many areas of applied science and engineering: filtration, mechanics (acoustics, geomechanics, soil mechanics, rock mechanics), engineering (petroleum engineering, bioremediation, construction engineering), geosciences (hydrogeology, petroleum geology, geophysics), biology and biophysics, material science etc.

There are two types of porous medium, namely, *saturated* and *unsaturated* porous medium. In saturated porous medium, all void space is filled with fluid while for unsaturated porous medium, the void is partially filled with liquid and the remaining part is occupied by air. There is a very important term called *porosity* which signifies the

amount of pores in a material of medium. Porosity or void fraction is a measure of the void (i.e., "empty") spaces in a material, and is a fraction of the volume of voids over the total volume, between 0 and 1. Let us select any point in a porous medium and its environment with a sufficiently large volume V_T, where

$$V_T = V_P + V_S,$$

with V_P as the void volume (pore volume) and V_S the volume of the solid material. Porosity, defined as the ratio of pore volume to total volume, can be expressed as and denoted by γ as follows:

$$\gamma = \frac{V_P}{V_T} = \frac{V_T - V_S}{V_T}.$$

Types of porosity

- Primary porosity (The porosity of a rock or any other natural porous material that happens at the depositing time.)
- Secondary porosity (The porosity that grows after deposition of the rock or any other natural porous material.)

Further, porosity can be categorized into six types depending on the size of the pores:

- Total Porosity (It is a ratio of the entire pore space in a rock to its bulk volume.)
- Effective Porosity (It is a measure of the void space that is filled by recoverable oil and gas),
  porosity$= \frac{\text{Vol. of interconnected pores + Vol. of deadend}}{\text{Total or bulk vol. of reservoir rock}}$.
- Dual porosity (It is a conceptual idea that there are two overlapping reservoirs which interact. In fractured rock aquifers, the rock mass and fractures are often simulated as being two overlapping but distinct bodies.)
- Microporosity (Pore size is smaller than 2 nanometers in diameter.)
- Mesoporosity (Pore size is greater than 2 nanometers and less than 50 nanometers in diameter.)
- Macroporosity (Pore size is greater than 50 nanometers in diameter.)

Porosity measuring method

There are several types of methods for finding porosity such as

- Direct method

- Optical method
- Computed tomography method
- Imbibition method
- Gas expansion method.

Darcy's law for flow in porous media

Darcy's law is a relation that describes the flow of a fluid through a porous medium. Historically, Darcy's law was proposed as an empirical relationship on the basis of laboratory experiments in 1856, while the theoretical basis was developed in later years. It is analogous to Fourier's law in the field of heat conduction, Ohm's law in the field of electrical networks, or Fick's law in diffusion theory.

Laminar stationary flow of an incompressible flow through a homogeneous porous medium can be expressed by Darcy's law as

$$\vec{u} = -\frac{\mathcal{K}}{\epsilon}\nabla p,$$

where, $\vec{u}$ is the fluid velocity, and p is fluid pressure at the pore scale. The symbol $\mathcal{K}$ represents the medium permeability and ϵ is the dynamic viscosity. The Carman-Kozeny equation gives a relation between particle diameter (d_p) and porosity (γ) as

$$\mathcal{K} = \frac{d_p^2\gamma^2}{180(1-\gamma)^2}.$$

Permeability has dimension of meter^2. In applications, one can expect to have a length scale for the device itself, say $\mathcal{L}$, and the ratio defined by $\mathcal{D} = \dfrac{\mathcal{K}}{\mathcal{L}^2}$ is called the Darcy number. Larger Darcy numbers indicate larger particle diameters and pore sizes. Darcy number zero means that no fluid can enter into the structure.

In our work, we deal with cylindrical porous structures. Therefore, we establish the porous wall condition on the cylindrical surface by using the Darcy's law. Equation (1.5) recalls that, for time-harmonic motions, a velocity potential can be expressed as

$$\Phi(r,\theta,z,t) = \mathrm{Re}[\phi(r,\theta,z)\exp(-\mathrm{i}\omega t)]. \tag{1.17}$$

Let $v(r,\theta,z)$ be the spatial component of the normal velocity of the fluid passing through the porous cylinder from the exterior region to the interior region, i.e.,

$$V(r,\theta,z,t) = \mathrm{Re}[v(r,\theta,z)\exp(-\mathrm{i}\omega t)]. \tag{1.18}$$

The fluid passing through the porous walls is assumed to obey Darcy's law. Therefore, the flow velocity is linearly proportional to the pressure difference across the boundary

of the porous cylinder as can be seen from Taylor [52]. Now the hydrodynamic pressure $P(r,\theta,z,t)$= Re$[p(r,\theta,z)\exp(-\mathrm{i}\omega t)]$ at any point in the fluid domain may be determined from the linearised Bernoulli's equation as $p = \mathrm{i}\rho\omega\phi$, where ρ is the fluid density. Therefore,

$$v(r,\theta,z) = \frac{\mathcal{L}\mathrm{i}\rho\omega}{\varepsilon}(\phi_1 - \phi_2) = \mathrm{i}k_0 G(\phi_1 - \phi_2) \tag{1.19}$$

is the condition at the boundary of the porous wall, where ϕ_1 and ϕ_2 are, respectively, the velocity potentials in the fluid region and porous region. The term $G = \dfrac{\mathcal{L}\rho\omega}{\varepsilon k_0}$ is the dimensionless porous parameter as used by Chwang [7], where k_0 is the incident wavenumber. The parameter G can be written as $G_r + \mathrm{i}G_i$ as used by Yu [64], where G_r denotes the real part and G_i the imaginary part. In practice, G always possesses positive real and imaginary parts except when the resistance effect against the flow dominates the inertial effect of the fluid inside the porous material in which case G becomes real. Similarly, when the inertial effect dominates the resistance effect, G becomes purely imaginary. The parameter G may be viewed as a Reynolds number for the flow passing through the fine pores of the wall (Chwang [7]). It is also a measure of the porous effect of the wall. $G = 0$ implies that the porous wall is impermeable. On the other hand, as G approaches infinity, the porous wall is completely permeable to fluid, that is, there would be no porous wall at all. Basically we work with Darcy's law, which is applicable for low Reynolds number flow through porous wall. Furthermore, Sankarbabu et al. [47] proposed to choose G as

$$\begin{aligned} G &= \frac{\mathcal{L}\rho\omega}{\varepsilon k_0} \\ &= \frac{\mathcal{L}\rho\sqrt{gk_0\tanh k_0 h}}{\varepsilon k_0} \qquad \text{(From dispersion relation)} \\ &= \frac{\rho\mathcal{L}\sqrt{gh}}{\varepsilon}\sqrt{\frac{\tanh k_0 h}{k_0 h}}, \end{aligned} \tag{1.20}$$

with h as the draft of the structure. Initially, the value of G for a given porosity can be obtained by the trial and error method. On substitution of the obtained G and other known values in the above equation, the unknown material constant ($\mathcal{L}$) for the given porosity of the outer cylinder may be calculated. Based on linear extrapolation, the material constant values for other porosities are computed resulting in values of G.

1.4 Interaction of linear water waves with a structure

Water waves interact with various types of structures or obstacles. Some of those structures are constructed in ocean by human for various applications, such as breakwater, platform, etc. and some others are naturally occurring obstacles like rocks, sand etc. at the ocean bottom. While looking into the interaction of waves with those, the phenomena

to be examined into are scattering and/or radiation.

On the surface of a structure, the normal component of the structural velocity must be equal to the velocity component in the same direction of an adjacent fluid particle. In general, it can be written as

$$\frac{\partial \Phi}{\partial n} = V_n,$$

where V_n is the component of the structural velocity in the direction of the normal co-ordinate n directed out of the fluid. In the linearised water wave theory, this condition is applied on the equilibrium surface of the structure which is denoted by S_B. A wave train incident upon a floating structure is diffracted to produce a scattered wave field and also sets the structure in motion to produce a radiated field. By linear superposition, the velocity potential may be decomposed into two parts as

$$\Phi = \Phi_S + \Phi_R.$$

The potential Φ_S is the solution of the scattering problem in which the structure is held fixed in the waves and it may be further decomposed as

$$\Phi_S = \Phi_{\text{inc}} + \Phi_D,$$

where Φ_{inc} represents the incident wave train and Φ_D the diffracted waves. When the structure is held fixed, the appropriate boundary condition is

$$\frac{\partial \Phi_S}{\partial n} = 0 \quad \text{on } S_B.$$

The potential Φ_R is the solution of the radiation problem, in which the structure is forced to oscillate in the absence of an incident wave, and satisfies

$$\frac{\partial \Phi_R}{\partial n} = V_n \quad \text{on } S_B. \tag{1.21}$$

In general, the normal velocity V_n is found from the equation of motion of the structure (Newman [37], Chapter 6) and will depend, in particular, on the forces that result from any incident wave.

It is known that a rigid floating structure in ocean can undergo six degrees of freedom: three translational motions in the x-, y- and z-directions, known as surge, sway and heave, respectively, and three rotational motions about the x-, y- and z-axes, known as roll, pitch and yaw, respectively (Figure 1.2). In general, the motion of the structure will be a combination of movements in all of these directions and the velocity of a point on the surface, measured normal to the surface, may be written as

$$V_n = \vec{U}.\vec{n} + \vec{\Omega}.(\vec{r} \times \vec{n}), \tag{1.22}$$

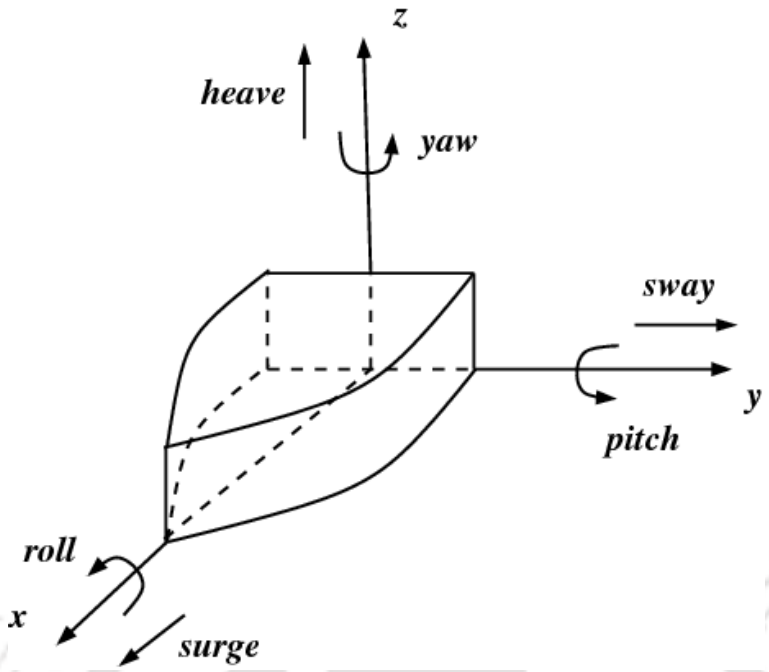

Figure 1.2: Motions of a floating body

where $\vec{r}$ is the position vector of the point measured from the centre of rotation and $\vec{n}$ is a normal vector to the structure's surface directed out of the fluid. Here, the translational velocity vector

$$\vec{U} = (U_1, U_2, U_3), \tag{1.23}$$

has components corresponding to surge, sway, and heave motions, respectively, and the rotational velocity vector

$$\vec{\Omega} = (U_4, U_5, U_6) \tag{1.24}$$

has components corresponding to roll, pitch, and yaw, respectively. The normal velocity V_n given by (1.22) may be rewritten as

$$V_n = \sum_{\mu=1}^{n} U_\mu n_\mu, \tag{1.25}$$

where $n_\mu; \mu = 1, 2, 3$ are the x, y, z components of the unit normal to the structure defined by the direction cosines

$$\begin{aligned} n_1 &= \cos(n, x), \\ n_2 &= \cos(n, y), \\ n_3 &= \cos(n, z), \end{aligned}$$

whereas $n_\mu; \mu = 4, 5, 6$ are the corresponding components of $(\vec{r} \times \vec{n})$. If a point on the structure's surface has coordinates (x, y, z), and if (x', y', z') is the equilibrium position of

the centre of rotation, then

$$\begin{aligned} n_4 &= (y-y')n_3 - (z-z')n_2, \\ n_5 &= (z-z')n_1 - (x-x')n_3, \\ n_6 &= (x-x')n_2 - (y-y')n_1. \end{aligned}$$

For time harmonic motions, each velocity component may be written as

$$U_\mu = \mathrm{Re}(u_\mu e^{-\mathrm{i}\omega t}), \tag{1.26}$$

by linear superposition of the radiated velocity potentials, defined in

$$\Phi_R = \mathrm{Re}(\phi_R(r,\theta,z)e^{-\mathrm{i}\omega t}),$$

which may be decomposed as

$$\phi_R = \sum_{\mu=1}^{6} u_\mu \phi_\mu,$$

where u_μ is the complex amplitude of the oscillations in mode μ. The potential ϕ_μ describes the wave field due to oscillations in mode μ with unit velocity amplitude. The boundary condition (1.21) can be rewritten as

$$\frac{\partial \phi_\mu}{\partial n} = n_\mu \quad \text{on } S_B \quad \mu = 1, 2, \cdots, 6. \tag{1.27}$$

Also the boundary condition at the porous wall is given by Williams et al. [60] as

$$\frac{\partial \phi}{\partial n} = n_\mu - w(r,\theta,z) \quad \text{on} \quad S_p, \tag{1.28}$$

where S_p denotes the porous boundary.

To obtain a unique solution of the diffracted potential Φ_D and the radiated potential Φ_R, respectively, each must satisfy a radiation condition specifying that the waves corresponding to these potentials propagate away from the structure. For Φ equal to either Φ_D or Φ_R, the radiation condition can be written as (known as Sommerfeld radiation condition)

$$\lim_{r\to\infty} \sqrt{r}\left[\frac{\partial \Phi}{\partial r} - \mathrm{i}k\Phi\right] = 0, \tag{1.29}$$

in three dimensions, where k is the wavenumber, r is the horizontal polar coordinate. Once the total velocity potential is known and the pressure on the surface of the structure is known from Bernoulli's equation, the total force $\vec{F}$ exerted on the body and moment

$\vec{M}$ of this force in vector notation may be obtained from the following formulas:

$$\begin{aligned} \vec{F} &= -\iint_{S_B} p\,\vec{n}\mathrm{d}S, \\ \vec{M} &= -\iint_{S_B} p\,(\vec{r}\times\vec{n})\mathrm{d}S, \end{aligned}$$

where S_B is the submerged surface of the body. Now, the hydrodynamic pressure due to the radiated potential is obtained from linearised Bernoulli's equation

$$p_j = \mathrm{i}\rho\omega\phi_{R,j}(r,\theta,z) \tag{1.30}$$

where $\phi_{R,j}$ is the radiated or forced potentials due to the oscillation of the structure in the j-th mode. The radiated force is the force due to the motion of the body. It can be computed from the radiated potential whereby the general radiated force on the body due to j-th motion can be written as

$$F_{j,l} = -\mathrm{i}\rho\omega\iint_{S_B}\phi_{R,j}(r,\theta,z)\;n_l\;\mathrm{d}S. \tag{1.31}$$

Here $F_{j,l}$ is the radiated force acting on the body in the l-th direction with amplitude in the j-th direction and n_l is the component of the unit normal vector pointing to the cylinder at the cylinder surface, which can be rewritten as (Rahman [41])

$$F_{j,l} = \mathrm{i}\omega\left(\chi_{jl}+\mathrm{i}\frac{\Lambda_{jl}}{\omega}\right). \tag{1.32}$$

The first term is that part of the equation (1.32) in phase with the acceleration in mode j, and the second term is that part in phase with the corresponding velocity. Also, the notations χ_{jl} and $\dfrac{\Lambda_{jl}}{\omega}$ denote the *added mass* and *damping coefficient*, respectively. Now from equations (1.31) and (1.32), we can write

$$\left(\chi_{jl}+\mathrm{i}\frac{\Lambda_{jl}}{\omega}\right) = -\rho\iint_{S_B}\phi_{R,j}(r,\theta,z)\;n_l\;\mathrm{d}S. \tag{1.33}$$

From equation (1.33), the added mass and damping coefficient can be evaluated by considering the real part and the imaginary part, respectively of the right hand side. In physical sense, the added mass is the weight added to a system in a fluid due to the fact that an accelerating or decelerating body must move some volume of surrounding fluid with it as it moves. Damping is an influence within or upon an oscillatory system that has the effect of reducing, restricting or preventing its oscillations. All bodies accelerating in a fluid will be affected by added mass, but since the added mass is dependent on the density of the fluid, the effect is often neglected for dense bodies moving in much less dense fluids. For situations where the density of the fluid is comparable to or greater than

the density of the body, the added mass can often be greater than the mass of the body. This property also applies to ships, submarines, and offshore platforms. For ships, the added mass can reach even 3 to 4 times the mass in heave mode and up to 2 times the mass in surge mode. Damping models refer to the energy dissipation during vibrations. These models are important for the stability of a structure in motion and its vibration amplitudes. Damping may arise from the structure and from the fluid surrounding it.

1.5 Evaluation of velocity potential in cylindrical coordinates

Evaluation of velocity potentials in various fluid regions for different problems considered in this thesis is a very important step. Since evaluation of these potentials are not discussed along with the problems, we deem it suitable to discuss the evaluation of one such potential by using methods of separation of variables and eigenfunction expansion. We discuss and evaluate velocity potential in the cylindrical coordinate system which we use throughout our problems due to consideration of cylindrical structure only. The incident velocity potential of amplitude H and angular wave frequency ω propagating along the positive x-direction in a uniform ocean depth h is given by (MacCamy and Fuchs [23])

$$\phi_{\text{inc}} = -\frac{\mathrm{i}gH}{\omega}\frac{\cosh k_0(z+h)}{\cosh k_0 h}e^{\mathrm{i}k_0 x}. \tag{1.34}$$

If the polar coordinates r and θ are used, then

$$e^{\mathrm{i}k_0 x} = e^{\mathrm{i}k_0 r\cos\theta} = \sum_{m=0}^{\infty}\tau_m J_m(k_0 r)\cos m\theta,$$

with

$$\tau_m = \begin{cases} 1, & m = 0, \\ 2\mathrm{i}^m, & m \geq 1, \end{cases}$$

where $J_m(.)$ is the Bessel function of first kind of order m. Subsequently,

$$\phi_{\text{inc}} = -\frac{\mathrm{i}gH}{\omega}\frac{\cosh k_0(z+h)}{\cosh k_0 h}\sum_{m=0}^{\infty}\tau_m J_m(k_0 r)\cos m\theta. \tag{1.35}$$

We consider the following three-dimensional Laplace's equation for the potential ϕ in cylindrical coordinate:

$$\frac{1}{r}\frac{\partial}{\partial r}\left(r\frac{\partial\phi}{\partial r}\right) + \frac{1}{r^2}\frac{\partial^2\phi}{\partial\theta^2} + \frac{\partial^2\phi}{\partial z^2} = 0. \tag{1.36}$$

Now when we substitute $\phi(r,\theta,z) = \Psi(r,\theta)Z(z)$, then equation (1.36) becomes

$$\frac{1}{\Psi}\left[\frac{1}{r}\frac{\partial}{\partial r}\left(r\frac{\partial \Psi}{\partial r}\right) + \frac{1}{r^2}\frac{\partial^2 \Psi}{\partial \theta^2}\right] = -\frac{1}{Z}\frac{\mathrm{d}^2 Z}{\mathrm{d}z^2} = \alpha^2, \tag{1.37}$$

where the separation constant, or eigenvalue, α is to be determined by the boundary conditions. The general solution for $Z(z)$ may be written as

$$Z(z) = E\cos\alpha(z+h) + F\sin\alpha(z+h), \tag{1.38}$$

by using flat bottom boundary condition $\dfrac{\partial \phi}{\partial z} = 0$ at $z = h$ which immediately gives $F = 0$ and the free surface condition is satisfied provided α is a root of the dispersion relation

$$\omega^2 = -g\alpha\tan\alpha h, \tag{1.39}$$

which has an infinite sequence of positive real roots, which are denoted by $k_n; n = 1, 2, 3, \ldots$. There is also a sequence of negative roots $-k_n; n = 1, 2, 3, \ldots$, but these lead to exactly the same eigenfunctions and so need not be considered separately. Also, k_0 can take purely imaginary values, say $-\mathrm{i}k$, and in that case k is the positive root of the dispersion relation

$$\omega^2 = g\alpha\tanh\alpha h. \tag{1.40}$$

Again it is sufficient to consider only the positive root.
Farther from the equation (1.37), we get

$$\frac{1}{r}\frac{\partial}{\partial r}\left(r\frac{\partial \Psi}{\partial r}\right) + \frac{1}{r^2}\frac{\partial^2 \Psi}{\partial \theta^2} = k_n^2\Psi. \tag{1.41}$$

Now we consider separable solution of the form $\Psi(r,\theta) = R(r)\Theta(\theta)$ and therefore

$$\frac{r^2}{R}\left(\frac{1}{r}\frac{d}{dr}\left(r\frac{\partial R}{\partial r}\right) - k_n^2 R\right) = -\frac{1}{\Theta}\frac{\mathrm{d}^2\Theta}{\mathrm{d}\theta^2} = \beta^2, \text{ say.} \tag{1.42}$$

The general solution for Θ is

$$\Theta(\theta) = A\cos(\beta\theta) + B\sin(\beta\theta) \tag{1.43}$$

for some constants A and B. Then the differential equation for $R(r)$ becomes

$$r\frac{d}{dr}\left(r\frac{\partial R}{\partial r}\right) - (m^2 + k_n^2 r^2)R = 0, \quad m = 0, 1, 2, \ldots, \tag{1.44}$$

which is modified Bessel's equation. Thus

$$R(r) = CI_m(k_n r) + DK_m(k_n r), \quad m, n = 0, 1, 2, \ldots, \tag{1.45}$$

for some constants C and D, and where $I_m(.)$ and $K_m(.)$ denote the modified Bessel functions of the first and second kind, respectively, of order m. Therefore ϕ is obtained as

$$\phi(r, \theta, z) = \sum_{m=0}^{\infty} \sum_{n=0}^{\infty} [A_{mn} \cos(m\theta) + B_{mn} \sin(m\theta)][C_{mn} I_m(k_n r) + D_{mn} K_m(k_n r)] Z_n(k_n z), \tag{1.46}$$

with

$$Z_n(k_n z) = \begin{cases} \frac{\cosh k_n(z+h)}{\cosh k_n h}; & n = 0, \\ \frac{\cos k_n(z+h)}{\cos k_n h}; & n \geq 1, \end{cases}$$

and

$$I_m(k_0 r) = (-1)^m J_m(kr), \tag{1.47}$$

$$K_m(k_0 r) = \mathrm{i}^{m+1} \frac{1}{2} \pi H_m^{(1)}(kr), \tag{1.48}$$

where $H_m^{(1)}(.)$ is Hankel function of the first kind of order m.
Since $k_0 = -\mathrm{i}k$, using the relations (1.47) and (1.48), the expression

$$[C_{mn} I_m(k_0 r) + D_{mn} K_m(k_0 r)]$$

can be written as

$$[C'_{mn} J_m(kr) + D'_{mn} H_m^{(1)}(kr)].$$

The behaviours of $J_m(.)$ and $H_m^{(1)}(.)$ for large argument are given by

$$J_m(kr) \approx \sqrt{\frac{2}{k\pi r}} \cos\left(kr - \frac{m\pi}{2} - \frac{\pi}{4}\right), \tag{1.49}$$

$$H_m^{(1)}(kr) \approx \sqrt{\frac{2}{k\pi r}} \exp\left[\mathrm{i}\left(kr - \frac{m\pi}{2} - \frac{\pi}{4}\right)\right]. \tag{1.50}$$

Therefore, propagating modes of scattered potential can be written as

$$\phi_{S_p}(r, \theta, z) = \sum_{m=0}^{\infty} [A_m \cos(m\theta) + B_m \sin(m\theta)] H_m^{(1)}(kr) Z(kz). \tag{1.51}$$

The other terms in (1.46) either become unbounded or decay as the radial coordinate increases. From $I_m(k_n r) \approx \sqrt{\frac{\pi}{2kr}} \exp(\mathrm{i}kr)$, it follows that all the terms $I_m(k_n r)$, $n > 0$, increase exponentially as $k_n r \to \infty$ and consequently, they are not present in the expansion of a potential in a region which extends to infinity. On the other hand, $K_m(k_n r) \approx$

$\sqrt{\frac{\pi}{2kr}}\exp(-ikr)$ shows that all the terms $K_m(k_nr)$, $n > 0$, decrease exponentially as $k_nr \to \infty$. These latter terms are the *evanescent modes*. Therefore evanescent modes of scattered potential can be written as

$$\phi_{S_e}(r,\theta,z) = \sum_{m=0}^{\infty}\sum_{n=1}^{\infty}[A_{mn}\cos(m\theta) + B_{mn}\sin(m\theta)]K_m(k_nr)Z_n(k_nz). \tag{1.52}$$

We assume that the reflected wave which admits of a similar expression satisfying Laplace's equation and boundary conditions and which radiates away can be written in the following symmetric form (about θ):

$$\phi_1 = \phi_{\text{inc}} + \phi_S = \phi_{\text{inc}} + \phi_{S_p} + \phi_{S_e},$$

or,

$$\phi(r,\theta,z) = -\frac{igH}{\omega}\left[\sum_{m=0}^{\infty}\tau_m J_m(k_0r)\cos m\theta Z_0(k_0z) + \sum_{m=0}^{\infty}\cos m\theta\sum_{n=0}^{\infty}A_{mn}Z_n(k_nz)U_m^{(1)}(k_nr)\right]. \tag{1.53}$$

Here the radial eigenfunctions $U_m^{(1)}(k_nr)$ are as follows:

$$U_m^{(1)}(k_nr) = \begin{cases} \frac{H_m^{(1)}(k_nr)}{H_m^{(1)'}(k_nb)}; & n = 0, \\ \frac{K_m(k_nr)}{K_m'(k_nb)}; & n \geqslant 1, \end{cases}$$

where b is the radius of the cylinder.

Also, the depth eigenfunctions $Z_n(k_nz)$ are given by

$$Z_n(k_nz) = \begin{cases} \frac{\cosh k_n(z+h)}{\cosh k_nh}; & n = 0, \\ \frac{\cos k_n(z+h)}{\cos k_nh}; & n \geq 1. \end{cases}$$

The velocity potential associated with all the problems in the subsequent chapters of this thesis are evaluated in a manner as detailed above.

1.6 Roots of the dispersion relation

Since the roots of the dispersion relations play an important role in each solution, we deem it suitable to discuss these roots in brief. Different dispersion relations will arise for different upper surfaces and bottom surfaces. Equation (1.40) may be rewritten as

$$\frac{h\omega^2}{g} = \mathcal{C}\tanh\mathcal{C}, \text{where } \mathcal{C} = kh. \tag{1.54}$$

The above equation has only one positive root and an infinite number of imaginary roots. We call the positive root $\mathcal{C}_0$ and other roots i$\mathcal{C}_n$ for $n = 1, 2, 3, \cdots$. Also, $\mathcal{C}_n$ are the real positive roots of

$$\frac{h\omega^2}{g} = -\mathcal{C}\tanh\mathcal{C}, \tag{1.55}$$

where the roots lie in $(n - \frac{1}{2})\pi < \mathcal{C}_n < n\pi$.
An approximation for $\mathcal{C}_0$ is given by Chamberlain and Porter [6] as

$$\mathcal{C}_0 = \mathcal{M}\left(1 - \frac{4(1-(1+\mathcal{M})e^{-2\mathcal{M}}}{2\mathcal{M}+\sinh 2\mathcal{M}}\right)^{-\frac{1}{4}}, \text{where } \mathcal{M} = \frac{h\omega^2}{g}. \tag{1.56}$$

To approximate $\mathcal{C}_n(n = 1, 2, \cdots)$, we again use an iterative method suggested by Chamberlain and Porter:

$$\mathcal{C}_{n,m+1} = t_n(\mathcal{C}_{n,m}), \tag{1.57}$$

where, $t_n(a_n) = \dfrac{a_n}{\sqrt{1 - \frac{2(a_n\tan a_n+\mathcal{M})\sin 2a_n}{\mathcal{M}(2a_n+\sin 2a_n)}}}$ and $\mathcal{C}_{n,0} = \beta_n = n\pi - \dfrac{\pi}{2}\tanh\dfrac{2\mathcal{M}}{n\pi^2}$. Once we obtain the values of $\mathcal{C}_n(n = 0, 1, 2, \cdots)$, k_n can be calculated by using the relation $\mathcal{C}_n = k_n h$. The corresponding errors are defined, for all n, by

$$\text{Error} = \left|\frac{\omega^2}{g} - k_n\tanh k_n h\right|. \tag{1.58}$$

1.7 Brief review of previous works

Various theoretical investigations have been carried out by researchers in analysing the wave motion and hydrodynamic forces on structure(s). Most of the investigations for water wave diffraction and radiation problems are found to be concerned mainly with a single structure, usually a circular cylinder. Ursell is considered to be the pioneer in water wave scattering problems and he studied a problem for a long and floating horizontal cylinder which oscillated with small amplitudes in water of infinite depth [53]. He evaluated the wave amplitude at some distance from the cylinder as well as the added mass of the cylinder due to its motion in sea. MacCamy and Fuchs [23] took up the problem of water wave interaction with cylindrical piles. They calculated the force and moment acting on the piles by using eigenfunction expansion method. This result is considered to be one of the most significant results in water wave mechanics. Garrett [15] investigated the excitation of waves inside a partially immersed open circular cylinder and obtained the solution by using the incident wave as a trial function. He proved that the phase of the solution was independent of depth and resonances corresponding to wavenumbers close to those of free oscillations for a bottom-mounted cylinder. Spring

and Monkmeyer [50], by applying the eigenfunction expansion approach, obtained an analytical solution for the diffraction problem of linear waves by an array of surface-piercing impermeable circular cylinders touching the bottom of the sea. This result can be seen as an extension of the result of MacCamy and Fuchs [23]. Miloh [34] discussed waveloads, wave motions and hydrodynamic coefficients for sway and roll motions and the coupling terms between these two modes for the case of a circular floating pond. Calisal and Subancu [5] investigated hydrodynamic coefficients for vertical composite circular cylinders at finite water depth by using matching technique through the continuity of pressure and normal velocity at the separation of surfaces. They also discussed the limiting value of the added mass for zero frequency. Yeung [62] investigated a set of data for added mass and wave damping for a floating circular cylinder in finite depth water. He calculated added mass and damping coefficients for heave, sway and roll motions, and also the coupling coefficients for sway and roll motions. While considering the heave oscillations of a submerged vertical cylinder, McIver and Evans [32] observed an interesting occurrence of negative added mass. They discussed the effect of free surface for the occurrence of negative added mass. They found that added mass became negative when the depth of submergence was small and free surface effects were remarkable. Linton and Evans [22] simplified the theory of Spring and Monkmeyer [50] by being able to directly evaluate the wave forces and run-up on the cylinders. Rahman and Bhatta [42] employed nonlinear water wave theory and derived the second-order wave forces acting on a pair of cylinders, having different radius, placed at some distance apart. For finding the solution, they considered two different coordinate systems and used Graf's addition theorem for Bessel functions [56]. Sahoo [45] studied the generation of cylindrical surface waves in infinite depth water by considering a rigid circular cylinder surrounded by a vertical coaxial permeable hollow cylinder. In this work, he utilized Havelock's expansion theorem and some properties of Bessel functions. Bhatta and Rahman [3] investigated the scattering and radiation for a floating cylinder in water of finite ocean depth. They calculated the waveload by decomposing the total velocity potential into one scattering potential and three radiation potentials. They split the fluid domain into interior and exterior regions to derive the velocity potentials. Bhatta [2] discussed computation of the hydrodynamic coefficients, displacement-amplitude ratios and loadings on a floating vertical circular cylinder by considering diffraction and radiation. He investigated three translational motions such as surge, pitch and yaw motions of the cylinder. He used JMSL (Java Mathematical and Statistical Library) to compute special functions and solve the complex matrix equations. Hassan and Bora [18] studied the radiation problem for a hollow cylinder placed above a coaxial cylinder in finite depth and discussed the behaviour of the hydrodynamic coefficients due to radiation, namely, added mass and damping coefficients.

Scattering problems due to porous structures are considered to be even more important. For modeling of wave-induced flow in a porous medium, the model which has found

the maximum attention is the one devised by Sollitt and Cross [49]. In this model, dissipation of wave energy inside a porous medium was taken into account and the linearised friction term f was evaluated by using Lorentz Principle and an iterative procedure. Chwang [7] developed a porous wave-maker theory by which the hydrodynamic pressure distribution and the total force on the wave-maker were investigated. He also established the significance of the wave-effect parameter and the porous-effect parameter.

Various researchers have also investigated wave diffraction problems involving porous barriers. Yu [64] established a new relation for the fluid motion through a thin porous structure, used as a breakwater, present in a sea. It was observed that if the inertial effect of the porous medium was neglected, it led to an underestimate of the performance of the thin porous structure. Sahoo et al. [46] examined the scattering of oblique incident surface waves by permeable vertical barriers in finite depth. They investigated the problem for four different types of barriers and made the observation that the finite angle of incidence and the porosity of the barriers had an important role in the reduction of reflection of the incident waves. Meng and Lu [33] studied scattering of gravity waves by a porous rectangular barrier on a sea-bed and they found that, corresponding to an increase in the values of wavenumber, the reflection coefficient exhibited a fluctuant behaviour and the transmission coefficient first showed a reduction and then an increase. Das and Bora [13] examined the oblique wave damping by two fully submerged vertical parallel porous plates of different heights in finite depth. They found that, by choosing the parameters and position of the plates appropriately, the reflection and transmission coefficients could be made to take much lower values and consequently, the porous plates could act efficiently as an adequate wave absorber.

Darwiche et al. [10] used eigenfunction expansion method to investigate wave interaction with a semi-porous cylindrical breakwater and they found a very important result that the wave force reduced due to the semi-porous portion of the cylinder. Williams and Li [57] investigated the interaction of linear water waves with a semi-porous cylindrical breakwater which surrounded a rigid vertical circular cylinder mounted on a storage tank. A significant change was observed in the wave field and it also showed significant reduction in hydrodynamic forces in the presence of the semi-porous cylindrical breakwater. By using eigenfunction expansion method, Williams and Li [59] further studied water wave interaction with an array of surface-piercing bottom-mounted porous cylinders and evaluated the hydrodynamic forces on the cylinders. Williams et al. [60] carried out an extension of this problem by considering water wave interaction with a floating porous cylinder. They found that the permeability, the size and the location of the porous region had a considerable influence on the hydrodynamic forces. Sankarbabu et al. [47] considered an array of surface-piercing bottom-mounted porous cylinders with porous outer walls. They discussed various effects of wave and structural parameters on the structures. Mandal et al. [26] discussed the hydroelastic analysis of gravity wave interaction with a system of concentric porous and flexible cylinders in which the inner cylinder was taken

to be rigid while the outer cylinder as porous and flexible. They mainly investigated three cases, namely, (a) surface-piercing truncated cylinders, (b) bottom-touching truncated cylinders, and (c) completely submerged cylinders extended from free surface to bottom. They also analysed the effects of porosity and flexibility of the outer cylinder in attenuating the hydrodynamic forces and dynamic overturning moments for different cylindrical configurations and wave characteristics. Mandal and Sahoo [28] discussed the hydroelastic analysis of a floating flexible circular cage system in finite water depth under the assumption of small amplitude waves and structural response. They mainly investigated hydrodynamic force, effect of structural porosity and deflections of the flexible walls and bed of the cage system. Ning et al. [38] investigated wave diffraction by a truncated cylinder having an upper porous sidewall and an inner column and they found that the wave forces and moments took decreasing values with an increase in the draft ratio.

A number of analytical investigations on water wave interaction with porous structure(s) for different bottom topography have also been carried out till date. Dalrymple et al. [9] studied the reflection and transmission of oblique incident waves due to the presence of infinitely long porous structures in sea. Das and Bora [12] discussed wave reflection by a vertical porous structure placed on an elevated impermeable sea-bed by considering two types of bottom topography in the form of a 2-step bottom and a p-step bottom. It was observed that higher values of the reflection coefficient corresponded to lower values of porosity. Das and Bora [11] further investigated oblique linear wave damping by a vertical porous structure placed on a multi-step bottom topography in which the cases of (i) a solid vertical wall placed at a finite distance from the porous structure in water medium after the porous structure and (ii) a special case of an unbounded water medium after the porous structure, were discussed.

In literature, some important works pertaining to scattering linear waves by porous structures in two-layer fluids have been reported. Sherief et al. [48] analysed the forced gravity wave motion by a porous wave-maker immersed vertically in a two-layer fluid under the assumption of linear water wave theory. The scattering of a harmonic wave normally incident on the wave-maker was also considered and subsequently, the reflection and transmission coefficients were evaluated and investigated. Manam and Sahoo [24] studied wave scattering by porous structures in a two-layer fluid for which they derived analytical solutions for the radiation or scattering of oblique water waves by a fully extended porous barrier for both cases of finite and infinite depths of water in a two-layer fluid with constant layer-wise densities. Various results concerning the generation and reflection of the axisymmetric surface or interfacial waves were derived in terms of Bessel functions. Mondal et al. [35] investigated surface gravity wave interaction with circular floating elastic plates of finite radius in both homogeneous and two-layer fluids in finite water depth. They used Fourier-Bessel series type expansion formulas for the velocity potentials to be obtained in the open water surface region and flexible plate/membrane covered region. They also computed and plotted structural deflection in order to understand the hydrodynamic

characteristics of the floating structures under the action of water. Mandal et al. [25] discussed oblique wave scattering by multiple flexible porous barriers in a two-layer fluid for both the cases of surface-piercing and bottom-standing partial barriers in water of finite depth. Wave scattering by multiple barriers was also studied by using a wide-spacing approximation method which was compared with the solution obtained through the least square approximation method in the case of double barriers. They found that multiple zeros in wave reflections occur for waves in surface and internal modes corresponding to various values of non-dimensional barrier spacing and an oblique angle of incidence.

Behera et al. [1] investigated trapping of obliquely incident surface waves due to permeable flexible barriers placed near a vertical rigid wall in a two-layer fluid having a free surface and an interface for both surface-piercing and bottom-standing partial barriers. They mainly focused on the effect of the critical angle of incidence on wave reflection and trapping by barriers, surface and interface wave elevations, deflection of the flexible barrier under wave action, pressure distribution on the barrier, waveloads on the barrier and the rigid wall. Mandal and Sahoo [27] examined axi-symmetric gravity wave interaction with a system of concentric flexible porous cylinders in a two-layer fluid having a free surface and an interface in water of finite depth. The cylinder system consisted of a rigid cylinder and an outer flexible porous cylinder and the authors mainly analysed the effectiveness of the cylinder system in trapping surface waves.

There are a lot of applications of cylindrical structures for constructing WEC (Wave Energy Converter). Park et al. [40] discussed soil structure interaction using substructure method while considering a wind turbine installed in ocean. They carried structural analysis of gravity substructure numerically by using the software ANSYS AQWA which is an analysis tool used mainly for investigating effects of wave, wind and current on various types of floating and fixed offshore and marine structures. Yueh and Chuang [65] employed linear water wave theory for investigating the performance of a piston-type porous wave energy converter comprising of a solid wall, a vertical porous plate, a transmission bar, a rigid block constrained by rollers, a spring and a damper. They performed a number of numerical experiments to determine hydrodynamic added mass, damping coefficient, converter response, and also instantaneous mechanical power extracted from the wave. Viselli et al. [54] developed a new floating wind turbine platform design called VolturnUS which included a fully operational commercial 20 KW wind turbine and was the first grid connected offshore wind turbine in the U.S. They also validated numerical codes for offshore floating wind turbines partially which was another benchmark for development and understanding of floating wind turbines. Young et al. [63] explored and validated a coupled boundary element method and finite element method to simulate the transient fluid-structure interaction response of tidal turbines subject to spatially varying inflow. The experiment showed that transient cavitation developed near the blade tip when the blades were near the free surface at highly-loaded off-design conditions, and the blades underwent excessive deformation because of the high fluid loading and slender blade profile.

Linear wave interaction with a wave energy device comprising of two coaxial vertical circular cylinders of different radii was investigated by Wu et al. [61]. They established that, at low frequencies, a relatively larger radius of the submerged cylinder had a significant influence on the hydrodynamic coefficients and exciting forces/moments.

1.8 Main motivation for the current work

Various types of porous breakwaters have been proposed by researchers for the protection of coastal regions and construction sites. Porous structures reduce the waveloads and wave run-up on them. Some of the relevant works have been discussed in the previous chapter. These structures are very flexible, reusable and can be used to develop low cost wave attenuation and protection systems. Vertical cylinders are generally used in the construction of coastal and offshore structures due to various applications. Examples are floating airports, semi-submersibles, wave power energy conversion system etc. Various porous structures are used to create oil rigs. Sea-cage culture is also based on porous structures. Further, Very Large Floating Structures (VLFS), such as floating airports, bridges, breakwaters, piers, docks etc. are constructed with the help of porous structures.

To design marine structures, it is necessary to take into account a number of atmospheric conditions and to devise accurate prediction of hydrodynamic impact on the structures. Therefore, research has especially been focused on optimizing the system to avoid significant hydrodynamic impacts. The concept to use porous surface bodies is to reduce the influence of wave-body interaction through the pores on the body surface. Especially, offshore wind energy has gained attention from many countries to find alternative and reliable source of energy. South Korea has decided to invest 9 billion dollars in building a 2.5 GW offshore wind force in the south west sea of Korea. The size of the substructure for wind turbine increases due to the size of the tower and the rotor nackle becomes larger with increment of gross generation. The substructures are substantially affected by the wave force. Therefore, an important goal is to reduce wave loads on substructures. One possible way is to use a structure with porous surface.

The whole world witnessed global fuel crisis in 1970. From then onwards, the concept of bringing renewable energy into fore has kicked off. Along side, a sizeable endeavour has been undertaken precisely on research and burgeoning activities, including solar, wind and ocean energy. This stepping forward has come to the aid of strengthening the study of the existing gap between renewable and non-renewable energy. In the recent past, it has been observed that WEC (Wave Energy Converter) systems require high cost in comparison with traditional electricity produced from coal power plants. The appealing power of the WEC can be enhanced through the consolidation of the WEC into other structures related to maritime such as breakwater pier or jetty. The following are the gathered outcomes from the consolidation of breakwater and wave energy device over the stand-alone wave energy device (Mustapa et. al. [36]):

1. Overtopping WEC-breakwater integration.
2. Oscillating water column and WEC-breakwater integration.
3. Piston-Type Porous Wave Energy Converter (PTPWEC) integration.

Two identified current important projects in connection with breakwater integration are "The Mutriku Wave Energy Plant" (Figure 1.3) situated in Mutriku on the northern coast of Spain between San Sebastian and Bilbao and "Siadar Wave Energy Project" (Figure 1.4) situated in Siadar Bay, in Lewis, Scotland. Another porous breakwater project is the semi-circular breakwater concept constructed at Miyazaki Port, Japan (Figure 1.5).

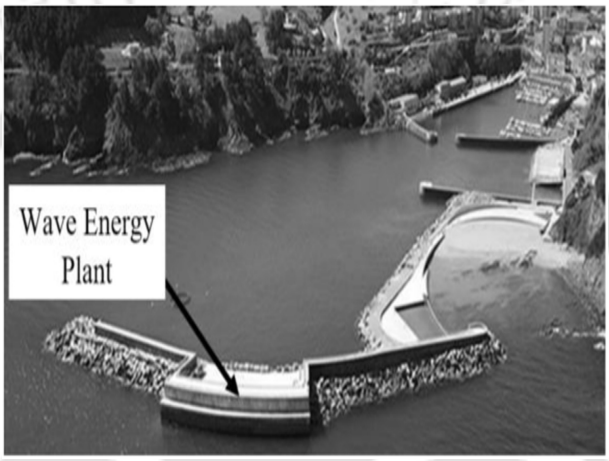

Figure 1.3: The Mutriku Wave Energy Plant (Courtesy Mustapa et al. [36])

Figure 1.4: Siadar Wave Energy Project (Courtesy Mustapa et al. [36])

Offshore wind power or wind energy can be harnessed by installing wind farms in any large water body, usually in an ocean on the continental shelf. The harvested wind energy can be appropriately converted to get electricity. A good number of wind energy power resources are available worldwide. The sea south-west to the Gulf of Cadiz in Spain is one such prime source of wind energy. Two identified current important projects

Figure 1.5: Semi-circular breakwater concept at Miyazaki Port, Japan (Courtesy Mustapa et al. [36])

in connection with wind energy harvesting are "Mar de Trafalgar" (Figure 1.6) in Spain and "A Pioneer Project of Aquaculture-Wind Farm Multi-Uses" in German North Sea. Both projects plan to integrate aquaculture with wind energy production. The main objective of such projects is to construct a storage tank surrounding the circular cylinder of the aerogenerators for aquaculture. Under appropriate conditions, multiple use of a marine site through co-location of such complementary activities will definitely lead to more efficient utilization of ocean space which augurs well for nature. The best way to explore the economic benefit and ocean space utilization through multi-use and co-location is probably to initiate developing aquaculture co-located within the structure serving as an ocean wind farm. Such co-location of two activities of aquaculture and wind energy generation will result in cutting down expenditure on both public and private fronts. The public benefits are due to such common structural arrangement not negatively affecting the ecosystem services derived from the ocean area which would have otherwise occupied and exhausted more space. The private benefits are in the form of cost savings arising from sharing of infrastructure, logistics efforts and systems. Details of such issues is addressed in details by Buck and Langan [4].

Having studied the above works, it is realized that sufficient work has not been accomplished for (i) a compound porous cylinder, (ii) a partial-porous cylinder, (iii) a cylindrical storage tank, and (iv) two coaxial cylindrical system. This type of structures will be helpful in reducing hydrodynamic impact on the structures that can be installed in ocean for various activities. In this context, we take up problems connected to diffraction and radiation by such wave absorbing structures which also act as wave energy devices.

In the present thesis, we are motivated to solve the diffraction and radiation problems of various types of porous cylinders such as compound porous cylinder, partial-porous cylinder, cylindrical storage tank and two coaxial porous cylinders in finite depth. The mathematical model for solving such problems is based on the assumption of linearised

Figure 1.6: Design of the structure compossed by the aerogenerator and the aquaculture cage. Courtesy of INR Eólica. [4]

water wave theory. In the study of interaction of water waves with floating structures, an eigenfunction expansion, along with the matching technique, is being widely used due to its considerable accuracy. Therefore, using an eigenfunction expansion approach and separation of variables technique, the analytical solutions for the diffraction and radiation problems are presented. Using the analytical solutions of the problems, the effect of various parameters on the wave force, wave run-up and hydrodynamic coefficients of cylinders is investigated. The obtained results are expected to provide some useful information to the designers of such structures.

To produce the maximum benefit out of a structure, it is important to design structures with proper parameters. We evaluate the forces and wave run-up due to diffraction and the hydrodynamic coefficients due to radiation. It is hoped that the results will be helpful in designing a suitable device which can host several marine activities as stated earlier. As far as our knowledge is concerned, till now no one else has attempted problems of this sort and we are hopeful that our results will throw some new light in this direction.

1.9 Outline of the thesis

This thesis is organized in ten chapters with the present chapter dealing with the basic concepts and relevant equations, previous important works and our motivation to carry out the present investigation.

In **Chapter 2**, the interaction with linear surface waves with a bottom-mounted compound porous cylinder is investigated theoretically. An analytical solution is obtained for each flow region based on eigenfunction expansion approach. The solutions in the two fluid domains are then matched using appropriate boundary conditions. Numerical results are discussed to illustrate the effects of the various wave and structural parameters such as radius ratio, draft ratio, porous coefficient etc., on the hydrodynamic loads and wave run-up in interior and the exterior flow regions. Comparison is carried out with

a compound cylinder, i.e., a totally impermeable cylinder. Good agreement is observed from this comparison. We also discuss a semi-porous single cylinder as a special case. We investigate hydrodynamic force and wave run-up for this cylinder too.

A study on hydrodynamic force and wave run-up due to the interaction of linear surface waves with a floating compound porous cylinder in finite depth is carried out in **Chapter 3**. The bottom ($0 \leq r \leq b$) and top ($a \leq r \leq b$) of the lower cylinder and the side-wall of the upper cylinder are assumed to be impermeable. The velocity potentials are analytically derived in each fluid region based on separation of variables technique. The velocity potentials satisfy appropriate free surface condition, bottom boundary condition, matching conditions and Sommerfeld radiation condition at infinity. By using matching conditions along the boundaries of the regions, a system of linear equations for the unknown coefficients is derived and solved. A set of values of hydrodynamic force and wave run-up are obtained for different radii, different drafts and different porosity of the cylinder. It is observed that change in values in radii, draft and porosity has significant effect on the hydrodynamic loads and wave run-up. For validating our result, we compare our result with a compound floating cylinder, when the side wall of the lower cylinder is impermeable.

Chapter 4 deals with the diffraction problem of ocean water waves in an ocean due to the presence of a specific type of cylinders for two configurations: (i) a floating surface-piercing truncated partial-porous cylinder, (ii) a surface-piercing truncated partial-porous cylinder placed at the bottom. In both cases, the configuration of the compound cylinder is such that it consists of an impermeable inner cylinder rising above the free surface and a coaxial truncated porous cylinder around the lower part of the inner cylinder with the top of the porous cylinder being impermeable. The behaviour of hydrodynamic coefficient, moment and wave run-up due to different relevant parameters is studied. The effect of various parameters, such as draft ratio, porous coefficient and radius ratio, on the hydrodynamic coefficient, moment and wave run-up are studied graphically for both the cylinders.

Chapter 5 is devoted to the problem related to the diffraction of linear waves by a cylindrical storage tank, the inner part of which contains a cylindrical pile and the outer part contains a coaxial thin hollow porous cylinder, in finite depth. The main aim is to construct a storage tank surrounding the cylindrical pile of the aerogenerators for aquaculture. Here we consider two cases: (i) an impermeable solid circular cylinder surrounded by an outer coaxial thin hollow porous cylinder of same height extending from free surface to sea-bed, (ii) a similar structure fully placed atop an impermeable solid circular cylinder with same radius. Appropriate matching conditions are applied at the interface of the regions to get a system of linear equations for the unknown coefficients and to solve it. By considering different sets of values of the radius and the porous coefficient of the cylinder, the hydrodynamic force and wave run-up are evaluated.

Chapter 6 deals with water wave radiation problem of a floating partial-porous com-

pound cylinder in finite depth. This work can be considered as an extension of the work carried out in Chapter 4 in which only diffraction for the same configuration was discussed. The configuration of the partial-porous compound cylinder is such that it consists of an impermeable inner cylinder rising above the free surface and a coaxial truncated porous cylinder around the lower part of the inner cylinder with the top of the porous cylinder being impermeable. Numerical investigation is taken up in order to examine the influence of submerged depth, radii, porous coefficient and water depth on added mass and radiation damping, two most important entities in radiation problems, here for surge and heave motions.

Chapter 7 deals with a train of linear water waves incident on a bottom-mounted surface-piercing compound partial-porous cylinder consisting of two coaxial cylinders of which the upper cylinder is hollow with a thin porous side wall and the lower impermeable cylinder, with radius greater than that of the upper one, is rigid and subsequently, we examine the associated hydrodynamic forces. Various numerical experiments show the effect of different parameters, such as porosity of the upper cylinder, draft ratio, the ratio of radii of the upper and lower cylinders and the depth of water on hydrodynamic force and wave run-up.

Chapter 8 is devoted to the evaluation of the exciting forces for an arrangement of two coaxial vertical cylinders – a riding porous cylinder and a bottom-mounted solid rigid cylinder. We take up two cases: first we consider a hollow porous cylinder at the top and secondly a solid porous cylinder at the top and for both the cases, there is a solid rigid cylinder at the bottom. Exciting force and wave run-up for the upper and lower cylinders are calculated through the velocity potentials which are evaluated by solving the diffraction problem.

Chapter 9 is devoted to the work which is an extension of the previous model in Chapter 8 by considering the same system of coaxial cylinders in taking up the associated radiation problem. The translational motions in the x- and z-directions, i.e., surge and heave motions, are investigated. Comparison is carried out with a single hollow impermeable cylinder. Good agreement is observed from this comparison. Numerical investigation is taken up in order to examine the influence of submerged depth, radii, porous coefficient and water depth on added mass and radiation damping for surge and heave motions.

At the end of the thesis, **Chapter 10** presents a brief summary of results highlighting the contribution made by this thesis. It also provides information for the scope of future investigations for such structures for various useful applications.

CHAPTER 2

Hydrodynamic Forces due to Water Wave Interaction with a Bottom-Mounted Surface-Piercing Compound Porous Cylinder

In this chapter, the interaction of linear surface waves with a compound porous cylinder is investigated theoretically under the assumption of linear wave theory and by splitting the fluid domain into a number of sub-domains. An analytical solution is obtained for each flow region based on eigenfunction expansion approach. The solutions in the fluid domains are then evaluated by using appropriate boundary conditions and matching conditions. Numerical results are discussed to illustrate the effects of the various wave and structural parameters on the hydrodynamic loads and in interior and the exterior flow regions. Our mathematical model is an extension of a number of earlier works, e.g., Isaacson [19], in which porosity was not a significant factor. However, the utilization of porous structures in reducing waveloads can be considered to be a more appropriate step. In other words, the model developed here states that for certain combination of the wave parameters, it will be helpful to reduce the waveloads on the structure. We claim that this model, never taken up earlier by anyone to the best of our knowledge, will fill the gap in this direction. Prior to taking up various investigations, the present model is validated against an available result in the literature which points towards an excellent agreement.

2.1 Mathematical formulation

We consider the fluid to be homogeneous, incompressible and inviscid, and the motion irrotational. The sea-bed is taken as flat and impermeable (Figure 2.1). We consider a cylindrical coordinate system (r, θ, z) with the origin at the undisturbed free surface and the z-axis taken in upward direction. Here we consider a train of small amplitude wave propagating from negative infinity towards the structure which comprises of an

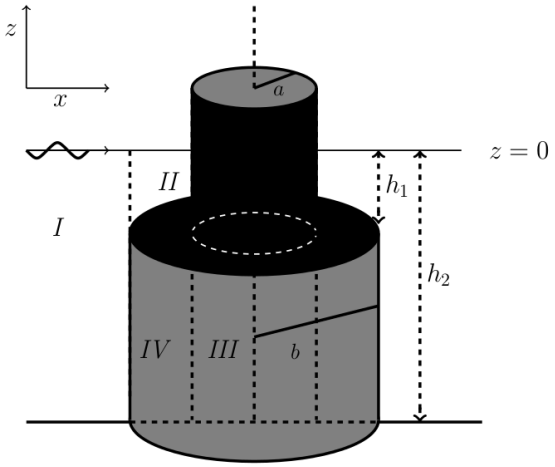

Figure 2.1: Compound porous cylinder with top of the bottom cylinder impermeable

inner cylinder of radius a and an outer porous cylinder of radius b possessing porosity G. The top of the lower cylinder ($a \leq r \leq b$) is considered to be impermeable. Further, the upper cylinder has an impermeable side-wall on which some appropriate boundary conditions are defined. We describe the fluid flow by introducing the potential $\Phi(r, \theta, z, t) = \mathrm{Re}[\phi(r, \theta, z) \exp(-\mathrm{i}\omega t)]$, where Re denote the real part of the quantity in brackets and ω is the angular wave frequency. The fluid domain is divided into four regions: Region I ($r \geq b, -h_2 \leq z \leq 0$); Region II ($a \leq r \leq b, -h_1 \leq z \leq 0$); Region III ($0 \leq r \leq a, -h_2 \leq z \leq 0$) and Region IV ($a \leq r \leq b, -h_2 \leq z \leq -h_1$). The velocity potential in each region is denoted by Φ_j for $j = 1, 2, 3, 4$.

Each potential satisfies Laplace's equation in respective flow region, namely,

$$\nabla^2 \phi_j = 0, \quad j = 1, 2, 3, 4, \tag{2.1}$$

where $\phi_j, \quad j = 1, 2, 3, 4$ refer to the potentials in Regions I, II, III and IV, respectively. The boundary conditions at the free surface and the sea-bed can be written as

$$\frac{\partial \phi_j}{\partial z} - \frac{\omega^2}{g}\phi_j = 0; \quad z = 0, \quad j = 1, 2, 3, \tag{2.2}$$

$$\frac{\partial \phi_1}{\partial z} = 0; \quad z = -h_2, \quad r > b, \tag{2.3}$$

$$\frac{\partial \phi_3}{\partial z} = 0; \quad z = -h_2, \quad 0 < r < a, \tag{2.4}$$

$$\frac{\partial \phi_4}{\partial z} = 0; \quad z = -h_2, \quad a < r < b. \tag{2.5}$$

The boundary conditions on the impermeable surfaces of the compound cylinder can be

expressed as

$$\frac{\partial \phi_2}{\partial r} = 0; \quad r = a, \quad -h_1 < z < 0, \tag{2.6}$$
$$\frac{\partial \phi_3}{\partial r} = 0; \quad r = a, \quad -h_1 < z < 0, \tag{2.7}$$
$$\frac{\partial \phi_2}{\partial z} = 0; \quad z = -h_1, \quad a < r < b, \tag{2.8}$$
$$\frac{\partial \phi_4}{\partial z} = 0; \quad z = -h_1, \quad a < r < b. \tag{2.9}$$

From equation (1.19), the boundary condition on the circular porous wall can be obtained as [59, 60]

$$\frac{\partial \phi_4}{\partial r} = \mathrm{i}k_0 G(\phi_4 - \phi_1), \quad r = b, \quad -h_2 < z < -h_1, \tag{2.10}$$

where k_0 is the wavenumber of the incident wave and G is the porous coefficient of the lower porous cylinder. Details of the porous coefficient G and the above relation is already discussed in Section 1.3.

On the cylindrical surface, the potentials satisfy the following matching conditions:

$$\phi_1 = \phi_2; \quad r = b, \quad -h_1 < z < 0, \tag{2.11}$$
$$\phi_3 = \phi_4; \quad r = a, \quad -h_2 < z < -h_1, \tag{2.12}$$
$$\frac{\partial \phi_3}{\partial r} = \frac{\partial \phi_4}{\partial r}; \quad r = a, \quad -h_2 < z < -h_1, \tag{2.13}$$
$$\frac{\partial \phi_1}{\partial r} = \begin{cases} \frac{\partial \phi_2}{\partial r}; & r = b, \quad -h_1 < z < 0, \\ \frac{\partial \phi_4}{\partial r}; & r = b, \quad -h_2 < z < -h_1. \end{cases} \tag{2.14}$$

Finally, the velocity potential in the exterior region must satisfy the Sommerfeld radiation condition in the following form:

$$\lim_{r\to\infty} \sqrt{r} \left[\frac{\partial(\phi_1 - \phi_{\text{inc}})}{\partial r} - \mathrm{i}k_0(\phi_1 - \phi_{\text{inc}}) \right] = 0, \tag{2.15}$$

where ϕ_{inc} is the incident velocity potential.

2.2 Diffracted potentials

Applying the separation of variables method in each sub-domain, expressions for the velocity potential are obtained. Each expression is obtained as an infinite series of orthogonal functions which is valid in the corresponding sub-domain. The velocity potential in Region I can be expressed in the following form:

$$\phi_1(r,\theta,z) = -\frac{\mathrm{i}gH}{\omega} \left[\sum_{m=0}^{\infty} \tau_m J_m(k_0 r) \cos m\theta Z_0^{(1)}(k_0 z) + \sum_{m=0}^{\infty} \cos m\theta \sum_{j=0}^{\infty} A_{mj} Z_j^{(1)}(k_j z) U_m^{(1)}(k_j r) \right], \tag{2.16}$$

where A_{mj} are unknown coefficients. Wavenumbers $k_j,\ j = 0, 1, 2, 3, \ldots$, can be derived from the following dispersion relation as in Chamberlain and Porter [6]:

$$\omega^2 = \begin{cases} gk_j \tanh k_j h_2; & j = 0, \\ -gk_j \tan k_j h_2; & j \geqslant 1. \end{cases}$$

The radial eigenfunctions $U_m^{(1)}(k_j r)$ appearing in (2.16) are as follows:

$$U_m^{(1)}(k_j r) = \begin{cases} \frac{H_m^{(1)}(k_j r)}{H_m^{(1)'}(k_j b)}; & j = 0, \\ \frac{K_m(k_j r)}{K'_m(k_j b)}; & j \geqslant 1, \end{cases}$$

where $H_m^{(1)}(k_j r)$ denotes the Hankel function of first kind and $K_m(k_j r)$ the modified Bessel function of second kind, of order m. The vertical eigenfunctions $Z_j^{(1)}(k_j z)$ are defined as

$$Z_j^{(1)}(k_j z) = \begin{cases} \frac{\cosh k_j(z+h_2)}{\cosh k_j h_2}; & j = 0, \\ \frac{\cos k_j(z+h_2)}{\cos k_j h_2}; & j \geqslant 1. \end{cases}$$

The scattered velocity potential ϕ_2 can be expressed as

$$\phi_2(r, \theta, z) = -\frac{\mathrm{igH}}{\omega} \left[\sum_{m=0}^{\infty} \cos m\theta \sum_{j=0}^{\infty} \left\{ B_{mj} U_m^{(2)}(\lambda_j r) + C_{mj} U_m^{(3)}(\lambda_j r) \right\} Z_j^{(2)}(\lambda_j z) \right], \quad (2.17)$$

where B_{mj} and C_{mj} are unknown coefficients and λ_j can be calculated from the following relation:

$$\omega^2 = \begin{cases} g\lambda_j \tanh \lambda_j h_1; & j = 0, \\ -g\lambda_j \tan \lambda_j h_1; & j \geqslant 1. \end{cases}$$

The radial eigenfunctions $U_m^{(2)}(\lambda_j r)$ and $U_m^{(3)}(\lambda_j r)$ appearing in (2.17)are as follows:

$$U_m^{(2)}(\lambda_j r) = \begin{cases} \frac{H_m^{(1)}(\lambda_j r)}{H_m^{(1)'}(\lambda_j b)}; & j = 0, \\ \frac{I_m(\lambda_j r)}{I'_m(\lambda_j b)}; & j \geqslant 1, \end{cases} \qquad U_m^{(3)}(\lambda_j r) = \begin{cases} \frac{H_m^{(2)}(\lambda_j r)}{H_m^{(2)'}(\lambda_j b)}; & j = 0, \\ \frac{K_m(\lambda_j r)}{K'_m(\lambda_j b)}; & j \geqslant 1, \end{cases}$$

where $H_m^{(2)}(\lambda_j r)$ denotes the Hankel function of second kind and $I_m(\lambda_j r)$ the modified Bessel function of first kind, of order m. The vertical eigenfunctions $Z_j^{(2)}(\lambda_j z)$ are defined as

$$Z_j^{(2)}(\lambda_j z) = \begin{cases} \frac{\cosh \lambda_j(z+h_1)}{\cosh \lambda_j h_1}; & j = 0, \\ \frac{\cos \lambda_j(z+h_1)}{\cos \lambda_j h_1}; & j \geqslant 1. \end{cases}$$

Next potential ϕ_3 in Region III can be expressed as

$$\phi_3(r,\theta,z) = -\frac{igH}{\omega}\left[\sum_{m=0}^{\infty}\cos m\theta \sum_{j=0}^{\infty} F_{mj} Z_j^{(3)}(\sigma_j z) U_m^{(4)}(\sigma_j r)\right], \tag{2.18}$$

where F_{mj} are unknown coefficients and σ_j can be calculated from the following relations:

$$\omega^2 = \begin{cases} g\sigma_j \tanh \sigma_j h_2; & j = 0, \\ -g\sigma_j \tan \sigma_j h_2; & j \geqslant 1, \end{cases}$$

with The radial eigenfunctions $U_m^{(4)}(\sigma_j r)$ given by

$$U_m^{(4)}(\sigma_j r) = \begin{cases} \frac{J_m(\sigma_j r)}{J_m'(\sigma_j a)}; & j = 0, \\ \frac{I_m(\sigma_j r)}{I_m'(\sigma_j a)}; & j \geqslant 1. \end{cases}$$

The potential given by equation (2.18), along with $U_m^{(4)}(\sigma_j r)$, is connected to a specific resonance phenomenon. The first term on the right side of the potential given by equation (2.18) is the most important contribution to the wave motion inside the cylinder, while the other terms describe waves which are localised near $r = a$. Each of the distinct modes $(m = 0, 1, 2, ...)$ resonates at different wavenumbers near the roots of $J_m'(ka) = 0$ where the roots correspond to the standing waves inside a cylindrical structure. This is what is known as sloshing mode resonance when water motion mostly occurs at the natural motion of the moonpool and due to the water moving back and forth in between the vertical walls. Similar resonance phenomenon due to sloshing can also be observed in the works of Garrett [15] and Mavrakos [29].
The vertical eigenfunctions $Z_j^{(3)}(\sigma_j z)$ in (2.18)are defined as

$$Z_j^{(3)}(\sigma_j z) = \begin{cases} \frac{\cosh \sigma_j (z+h_2)}{\cosh \sigma_j h_2}; & j = 0, \\ \frac{\cos \sigma_j (z+h_2)}{\cos \sigma_j h_2}; & j \geqslant 1. \end{cases}$$

Further, potential ϕ_4 in Region IV can be expressed as

$$\phi_4(r,\theta,z) = -\frac{igH}{\omega}\left[\sum_{m=0}^{\infty}\cos m\theta \sum_{j=0}^{\infty} \left[D_{mj} U_m^{(5)}(\mu_j r) + E_{mj} U_m^{(6)}(\mu_j r)\right] Z_j^{(4)}(\mu_j z)\right], \tag{2.19}$$

where D_{mj} and E_{mj} are unknown coefficients and μ_j can be calculated from the following relation:

$$\mu_j = \frac{\pi j}{h_2 - h_1}, \quad j = 0, 1, 2, ...$$

The radial eigenfunctions $U_m^{(5)}(\mu_j r)$ and $U_m^{(6)}(\mu_j r)$ are as follows:

$$U_m^{(5)}(\mu_j r) = \begin{cases} \frac{r^{-m}}{b^{-m-1}}; & j = 0, \\ \frac{K_m(\mu_j r)}{K'_m(\mu_j b)}; & j \geqslant 1, \end{cases} \qquad U_m^{(6)}(\mu_j r) = \begin{cases} \frac{r^m}{b^{m-1}}; & j = 0, \\ \frac{I_m(\mu_j r)}{I'_m(\mu_j b)}; & j \geqslant 1. \end{cases}$$

The vertical eigenfunctions $Z_j^{(4)}(\mu_j z)$ are defined as

$$Z_j^{(4)}(\mu_j z) = \begin{cases} \frac{1}{\sqrt{2}}; & j = 0, \\ \cos \mu_j (z + h_2); & j \geqslant 1. \end{cases}$$

2.3 Solution for the unknown coefficients

Application of the boundary condition (2.6) and the use of the orthogonal property of the eigenfunctions lead to the following relationship between the coefficients $B_{m\alpha}$ and $C_{m\alpha}$ appearing in (2.17):

$$\frac{H_m^{(1)'}(\lambda_0 a)}{H_m^{(1)'}(\lambda_0 b)} B_{m0} + \frac{H_m^{(2)'}(\lambda_0 a)}{H_m^{(2)'}(\lambda_0 b)} C_{m0} = 0, \tag{2.20}$$

$$\frac{I'_m(\lambda_\alpha a)}{I'_m(\lambda_\alpha b)} B_{m\alpha} + \frac{K'_m(\lambda_\alpha a)}{K'_m(\lambda_\alpha b)} C_{m\alpha} = 0, \quad \alpha \geqslant 1. \tag{2.21}$$

Using these relationships, the expression for ϕ_2 can be modified to

$$\phi_2(r, \theta, z) = -\frac{\mathrm{i}gH}{\omega} \left[\sum_{m=0}^{\infty} \cos m\theta \sum_{j=0}^{\infty} C_{mj} Z_j^{(2)}(\lambda_j z) U_m^{(7)}(\lambda_j r) \right], \tag{2.22}$$

where the radial eigenfunctions $U_m^{(7)}(\lambda_j r)$ are as follows:

$$U_m^{(7)}(\lambda_j r) = \begin{cases} \frac{H_m^{(2)}(\lambda_j r)}{H_m^{(2)'}(\lambda_j b)} - \frac{H_m^{(2)'}(\lambda_j a)}{H_m^{(2)'}(\lambda_j b)} \frac{H_m^{(1)}(\lambda_j r)}{H_m^{(1)'}(\lambda_j a)}; & j = 0, \\ \frac{K_m(\lambda_j r)}{K'_m(\lambda_j b)} - \frac{K'_m(\lambda_j a)}{K'_m(\lambda_j b)} \frac{I_m(\lambda_j r)}{I'_m(\lambda_j a)}; & j \geqslant 1. \end{cases}$$

Using the matching conditions (2.11) and (2.14) for the depth $-h_1 < z < 0$, and using the orthogonal property of the eigenfunctions, we get

$$\sum_{j=0}^{\infty} A_{mj} U_m^{(1)}(k_j b) Q_{0j} - C_{m0} U_m^{(7)}(\lambda_0 b) R_{00} = -\tau_m J_m(k_0 b) Q_{00}, \tag{2.23}$$

$$\sum_{j=0}^{\infty} A_{mj} U_m^{(1)}(k_j b) Q_{\alpha j} - C_{m\alpha} U_m^{(7)}(\lambda_\alpha b) R_{\alpha\alpha} = -\tau_m J_m(k_0 b) Q_{\alpha 0}, \quad \alpha \geqslant 1, \tag{2.24}$$

$$\sum_{j=0}^{\infty} A_{mj} Q_{0j} - C_{m0} U_m^{(7)'}(\lambda_0 b) R_{00} = -\tau_m J'_m(k_0 b) Q_{00}, \tag{2.25}$$

$$\sum_{j=0}^{\infty} A_{mj} Q_{\alpha j} - C_{m\alpha} U_m^{(7)'}(\lambda_\alpha b) R_{\alpha\alpha} = -\tau_m J'_m(k_0 b) Q_{\alpha 0}, \quad \alpha \geqslant 1. \tag{2.26}$$

Using the matching conditions (2.10) and (2.14) for the depth $-h_2 < z < -h_1$, and using the orthogonal property of the eigenfunctions, we obtain

$$\begin{aligned} \mathrm{i}k_0 G\left(D_{m0} + E_{m0}\right) bT_{00} &- \sum_{j=0}^{\infty} A_{mj}(1 + \mathrm{i}k_0 G U_m^{(1)}(k_j b)) P_{0j} \\ &= \tau_m P_{00}(J'_m(k_0 b) + \mathrm{i}k_0 G J_m(k_0 b)), \end{aligned} \tag{2.27}$$

$$\begin{aligned} \mathrm{i}k_0 G\left(D_{m\alpha}\frac{K_m(\mu_\alpha b)}{K'_m(\mu_\alpha b)} + E_{m\alpha}\frac{I_m(\mu_\alpha b)}{I'_m(\mu_\alpha b)}\right) T_{\alpha\alpha} &- \sum_{j=0}^{\infty} A_{mj}(1 + \mathrm{i}k_0 G U_m^{(1)}(k_j b)) P_{\alpha j} \\ &= \tau_m P_{\alpha 0}(J'_m(k_0 b) + \mathrm{i}k_0 G J_m(k_0 b)), \alpha \geqslant 1, \end{aligned} \tag{2.28}$$

$$\left(-mD_{m0} + mE_{m0}\right) T_{00} - \sum_{j=0}^{\infty} A_{mj} P_{0j} = \tau_m P_{00} J'_m(k_0 b), \tag{2.29}$$

$$\left(D_{m\alpha} + E_{m\alpha}\right) T_{\alpha\alpha} - \sum_{j=0}^{\infty} A_{mj} P_{\alpha j} = \tau_m P_{\alpha 0} J'_m(k_0 b), \quad \alpha \geqslant 1. \tag{2.30}$$

Equations (2.6), (2.7) and (2.13) across the boundary $r = a$ in the interval $-h_2 < z < 0$ can be written as a single condition, as in Darwiche et al. [10], as follows:

$$\frac{\partial \phi_3}{\partial r} = \frac{\partial(\phi_2 + \phi_4)}{\partial r}; \quad r = a, \quad -h_2 < z < 0. \tag{2.31}$$

Substitution of ϕ_3, ϕ_2 and ϕ_4, and use of the orthogonal property of the eigenfunctions lead to following equations:

$$\begin{aligned} &\sum_{j=0}^{\infty} \left[D_{mj} U_m^{(5)'}(\mu_j a) + E_{mj} U_m^{(6)'}(\mu_j a)\right] M_{0j} - F_{m0} N_{00} \\ &+ \sum_{j=0}^{\infty} \left[B_{mj} U_m^{(2)'}(\lambda_j a) + C_{mj} U_m^{(3)'}(\lambda_j a)\right] L_{0j} = 0, \end{aligned} \tag{2.32}$$

$$\begin{aligned} &\sum_{j=0}^{\infty} \left[D_{mj} U_m^{(5)'}(\mu_j a) + E_{mj} U_m^{(6)'}(\mu_j a)\right] M_{\alpha j} - F_{m\alpha} N_{\alpha\alpha} \\ &+ \sum_{j=0}^{\infty} \left[B_{mj} U_m^{(2)'}(\lambda_j a) + C_{mj} U_m^{(3)'}(\lambda_j a)\right] L_{\alpha j} = 0, \quad \alpha \geqslant 1, \end{aligned} \tag{2.33}$$

where

$$Q_{\alpha,j} = \int_{-h_1}^{0} Z_\alpha^{(2)}(\lambda_\alpha z) Z_j^{(1)}(k_j z) \mathrm{d}z, \tag{2.34}$$

$$R_{\alpha,\alpha} = \int_{-h_1}^{0} Z_\alpha^{(2)}(\lambda_\alpha z) Z_\alpha^{(2)}(\lambda_\alpha z)\mathrm{d}z, \tag{2.35}$$

$$P_{\alpha,j} = \int_{-h_2}^{-h_1} Z_\alpha^{(4)}(\mu_\alpha z) Z_j^{(1)}(k_j z)\mathrm{d}z, \tag{2.36}$$

$$T_{\alpha,\alpha} = \int_{-h_2}^{-h_1} Z_\alpha^{(4)}(\mu_\alpha z) Z_\alpha^{(4)}(\mu_\alpha z)\mathrm{d}z, \tag{2.37}$$

$$L_{\alpha,j} = \int_{-h_2}^{0} Z_\alpha^{(3)}(\sigma_\alpha z) Z_j^{(2)}(\lambda_j z)\mathrm{d}z, \tag{2.38}$$

$$N_{\alpha,\alpha} = \int_{-h_2}^{0} Z_\alpha^{(3)}(\sigma_\alpha z) Z_\alpha^{(3)}(\sigma_\alpha z)\mathrm{d}z, \tag{2.39}$$

$$M_{\alpha,j} = \int_{-h_2}^{0} Z_\alpha^{(3)}(\sigma_\alpha z) Z_j^{(4)}(\mu_j z)\mathrm{d}z. \tag{2.40}$$

Truncation of the infinite series (2.23)-(2.33) after a finite number of terms, say $N = 20$, just like as in [38] and the use of (2.20) and (2.21) lead to simultaneous matrix equations for the potential coefficients A_{mj}, B_{mj}, C_{mj}, D_{mj}, E_{mj} and F_{mj}. Subsequently, in order to determine the unknown coefficients, we arrive at a linear system of algebraic equations

$$\mathcal{A}_l \mathcal{X}_l = \mathcal{B}_l, \tag{2.41}$$

where,
$\mathcal{X}_l = [A_{l1}, A_{l2}, ..., A_{lN}, B_{l1}, B_{l2}, ..., B_{lN}, C_{l1}, C_{l2}, ..., C_{lN}, D_{l1}, D_{l2}, ..., D_{lN}, E_{l1}, E_{l2}, ..., E_{lN}, F_{l1}, F_{l2}, ..., F_{lN}]^t$; $\mathcal{A}_l$ are coefficient matrices and $\mathcal{B}_l$ are the right hand vectors.

To justify the selection of $N = 20$ for evaluating the coefficients A_{mj}, B_{mj}, C_{mj}, D_{mj}, E_{mj} and F_{mj}, we present the following two tables (Table 2.1 and Table 2.2) for the coefficients A_{mj} and B_{mj} from which it becomes clear why $N = 20$ is selected. Tables for the rest of the coefficients are not presented since the values for those follow a similar trend. However, for each table we choose only five coefficients for want of space.

A_{1N}	$N = 5$	$N = 15$
A_{11}	0.0399198828146713 + 0.157390877624088$\imath$	0.0389500335087883 + 0.156563114159416$\imath$
A_{12}	-0.0552196275048478 + 0.0327443468844879$\imath$	-0.0533745333482868 + 0.0318282272756205$\imath$
A_{13}	0.0227656909369019 - 0.0332035741919368$\imath$	0.0214397512029566 - 0.0325976010766253$\imath$
A_{14}	-0.0180829240929113 + 0.0277393820040069$\imath$	-0.0172723558995368 + 0.0260160494793762$\imath$
A_{15}	0.00488767902090638 + 0.00776603134644560$\imath$	0.00467511982515278 + 0.00724606567390220$\imath$

A_{1N}	$N = 20$	$N = 25$
A_{11}	0.0378188476598254 + 0.155017539856432$\imath$	0.0378184692209491 + 0.155019396864606$\imath$
A_{12}	-0.0520927684653245+ 0.0302155437653451$\imath$	-0.0520925712207769 + 0.0302134069981799$\imath$
A_{13}	0.0204944354376573- 0.0310675365476286$\imath$	0.0204942656776200 - 0.0310672561174914$\imath$
A_{14}	-0.0163945432187654 + 0.0250106543294723$\imath$	-0.0163943395411930 + 0.0250105577861418$\imath$
A_{15}	0.00425315768342654 + 0.00699772547832671$\imath$	0.00425313176121768 + 0.00699771512744155$\imath$

Table 2.1: Table for the coefficients A_{1N} for $G = 1$, $a/b = 0.75$ and $h_1/h_2 = 2/3$.

Now for engineering purpose, we calculate various quantities. Water wave elevation for exterior and interior regions given by $\eta_j(r, \theta, t) = \mathrm{Re}[\zeta_j(r, \theta) \exp(-\mathrm{i}\omega t)]$ for $j = 1, 2, 3$, can be evaluated by the dynamic free surface condition

$$\eta_j = -\frac{1}{g}\frac{\partial \Phi_j}{\partial t} \quad \text{on} \quad z = 0 \quad \text{for} \quad j = 1, 2, 3. \tag{2.42}$$

B_{1N}	$N = 5$	$N = 15$
B_{11}	-0.0467219327962820 - 0.178445863219133$\imath$	-0.0460987774553323 - 0.178375064607398$\imath$
B_{12}	-0.00396236790689707 + 0.0127263039187783$\imath$	-0.00380032325360305 + 0.0120298305690187$\imath$
B_{13}	-0.0127767758905089 + 0.00562142688454270$\imath$	-0.0124924067976358 + 0.00521760090410782$\imath$
B_{14}	0.02414958313805186 + 0.00946605776896602$\imath$	0.0163515717622042 + 0.00769680021005352$\imath$
B_{15}	0.00360332879789096 + 0.000577181235148305$\imath$	0.00359315776997560 + 0.0004959653934956$\imath$

B_{1N}	$N = 20$	$N = 25$
B_{11}	-0.0460697257253683 - 0.178333467354268$\imath$	-0.0460695282319301 - 0.178333414794423$\imath$
B_{12}	-0.00324197435213775 + 0.0109087436254371$\imath$	-0.00324196362201789 + 0.0109087246932737$\imath$
B_{13}	-0.0108771457814327 + 0.00471072456189131$\imath$	-0.0108771993171527 + 0.00471073425677183$\imath$
B_{14}	0.0139166123825146 + 0.00583642162712541$\imath$	0.0139165652990607 + 0.00583640426363281$\imath$
B_{15}	0.00342798425617465 + 0.00048055154368134$\imath$	0.00342799966955179 + 0.00048058132424819$\imath$

Table 2.2: Table for the coefficients B_{1N} for $G = 1$, $a/b = 0.75$ and $h_1/h_2 = 2/3$.

Then

$$\zeta_1 = H\left[\sum_{m=0}^{\infty}\tau_m J_m(k_0 b)\cos m\theta Z_0^{(1)}(0) + \sum_{m=0}^{\infty}\cos m\theta\sum_{j=0}^{\infty}A_{mj}Z_j^{(1)}(0)U_m^{(1)}(k_j b)\right], \quad (2.43)$$

$$\zeta_2 = H\left[\sum_{m=0}^{\infty}\cos m\theta\sum_{j=0}^{\infty}\left[B_{mj}U_m^{(2)}(\lambda_j a) + C_{mj}U_m^{(3)}(\lambda_j a)\right]Z_j^{(2)}(0)\right], \quad (2.44)$$

$$\zeta_3 = H\left[\sum_{m=0}^{\infty}\cos m\theta\sum_{j=0}^{\infty}F_{mj}Z_j^{(3)}(0)U_m^{(4)}(\sigma_j a)\right]. \quad (2.45)$$

The total hydrodynamic force in the direction of wave propagation on the upper and the lower cylinder can be evaluated by integrating the pressure distribution on the structures. We define $\tilde{F}_x^j(t) = \mathrm{Re}[\tilde{F}_x^j \exp(-\imath\omega t)]$ for $j = 1, 2$ as

$$\tilde{F}_x^1 = \mathrm{i}\omega\rho\int_{-h_1}^{0}\int_0^{2\pi}\phi_3(a,\theta,z)\cos\theta \quad \mathrm{d}z\mathrm{d}\theta - \mathrm{i}\omega\rho\int_{-h_1}^{0}\int_0^{2\pi}\phi_2(a,\theta,z)\cos\theta \quad \mathrm{d}z\mathrm{d}\theta, \quad (2.46)$$

$$\tilde{F}_x^2 = \mathrm{i}\omega\rho\int_{-h_2}^{-h_1}\int_0^{2\pi}\phi_4(b,\theta,z)\cos\theta \quad \mathrm{d}z\mathrm{d}\theta - \mathrm{i}\omega\rho\int_{-h_2}^{-h_1}\int_0^{2\pi}\phi_1(b,\theta,z)\cos\theta \quad \mathrm{d}z\mathrm{d}\theta. \quad (2.47)$$

Simplifying, we get

$$\begin{aligned}\tilde{F}_x^1 &= g\rho\pi a H\left[\sum_{j=0}^{\infty}F_{1j}U_1^{(4)}(\sigma_j a)\right]\tilde{W}_j^{(1)} \\ &- g\rho\pi a H\left[\sum_{j=0}^{\infty}B_{1j}U_1^{(2)}(\lambda_j a) + C_{1j}U_1^{(3)}(\lambda_j a)\right]\tilde{W}_j^{(2)}, \end{aligned} \quad (2.48)$$

$$\tilde{F}_x^2 = g\rho\pi b H\left[\sum_{j=0}^{\infty}D_{1j}U_1^{(5)}(\mu_j b) + E_{1j}U_1^{(6)}(\mu_j b)\right]\tilde{W}_j^{(3)}$$

$$- \quad g\rho\pi bH\left[\tau_1 J_1(k_0 b) + \sum_{j=0}^{\infty} A_{1j} U_1^{(1)}(k_j b)\right] \tilde{W}_j^{(4)}, \tag{2.49}$$

where,

$$\tilde{W}_j^{(1)} = \int_{-h_1}^{0} Z_j^{(3)}(\sigma_j z)\mathrm{d}z,$$
$$\tilde{W}_j^{(2)} = \int_{-h_1}^{0} Z_j^{(2)}(\lambda_j z)\mathrm{d}z,$$
$$\tilde{W}_j^{(3)} = \int_{-h_2}^{-h_1} Z_j^{(4)}(\mu_j z)\mathrm{d}z,$$
$$\tilde{W}_j^{(4)} = \int_{-h_2}^{-h_1} Z_j^{(1)}(k_j z)\mathrm{d}z.$$

2.4 Validation

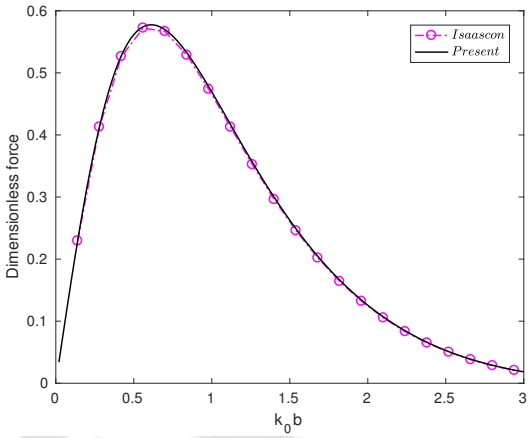

Figure 2.2: Comparison between present model and Isaacson's [19] model

To validate our analytical model, we consider the results of Isaacson [19] to compare with our result when the side wall of the bottom cylinder is impermeable. We consider a bottom-mounted compound cylinder corresponding to $G = 0$, $h_1/h_2 = 0.5$, $h_2/b = 2$, $a/b = 0.5$. Figure 2.2 shows the dimensionless force acting on the base of the cylinder for Isaacson's and the present result from which an excellent agreement can be observed. This confirms that our model is valid and hence can be employed effectively to investigate various issues with respect to the parameters.

2.5 Results and discussion

In practice, porous coefficient G always possesses positive real and imaginary parts but when the resistance effect against the flow dominates the inertial effect of the fluid inside

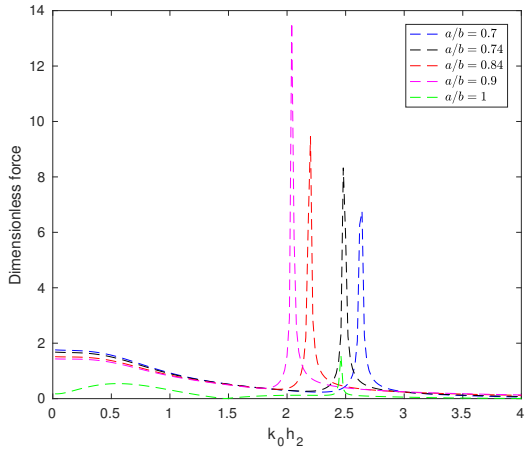

Figure 2.3: Variation of dimensionless hydrodynamic force on upper cylinder against the wavenumber for various values of a/b corresponding to $G = 1$ and $h_1/h_2 = 2/3$

the porous material, then G becomes real. Conforming to our problem, we consider only the real part of G which means the situation when resistance effect dominates inertial effect. Further, it is observed that even if G is imaginary or a mix of real and imaginary, there is no significant deviation at all from present results.

In Figure 2.3, the hydrodynamic force $\dfrac{|\tilde{F}_x^1|}{|\rho g a h_2 H|}$ for the upper cylinder is plotted against the wavenumber for various values of radius ratio a/b corresponding to $G = 1$ and $h_1/h_2 = 2/3$. It is to be noted that the very high oscillating behaviour is attributed to the resonance situation. Similar resonance phenomenon due to sloshing can also be observed in the works of Garrett [15] and Mavrakos [29]. This peculiar behaviour in the neighbourhood of $2 < k_0h_2 < 3$ is due to the wavenumber corresponding to the wavelength close to those of the free fluid motion. It is found that the force spikes become steeper for increasing values of a/b. However, it is observed that, except for $a/b = 1$, i.e., when radii of both outer and inner cylinder are same, the peak gets lowered to a large extent.

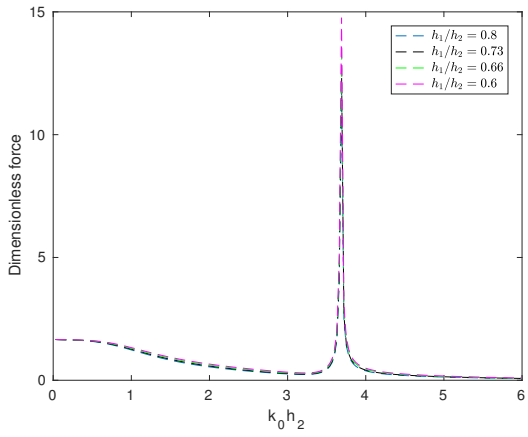

Figure 2.4: Variation of dimensionless hydrodynamic force on upper cylinder against the wavenumber for various values of h_1/h_2 corresponding to $G = 1$ and $a/b = 0.75$

In Figure 2.4, the hydrodynamic force $\frac{|\tilde{F}_x^1|}{|\rho g a h_2 H|}$ for the upper cylinder is plotted against the wavenumber for various values of draft h_1/h_2 corresponding to $G = 1$ and $a/b = 0.75$. It is observed that very high oscillating behaviour exists which can be attributed to the resonance situation. This peculiar behaviour in the neighbourhood of $k_0h_2 = 3.8$ occurs due to the wavenumber corresponding to the wavelength close to those of the free fluid motion. It is found that force spikes become steeper for decreasing values of h_1/h_2.

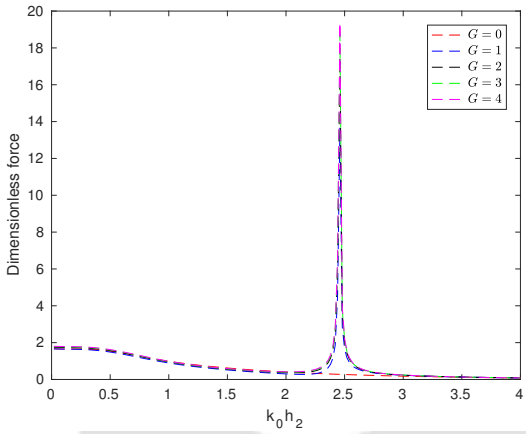

Figure 2.5: Variation of dimensionless hydrodynamic force on upper cylinder against the wavenumber for various values of G corresponding to $h_1/h_2 = 2/3$ and $a/b = 0.75$.

In Figure 2.5, the hydrodynamic force $\frac{|\tilde{F}_x^1|}{|\rho g a h_2 H|}$ for the upper cylinder is plotted against the wavenumber for various values of G corresponding to $h_1/h_2 = 2/3$ and $a/b = 0.75$. It is observed that, except for $G = 0$, the spikes of the force on the the upper cylinder increase for increasing values of the porosity of the lower cylinder. In the neighbourhood of $k_0h_2 = 2.5$, the value is very high. This also is the effect of the resonance situation. However, for $G = 0$, we do not observe such phenomenon mainly due to the fact $G = 0$ is equivalent to the lower cylinder rendered impermeable.

In Figure 2.6, the hydrodynamic force $\frac{|\tilde{F}_x^2|}{|\rho g b h_2 H|}$ for the lower cylinder is plotted against the wavenumber for various values of radius ratio a/b corresponding to $G = 1$ and $h_1/h_2 = 2/3$. It is to be noted that the wave force acting on the lower cylinder increases initially as the wave parameter k_0h_2 increases and further decreases with an increase for $k_0h_2 > 2.8$ approximately. A similar trend of wave force magnitude as in [10] is observed here too. Approximately the maximum force occurs in the neighbourhood of $k_0h_2 = 1$. The higher values of the force occur for lower values of a/b. The force diminishes for higher values of k_0h_2.

In Figure 2.7, the hydrodynamic force $\frac{|\tilde{F}_x^2|}{|\rho g b h_2 H|}$ for the lower cylinder is plotted against the wavenumber for various values of h_1/h_2 corresponding to $G = 1$ and $a/b = 0.75$. It is to be noted that the wave force acting on the lower cylinder increases initially as the wave parameter k_0h_2 increases but later it decreases corresponding to an increase in this

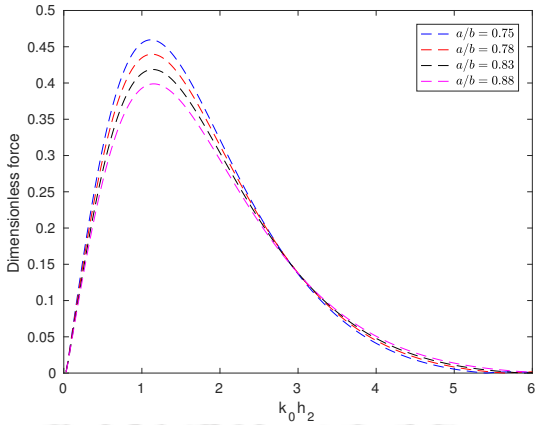

Figure 2.6: Variation of dimensionless hydrodynamic force on lower cylinder against the wavenumber for various values of a/b corresponding to $G = 1$ and $h_1/h_2 = 2/3$

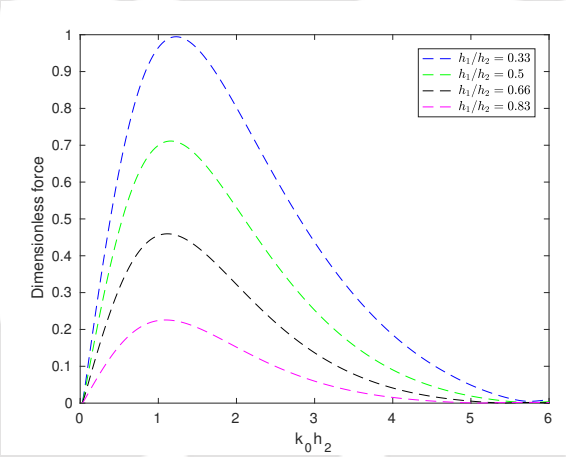

Figure 2.7: Variation of dimensionless hydrodynamic force on lower cylinder against the wavenumber for various values of h_1/h_2 corresponding to $G = 1$ and $a/b = 0.75$

parameter for $k_0h_2 > 2$. A similar trend of wave force magnitude as like in Figure 2.6 is observed here too. Approximately the maximum force occurs in the neighbourhood of $k_0h_2 = 1.5$. The main observation is that the higher values of the force occur within lower values of h_1/h_2.

In Figure 2.8, the hydrodynamic force $\dfrac{|\tilde{F}_x^2|}{|\rho g b h_2 H|}$ for the lower cylinder is plotted against the wavenumber for various values of G corresponding to $h_1/h_2 = 2/3$ and $a/b = 0.75$. Same type of graphical representation as earlier is observed here. The maximum value of the force occurs in the neighbourhood of $k_0h_2 = 1.5$. The main observation is that the force on the lower cylinder decreases for increasing values of the porosity. We observe that for $G = 0$, the force profile is of the same type as we observe for $G = 1, 2, 3, 4$, but higher than the other cases. This happens due to the lower portion of the cylinder becoming impermeable.

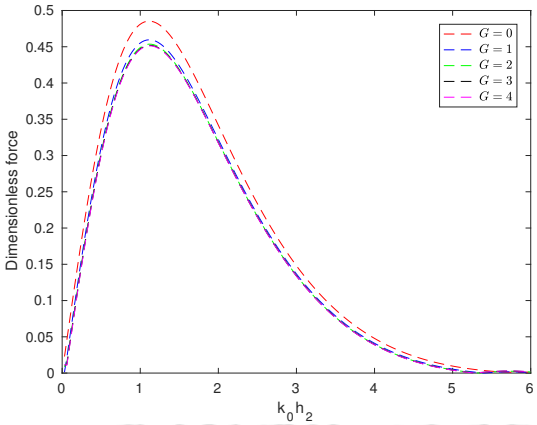

Figure 2.8: Variation of dimensionless hydrodynamic force on lower cylinder against the wavenumber for various values of G corresponding to $h_1/h_2 = 2/3$ and $a/b = 0.75$

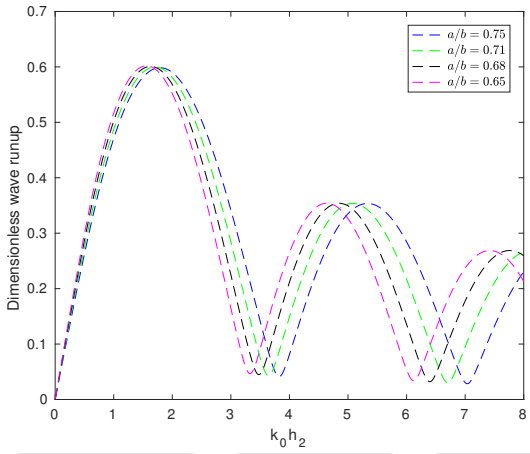

Figure 2.9: Variation of dimensionless wave run-up $|\zeta_1(b,\theta)|/H$ against the wavenumber for various values of a/b, $G = 1$ and $h_1/h_2 = 2/3$

In Figure 2.9, the maximum dimensionless wave run-up amplitude $|\zeta_1(b,\theta)|/H$ in the exterior region is investigated. It is plotted against the wavenumber for various values of a/b, $G = 1$ and $h_1/h_2 = 2/3$. In general, the maximum run-up occurs in the neighbourhood of $k_0h_2 = 2$.

In Figure 2.10, the maximum dimensionless wave run-up amplitude $|\zeta_1(b,\theta)|/H$ in the exterior region is investigated. It is plotted against the wavenumber for various values of G, $a/b = 0.75$ and $h_1/h_2 = 2/3$. The highest value of the run-up occurs in the neighbourhood of $k_0h_2 = 2$. The influence of the values of G on the maximum run-up is not that much significant. For $G = 0$, the wave run-up becomes more effective than the other cases.

In Figure 2.11, the maximum dimensionless wave run-up amplitude $|\zeta_2(a,\theta)|/H$ in the exterior region is investigated. It is plotted against the wavenumber for various values of a/b, $G = 1$ and $h_1/h_2 = 2/3$. The highest value of the run-up occurs in the neighbourhood of $k_0h_2 = 0.5$. The main observation is that maximum run-up occurs for the smaller values

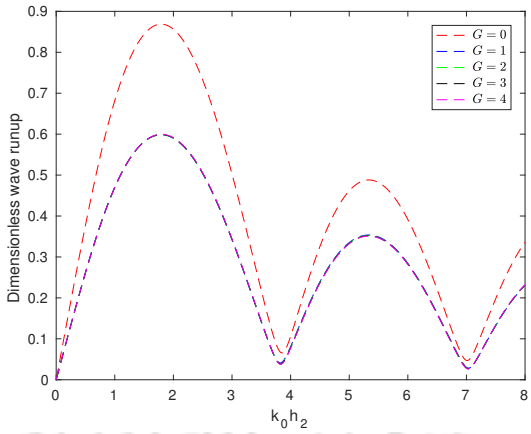

Figure 2.10: Variation of dimensionless wave run-up $|\zeta_1(b,\theta)|/H$ against the wavenumber for various values of G, $a/b = 0.75$ and $h_1/h_2 = 2/3$

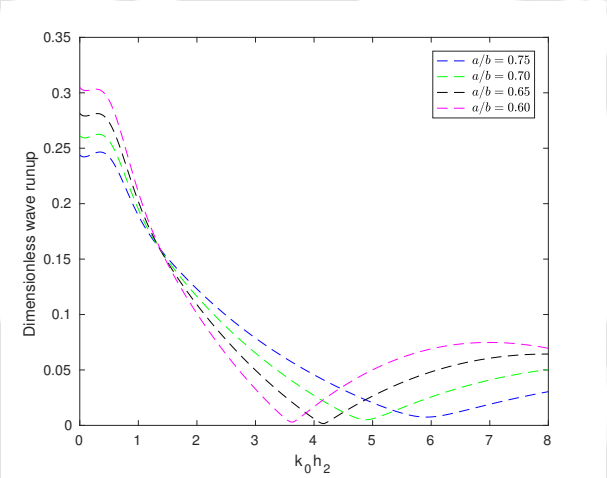

Figure 2.11: Variation of dimensionless wave run-up $|\zeta_2(a,\theta)|/H$ against the wavenumber for various values of a/b, $G = 1$ and $h_1/h_2 = 2/3$

of a/b.

In Figure 2.12, the maximum dimensionless wave run-up amplitude $|\zeta_2(a,\theta)|/H$ in the exterior region is investigated. It is plotted against the wavenumber for various values of G, $a/b = 0.75$ and $h_1/h_2 = 2/3$. The maximum value occurs in the neighbourhood of $k_0h_2 = 0.5$. The main observation is that the run-up increases for increasing values of the porosity. For $G = 0$, the wave run-up becomes more effective than the other cases.

In Figures 2.13 and 2.14, contour plots of the free surface elevation near the free surface for two different values of frequency are discussed. The figures depict that the flow is scattered by the cylinder and the elevation decreases. If we compare these two figures, it can be observed that for higher frequency incident wave, the diffracted wave pattern becomes more pronounced, and more number of ripples in waves are observed in the annular region. It may be noted that in all cases we consider only real values of G.

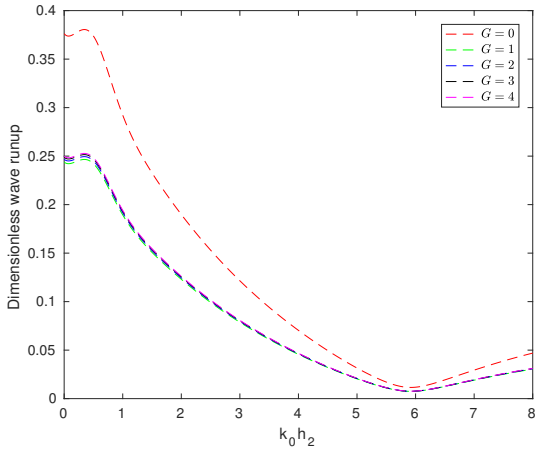

Figure 2.12: Variation of dimensionless wave run-up $|\zeta_2(a,\theta)|/H$ against the wavenumber for various values of G, $a/b = 0.75$ and $h_1/h_2 = 2/3$

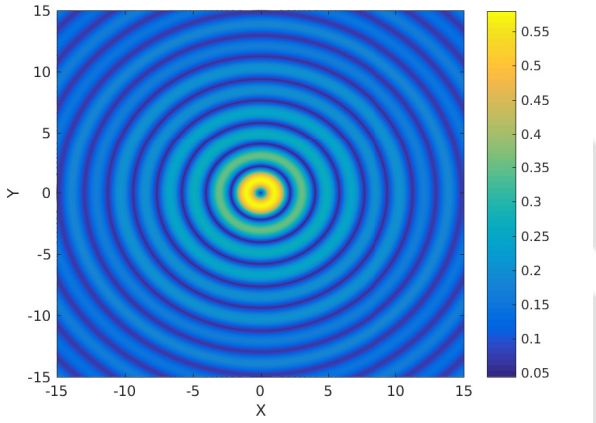

Figure 2.13: Contour plot for free surface elevation $|\zeta_1(r,\theta)|/H$ at free surface for $k_0b = 3.5$, $a/b = 0.75$, $h_1/h_2 = 2/3$ and $G = 1$

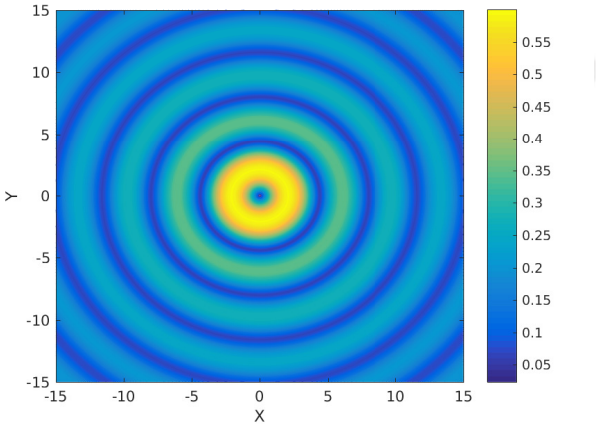

Figure 2.14: Contour plot for free surface elevation $|\zeta_1(r,\theta)|/H$ at free surface for $k_0b = 1.75$, $a/b = 0.75$, $h_1/h_2 = 2/3$ and $G = 1$

In fact while observing various graphs for complex G (either wholly complex or purely imaginary), it turns out that there is no significant change in any result. Therefore, we do not include here any result where G takes complex values.

2.6 Particular case: semi-porous single cylinder

Our earlier model is based on a compound porous cylinder. Now we discuss a semi-porous single cylinder which means that two potentials from earlier case will vanish. Only two potentials are effective here: one is inside the structure and the other outside of it. Here the cylinder is totally porous, except for the upper part having an impermeable side-wall. After evaluating potentials, we compute the hydrodynamic force acting on the upper part and lower part of the cylinder. We also discuss the effect of draft ratio and porous coefficient on the hydrodynamic force.

2.6.1 Mathematical formulation

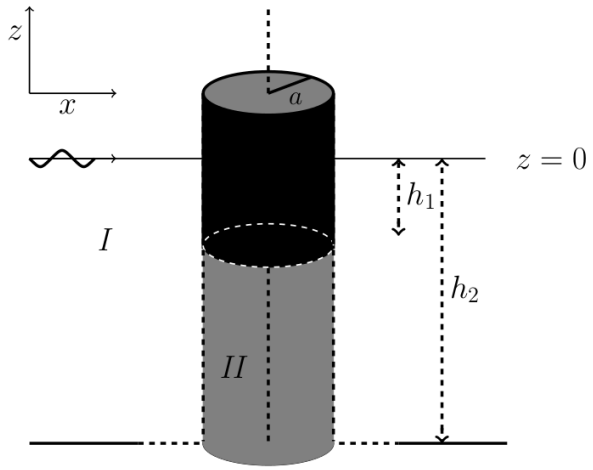

Figure 2.15: Semi-porous single cylinder

We consider a bottom-mounted surface-piercing semi-porous cylinder in finite depth (Figure 2.15). The cylinder is porous except for the upper part ($-h_1 \leq z \leq 0$) which has an impermeable side-wall. Fluid region is divided into two regions for $r \leq a$ and $r > a$. Then the scattered potential in the region $r > a$ is given by

$$\phi_1(r,\theta,z) = -\frac{\mathrm{i}gH}{\omega}\left[\sum_{m=0}^{\infty}\tau_m J_m(k_0 r)\cos m\theta Z_0^{(1)}(k_0 z) + \sum_{m=0}^{\infty}\cos m\theta \sum_{j=0}^{\infty} A_{mj} Z_j^{(1)}(k_j z) U_m^{(8)}(k_j r)\right]. \tag{2.50}$$

The radial eigenfunctions $U_m^{(8)}(k_j r)$ are as follows:

$$U_m^{(8)}(k_j r) = \begin{cases} \frac{H_m^{(1)}(k_j r)}{H_m^{(1)'}(k_j a)}; & j = 0, \\ \frac{K_m(k_j r)}{K_m'(k_j a)}; & j \geqslant 1. \end{cases}$$

Then the scattered potential in the region $r \leq a$ is given by

$$\phi_3(r, \theta, z) = -\frac{igH}{\omega} \left[\sum_{m=0}^{\infty} \cos m\theta \sum_{j=0}^{\infty} F_{mj} Z_j^{(1)}(k_j z) U_m^{(9)}(k_j r) \right]. \tag{2.51}$$

The radial eigenfunctions $U_m^{(9)}(k_j r)$ are as follows:

$$U_m^{(9)}(k_j r) = \begin{cases} \frac{J_m(k_j r)}{J_m'(k_j a)}; & j = 0, \\ \frac{I_m(k_j r)}{I_m'(k_j a)}; & j \geqslant 1. \end{cases}$$

Proceeding exactly in a similar way the earlier problem was handled, and by using matching conditions and standard matrix technique, we calculate the unknown coefficients A_{mj} and F_{mj}.

2.6.2 Results and discussion

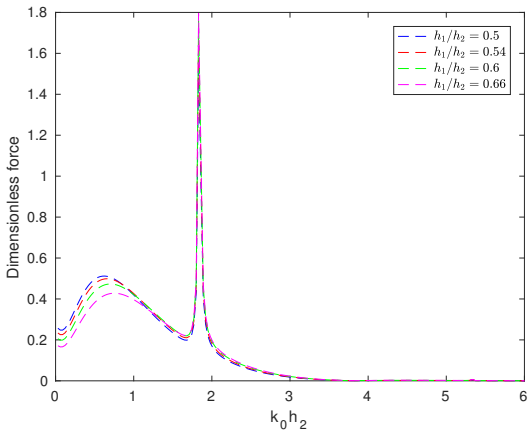

Figure 2.16: Variation of dimensionless hydrodynamic force on lower part of the cylinder against the wavenumber for various values of h_1/h_2 corresponding to $G = 1$

In Figure 2.16, the hydrodynamic force on the lower part of the cylinder is plotted against the wavenumber for various values of h_1/h_2 corresponding to $G = 1$. In this case also, the resonance situation is observed. The fluctuations become higher in the neighbourhood of $k_0h_2 = 1.9$. The force diminishes for higher values of k_0h_2.

In Figure 2.17, the hydrodynamic force on the upper part of the cylinder is plotted against the wavenumber for various values of h_1/h_2 corresponding to $G = 1$. A peculiar

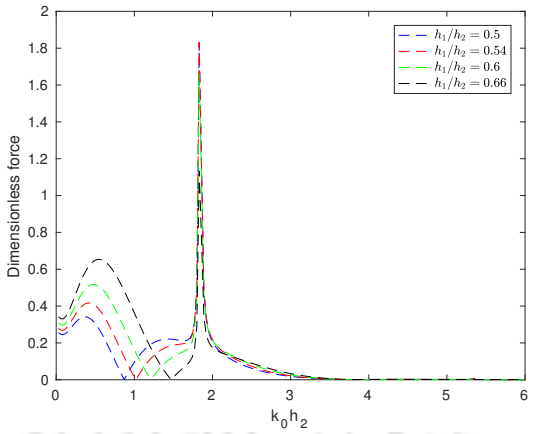

Figure 2.17: Variation of dimensionless hydrodynamic force on upper part of the cylinder against the wavenumber for various values of h_1/h_2 corresponding to $G = 1$

behaviour occurs in the neighbourhood of $k_0h_2 = 1.9$.

In Figure 2.18, the hydrodynamic force on the lower part of the cylinder is plotted against

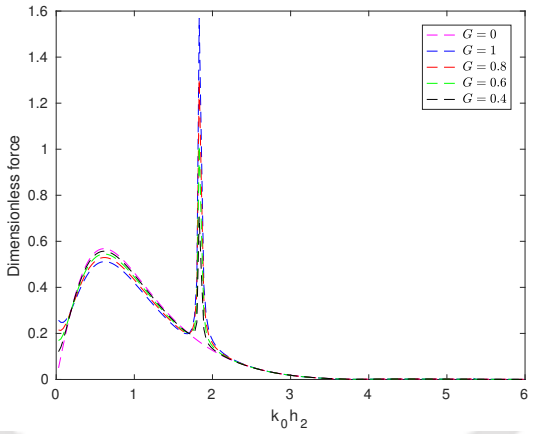

Figure 2.18: Variation of dimensionless hydrodynamic force on lower part of the cylinder against the wavenumber for various values of G corresponding to $h_1/h_2 = 1/2$

the wavenumber for various values of G corresponding to $h_1/h_2 = 1/2$. It is observed that force spikes become steeper for increasing values of G. For $G = 0$, the spikes are not present in the hydrodynamic force. This is due to the fact that $G = 0$ implies that the semi-porous cylinder becomes a non-porous cylinder.

In Figure 2.19, the hydrodynamic force on the upper part of the cylinder is plotted against the wavenumber for various values of G corresponding to $h_1/h_2 = 1/2$. The force spikes become steeper for increasing values of G. Similarly for $G = 0$, which means the semi-porous cylinder becomes a non-porous cylinder, the force spikes are not seen. Comparing the first model and second model in Figures 2.20 and 2.21 by taking $h_1/h_2 = 2/3$, $a/b = 1$ and $G = 1$, we observe that for both cases of the upper cylinder and the lower cylinder, the resonance effect exists but for the first model, the spike is steeper.

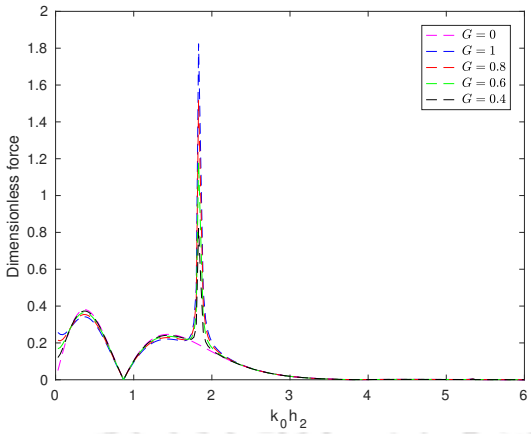

Figure 2.19: Variation of dimensionless hydrodynamic force on upper part of the cylinder against the wavenumber for various values of G corresponding to $h_1/h_2 = 1/2$

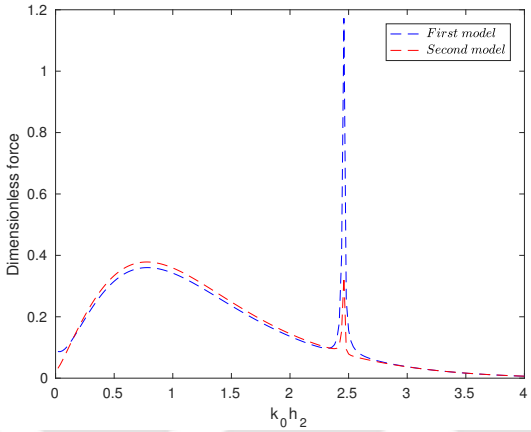

Figure 2.20: Comparison with first model and second model for lower part of the cylinder

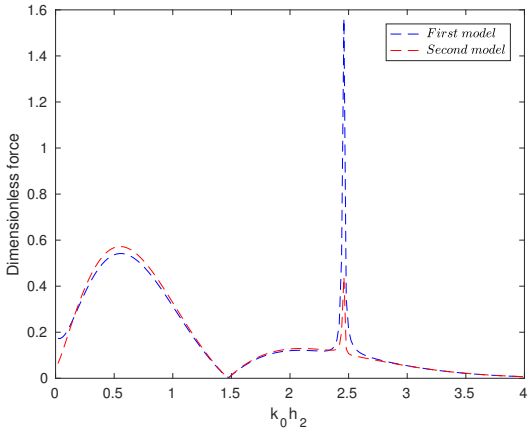

Figure 2.21: Comparison with first model and second model for upper part of the cylinder

2.7 Conclusion

This chapter presents an analytical study on the interaction of linear water waves with a bottom-mounted surface-piercing compound porous cylinder. An eigenfunction expansion approach and separation of variables technique are used to solve this diffraction problem governed by Laplace's equation. It is observed that change in values in radii, draft and porosity have significant effect on the hydrodynamic loads and wave run-up. The behaviour of hydrodynamic load is found to be steady in the lower frequency. However, a peculiar behaviour occurs due to the resonance situation in the neighbourhood of a specific frequency range. A similar phenomenon was also observed by Garrett [15] and Mavrakos [30]. For validating our result, we compare our result with the result of Isaacson [19], when the lower portion of the cylinder is impermeable. Good agreement can be seen between both results. This confirms that our model is valid and hence can be employed effectively to investigate various issues of the parameters. From Figure 2.8, it is clear that for $G = 0$, i.e., for an impermeable cylinder case, the force becomes higher. Also from Figures 2.10 and 2.12, it is observed that the wave run-up becomes more effective in the impermeable cylinder case. Figures 2.5, 2.18 and 2.19 show that for the impermeable cylinder case, the resonance effect does not exist. We expect that our results will be helpful in designing suitable structures to reduce the waveload.

CHAPTER 3

Water Wave Diffraction by a Surface-piercing Floating Compound Porous Cylinder in Finite Depth

In the current chapter, we specifically study the diffraction problem by a floating compound porous cylinder. The mathematical model is based on linear water wave theory. In this investigation of a floating compound porous cylinder, an eigenfunction expansion, along with the matching technique, is extensively used due to its considerable accuracy. Therefore, using these techniques, the analytical expressions for the diffraction of an incident wave acting on the cylinder are obtained. We investigate the hydrodynamic forces due to different radii, different porosity, different drafts. The effects of various parameters on hydrodynamic forces are presented and analysed. This problem can be considered as an extension of the work in Chapter 2 accomplished by raising the bottom-mounted cylinder thereby exposing the bottom part of the cylinder to the wave action. The model developed here is validated by comparing a result with an available one in the literature - the excellent agreement of which justifies the use of the present model for various investigations.

3.1 Mathematical formulation

Using linear water wave theory, we discuss wave interaction with a floating compound porous cylinder with porous coefficient G in finite depth. We consider the fluid to be homogeneous, incompressible and inviscid, and the motion irrotational. The sea-bed is considered as flat and impermeable (Figure 3.1). We consider a cylindrical coordinate system (r, θ, z) with the origin at the undisturbed free surface and the z-axis taken in upward direction. Here we consider a train of small-amplitude wave propagating from negative infinity towards the structure which comprises of an inner cylinder of radius a

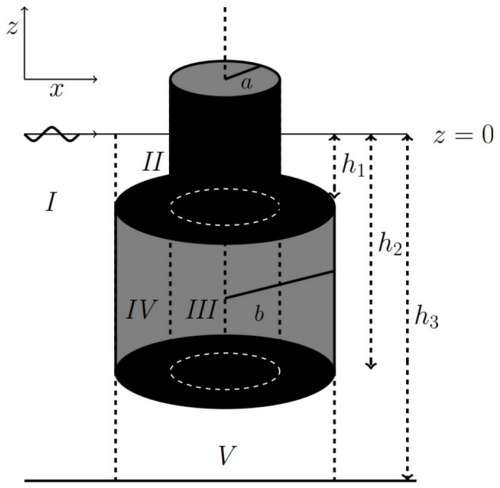

Figure 3.1: Floating compound porous cylinder at finite depth with top of the lower cylinder impermeable

and an outer cylinder of radius b. The bottom $(0 \leq r \leq b)$ and top of the lower cylinder $(a \leq r \leq b)$ are considered to be impermeable. Further, the upper cylinder has an impermeable side-wall on which some boundary conditions are appropriately defined. We describe the fluid flow by introducing the potential $\Phi(r, \theta, z, t) = \mathrm{Re}[\phi(r, \theta, z) \exp(-\mathrm{i}\omega t)]$. The fluid domain is divided into five regions: Region I $(r \geq b, -h_3 \leq z \leq 0)$; Region II $(a \leq r \leq b, -h_1 \leq z \leq 0)$; Region III $(0 \leq r \leq a, -h_2 \leq z \leq 0)$; Region IV $(a \leq r \leq b, -h_2 \leq z \leq -h_1)$ and Region V $(0 \leq r \leq b, -h_3 \leq z \leq -h_2)$. The velocity potential in each region is denoted by Φ_j for $j = 1, 2, 3, 4, 5$.

3.2 The boundary value problem

In this section we will set up the boundary value problem with suitable boundary conditions and matching conditions. We will also calculate diffracted potentials in each subdomain. There may be equations, conditions and expressions same or similar to those used in Chapter 2. Instead of eliminating them and referring them from Chapter 1, some of them are kept in this section so as to have a free flow in reading this chapter.

3.2.1 Governing equations and boundary conditions

Each potential satisfies Laplace's equation in respective flow region, namely,

$$\nabla^2 \phi_j = 0; \quad j = 1, 2, 3, 4, 5, \tag{3.1}$$

where $\phi_j, \quad j = 1, 2, 3, 4, 5$ refer to the potentials in Regions I, II, III, IV and V, respectively. The boundary conditions on the free surface and sea-bed can be expressed

as

$$\frac{\partial \phi_j}{\partial z} - \frac{\omega^2}{g}\phi_j = 0; \quad z = 0, \quad j = 1, 2, 3, \tag{3.2}$$

$$\frac{\partial \phi_1}{\partial z} = 0; \quad z = -h_3, \quad r > b, \tag{3.3}$$

$$\frac{\partial \phi_5}{\partial z} = 0; \quad z = -h_3, \quad 0 < r < b. \tag{3.4}$$

The boundary conditions on the impermeable surface of the cylinder can be expressed as

$$\frac{\partial \phi_2}{\partial r} = 0; \quad r = a, \quad -h_1 < z < 0, \tag{3.5}$$

$$\frac{\partial \phi_3}{\partial r} = 0; \quad r = a, \quad -h_1 < z < 0, \tag{3.6}$$

$$\frac{\partial \phi_2}{\partial z} = 0; \quad z = -h_1, \quad a < r < b, \tag{3.7}$$

$$\frac{\partial \phi_4}{\partial z} = 0; \quad z = -h_1, \quad a < r < b, \tag{3.8}$$

$$\frac{\partial \phi_4}{\partial z} = 0; \quad z = -h_2, \quad a < r < b, \tag{3.9}$$

$$\frac{\partial \phi_3}{\partial z} = 0; \quad z = -h_2, \quad 0 < r < a, \tag{3.10}$$

$$\frac{\partial \phi_5}{\partial z} = 0; \quad z = -h_2, \quad 0 < r < b. \tag{3.11}$$

The boundary condition on the porous circular wall is (as in Williams and Li [59])

$$\frac{\partial \phi_4}{\partial r} = \mathrm{i}k_0 G(\phi_4 - \phi_1), \quad r = b, \quad -h_2 < z < -h_1, \tag{3.12}$$

where G and k_0 are complex porous coefficient and incident wavenumber, respectively. The velocity potential in the exterior region must satisfy the Sommerfeld radiation condition given by equation (2.15).

3.2.2 Matching conditions

On the cylindrical surface, the potentials satisfy the following matching conditions:

$$\phi_1 = \phi_2; \quad r = b, \quad -h_1 < z < 0, \tag{3.13}$$

$$\phi_1 = \phi_5; \quad r = b, \quad -h_3 < z < -h_2, \tag{3.14}$$

$$\phi_3 = \phi_4; \quad r = a, \quad -h_2 < z < -h_1, \tag{3.15}$$

$$\frac{\partial \phi_3}{\partial r} = \frac{\partial \phi_4}{\partial r}; \quad r = a, \quad -h_2 < z < -h_1, \tag{3.16}$$

$$\frac{\partial \phi_1}{\partial r} = \begin{cases} \frac{\partial \phi_2}{\partial r}; & r = b, \quad -h_1 < z < 0, \\ \frac{\partial \phi_4}{\partial r}; & r = b, \quad -h_2 < z < -h_1, \\ \frac{\partial \phi_5}{\partial r}; & r = b, \quad -h_3 < z < -h_2. \end{cases} \tag{3.17}$$

Equations (3.5), (3.6) and (3.16) across the boundary $r = a$ in the interval $-h_2 < z < 0$ can be written as a single condition, as in Darwiche et al. [10], as follows:

$$\frac{\partial \phi_3}{\partial r} = \frac{\partial(\phi_2 + \phi_4)}{\partial r}; \quad r = a, \quad -h_2 < z < 0. \tag{3.18}$$

3.2.3 Diffracted potentials

Applying the separation of variables method in each sub-domain, expressions for the velocity potential are obtained. Each expression is obtained as an infinite series of orthogonal functions which is valid in the corresponding sub-domain. The velocity potential in region I can be expressed in the following form:

$$\phi_1(r,\theta,z) = -\frac{\mathrm{i}gH}{\omega}\left[\sum_{m=0}^{\infty}\tau_m J_m(k_0 r)\cos m\theta Z_0^{(1)}(k_0 z) + \sum_{m=0}^{\infty}\cos m\theta \sum_{j=0}^{\infty} A_{mj} Z_j^{(1)}(k_j z) U_m^{(1)}(k_j r)\right], \tag{3.19}$$

where A_{mj} are unknown coefficients. Wavenumbers k_j $(j = 0, 1, 2, 3, \ldots)$ can be derived by the following dispersion relation (as in Chamberlain and Porter [6]):

$$\omega^2 = \begin{cases} gk_j \tanh k_j h_3; & j = 0, \\ -gk_j \tan k_j h_3; & j \geqslant 1. \end{cases}$$

The radial eigenfunctions $U_m^{(1)}(k_j r)$ are as follows:

$$U_m^{(1)}(k_j r) = \begin{cases} \frac{H_m^{(1)}(k_j r)}{H_m^{(1)\prime}(k_j b)}; & j = 0, \\ \frac{K_m(k_j r)}{K_m'(k_j b)}; & j \geqslant 1. \end{cases}$$

The vertical eigenfunctions $Z_j^{(1)}(k_j z)$ are defined as

$$Z_j^{(1)}(k_j z) = \begin{cases} \frac{\cosh k_j(z+h_3)}{\cosh k_j h_3}; & j = 0, \\ \frac{\cos k_j(z+h_3)}{\cos k_j h_3}; & j \geqslant 1. \end{cases}$$

The scattered velocity potential ϕ_2 can be expressed as

$$\phi_2(r,\theta,z) = -\frac{\mathrm{i}gH}{\omega}\left[\sum_{m=0}^{\infty}\cos m\theta \sum_{j=0}^{\infty}\left[B_{mj}U_m^{(2)}(\lambda_j r) + C_{mj}U_m^{(3)}(\lambda_j r)\right] Z_j^{(2)}(\lambda_j z)\right], \tag{3.20}$$

where B_{mj} and C_{mj} are unknown coefficients and λ_j can be calculated from the following relation:

$$\omega^2 = \begin{cases} g\lambda_j \tanh \lambda_j h_1; & j = 0, \\ -g\lambda_j \tan \lambda_j h_1; & j \geqslant 1. \end{cases}$$

The radial eigenfunctions $U_m^{(2)}(\lambda_j r)$ and $U_m^{(3)}(\lambda_j r)$ are as follows:

$$U_m^{(2)}(\lambda_j r) = \begin{cases} \frac{H_m^{(1)}(\lambda_j r)}{H_m^{(1)'}(\lambda_j b)}; & j = 0, \\ \frac{I_m(\lambda_j r)}{I'_m(\lambda_j b)}; & j \geqslant 1, \end{cases} \qquad U_m^{(3)}(\lambda_j r) = \begin{cases} \frac{H_m^{(2)}(\lambda_j r)}{H_m^{(2)'}(\lambda_j b)}; & j = 0, \\ \frac{K_m(\lambda_j r)}{K'_m(\lambda_j b)}; & j \geqslant 1. \end{cases}$$

The vertical eigenfunctions $Z_j^{(2)}(\lambda_j z)$ are defined as

$$Z_j^{(2)}(\lambda_j z) = \begin{cases} \frac{\cosh \lambda_j (z+h_1)}{\cosh \lambda_j h_1}; & j = 0, \\ \frac{\cos \lambda_j (z+h_1)}{\cos \lambda_j h_1}; & j \geqslant 1. \end{cases}$$

Now the velocity potential ϕ_3 in Region III can be expressed as

$$\phi_3(r, \theta, z) = -\frac{igH}{\omega} \left[\sum_{m=0}^{\infty} \cos m\theta \sum_{j=0}^{\infty} F_{mj} Z_j^{(3)}(\sigma_j z) U_m^{(4)}(\sigma_j r) \right], \tag{3.21}$$

where F_{mj} are unknown coefficients and σ_j can be calculated from the following relation:

$$\omega^2 = \begin{cases} g\sigma_j \tanh \sigma_j h_2; & j = 0, \\ -g\sigma_j \tan \sigma_j h_2; & j \geqslant 1. \end{cases}$$

The radial eigenfunctions $U_m^{(4)}(\sigma_j r)$ are as follows:

$$U_m^{(4)}(\sigma_j r) = \begin{cases} \frac{J_m(\sigma_j r)}{J'_m(\sigma_j a)}; & j = 0, \\ \frac{I_m(\sigma_j r)}{I'_m(\sigma_j a)}; & j \geqslant 1. \end{cases}$$

The potential given by equation (3.21), along with $U_m^{(4)}(\sigma_j r)$, is connected to a specific resonance phenomenon. The first term on the right side of (3.21) is the most important contribution to the wave motion inside the cylinder. Similar resonance phenomenon due to sloshing can also be observed in the works of Garrett [15] and Mavrakos [29], as already mentioned in the previous chapter.

The vertical eigenfunctions $Z_j^{(3)}(\sigma_j z)$ are defined as

$$Z_j^{(3)}(\sigma_j z) = \begin{cases} \frac{\cosh \sigma_j (z+h_2)}{\cosh \sigma_j h_2}; & j = 0, \\ \frac{\cos \sigma_j (z+h_2)}{\cos \sigma_j h_2}; & j \geqslant 1. \end{cases}$$

The velocity potential ϕ_4 in Region IV can be expressed as

$$\phi_4(r, \theta, z) = -\frac{igH}{\omega} \left[\sum_{m=0}^{\infty} \cos m\theta \sum_{j=0}^{\infty} \left[D_{mj} U_m^{(5)}(\mu_j r) + E_{mj} U_m^{(6)}(\mu_j r) \right] Z_j^{(4)}(\mu_j z) \right], \tag{3.22}$$

where D_{mj} and E_{mj} are unknown coefficients and μ_j can be calculated from the following

relation (as in Ning et al. [38]):

$$\mu_j = \frac{\pi j}{h_2 - h_1}, \quad j = 0, 1, 2, \ldots.$$

The radial eigenfunctions $U_m^{(5)}(\mu_j r)$ and $U_m^{(6)}(\mu_j r)$ are as follows:

$$U_m^{(5)}(\mu_j r) = \begin{cases} \frac{r^{-m}}{b^{-m-1}}; & j = 0, \\ \frac{K_m(\mu_j r)}{K'_m(\mu_j b)}; & j \geqslant 1, \end{cases} \qquad U_m^{(6)}(\mu_j r) = \begin{cases} \frac{r^m}{b^{m-1}}; & j = 0, \\ \frac{I_m(\mu_j r)}{I'_m(\mu_j b)}; & j \geqslant 1. \end{cases}$$

The vertical eigenfunctions $Z_j^{(4)}(\mu_j z)$ are defined as

$$Z_j^{(4)}(\mu_j z) = \begin{cases} \frac{\sqrt{2}}{2}; & j = 0, \\ \cos \mu_j (z + h_2); & j \geqslant 1. \end{cases}$$

The velocity potential ϕ_5 in Region V can be expressed as

$$\phi_5(r, \theta, z) = -\frac{\mathrm{i}gH}{\omega} \left[\sum_{m=0}^{\infty} \cos m\theta \sum_{j=0}^{\infty} \tilde{G}_{mj} Z_j^{(5)}(\gamma_j z) U_m^{(7)}(\gamma_j r) \right], \tag{3.23}$$

where $\tilde{G}_{mj}$ are unknown coefficients and γ_j can be calculated from the following relation:

$$\gamma_j = \frac{\pi j}{h_3 - h_2}, \quad j = 0, 1, 2, \ldots.$$

The radial eigenfunctions $U_m^{(7)}(\gamma_j r)$ are as follows:

$$U_m^{(7)}(\gamma_j r) = \begin{cases} \frac{r^m}{b^{m-1}}; & j = 0, \\ \frac{I_m(\gamma_j r)}{I'_m(\gamma_j b)}; & j \geqslant 1. \end{cases}$$

The vertical eigenfunctions $Z_j^{(5)}(\gamma_j z)$ are defined as

$$Z_j^{(5)}(\gamma_j z) = \begin{cases} \frac{1}{\sqrt{2}}; & j = 0, \\ \cos \gamma_j (z + h_3); & j \geqslant 1. \end{cases}$$

3.3 Solution for the unknown coefficients

Application of the boundary condition (3.5) and the use of the orthogonal property of the eigenfunctions lead to the following relationship between the potential coefficients $B_{m\alpha}$ and $C_{m\alpha}$:

$$\frac{H_m^{(1)'}(\lambda_0 a)}{H_m^{(1)'}(\lambda_0 b)} B_{m0} + \frac{H_m^{(2)'}(\lambda_0 a)}{H_m^{(2)'}(\lambda_0 b)} C_{m0} = 0, \tag{3.24}$$

$$\frac{I'_m(\lambda_\alpha a)}{I'_m(\lambda_\alpha b)}B_{m\alpha}+\frac{K'_m(\lambda_\alpha a)}{K'_m(\lambda_\alpha b)}C_{m\alpha} = 0, \quad \alpha \geqslant 1. \tag{3.25}$$

Using these relationships, the expression for ϕ_2 can be modified as

$$\phi_2(r,\theta,z)=-\frac{igH}{\omega}\left[\sum_{m=0}^{\infty}\cos m\theta\sum_{j=0}^{\infty}C_{mj}Z_j^{(2)}(\lambda_j z)U_m^{(8)}(\lambda_j r)\right]. \tag{3.26}$$

The radial eigenfunctions $U_m^{(8)}(\lambda_j r)$ are as follows:

$$U_m^{(8)}(\lambda_j r)=\begin{cases}\frac{H_m^{(2)}(\lambda_j r)}{H_m^{(2)'}(\lambda_j b)}-\frac{H_m^{(2)'}(\lambda_j a)}{H_m^{(2)'}(\lambda_j b)}\frac{H_m^{(1)}(\lambda_j r)}{H_m^{(1)'}(\lambda_j a)}; & j=0,\\ \frac{K_m(\lambda_j r)}{K'_m(\lambda_j b)}-\frac{K'_m(\lambda_j a)}{K'_m(\lambda_j b)}\frac{I_m(\lambda_j r)}{I'_m(\lambda_j a)}; & j\geqslant 1.\end{cases}$$

Using the matching conditions (3.13) and (3.17) for the depth $-h_1<z<0$, we get

$$\sum_{j=0}^{\infty}A_{mj}U_m^{(1)}(k_j b)Z_j^{(1)}(k_j z)-\sum_{j=0}^{\infty}C_{mj}U_m^{(8)}(\lambda_j b)Z_j^{(2)}(\lambda_j z) = -\tau_m J_m(k_0 b)Z_0^{(1)}(k_0 z), \tag{3.27}$$

$$\sum_{j=0}^{\infty}A_{mj}U_m^{(1)'}(k_j b)Z_j^{(1)}(k_j z)-\sum_{j=0}^{\infty}C_{mj}U_m^{(8)'}(\lambda_j b)Z_j^{(2)}(\lambda_j z) = -\tau_m J'_m(k_0 b)Z_0^{(1)}(k_0 z). \tag{3.28}$$

Now using orthogonal property of the eigenfunctions $Z_0^{(2)}(\lambda_0 z)$ and $Z_\alpha^{(2)}(\lambda_\alpha z)$ $(\alpha=1,2,3,\ldots)$, we get

$$\sum_{j=0}^{\infty}A_{mj}U_m^{(1)}(k_j b)Q_{0j}-C_{m0}U_m^{(8)}(\lambda_0 b)R_{00} = -\tau_m J_m(k_0 b)Q_{00}, \tag{3.29}$$

$$\sum_{j=0}^{\infty}A_{mj}U_m^{(1)}(k_j b)Q_{\alpha j}-C_{m\alpha}U_m^{(8)}(\lambda_\alpha b)R_{\alpha\alpha} = -\tau_m J_m(k_0 b)Q_{\alpha 0}, \quad \alpha\geqslant 1, \tag{3.30}$$

$$\sum_{j=0}^{\infty}A_{mj}Q_{0j}-C_{m0}U_m^{(8)'}(\lambda_0 b)R_{00} = -\tau_m J'_m(k_0 b)Q_{00}, \tag{3.31}$$

$$\sum_{j=0}^{\infty}A_{mj}Q_{\alpha j}-C_{m\alpha}U_m^{(8)'}(\lambda_\alpha b)R_{\alpha\alpha} = -\tau_m J'_m(k_0 b)Q_{\alpha 0}, \quad \alpha\geqslant 1, \tag{3.32}$$

where,

$$Q_{\alpha,j} = \int_{-h_1}^{0}Z_\alpha^{(2)}(\lambda_\alpha z)Z_j^{(1)}(k_j z)\mathrm{d}z, \tag{3.33}$$

$$R_{\alpha,\alpha} = \int_{-h_1}^{0}Z_\alpha^{(2)}(\lambda_\alpha z)Z_\alpha^{(2)}(\lambda_\alpha z)\mathrm{d}z. \tag{3.34}$$

After that, using matching conditions (3.12) and (3.17) for the depth $-h_2<z<-h_1$,

we get

$$\mathrm{i}k_0G\sum_{j=0}^{\infty}\left(D_{mj}U_m^{(5)}(\mu_j b)+E_{mj}U_m^{(6)}(\mu_j b)\right)Z_j^{(4)}(\mu_j z)$$
$$-\sum_{j=0}^{\infty}A_{mj}(1+\mathrm{i}k_0GU_m^{(1)}(k_j b))Z_j^{(1)}(k_j z)=\tau_m(J_m'(k_0b)+\mathrm{i}k_0GJ_m(k_0b))Z_0^{(1)}(k_0z), \quad (3.35)$$
$$\sum_{j=0}^{\infty}\left(D_{mj}U_m^{(5)\prime}(\mu_j b)+E_{mj}U_m^{(6)\prime}(\mu_j b)\right)Z_j^{(4)}(\mu_j z)-\sum_{j=0}^{\infty}A_{mj}U_m^{(1)\prime}(k_j b)Z_j^{(1)}(k_j z)$$
$$=\tau_m J_m'(k_0b)Z_0^{(1)}(k_0z). \quad (3.36)$$

Now using orthogonal property of the eigenfunctions $Z_0^{(4)}(\mu_0 z)$, $Z_\alpha^{(4)}(\mu_\alpha z)$ $(\alpha=1,2,3,\ldots)$, we obtain

$$\mathrm{i}k_0G\left(D_{m0}+E_{m0}\right)bT_{00}-\sum_{j=0}^{\infty}A_{mj}(1+\mathrm{i}k_0GU_m^{(1)}(k_j b))P_{0j}$$
$$=\tau_m P_{00}(J_m'(k_0b)+\mathrm{i}k_0GJ_m(k_0b)), \quad (3.37)$$

$$\mathrm{i}k_0G\left(D_{m\alpha}\frac{K_m(\mu_\alpha b)}{K_m'(\mu_\alpha b)}+E_{m\alpha}\frac{I_m(\mu_\alpha b)}{I_m'(\mu_\alpha b)}\right)T_{\alpha\alpha}-\sum_{j=0}^{\infty}A_{mj}(1+\mathrm{i}k_0GU_m^{(1)}(k_j b))P_{\alpha j}$$
$$=\tau_m P_{\alpha0}(J_m'(k_0b)+\mathrm{i}k_0GJ_m(k_0b)), \quad \alpha\geqslant 1, \quad (3.38)$$

$$\left(-mD_{m0}+mE_{m0}\right)T_{00}-\sum_{j=0}^{\infty}A_{mj}P_{0j} = \tau_m P_{00}J_m'(k_0b), \quad (3.39)$$

$$\left(D_{m\alpha}+E_{m\alpha}\right)T_{\alpha\alpha}-\sum_{j=0}^{\infty}A_{mj}P_{\alpha j} = \tau_m P_{\alpha0}J_m'(k_0b), \quad \alpha\geqslant 1, \quad (3.40)$$

where,

$$P_{\alpha,j} = \int_{-h_2}^{-h_1}Z_\alpha^{(4)}(\mu_\alpha z)Z_j^{(1)}(k_j z)\mathrm{d}z, \quad (3.41)$$

$$T_{\alpha,\alpha} = \int_{-h_2}^{-h_1}Z_\alpha^{(4)}(\mu_\alpha z)Z_\alpha^{(4)}(\mu_\alpha z)\mathrm{d}z. \quad (3.42)$$

Substitution of ϕ_3, ϕ_2 and ϕ_4 in equation (3.18) leads to

$$\sum_{j=0}^{\infty}\left[D_{mj}U_m^{(5)\prime}(\mu_j a)+E_{mj}U_m^{(6)\prime}(\mu_j a)\right]Z_j^{(4)}(\mu_j z)-\sum_{j=0}^{\infty}F_{mj}Z_j^{(3)}(\sigma_j z)$$
$$+\sum_{j=0}^{\infty}\left[B_{mj}U_m^{(2)\prime}(\lambda_j a)+C_{mj}U_m^{(3)\prime}(\lambda_j a)\right]Z_j^{(2)}(\lambda_j z)=0. \quad (3.43)$$

Now using orthogonal property of the eigenfunctions $Z_0^{(3)}(\sigma_0 z)$, $Z_\alpha^{(3)}(\sigma_\alpha z)$ $(\alpha = 1, 2, 3, \ldots)$, we get

$$\sum_{j=0}^{\infty}\left[D_{mj}U_m^{(5)'}(\mu_j a)+E_{mj}U_m^{(6)'}(\mu_j a)\right]M_{0j}-F_{m0}N_{00}$$
$$+\sum_{j=0}^{\infty}\left[B_{mj}U_m^{(2)'}(\lambda_j a)+C_{mj}U_m^{(3)'}(\lambda_j a)\right]L_{0j}=0, \tag{3.44}$$
$$\sum_{j=0}^{\infty}\left[D_{mj}U_m^{(5)'}(\mu_j a)+E_{mj}U_m^{(6)'}(\mu_j a)\right]M_{\alpha j}-F_{m\alpha}N_{\alpha\alpha}$$
$$+\sum_{j=0}^{\infty}\left[B_{mj}U_m^{(2)'}(\lambda_j a)+C_{mj}U_m^{(3)'}(\lambda_j a)\right]L_{\alpha j}=0,\quad \alpha\geqslant 1, \tag{3.45}$$

where,

$$L_{\alpha,j} = \int_{-h_2}^{0} Z_\alpha^{(3)}(\sigma_\alpha z)Z_j^{(2)}(\lambda_j z)\mathrm{d}z, \tag{3.46}$$
$$N_{\alpha,\alpha} = \int_{-h_2}^{0} Z_\alpha^{(3)}(\sigma_\alpha z)Z_\alpha^{(3)}(\sigma_\alpha z)\mathrm{d}z, \tag{3.47}$$
$$M_{\alpha,j} = \int_{-h_2}^{0} Z_\alpha^{(3)}(\sigma_\alpha z)Z_j^{(4)}(\mu_j z)\mathrm{d}z. \tag{3.48}$$

Further, using the matching condition (3.17) across the boundary $r = b$ in the interval $-h_3 < z < -h_2$, we obtain

$$\tau_m J_m'(k_0 b)Z_0^{(1)}(k_0 z)+\sum_{j=0}^{\infty}A_{mj}U_m^{(1)'}(k_j b)Z_j^{(1)}(k_j z)-\sum_{j=0}^{\infty}\tilde{G}_{mj}U_m^{(7)'}(\gamma_j b)Z_j^{(5)}(\gamma_j z)=0. \tag{3.49}$$

Now use of orthogonal property of the eigenfunctions $Z_0^{(5)}(\gamma_0 z)$ and $Z_\alpha^{(5)}(\gamma_\alpha z)$ $(\alpha = 1, 2, 3, ...)$ gives

$$\tau_m J_m'(k_0 b)S_{00}+\sum_{j=0}^{\infty}A_{mj}S_{0j}-\tilde{G}_{m0}\tilde{S}_{00} = 0, \tag{3.50}$$
$$\tau_m J_m'(k_0 b)S_{\alpha 0}+\sum_{j=0}^{\infty}A_{mj}S_{\alpha j}-\tilde{G}_{m\alpha}\tilde{S}_{\alpha\alpha} = 0,\quad \alpha\geqslant 1, \tag{3.51}$$

where,

$$S_{\alpha,j} = \int_{-h_3}^{-h_2} Z_\alpha^{(5)}(\gamma_\alpha z)Z_j^{(1)}(k_j z)\mathrm{d}z, \tag{3.52}$$
$$\tilde{S}_{\alpha,\alpha} = \int_{-h_3}^{-h_2} Z_\alpha^{(5)}(\gamma_\alpha z)Z_\alpha^{(5)}(\gamma_\alpha z)\mathrm{d}z. \tag{3.53}$$

In order to obtain the hydrodynamic force and wave run-up, we need to find the unknown coefficients A_{mj}, B_{mj}, C_{mj}, D_{mj}, E_{mj}, F_{mj} and $\tilde{G}_{mj}$. Since each expression is an infinite series, there is a need to truncate each series suitably to compute coefficients. Truncation of the infinite series (3.29)-(3.51) after a finite number of terms (as in Ning et al. [38]), say $N = 20$, and the use of (3.24) and (3.25) lead to simultaneous matrix equations. Note that excellent convergence can be achieved by truncating the expansion series after the first 20 terms. The convergence follows similarly as demonstrated in Chapter 2. Subsequently, in order to determine the unknown coefficients, we arrive at a linear system of algebraic equations

$$\mathcal{A}_l \mathcal{X}_l = \mathcal{B}_l, \tag{3.54}$$

where, $\mathcal{X}_l = [A_{l1}, A_{l2}, ..., A_{lN}, B_{l1}, B_{l2}, ..., B_{lN}, C_{l1}, C_{l2}, ..., C_{lN}, D_{l1}, D_{l2}, ..., D_{lN}, E_{l1}, E_{l2}, ..., E_{lN}, F_{l1}, F_{l2}, ..., F_{lN}, \tilde{G}_{l1}, \tilde{G}_{l2}, ..., \tilde{G}_{lN}]^t$, $\mathcal{A}_l$ are coefficient matrices and $\mathcal{B}_l$ are the right hand vectors.

3.4 Hydrodynamic force and wave run-up

The total hydrodynamic force in the direction of wave propagation on the upper and the lower cylinders can be evaluated by integrating the pressure distribution on the structures. We define $\tilde{F}_x^j(t) = \mathrm{Re}[\tilde{F}_x^j \exp(-\mathrm{i}\omega t)]$ for $j = 1, 2$ as

$$\tilde{F}_x^1 = \mathrm{i}\omega\rho \int_{-h_1}^{0} \int_0^{2\pi} \phi_3(a, \theta, z) \cos\theta \quad \mathrm{d}z\mathrm{d}\theta - \mathrm{i}\omega\rho \int_{-h_1}^{0} \int_0^{2\pi} \phi_2(a, \theta, z) \cos\theta \quad \mathrm{d}z\mathrm{d}\theta, \tag{3.55}$$

$$\tilde{F}_x^2 = \mathrm{i}\omega\rho \int_{-h_2}^{-h_1} \int_0^{2\pi} \phi_4(b, \theta, z) \cos\theta \quad \mathrm{d}z\mathrm{d}\theta - \mathrm{i}\omega\rho \int_{-h_2}^{-h_1} \int_0^{2\pi} \phi_1(b, \theta, z) \cos\theta \quad \mathrm{d}z\mathrm{d}\theta. \tag{3.56}$$

Upon simplification, we get

$$\begin{aligned} \tilde{F}_x^1 &= g\rho\pi a H \left[\sum_{j=0}^{\infty} F_{1j} U_1^{(4)}(\sigma_j a) \right] \tilde{W}_j^{(1)} \\ &- g\rho\pi a H \left[\sum_{j=0}^{\infty} B_{1j} U_1^{(2)}(\lambda_j a) + C_{1j} U_1^{(3)}(\lambda_j a) \right] \tilde{W}_j^{(2)}, \end{aligned} \tag{3.57}$$

$$\begin{aligned} \tilde{F}_x^2 &= g\rho\pi b H \left[\sum_{j=0}^{\infty} D_{1j} U_1^{(5)}(\mu_j b) + E_{1j} U_1^{(6)}(\mu_j b) \right] \tilde{W}_j^{(3)} \\ &- g\rho\pi b H \left[\tau_1 J_1(k_0 b) + \sum_{j=0}^{\infty} A_{1j} U_1^{(1)}(k_j b) \right] \tilde{W}_j^{(4)}, \end{aligned} \tag{3.58}$$

where,

$$\tilde{W}_j^{(1)} = \int_{-h_1}^{0} Z_j^{(3)}(\sigma_j z)\mathrm{d}z,$$
$$\tilde{W}_j^{(2)} = \int_{-h_1}^{0} Z_j^{(2)}(\lambda_j z)\mathrm{d}z,$$
$$\tilde{W}_j^{(3)} = \int_{-h_2}^{-h_1} Z_j^{(4)}(\mu_j z)\mathrm{d}z,$$
$$\tilde{W}_j^{(4)} = \int_{-h_2}^{-h_1} Z_j^{(1)}(k_j z)\mathrm{d}z.$$

Water wave elevation for exterior and interior regions given by $\eta_j(r,\theta,t) = \mathrm{Re}[\zeta_j(r,\theta)\exp(-\mathrm{i}\omega t)]$ for $j = 1,2,3$, can be evaluated by the dynamic free surface condition

$$\eta_j = -\frac{1}{g}\frac{\partial \Phi_j}{\partial t} \quad \text{on} \quad z = 0 \quad \text{for} \quad j = 1,2,3. \tag{3.59}$$

Then

$$\zeta_1 = H\left[\sum_{m=0}^{\infty} \tau_m J_m(k_0 b)\cos m\theta Z_0^{(1)}(0) + \sum_{m=0}^{\infty}\cos m\theta \sum_{j=0}^{\infty} A_{mj} Z_j^{(1)}(0) U_m^{(1)}(k_j b)\right], \tag{3.60}$$

$$\zeta_2 = H\left[\sum_{m=0}^{\infty}\cos m\theta \sum_{j=0}^{\infty}\left[B_{mj}U_m^{(2)}(\lambda_j a) + C_{mj}U_m^{(3)}(\lambda_j a)\right] Z_j^{(2)}(0)\right], \tag{3.61}$$

$$\zeta_3 = H\left[\sum_{m=0}^{\infty}\cos m\theta \sum_{j=0}^{\infty} F_{mj} Z_j^{(3)}(0) U_m^{(4)}(\sigma_j a)\right]. \tag{3.62}$$

3.5 Validation

A truncated compound cylinder is used to validate the present formulation, i.e., by taking the porous parameter G as zero. Therefore, no water can enter the cylinder because in this case the lower wall becomes impermeable. While comparing our work, we take the permeability to be zero which means that the wall becomes impermeable (Ning et al. [38], Sankarbabu et al. [47]). We consider the floating compound cylinder corresponding to $G = 0, h_2/h_1 = 4, h_2/b = 3, h_3/b = 6, b/a = 2$. Figure 3.2 shows the dimensionless force acting on the base of the cylinder for the result of Kokkinowrachos et al. [21] and the present result. The excellent agreement between our result and that of Kokkinowrachos et al. [21] can be observed from this figure. This confirms that our model is valid and hence can be employed effectively to investigate variation of various parameters.

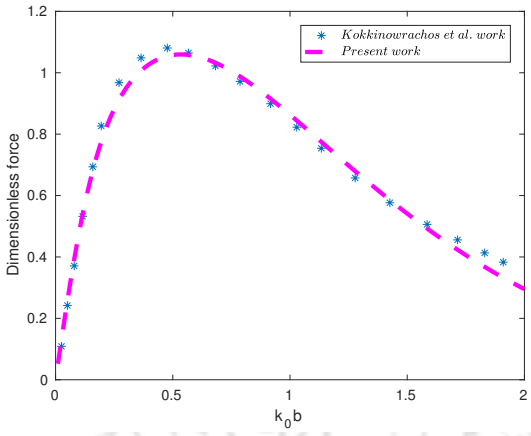

Figure 3.2: Comparison between present model and Kokkinowrachos et al. (1986) model

3.6 Results and discussion

Now we discuss the effects of various parameters on the hydrodynamic forces acting on the cylindrical structure. This section details all the results.

In Figure 3.3, the hydrodynamic force $\frac{|\tilde{F}_x^1|}{|\rho g a h_3 H|}$ for the upper cylinder is plotted against the wavenumber for various values of radius ratio a/b corresponding to $G = 1$, $h_1/h_2 = 1/2$, $h_2/h_3 = 2/3$ and $h_1/h_3 = 1/3$. We find that initially the forces increase and after that decrease for increasing values of $k_0 h_3$. It is to be noted that the high oscillating behaviour can be attributed to the resonance situation. Similar resonance phenomenon due to sloshing can also be observed in the works of Garrett [15], Mavrakos [29], as mentioned earlier. This peculiar behaviour in the neighbourhood of $k_0 h_3 = 3.8$ is due to the wavenumber corresponding to the wavelength close to those of the free fluid motion. The value of hydrodynamic force depends on the potential coefficients B_{mn}, C_{mn} and F_{mn}. In this case we obtain very low values of B_{mn}, C_{mn} and F_{mn} and that is why the hydrodynamics forces also take very low values.

In Figure 3.4, the hydrodynamic force $\frac{|\tilde{F}_x^1|}{|\rho g a h_3 H|}$ for the upper cylinder is plotted against the wavenumber for various values of draft h_1/h_2 corresponding to $G = 1$, $h_2/h_3 = 2/3$ and $a/b = 2/3$. It is observed that very high oscillating behaviour exists in the neighbourhood of $k_0 h_3 = 3.8$ which can be attributed to the resonance situation. It is observed that force spikes become steeper for increasing values of h_1/h_2.

In Figure 3.5, the hydrodynamic force $\frac{|\tilde{F}_x^1|}{|\rho g a h_3 H|}$ for the upper cylinder is plotted against the wavenumber for various values of porous coefficient G corresponding to $h_1/h_2 = 1/2$, $h_1/h_3 = 1/3$, $h_2/h_3 = 2/3$ and $a/b = 2/3$. The first term on the right side of the third potential given by equation (3.21) is the most important contribution to the wave motion inside the cylinder, while the other terms describe waves which are localised near $r = a$. Each of the distinct modes ($m = 0, 1, 2, \ldots$) resonates at different wavenumbers near the

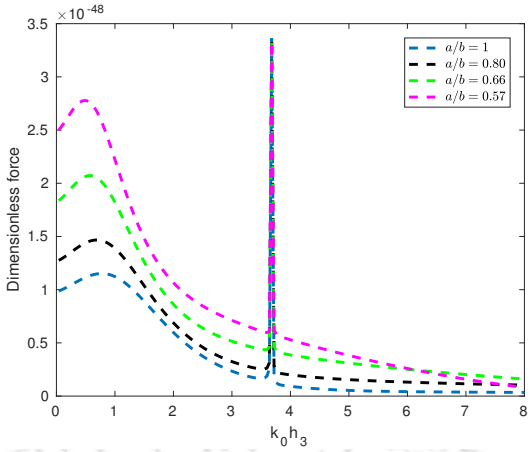

Figure 3.3: Variation of dimensionless hydrodynamic force on upper cylinder against the wavenumber for various values of a/b corresponding to $G = 1$, $h_1/h_2 = 1/2$, $h_2/h_3 = 2/3$ and $h_1/h_3 = 1/3$

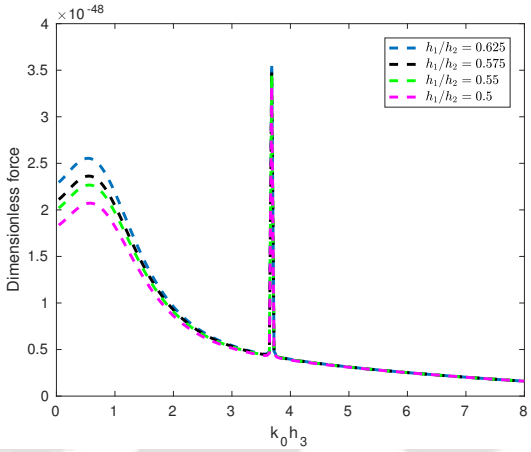

Figure 3.4: Variation of dimensionless hydrodynamic force on upper cylinder against the wavenumber for various values of h_1/h_2 corresponding to $G = 1$, $h_2/h_3 = 2/3$ and $a/b = 2/3$

roots of $J'_m(ka) = 0$ where the roots correspond to the standing waves inside a cylindrical structure. This is the sloshing mode resonance when water motion mostly occurs at the natural motion of the moonpool and due to the water moving back and forth in between the vertical walls. The dimensionless hydrodynamic force maintains a similar trend in the neighbourhood of $0 < k_0h_3 < 2$. Only for $G = 0$, which means when lower wall of the cylinder is impermeable, the resonance effect is not visible. The sharpness of the resonance ($G = 1, 2, 3, 5$) depend on the coefficient F_{mn} of the third potential (Miloh [34], Gerrett [15]). In this case, for $G = 3$ and $G = 5$, the value of this coefficient is less compared to those for $G = 1$ and 2. Lower amount of oscillation is observed for $G = 3$ and $G = 5$. An analogous phenomenon has also been observed by Ogilvie [39], Miloh [34], Mavrakos [29], Mavrakos [30] and McIver [31]. More precisely, Garrett [15] and Miloh [34] obtained the exact values of frequency at which resonance occurs. Especially Miloh [34]

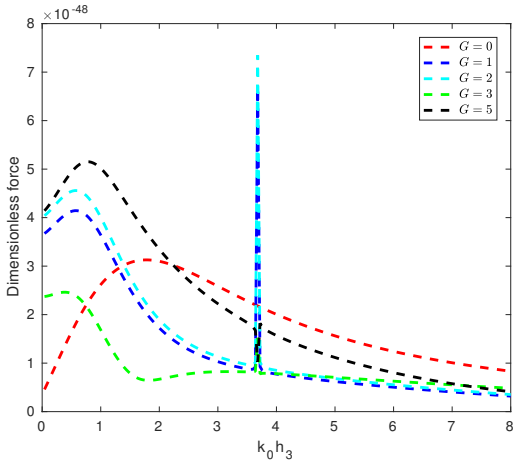

Figure 3.5: Variation of dimensionless hydrodynamic force on upper cylinder against the wavenumber for various values of G corresponding to $h_1/h_2 = 1/2$, $h_1/h_3 = 1/3$, $h_2/h_3 = 2/3$ and $a/b = 2/3$

has provided a relation to calculate the unknown coefficient at which the maximum and minimum resonance occur.

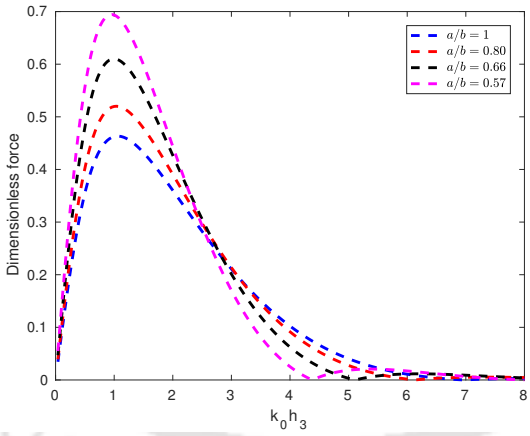

Figure 3.6: Variation of dimensionless hydrodynamic force on lower cylinder against the wavenumber for various values of a/b corresponding to $G = 1$, $h_2/h_3 = 2/3$, $h_1/h_3 = 1/3$ and $h_1/h_2 = 1/2$

In Figure 3.6, the hydrodynamic force $\dfrac{|\tilde{F}_x^2|}{|\rho g b h_3 H|}$ for the lower cylinder is plotted against the wavenumber for various values of a/b corresponding to $G = 1$, $h_2/h_3 = 2/3$, $h_1/h_3 = 1/3$ and $h_1/h_2 = 1/2$. It is observed that the wave force acting on the lower cylinder increases initially as the wave parameter k_0h_3 increases and further decreases with a further increase of wavenumber for approximately $k_0h_3 > 2$. A similar trend as observed in Darwiche et al. [10] of wave force magnitude is found. Thereabout the maximum force occurs in the neighbourhood of $k_0h_3 = 1.1$. The higher values of the force occur for lower values of a/b. The force diminishes for higher values of k_0h_3.

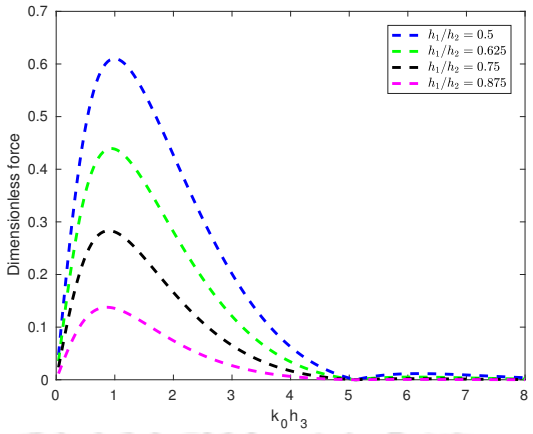

Figure 3.7: Variation of dimensionless hydrodynamic force on lower cylinder against the wavenumber for various values of h_1/h_2 corresponding to $G = 1$, $h_2/h_3 = 2/3$ and $a/b = 2/3$

In Figure 3.7, the hydrodynamic force $\frac{|\tilde{F}_x^2|}{|\rho g b h_3 H|}$ for the lower cylinder is plotted against the wavenumber for various values of h_1/h_2 corresponding to $G = 1$, $h_2/h_3 = 2/3$ and $a/b = 2/3$. Approximately the maximum force occurs in the neighbourhood of $k_0h_3 = 1.2$. It is to be noted that the higher values of the force occur within lower values of h_1/h_2.

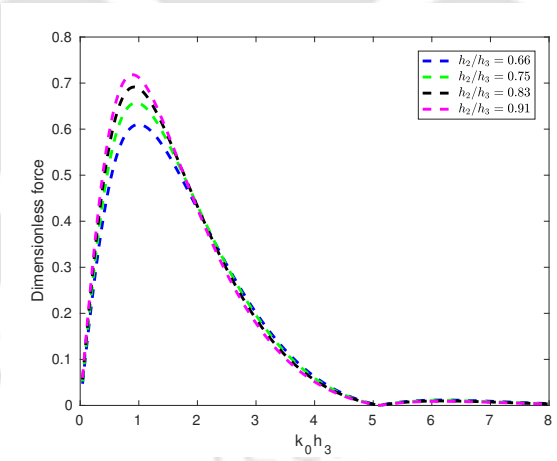

Figure 3.8: Variation of dimensionless hydrodynamic force on lower cylinder against the wavenumber for various values of h_2/h_3 corresponding to $G = 1$, $h_1/h_3 = 1/3$ and $a/b = 2/3$

In Figure 3.8, the hydrodynamic force $\frac{|\tilde{F}_x^2|}{|\rho g b h_3 H|}$ for the lower cylinder is plotted against the wavenumber for various values of h_2/h_3 corresponding to $G = 1$, $h_1/h_3 = 1/3$ and $a/b = 2/3$. It is to be noted that the wave force acting on the lower cylinder increases initially as the wave parameter k_0h_3 increases and further decreases with an increase of this parameter for $k_0h_3 > 1.2$. A similar trend of wave force magnitude is observed here. Approximately the maximum force occurs in the neighbourhood of $k_0h_3 = 1.1$. The main

observation is that the higher values of the force occur within higher values of h_2/h_3.

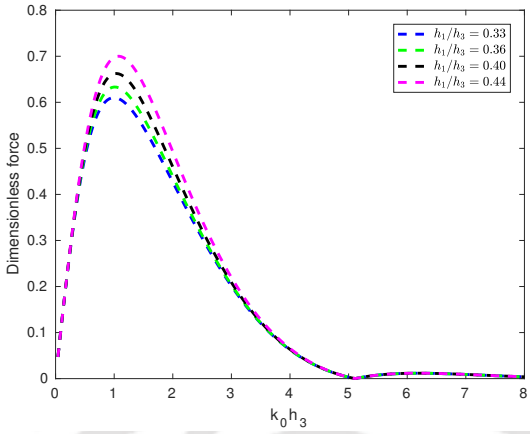

Figure 3.9: Variation of dimensionless hydrodynamic force on lower cylinder against the wavenumber for various values of h_1/h_3 corresponding to $G = 1$, $h_1/h_2 = 1/2$ and $a/b = 2/3$

In Figure 3.9, the hydrodynamic force $\frac{|\tilde{F}_x^2|}{|\rho g b h_3 H|}$ for the lower cylinder is plotted against the wavenumber for various values of h_1/h_3 corresponding to $G = 1$, $h_1/h_2 = 1/2$ and $a/b = 2/3$. Same type of graphical representation is observed here. Roughly, the maximum force occurs in the neighbourhood of $k_0h_3 = 1.1$. The main observation is that the higher values of the force occur within higher values of h_1/h_3.

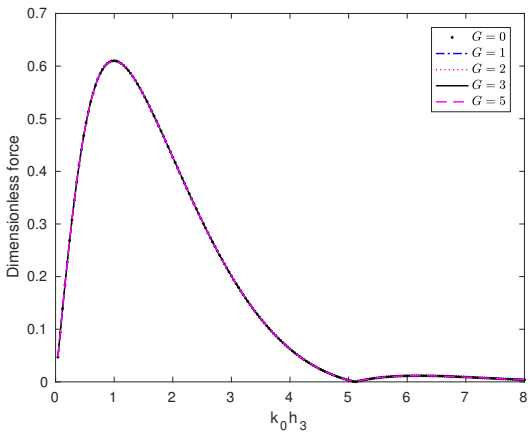

Figure 3.10: Variation of dimensionless hydrodynamic force on lower cylinder against the wavenumber for various values of G corresponding to $h_2/h_3 = 2/3$, $h_1/h_3 = 1/3$, $h_1/h_2 = 1/2$ and $a/b = 2/3$

In Figure 3.10, the hydrodynamic force $\frac{|\tilde{F}_x^2|}{|\rho g b h_3 H|}$ for the lower cylinder is plotted against the wavenumber for various values of G corresponding to $h_2/h_3 = 2/3$, $h_1/h_3 = 1/3$, $h_1/h_2 = 1/2$ and $a/b = 2/3$. Initially the force increases and afterwards it decreases. The

highest value of the force is observed in the neighbourhood of $k_0h_3 = 1.2$. One important observation is that the force does not vary much even for different values of G. This is due to the fact that the force on the lower cylinder depends on the coefficients A_{mn}, D_{mn} and E_{mn} which do not change appreciably and that is why the hydrodynamic forces also do not get changed.

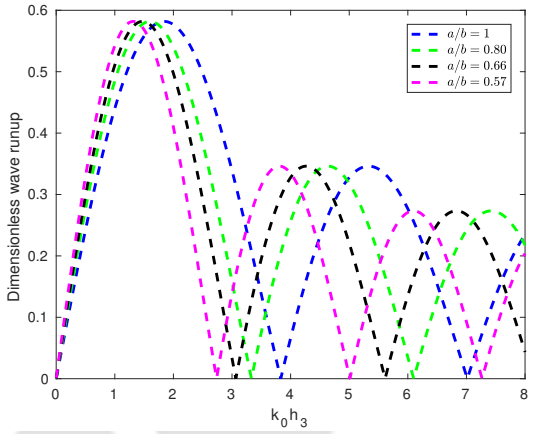

Figure 3.11: Variation of dimensionless wave run-up $|\zeta_1(b,\theta)|/H$ against the wavenumber for various values of a/b corresponding to $G = 1$, $h_1/h_2 = 1/2$, $h_2/h_3 = 2/3$ and $h_1/h_3 = 1/3$

In Figure 3.11, the maximum dimensionless wave run-up $|\zeta_1(b,\theta)|/H$ on the exterior region is investigated in which it is plotted against the wavenumber for various values of a/b corresponding to $G = 1$, $h_1/h_2 = 1/2$, $h_2/h_3 = 2/3$ and $h_1/h_3 = 1/3$. Same trend of wave run-up is observed here too. Thereabout the maximum run-up occurs in the neighbourhood of $k_0h_3 = 1.5$.

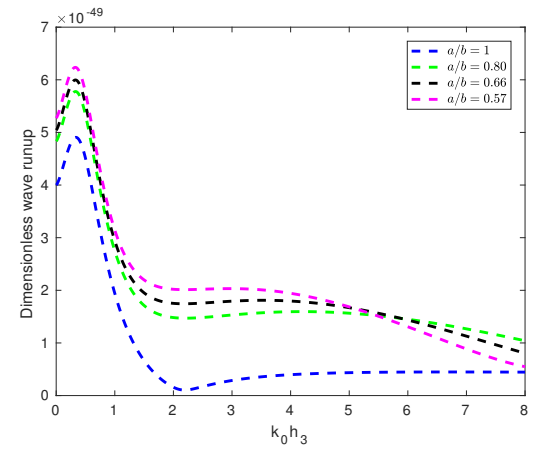

Figure 3.12: Variation of dimensionless wave run-up $|\zeta_2(a,\theta)|/H$ against the wavenumber for various values of a/b corresponding to $G = 1$, $h_1/h_2 = 1/2$, $h_2/h_3 = 2/3$ and $h_1/h_3 = 1/3$

In Figure 3.12, the maximum dimensionless wave run-up $|\zeta_2(a,\theta)|/H$ on the exterior region is investigated against the wavenumber for various values of a/b corresponding to

$G = 1$, $h_1/h_2 = 1/2$, $h_2/h_3 = 2/3$ and $h_1/h_3 = 1/3$. The highest value of the run-up occurs in the neighbourhood of $k_0 h_3 = 0.5$. The main observation is that maximum run-up occurs for the smaller values of a/b.

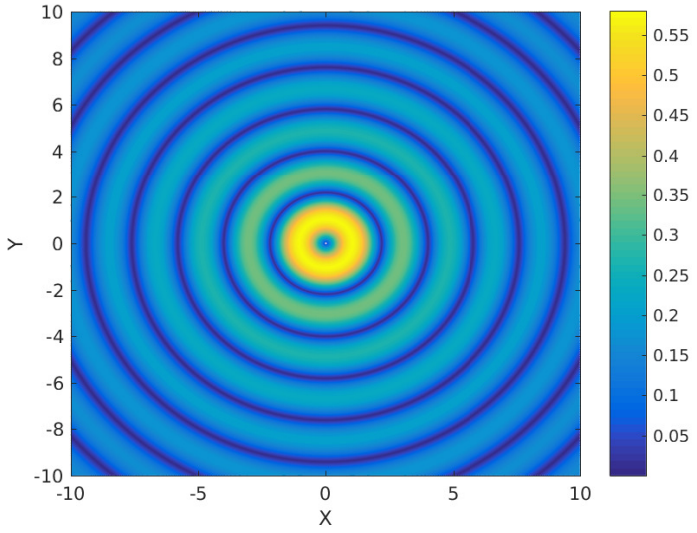

Figure 3.13: Contour plot for free surface elevation $|\zeta_1(r,\theta)|/H$ at free surface for $k_0 b = 1.75$, $a/b = 2/3$, $G = 1$, $h_1/h_2 = 1/2$, $h_2/h_3 = 2/3$ and $h_1/h_3 = 1/3$

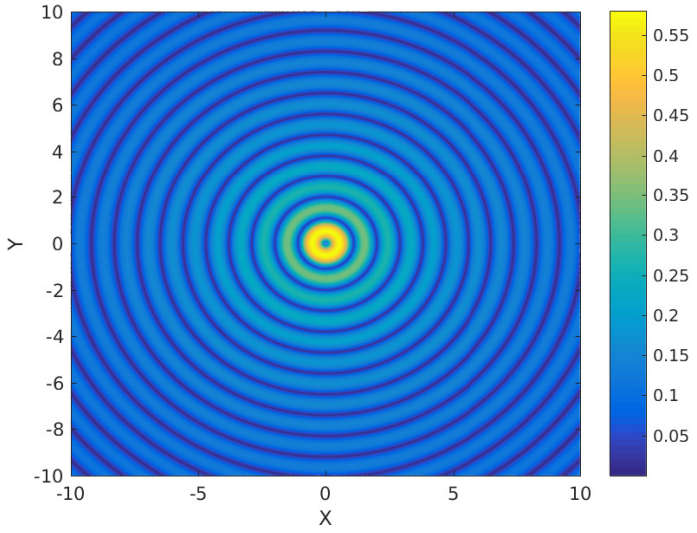

Figure 3.14: Contour plot for free surface elevation $|\zeta_1(r,\theta)|/H$ at free surface for $k_0 b = 3.5$, $a/b = 2/3$, $G = 1$, $h_1/h_2 = 1/2$, $h_2/h_3 = 2/3$ and $h_1/h_3 = 1/3$

In Figures 3.13 and 3.14, contour plots of the free surface elevation near the free surface for two different values of frequency are presented. If we compare these two figures, it can be found that for higher frequency incident wave, the diffracted wave pattern becomes more pronounced and more number of ripples in the waves are observed in the wave field.

3.7 Conclusion

In this chapter, we present a theoretical study on the interaction of linear water waves with a floating compound porous cylinder in finite ocean depth. The whole fluid domain is divided into five regions. We use eigenfunction expansion approach and separation of variables technique to solve this diffraction problem governed by Laplace's equation. The unknown coefficients are calculated by using matching conditions and standard matrix technique. It is observed that change in values in radius, draft and porosity have significant effect on the hydrodynamic loads. The behaviour of hydrodynamic load is found to be steady in the lower frequency. However, fluctuation occurs due to the resonance situation in the neighbourhood of a specific frequency. Similar phenomenon was also observed by Garrett [15] and Mavrakos [29]. It is observed that for the upper cylinder, force spikes become steeper for increasing values of h_1/h_2. For the lower cylinder, higher values of the force occur for lower values of a/b. We observe that for the lower cylinder, the higher values of the force occur within higher values of h_1/h_3. For validating our result, we compare our result with that of Kokkinowrachos et al. [21] when the side wall of the lower cylinder is impermeable. Suitable agreement can be observed between both results. This confirms that our model is valid and hence can be employed effectively to investigate various issues of the parameters. Taking into consideration the behaviour of the hydrodynamic force under different parameter combination, our solutions are likely to help in squeezing the maximum benefit for designing appropriate marine structures. It may be interesting and useful to modify our problem by considering a multi-layer fluid.

CHAPTER 4

Hydrodynamic Forces and Moments due to Interaction of Linear Water Waves with Truncated Partial-Porous Cylinders in Finite Depth

In this chapter, we discuss the interaction of linear water waves with a truncated partial-porous cylinder in finite depth. For this work, two models are studied: (i) a floating surface-piercing truncated partial-porous cylinder, and (ii) a surface-piercing truncated partial-porous cylinder placed at the bottom. In both cases, the configuration of the partial-porous cylinder is such that it consists of an impermeable inner cylinder rising above the free surface and a coaxial truncated porous cylinder around the lower part of the inner cylinder with the top of the porous cylinder being impermeable. The hydrodynamic force, moment and wave run-up are studied graphically for various relevant parameters and the corresponding observations are made.

4.1 Floating surface-piercing partial-porous cylinder

In this section we will set up the boundary value problem with suitable boundary conditions and matching conditions. Further, we will calculate diffracted potentials in each sub-domain. There may be equations, conditions and expressions same or similar to those earlier chapters. Instead of eliminating them here and referring them from earlier, some of them are kept so as to have a free flow in reading this chapter.

4.1.1 Formulation of the problem

By adopting linear water wave theory, the solution for the boundary value problem for wave diffraction by a partial-porous cylinder (Figure 4.1) can be found. The radii of the

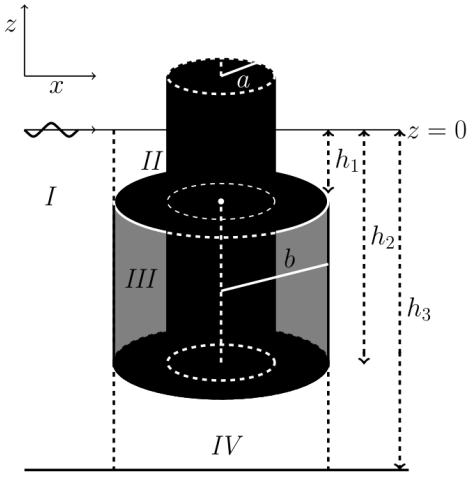

Figure 4.1: Floating surface-piercing partial-porous cylinder

inner and outer cylinders are taken as a and b, respectively. Assuming the fluid to be homogeneous, incompressible and inviscid, the motion irrotational and the sea-bed flat and impermeable, the associated problem is formulated. A cylindrical coordinate system (r, θ, z) with the origin at the undisturbed free surface $z = 0$ and the z-axis in upward direction is considered. A velocity potential $\Phi(r, \theta, z, t) = \mathrm{Re}[\phi(r, \theta, z) \exp(-\mathrm{i}\omega t)]$, where ω is the angular wave frequency, is considered to describe the fluid flow. In this case, we split the fluid domain into four regions: Region I $(r \geq b, -h_3 \leq z \leq 0)$; Region II $(a \leq r \leq b, -h_1 \leq z \leq 0)$; Region III $(a \leq r \leq b, -h_2 \leq z \leq -h_1)$ and Region IV $(0 \leq r \leq b, -h_3 \leq z \leq -h_2)$. Further, each potential satisfies three-dimensional Laplace's equation in respective flow region as given below:

$$\nabla^2 \phi_j = 0, \quad j = 1, 2, 3, 4, \tag{4.1}$$

where $\phi_j, \quad j = 1, 2, 3, 4$, denote potentials in Regions I, II, III and IV, respectively. The free surface condition at $z = 0$ and the bottom boundary conditions on the sea-bed at $z = -h_3$ are of the following form:

$$\frac{\partial \phi_j}{\partial z} - \frac{\omega^2}{g} \phi_j = 0; \quad z = 0, \quad j = 1, 2, \tag{4.2}$$

$$\frac{\partial \phi_1}{\partial z} = 0; \quad z = -h_3, \quad r > b, \tag{4.3}$$

$$\frac{\partial \phi_4}{\partial z} = 0; \quad z = -h_3, \quad 0 < r < b. \tag{4.4}$$

The important boundary conditions on the impermeable surface of the compound cylinder are as follows:

$$\frac{\partial \phi_2}{\partial r} = 0; \quad r = a, \quad -h_1 < z < 0, \tag{4.5}$$

$$\frac{\partial \phi_2}{\partial z} = 0; \quad z = -h_1, \quad a < r < b, \tag{4.6}$$
$$\frac{\partial \phi_3}{\partial r} = 0; \quad r = a, \quad -h_2 < z < -h_1, \tag{4.7}$$
$$\frac{\partial \phi_3}{\partial z} = 0; \quad z = -h_1, \quad a < r < b, \tag{4.8}$$
$$\frac{\partial \phi_3}{\partial z} = 0; \quad z = -h_2, \quad a < r < b, \tag{4.9}$$
$$\frac{\partial \phi_4}{\partial z} = 0; \quad z = -h_2, \quad 0 < r < b. \tag{4.10}$$

The boundary condition on the surface of porous cylinder can be expressed as (Wang and Ren [55])

$$\frac{\partial \phi_3}{\partial r} = \mathrm{i}k_0 G(\phi_3 - \phi_1), \quad r = b, \quad -h_2 < z < -h_1, \tag{4.11}$$

where G and k_0 are complex porous coefficient and incident wavenumber, respectively.

The velocity potential in the exterior region must satisfy the Sommerfeld radiation condition given by the equation (2.15). On the cylinder surface $r = b$, the following matching conditions are satisfied:

$$\phi_1 = \phi_2; \quad r = b, \quad -h_1 < z < 0, \tag{4.12}$$
$$\frac{\partial \phi_1}{\partial r} = \frac{\partial \phi_2}{\partial r}; \quad r = b, \quad -h_1 < z < 0, \tag{4.13}$$
$$\frac{\partial \phi_1}{\partial r} = \frac{\partial \phi_3}{\partial r}; \quad r = b, \quad -h_2 < z < -h_1, \tag{4.14}$$
$$\phi_1 = \phi_4; \quad r = b, \quad -h_3 < z < -h_2, \tag{4.15}$$
$$\frac{\partial \phi_1}{\partial r} = \frac{\partial \phi_4}{\partial r}; \quad r = b, \quad -h_3 < z < -h_2. \tag{4.16}$$

The above matching conditions arise due to the continuity of pressure (equations (4.12) and (4.15)) and continuity of velocity (equations (4.13), (4.14) and (4.16)) across the boundary $r = b$ [38].

4.1.2 Diffracted potentials in sub-domains

Using eigenfunction expansion method, the velocity potential ϕ_1 for Region I has the following form [10]:

$$\phi_1(r,\theta,z) = -\frac{\mathrm{i}gH}{\omega}\left[\sum_{m=0}^{\infty}\tau_m J_m(k_0 r)\cos m\theta Z_0^{(1)}(k_0 z) + \sum_{m=0}^{\infty}\cos m\theta \sum_{j=0}^{\infty} A_{mj} Z_j^{(1)}(k_j z) U_m^{(1)}(k_j r)\right], \tag{4.17}$$

where A_{mj} are the unknown coefficients. Wavenumbers k_j, $j = 0, 1, 2, 3, \ldots$, are derived from the following dispersion relation by using the technique adopted in earlier chapters:

$$\omega^2 = \begin{cases} gk_j \tanh k_j h_3; & j = 0, \\ -gk_j \tan k_j h_3; & j \geq 1. \end{cases}$$

The radial eigenfunctions $U_m^{(1)}(k_j r)$ in (4.17) have the following form:

$$U_m^{(1)}(k_j r) = \begin{cases} \frac{H_m^{(1)}(k_j r)}{H_m^{(1)'}(k_j b)}; & j = 0, \\ \frac{K_m(k_j r)}{K_m'(k_j b)}; & j \geq 1. \end{cases}$$

The vertical eigenfunctions $Z_j^{(1)}(k_j z)$ are as follows:

$$Z_j^{(1)}(k_j z) = \begin{cases} \frac{\cosh k_j(z+h_3)}{\cosh k_j h_3}; & j = 0, \\ \frac{\cos k_j(z+h_3)}{\cos k_j h_3}; & j \geq 1. \end{cases}$$

ϕ_2, the scattered velocity potential in Region II, has the form [10]

$$\phi_2(r,\theta,z) = -\frac{igH}{\omega}\left[\sum_{m=0}^{\infty}\cos m\theta \sum_{j=0}^{\infty}\left\{B_{mj}U_m^{(2)}(\lambda_j r) + C_{mj}U_m^{(3)}(\lambda_j r)\right\} Z_j^{(2)}(\lambda_j z)\right], \quad (4.18)$$

where B_{mj} and C_{mj} are unknown and λ_j can be computed from

$$\omega^2 = \begin{cases} g\lambda_j \tanh \lambda_j h_1; & j = 0, \\ -g\lambda_j \tan \lambda_j h_1; & j \geq 1. \end{cases}$$

The radial eigenfunctions $U_m^{(2)}(\lambda_j r)$ and $U_m^{(3)}(\lambda_j r)$ are as follows:

$$U_m^{(2)}(\lambda_j r) = \begin{cases} \frac{H_m^{(1)}(\lambda_j r)}{H_m^{(1)'}(\lambda_j b)}; & j = 0, \\ \frac{I_m(\lambda_j r)}{I_m'(\lambda_j b)}; & j \geq 1, \end{cases} \qquad U_m^{(3)}(\lambda_j r) = \begin{cases} \frac{H_m^{(2)}(\lambda_j r)}{H_m^{(2)'}(\lambda_j b)}; & j = 0, \\ \frac{K_m(\lambda_j r)}{K_m'(\lambda_j b)}; & j \geq 1. \end{cases}$$

The vertical eigenfunctions $Z_j^{(2)}(\lambda_j z)$ are defined as

$$Z_j^{(2)}(\lambda_j z) = \begin{cases} \frac{\cosh \lambda_j(z+h_1)}{\cosh \lambda_j h_1}; & j = 0, \\ \frac{\cos \lambda_j(z+h_1)}{\cos \lambda_j h_1}; & j \geq 1. \end{cases}$$

In Region III, the velocity potential ϕ_3 is found as

$$\phi_3(r,\theta,z) = -\frac{igH}{\omega}\left[\sum_{m=0}^{\infty}\cos m\theta \sum_{j=0}^{\infty}\left[D_{mj}U_m^{(4)}(\mu_j r) + E_{mj}U_m^{(5)}(\mu_j r)\right] Z_j^{(3)}(\mu_j z)\right], \quad (4.19)$$

where D_{mj} and E_{mj} are unknown and μ_j can be computed as

$$\mu_j = \frac{\pi j}{h_2 - h_1}, \quad j = 0, 1, 2, ...$$

The radial eigenfunctions $U_m^{(4)}(\mu_j r)$ and $U_m^{(5)}(\mu_j r)$ have the following forms:

$$U_m^{(4)}(\mu_j r) = \begin{cases} \frac{r^{-m}}{b^{-m-1}}; & j = 0, \\ \frac{K_m(\mu_j r)}{K'_m(\mu_j b)}; & j \geq 1, \end{cases} \qquad U_m^{(5)}(\mu_j r) = \begin{cases} \frac{r^m}{b^{m-1}}; & j = 0, \\ \frac{I_m(\mu_j r)}{I'_m(\mu_j b)}; & j \geq 1. \end{cases}$$

The vertical eigenfunctions $Z_j^{(3)}(\mu_j z)$ are defined as

$$Z_j^{(3)}(\mu_j z) = \begin{cases} \frac{1}{\sqrt{2}}; & j = 0, \\ \cos \mu_j (z + h_2); & j \geq 1. \end{cases}$$

In Region IV, the potential ϕ_4 is of the following form:

$$\phi_4(r, \theta, z) = -\frac{\mathrm{i}gH}{\omega} \left[\sum_{m=0}^{\infty} \cos m\theta \sum_{j=0}^{\infty} F_{mj} Z_j^{(4)}(\gamma_j z) U_m^{(7)}(\gamma_j r) \right], \tag{4.20}$$

where F_{mj} are unknowns and γ_j can be computed from

$$\gamma_j = \frac{\pi j}{h_3 - h_2}, \quad j = 0, 1, 2, ...$$

The radial eigenfunctions $U_m^{(7)}(\gamma_j r)$ are as follows:

$$U_m^{(7)}(\gamma_j r) = \begin{cases} \frac{r^m}{b^{m-1}}; & j = 0, \\ \frac{I_m(\gamma_j r)}{I'_m(\gamma_j b)}; & j \geq 1. \end{cases}$$

The vertical eigenfunctions $Z_j^{(4)}(\gamma_j z)$ are defined as

$$Z_j^{(4)}(\gamma_j z) = \begin{cases} \frac{\sqrt{2}}{2}; & j = 0, \\ \cos \gamma_j (z + h_3); & j \geq 1. \end{cases}$$

4.1.3 Computation of unknown coefficients

By applying the boundary condition given by equation (4.5) and the orthogonal property of the eigenfunctions, the following relationship between the coefficients $B_{m\alpha}$ and $C_{m\alpha}$ appearing in ϕ_2 is derived:

$$\frac{H_m^{(1)'}(\lambda_0 a)}{H_m^{(1)'}(\lambda_0 b)} B_{m0} + \frac{H_m^{(2)'}(\lambda_0 a)}{H_m^{(2)'}(\lambda_0 b)} C_{m0} = 0, \tag{4.21}$$

$$\frac{I'_m(\lambda_\alpha a)}{I'_m(\lambda_\alpha b)} B_{m\alpha} + \frac{K'_m(\lambda_\alpha a)}{K'_m(\lambda_\alpha b)} C_{m\alpha} = 0, \quad \alpha \geq 1. \tag{4.22}$$

Using (4.21) and (4.22), the modified expression for ϕ_2 becomes

$$\phi_2(r,\theta,z) = -\frac{\mathrm{i}gH}{\omega}\left[\sum_{m=0}^{\infty}\cos m\theta \sum_{j=0}^{\infty} C_{mj} Z_j^{(2)}(\lambda_j z) U_m^{(6)}(\lambda_j r)\right]. \tag{4.23}$$

The radial eigenfunctions $U_m^{(6)}(\lambda_j r)$ are as follows:

$$U_m^{(6)}(\lambda_j r) = \begin{cases} \frac{H_m^{(2)}(\lambda_j r)}{H_m^{(2)'}(\lambda_j b)} - \frac{H_m^{(2)'}(\lambda_j a)}{H_m^{(2)'}(\lambda_j b)} \frac{H_m^{(1)}(\lambda_j r)}{H_m^{(1)'}(\lambda_j a)}; & j = 0, \\ \frac{K_m(\lambda_j r)}{K_m'(\lambda_j b)} - \frac{K_m'(\lambda_j a)}{K_m'(\lambda_j b)} \frac{I_m(\lambda_j r)}{I_m'(\lambda_j a)}; & j \geq 1. \end{cases}$$

Using the matching conditions given by equations (4.12) and (4.13) for the depth $-h_1 < z < 0$, along with the orthogonal property of the eigenfunctions, we obtain

$$\sum_{j=0}^{\infty} A_{mj} U_m^{(1)}(k_j b) Q_{0j} - C_{m0} U_m^{(6)}(\lambda_0 b) R_{00} = -\tau_m J_m(k_0 b) Q_{00}, \tag{4.24}$$

$$\sum_{j=0}^{\infty} A_{mj} U_m^{(1)}(k_j b) Q_{\alpha j} - C_{m\alpha} U_m^{(6)}(\lambda_\alpha b) R_{\alpha\alpha} = -\tau_m J_m(k_0 b) Q_{\alpha 0}, \alpha \geq 1, \tag{4.25}$$

$$\sum_{j=0}^{\infty} A_{mj} Q_{0j} - C_{m0} U_m^{(6)'}(\lambda_0 b) R_{00} = -\tau_m J_m'(k_0 b) Q_{00}, \tag{4.26}$$

$$\sum_{j=0}^{\infty} A_{mj} Q_{\alpha j} - C_{m\alpha} U_m^{(6)'}(\lambda_\alpha b) R_{\alpha\alpha} = -\tau_m J_m'(k_0 b) Q_{\alpha 0}, \ \alpha \geq 1. \tag{4.27}$$

Using the matching conditions given by equations (4.11) and (4.14) for the depth $-h_2 < z < -h_1$, and the orthogonal property of the eigenfunctions, we get

$$\mathrm{i}k_0 G\left(D_{m0} + E_{m0}\right) bT_{00} - \sum_{j=0}^{\infty} A_{mj}(1 + \mathrm{i}k_0 G U_m^{(1)}(k_j b)) P_{0j} = \tau_m P_{00}(J_m'(k_0 b) + \mathrm{i}k_0 G J_m(k_0 b)), \tag{4.28}$$

$$\mathrm{i}k_0 G\left(D_{m\alpha}\frac{K_m(\mu_\alpha b)}{K_m'(\mu_\alpha b)} + E_{m\alpha}\frac{I_m(\mu_\alpha b)}{I_m'(\mu_\alpha b)}\right) T_{\alpha\alpha} - \sum_{j=0}^{\infty} A_{mj}(1 + \mathrm{i}k_0 G U_m^{(1)}(k_j b)) P_{\alpha j} = \tau_m P_{\alpha 0}(J_m'(k_0 b) + \mathrm{i}k_0 G J_m(k_0 b)), \ \alpha \geq 1, \tag{4.29}$$

$$\left(-mD_{m0} + mE_{m0}\right) T_{00} - \sum_{j=0}^{\infty} A_{mj} P_{0j} = \tau_m P_{00} J_m'(k_0 b), \tag{4.30}$$

$$\left(D_{m\alpha} + E_{m\alpha}\right) T_{\alpha\alpha} - \sum_{j=0}^{\infty} A_{mj} P_{\alpha j} = \tau_m P_{\alpha 0} J_m'(k_0 b), \quad \alpha \geq 1. \tag{4.31}$$

Now from the matching condition given by equation (4.16) across the boundary $r = b$ in the interval $-h_3 < z < -h_2$, and using the orthogonal property of the eigenfunctions, we get

$$\tau_m J'_m(k_0 b) S_{00} + \sum_{j=0}^{\infty} A_{mj} S_{0j} - F_{m0} L_{00} = 0, \tag{4.32}$$

$$\tau_m J'_m(k_0 b) S_{\alpha 0} + \sum_{j=0}^{\infty} A_{mj} S_{\alpha j} - F_{m\alpha} L_{\alpha\alpha} = 0, \quad \alpha \geq 1, \tag{4.33}$$

where

$$Q_{\alpha,j} = \int_{-h_1}^{0} Z_\alpha^{(2)}(\lambda_\alpha z) Z_j^{(1)}(k_j z) \mathrm{d}z, \tag{4.34}$$

$$R_{\alpha,\alpha} = \int_{-h_1}^{0} Z_\alpha^{(2)}(\lambda_\alpha z) Z_\alpha^{(2)}(\lambda_\alpha z) \mathrm{d}z, \tag{4.35}$$

$$P_{\alpha,j} = \int_{-h_2}^{-h_1} Z_\alpha^{(3)}(\mu_\alpha z) Z_j^{(1)}(k_j z) \mathrm{d}z, \tag{4.36}$$

$$T_{\alpha,\alpha} = \int_{-h_2}^{-h_1} Z_\alpha^{(3)}(\mu_\alpha z) Z_\alpha^{(3)}(\mu_\alpha z) \mathrm{d}z, \tag{4.37}$$

$$S_{\alpha,j} = \int_{-h_3}^{-h_2} Z_\alpha^{(4)}(\gamma_\alpha z) Z_j^{(1)}(k_j z) \mathrm{d}z, \tag{4.38}$$

$$L_{\alpha,\alpha} = \int_{-h_3}^{-h_2} Z_\alpha^{(4)}(\gamma_\alpha z) Z_\alpha^{(4)}(\gamma_\alpha z) \mathrm{d}z. \tag{4.39}$$

For obtaining the hydrodynamic forces and wave run-up, it is required to find the unknown coefficients. Truncating the infinite series given by equations (4.24) – (4.33) after some terms $N = 20$, and using equations (4.21) and (4.22), the values of the coefficients A_{mj}, B_{mj}, C_{mj}, D_{mj}, E_{mj} and F_{mj} are computed. Excellent convergence can be achieved by truncating the expansion series after the first 20 terms. Similar convergence is shown in details in tabular form in Chapter 2. The hydrodynamic forces basically depend on the potential coefficients A_{mj}, B_{mj}, C_{mj}, D_{mj}, E_{mj} and F_{mj}. It is found that the values of the potential coefficients are correct up to six decimal places. In this work also, we consider the potential coefficients correct up to six decimal places as considered in our earlier work. A similar convergence was observed and considered by Mandal et al. [26] too. As a consequence, the following linear system of algebraic equations is found for determining the unknown coefficients:

$$\mathcal{T}_l \mathcal{X}_l = \mathcal{B}_l, \tag{4.40}$$

where, $\mathcal{X}_l = [A_{l1}, A_{l2}, ..., A_{lN}, B_{l1}, B_{l2}, ..., B_{lN}, C_{l1}, C_{l2}, ..., C_{lN}, D_{l1}, D_{l2}, ..., D_{lN}, E_{l1}, E_{l2}, ..., E_{lN}, F_{l1}, F_{l2}, ..., F_{lN}]^t$, $\mathcal{T}_l$ are coefficient matrices and $\mathcal{B}_l$ are the right-hand vectors.

4.1.4 Horizontal and vertical hydrodynamic forces and wave run-up

Total hydrodynamic forces in the direction of wave propagation acting on the inner and the outer cylinders can be appropriately evaluated by carrying out integration on the pressure distribution at the surface of the structure. The forces $\tilde{F}_x^j(t) = \mathrm{Re}[\tilde{F}_x^j \exp(-\mathrm{i}\omega t)]$ for $j = 1, 2$ are defined as follows:

$$\tilde{F}_x^1 = -\mathrm{i}\omega\rho \int_{-h_2}^{-h_1}\int_0^{2\pi} \phi_3(a,\theta,z)\cos\theta \,\mathrm{d}z\mathrm{d}\theta - \mathrm{i}\omega\rho \int_{-h_1}^{0}\int_0^{2\pi} \phi_2(a,\theta,z)\cos\theta \,\mathrm{d}z\mathrm{d}\theta, \tag{4.41}$$

$$\tilde{F}_x^2 = \mathrm{i}\omega\rho \int_{-h_2}^{-h_1}\int_0^{2\pi} \phi_3(b,\theta,z)\cos\theta \,\mathrm{d}z\mathrm{d}\theta - \mathrm{i}\omega\rho \int_{-h_2}^{-h_1}\int_0^{2\pi} \phi_1(b,\theta,z)\cos\theta \,\mathrm{d}z\mathrm{d}\theta \tag{4.42}$$

Upon simplification, we get

$$\tilde{F}_x^1 = -g\rho\pi aH \left[\sum_{j=0}^{\infty} D_{1j}U_1^{(4)}(\mu_j a) + E_{1j}U_1^{(5)}(\mu_j a)\right]\tilde{W}_j^{(1)} - g\rho\pi aH \left[\sum_{j=0}^{\infty} B_{1j}U_1^{(2)}(\lambda_j a) + C_{1j}U_1^{(3)}(\lambda_j a)\right]\tilde{W}_j^{(2)}, \tag{4.43}$$

$$\tilde{F}_x^2 = g\rho\pi bH \left[\sum_{j=0}^{\infty} D_{1j}U_1^{(4)}(\mu_j b) + E_{1j}U_1^{(5)}(\mu_j b)\right]\tilde{W}_j^{(3)} - g\rho\pi bH \left[\tau_1 J_1(k_0 b) + \sum_{j=0}^{\infty} A_{1j}U_1^{(1)}(k_j b)\right]\tilde{W}_j^{(4)}, \tag{4.44}$$

where, $\tilde{W}_j^{(1)} = \int_{-h_2}^{-h_1} Z_j^{(3)}(\mu_j z)\mathrm{d}z$, $\tilde{W}_j^{(2)} = \int_{-h_1}^{0} Z_j^{(2)}(\lambda_j z)\mathrm{d}z$, $\tilde{W}_j^{(3)} = \int_{-h_2}^{-h_1} Z_j^{(3)}(\mu_j z)\mathrm{d}z$, $\tilde{W}_j^{(4)} = \int_{-h_2}^{-h_1} Z_j^{(1)}(k_j z)\mathrm{d}z$.

The total vertical force F_z is written as the sum of two forces, namely, F_z^1 and F_z^2, on the surfaces $[(a < r < b, z = -h_1^+) \cup (a < r < b, z = -h_1^-)]$ and $[(a < r < b, z = -h_2^-) \cup (0 < r < b, z = -h_2^+)]$, respectively, as follows:

$$F_z = \iint_s p n_z \mathrm{d}s = F_z^1 + F_z^2. \tag{4.45}$$

That is,

$$F_z^1 = -\mathrm{i}\omega\rho \int_a^b\int_0^{2\pi} \phi_3(r,\theta,-h_1) r \,\mathrm{d}r\mathrm{d}\theta + \mathrm{i}\omega\rho \int_a^b\int_0^{2\pi} \phi_2(r,\theta,-h_1) r \,\mathrm{d}r\mathrm{d}\theta, \tag{4.46}$$

$$F_z^2 = \mathrm{i}\omega\rho \int_a^b\int_0^{2\pi} \phi_3(r,\theta,-h_2) r \,\mathrm{d}r\mathrm{d}\theta - \mathrm{i}\omega\rho \int_0^b\int_0^{2\pi} \phi_4(r,\theta,-h_2) r \,\mathrm{d}r\mathrm{d}\theta. \tag{4.47}$$

Simplifying, we get

$$\begin{aligned}
F_z^1 &= -g\rho\pi H\Big[D_{00}b\Big(\frac{b^2-a^2}{2}\Big)Z_0^{(3)}(\mu_0(-h_1)) \\
&+ \sum_{j=1}^{\infty} D_{0j}\frac{bK_1(\mu_j b)-aK_1(\mu_j a)}{\mu_j K_0'(\mu_j b)}Z_j^{(3)}(\mu_j(-h_1))\Big] \\
&- g\rho\pi H\Big[E_{00}b\Big(\frac{b^2-a^2}{2}\Big)Z_0^{(3)}(\mu_0(-h_1)) \\
&+ \sum_{j=1}^{\infty} E_{0j}\frac{bI_1(\mu_j b)-aI_1(\mu_j a)}{\mu_j I_0'(\mu_j b)}Z_j^{(3)}(\mu_j(-h_1))\Big] \\
&+ g\rho\pi H\Big[B_{00}\frac{bH_1^{(1)}(\lambda_0 b)-aH_1^{(1)}(\lambda_0 a)}{\lambda_0 H_1^{(1)'}(\lambda_0 b)}Z_0^{(2)}(\lambda_0(-h_1)) \\
&+ \sum_{j=1}^{\infty} B_{0j}\frac{bI_1(\lambda_j b)-aI_1(\lambda_j a)}{\lambda_j I_0'(\lambda_j b)}Z_j^{(2)}(\lambda_j(-h_1))\Big] \\
&+ g\rho\pi H\Big[C_{00}\frac{bH_1^{(2)}(\lambda_0 b)-aH_1^{(2)}(\lambda_0 a)}{\lambda_0 H_1^{(2)'}(\lambda_0 b)}Z_0^{(2)}(\lambda_0(-h_1)) \\
&+ \sum_{j=1}^{\infty} C_{0j}\frac{bK_1(\lambda_j b)-aK_1(\lambda_j a)}{\lambda_j K_0'(\lambda_j b)}Z_j^{(2)}(\lambda_j(-h_1))Z_j^{(2)}(\lambda_j(-h_1))\Big], \qquad (4.48)\\
F_z^2 &= g\rho\pi H\Big[D_{00}b\Big(\frac{b^2-a^2}{2}\Big)Z_0^{(3)}(\mu_0(-h_2)) \\
&+ \sum_{j=1}^{\infty} D_{0j}\frac{bK_1(\mu_j b)-aK_1(\mu_j a)}{\mu_j K_0'(\mu_j b)}Z_j^{(3)}(\mu_j(-h_2))\Big] \\
&+ g\rho\pi H\Big[E_{00}b\Big(\frac{b^2-a^2}{2}\Big)Z_0^{(3)}(\mu_0(-h_2)) \\
&+ \sum_{j=1}^{\infty} E_{0j}\frac{bI_1(\mu_j b)-aI_1(\mu_j a)}{\mu_j I_0'(\mu_j b)}Z_j^{(3)}(\mu_j(-h_2))\Big] \\
&- g\rho\pi H\Big[F_{00}b^2 Z_0^{(4)}(\gamma_0(-h_2)) + \sum_{j=1}^{\infty} F_{0j}\frac{bI_1(\gamma_j b)}{\gamma_j I_0'(\gamma_j b)}Z_j^{(4)}(\gamma_j(-h_2))\Big]. \qquad (4.49)
\end{aligned}$$

The wave run-up for the exterior regions, as given by $\eta_j(r,\theta,t) = \mathrm{Re}[\zeta_j(r,\theta)\exp(-\mathrm{i}\omega t)]$ for $j = 1, 2$, is evaluated with the help of the dynamic free surface condition

$$\eta_j = -\frac{1}{g}\frac{\partial \Phi_j}{\partial t}, \quad z = 0, \quad j = 1, 2. \qquad (4.50)$$

Subsequently,

$$\zeta_1 = H\Big[\sum_{m=0}^{\infty}\tau_m J_m(k_0 b)\cos m\theta Z_0^{(1)}(0) + \sum_{m=0}^{\infty}\cos m\theta\sum_{j=0}^{\infty}A_{mj}Z_j^{(1)}(0)U_m^{(1)}(k_j b)\Big], \qquad (4.51)$$

$$\zeta_2 = H\left[\sum_{m=0}^{\infty}\cos m\theta\sum_{j=0}^{\infty}\left[B_{mj}U_m^{(2)}(\lambda_j a)+C_{mj}U_m^{(3)}(\lambda_j a)\right]Z_j^{(2)}(0)\right]. \tag{4.52}$$

Now the overturning moment about the y-axis through the rotational center $(0,0,z_0)$ can be calculated by carrying out integration of pressure over the cylinder surface. The moment M_y comprises of two parts as follows:

$$M_y = \iint_s p((z-z_0)n_x - xn_z)\mathrm{d}s = M_{y1}+M_{y2}, \tag{4.53}$$

where M_{y1} and M_{y2} are the moments due to the horizontal force and vertical force, respectively. Further, M_{y1} can again be split into the following two components:

$$M_{y1} = M_{y1}^1 + M_{y1}^2, \tag{4.54}$$

where M_{y1}^1 and M_{y1}^2 are, respectively, the moments induced by the force on the regions $(-h_2<z<-h_1, r=b^+)\cup(-h_2<z<-h_1, r=b^-)$ and $(-h_2<z<0, r=a)$, and are given by

$$\begin{aligned}
M_{y1}^1 &= \mathrm{i}\omega\rho\int_{-h_2}^{-h_1}\int_0^{2\pi} b\phi_1(b,\theta,z)(z-z_0)(-\cos\theta)\,\mathrm{d}z\mathrm{d}\theta \qquad (4.55)\\
&- \mathrm{i}\omega\rho\int_{-h_2}^{-h_1}\int_0^{2\pi} b\phi_4(b,\theta,z)(z-z_0)(-\cos\theta)\,\mathrm{d}z\mathrm{d}\theta\\
&= -g\rho\pi bH\left[2\mathrm{i}J_1(k_0b)+\sum_{j=0}^{\infty}A_{1j}U_1^{(1)}(k_jb)\right]\int_{-h_2}^{-h_1}(z-z_0)Z_j^{(1)}(k_jz)\mathrm{d}z\\
&+ g\rho\pi bH\sum_{j=0}^{\infty}\left[D_{1j}U_1^{(4)}(\mu_jb)+E_{1j}U_1^{(5)}(\mu_jb)\right]\int_{-h_2}^{-h_1}(z-z_0)Z_j^{(3)}(\mu_jz)\mathrm{d}z, \qquad (4.56)\\
M_{y1}^2 &= \mathrm{i}\omega\rho\int_{-h_2}^{0}\int_0^{2\pi} a(\phi_2(a,\theta,z)+\phi_3(a,\theta,z))(z-z_0)(-\cos\theta)\,\mathrm{d}z\mathrm{d}\theta\\
&= -g\rho\pi aH\left[\sum_{j=0}^{\infty}C_{1j}U_1^{(6)}(\lambda_ja)\right]\int_{-h_1}^{0}(z-z_0)Z_j^{(2)}(\lambda_jz)\mathrm{d}z\\
&- g\rho\pi aH\sum_{j=0}^{\infty}\left[D_{1j}U_1^{(4)}(\mu_ja)+E_{1j}U_1^{(5)}(\mu_ja)\right]\int_{-h_2}^{-h_1}(z-z_0)Z_j^{(3)}(\mu_jz)\mathrm{d}z. \qquad (4.57)
\end{aligned}$$

Similarly, M_{y2} can be split into the following two components:

$$M_{y2} = M_{y2}^1 + M_{y2}^2, \tag{4.58}$$

where M_{y2}^1 and M_{y2}^2, respectively, refer to the moment induced by the force on the regions $(a<r<b, z=-h_1^+)\cup(a<r<b, z=-h_1^-)$ and $(a<r<b, z=-h_2^-)\cup(0<r<$

$b, z = -h_2^+$) and are given by

$$\begin{aligned} M_{y2}^1 &= -\mathrm{i}\omega\rho \int_a^b \int_0^{2\pi} \phi_3(r,\theta,-h_1) r^2 \cos\theta \, \mathrm{d}r\mathrm{d}\theta \\ &+ \mathrm{i}\omega\rho \int_a^b \int_0^{2\pi} \phi_2(r,\theta,-h_1) r^2 \cos\theta \, \mathrm{d}r\mathrm{d}\theta, \qquad (4.59) \\ M_{y2}^2 &= \mathrm{i}\omega\rho \int_a^b \int_0^{2\pi} \phi_3(r,\theta,-h_2) r^2 \cos\theta \, \mathrm{d}r\mathrm{d}\theta \\ &- \mathrm{i}\omega\rho \int_0^b \int_0^{2\pi} \phi_4(r,\theta,-h_2) r^2 \cos\theta \, \mathrm{d}r\mathrm{d}\theta. \qquad (4.60) \end{aligned}$$

Simplifying, we get

$$\begin{aligned} M_{y2}^1 &= -g\mathrm{i}\rho\pi H \Bigg[D_{10} b^2 \Big(\frac{b^2-a^2}{2}\Big) Z_0^{(3)}(\mu_0(-h_1)) \\ &+ \sum_{j=1}^{\infty} D_{1j} \frac{b^2 K_2(\mu_j b) - a^2 K_2(\mu_j a)}{\mu_j K_1'(\mu_j b)} Z_j^{(3)}(\mu_j(-h_1)) \Bigg] \\ &- g\mathrm{i}\rho\pi H \Bigg[E_{10} b^2 \Big(\frac{b^4-a^4}{4}\Big) Z_0^{(3)}(\mu_0(-h_1)) \\ &+ \sum_{j=1}^{\infty} E_{1j} \frac{b^2 I_2(\mu_j b) - a^2 I_2(\mu_j a)}{\mu_j I_1'(\mu_j b)} Z_j^{(3)}(\mu_j(-h_1)) \Bigg] \\ &+ g\mathrm{i}\rho\pi H \Bigg[B_{10} \frac{b^2 H_2^{(1)}(\lambda_0 b) - a^2 H_2^{(1)}(\lambda_0 a)}{\lambda_0 H_2^{(1)'}(\lambda_0 b)} Z_0^{(2)}(\lambda_0(-h_1)) \\ &+ \sum_{j=1}^{\infty} B_{1j} \frac{b^2 I_2(\lambda_j b) - a^2 I_2(\lambda_j a)}{\lambda_j I_1'(\lambda_j b)} Z_j^{(2)}(\lambda_j(-h_1)) \Bigg] \\ &+ g\mathrm{i}\rho\pi H \Bigg[C_{10} \frac{b^2 H_2^{(2)}(\lambda_0 b) - a^2 H_2^{(2)}(\lambda_0 a)}{\lambda_0 H_2^{(2)'}(\lambda_0 b)} Z_0^{(2)}(\lambda_0(-h_1)) \\ &+ \sum_{j=1}^{\infty} C_{1j} \frac{b^2 K_2(\lambda_j b) - a^2 K_2(\lambda_j a)}{\lambda_j K_1'(\lambda_j b)} Z_j^{(2)}(\lambda_j(-h_1)) Z_j^{(2)}(\lambda_j(-h_1)) \Bigg], \qquad (4.61) \\ M_{y2}^2 &= g\mathrm{i}\rho\pi H \Bigg[D_{10} b^2 \Big(\frac{b^2-a^2}{2}\Big) Z_0^{(3)}(\mu_0(-h_2)) \\ &+ \sum_{j=1}^{\infty} D_{1j} \frac{b^2 K_2(\mu_j b) - a^2 K_2(\mu_j a)}{\mu_j K_1'(\mu_j b)} Z_j^{(3)}(\mu_j(-h_2)) \Bigg] \\ &+ g\mathrm{i}\rho\pi H \Bigg[E_{10} b^2 \Big(\frac{b^4-a^4}{4}\Big) Z_0^{(3)}(\mu_0(-h_2)) \\ &+ \sum_{j=1}^{\infty} E_{1j} \frac{b^2 I_2(\mu_j b) - a^2 I_2(\mu_j a)}{\mu_j I_1'(\mu_j b)} Z_j^{(3)}(\mu_j(-h_2)) \Bigg] \\ &- g\mathrm{i}\rho\pi H \Bigg[F_{10} \frac{b^4}{4} Z_0^{(4)}(\gamma_0(-h_2)) + \sum_{j=1}^{\infty} F_{1j} \frac{b^2 I_2(\gamma_j b)}{\gamma_j I_1'(\gamma_j b)} Z_j^{(4)}(\gamma_j(-h_2)) \Bigg]. \qquad (4.62) \end{aligned}$$

4.1.5 Results and discussion

Now we discuss the effects of various parameters on the hydrodynamic forces acting on the cylindrical structure. This section details all the results.

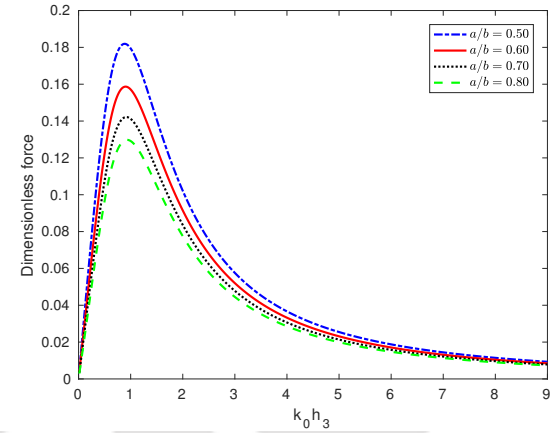

Figure 4.2: Dimensionless hydrodynamic force $\frac{|\tilde{F}_x^1|}{|\rho g a h_3 H|}$ acting on the inner cylinder against wavenumber corresponding to different values of a/b with $G = 1$, $h_1/h_2 = 0.25$ and $h_1/h_3 = 0.125$

Effect of radius ratio a/b on hydrodynamic force acting on the inner cylinder

Figure 4.2 shows the plots of hydrodynamic force $\frac{|\tilde{F}_x^1|}{|\rho g a h_3 H|}$ for the inner cylinder against the wavenumber corresponding to various values of radius ratio a/b with $G = 1$, $h_1/h_2 = 0.25$ and $h_1/h_3 = 0.125$. The force initially starts from non-zero values. In general, the force decreases for increasing values of k_0h_3. It is clear that occurrence of higher values of force correspond to lower values of a/b. In the neighbourhood of $k_0h_3 = 1$, a spike of decreasing magnitude is observed in the amplitude of the wave force. This force spike is associated with the resonant frequencies of the wave. Similar observation in some of the latter figures in this work can also be attributed to the same phenomenon of resonance as observed in Darwiche et al. [10] and Mandal et al. [26]. It is worth mentioning that the expressions of various potentials contain as numerator the derivatives of variants of Bessel functions, such as $I_m(.)$, $K_m(.)$, $H_m^{(1)}(.)$, $H_m^{(2)}(.)$. The zeros of these derivatives evaluated at the cylinder surface play a very important role for the resonance phenomenon. Each of the zeros corresponds to the standing waves near the wall. It can be seen that the maximum force occurs in the neighbourhood of $k_0h_3 = 1$. It is also observed that for decreasing a/b, the force at the inner cylinder increases. It may have happened due to more energy concentration near the inner cylinder and thus resulting in an increase of waveload.

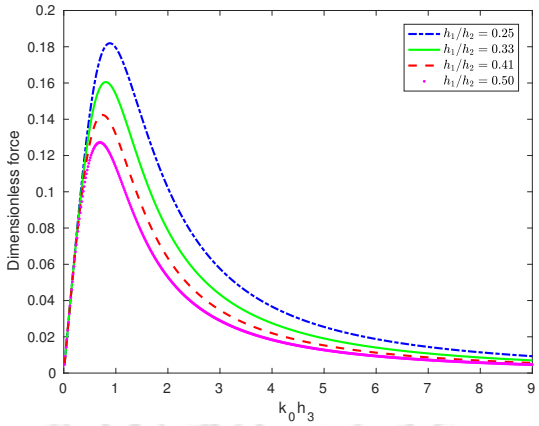

Figure 4.3: Dimensionless hydrodynamic force $\frac{|\tilde{F}_x^1|}{|\rho g a h_3 H|}$ acting on the inner cylinder against wavenumber corresponding to different values of h_1/h_2 with $G = 1$, $h_2/h_3 = 0.5$ and $a/b = 0.5$

Effect of draft ratio h_1/h_2 on hydrodynamic force acting on the inner cylinder

The plots of hydrodynamic force $\frac{|\tilde{F}_x^1|}{|\rho g a h_3 H|}$ for the inner cylinder against wavenumber corresponding to different values of h_1/h_2 with $G = 1$, $h_2/h_3 = 0.5$ and $a/b = 0.5$ are shown in Figure 4.3. Same trend of graph pattern as observed in Figure 4.2 is observed here too. It is noticed that lower values of h_1/h_2 give rise to higher values of force. All force values start from zero and are more pronounced only between $k_0h_3 = 0.5$ and $k_0h_3 = 1.5$. Beyond $k_0h_3 = 1.5$, the force value decreases. There is a shift in the maxima of these curves which may be due to the phase shift of the wave as the drafts of the porous cylindrical system change. Same type of phase shift is also observed in the work of Mandal et al. [26]. The resonating pattern of waveloads reduces exponentially with an increase in the values of wavenumber.

Effect of porous coefficient G on hydrodynamic force acting on the inner cylinder

In Figure 4.4, the hydrodynamic force $\frac{|\tilde{F}_x^1|}{|\rho g a h_3 H|}$ for the inner cylinder is plotted against wavenumber corresponding to different values of porous coefficient G with $a/b = 0.5$, $h_1/h_3 = 0.125$ and $h_1/h_2 = 0.25$. It is evident that G has a substantial impact on hydrodynamic loads acting on the porous structures. It is observed that all curves have similar trend as like in the earlier cases. Further, higher values of force correspond to higher values of porous coefficients which may be due to the transmission of more wave energy through the porous cylinder. Therefore, the resonating pattern of the wave force in the inner cylinder increases for increasing G.

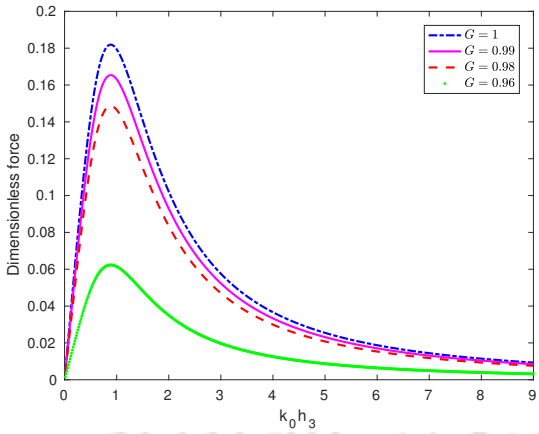

Figure 4.4: Dimensionless hydrodynamic force $\frac{|\tilde{F}_x^1|}{|\rho g a h_3 H|}$ on the inner cylinder against wavenumber corresponding to different values of G with $h_1/h_2 = 0.25$, $h_1/h_3 = 0.125$ and $a/b = 0.5$

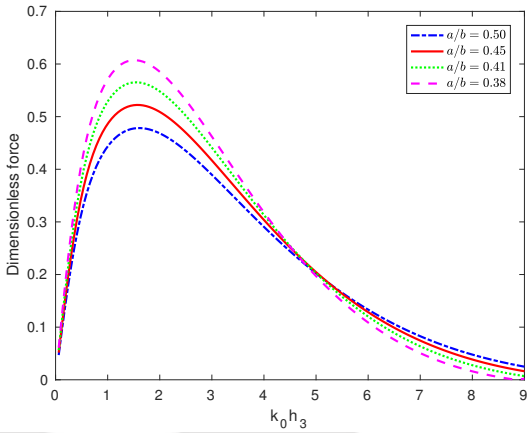

Figure 4.5: Dimensionless hydrodynamic force $\frac{|\tilde{F}_x^2|}{|\rho g b h_3 H|}$ on the outer cylinder against the wavenumber corresponding to different values of radius ratio a/b with $G = 1$, $h_1/h_2 = 0.25$ and $h_1/h_3 = 0.125$

Effect of radius ratio a/b on hydrodynamic force acting on the outer cylinder

Figure 4.5 presents the hydrodynamic force $\frac{|\tilde{F}_x^2|}{|\rho g b h_3 H|}$ for the outer cylinder plotted against wavenumber corresponding to different values of a/b with parameter values $G = 1$, $h_1/h_2 = 0.25$ and $h_1/h_3 = 0.125$. It is observed that the shapes of all curves maintain a similar trend (i.e., shows an increase first and then shows a reduction when the wavenumber increases). The maximum force corresponds to lower values of a/b. In $1.8 < k_0h_3 < 2$, the force assumes higher values but diminishes for higher values of k_0h_3. The maxima for the wave force on the structure may be due to the constructive interference between the incident and reflected waves.

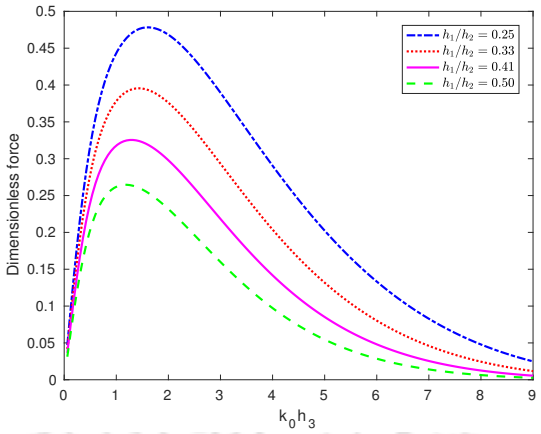

Figure 4.6: Dimensionless hydrodynamic force $\frac{|\tilde{F}_x^2|}{|\rho g b h_3 H|}$ on the outer cylinder against wavenumber corresponding to different values of h_1/h_2 with $G = 1$, $h_2/h_3 = 0.5$ and $a/b = 0.5$

Effect of h_1/h_2 on hydrodynamic force acting on the outer cylinder

Figure 4.6 shows the hydrodynamic force $\frac{|\tilde{F}_x^2|}{|\rho g b h_3 H|}$ for the outer cylinder plotted against wavenumber corresponding to various values of h_1/h_2 with $G = 1$, $h_2/h_3 = 0.5$ and $a/b = 0.5$. All the forces start from some non-zero values and are clearly evident only between $k_0h_3 = 1$ and $k_0h_3 = 2$. Beyond $k_0h_3 = 2$, the force value decreases. The force takes higher values corresponding to lower values of h_1/h_2. However, for larger values of the wavenumber k_0h_3, the forces on the outer cylinder diminish. This may be due to the fact that short waves are dissipated at a faster rate by the porous cylinder as compared to long waves.

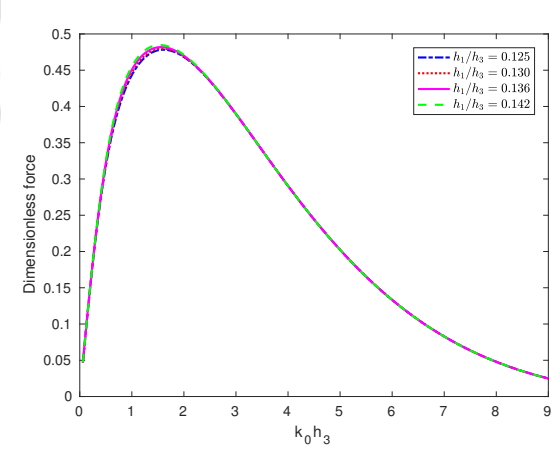

Figure 4.7: Dimensionless hydrodynamic force $\frac{|\tilde{F}_x^2|}{|\rho g b h_3 H|}$ on the outer cylinder against wavenumber corresponding to various values of h_1/h_3 with $G = 1$, $h_1/h_2 = 0.25$ and $a/b = 0.5$

Effect of h_1/h_3 on hydrodynamic force acting on the outer cylinder

Figure 4.7 presents the hydrodynamic force $\frac{|\tilde{F}_x^2|}{|\rho g b h_3 H|}$ for the outer cylinder plotted against wavenumber corresponding to various values of h_1/h_3 with parameter values $G = 1$, $h_1/h_2 = 0.25$ and $a/b = 0.5$. We observe the same pattern of curves which shows higher values of force occurring corresponding to higher values of h_1/h_3.

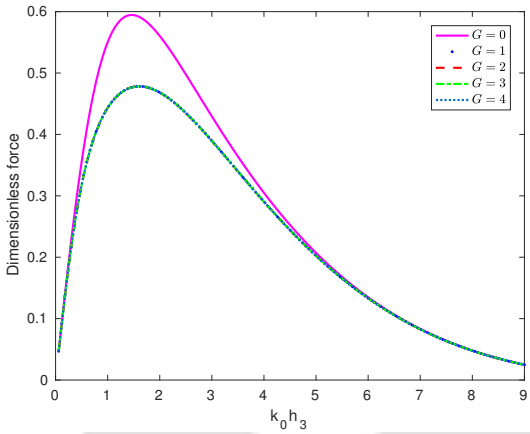

Figure 4.8: Dimensionless hydrodynamic force $\frac{|\tilde{F}_x^2|}{|\rho g b h_3 H|}$ on the outer cylinder against wavenumber corresponding to different values of G with $h_1/h_2 = 0.25$, $h_1/h_3 = 0.125$ and $a/b = 0.5$

Effect of porous coefficient G on hydrodynamic force acting on the outer cylinder

Porous coefficient plays a very important role in hydrodynamic forces. Figure 4.8 presents the hydrodynamic force $\frac{|\tilde{F}_x^2|}{|\rho g b h_3 H|}$ for the outer cylinder plotted against wavenumber corresponding to different values of G with $a/b = 0.5$, $h_1/h_2 = 0.25$ and $h_1/h_3 = 0.125$. All the curves start from some non-zero values, after which they decrease. Forces take higher values in $1.8 < k_0h_3 < 2.1$. It is noticed that the force decreases when k_0h_3 takes higher values. Further, for $G = 0$, the force profile has the same trend as was observed for other values $G = 1, 2, 3, 4$, but is significantly higher than the other cases. This happens because the lower wall of the cylinder is assumed impermeable due to consideration of $G = 0$.

Effect of a/b on wave run-up ζ_1

In Figure 4.9, the maximum dimensionless wave run-up $|\zeta_1(b, \theta)|/H$ in the exterior region is plotted against wavenumber corresponding to various values of a/b with parameter values $G = 1$, $h_1/h_2 = 0.25$ and $h_1/h_3 = 0.125$. It is noticed that the maximum wave run-up occurs in $1 < k_0h_3 < 2$.

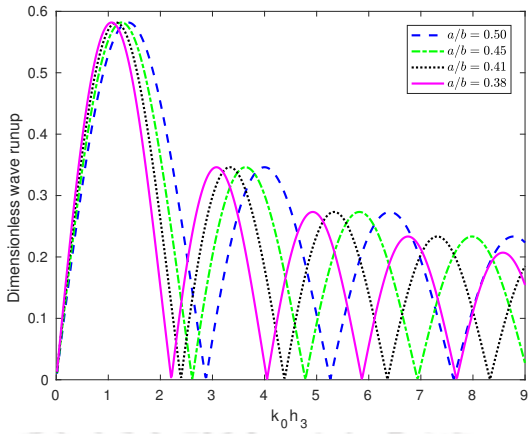

Figure 4.9: Dimensionless wave run-up $|\zeta_1(b,\theta)|/H$ against wavenumber corresponding to different values of a/b with $G = 1$, $h_1/h_2 = 0.25$ and $h_1/h_3 = 0.125$

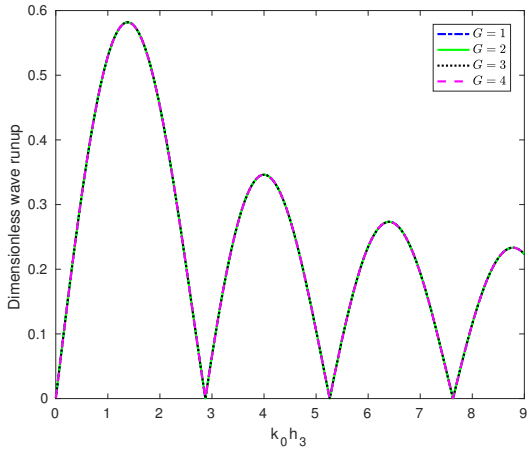

Figure 4.10: Dimensionless wave run-up $|\zeta_1(b,\theta)|/H$ against wavenumber corresponding to different values of G with $a/b = 0.5$, $h_1/h_2 = 0.25$ and $h_1/h_3 = 0.125$

Effect of porous parameter G on wave run-up ζ_1

Figure 4.10 presents the maximum dimensionless wave run-up $|\zeta_1(b,\theta)|/H$ in the exterior region plotted against wavenumber corresponding to different values of G with $a/b = 0.5$, $h_1/h_2 = 0.25$ and $h_1/h_2 = 0.125$. Similar pattern of graph is observed here just as in Figure 4.9. It starts from zero and after that it increases for increasing values of k_0h_3. The wave run-up decreases for higher values of k_0h_3.

Effect of radius ratio a/b on wave run-up ζ_2

Figure 4.11 presents the maximum dimensionless wave run-up $|\zeta_2(a,\theta)|/H$ in the exterior region plotted against wavenumber corresponding to various values of a/b with $G = 1$, $h_1/h_2 = 0.25$ and $h_1/h_3 = 0.125$. From the figure, it can be concluded that the maximum wave run-up occurs corresponding to smaller values of a/b, that is, for the case when the inner cylinder is much smaller than the outer cylinder.

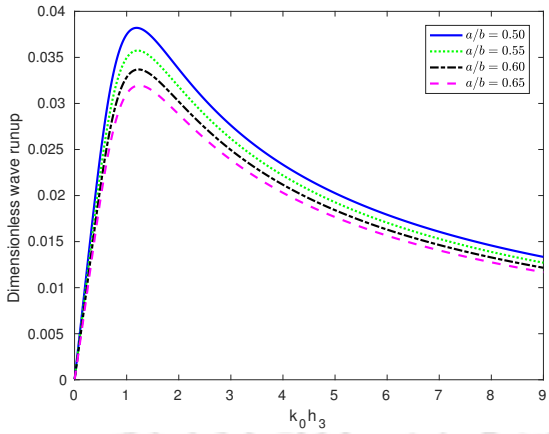

Figure 4.11: Dimensionless wave run-up $|\zeta_2(a,\theta)|/H$ against wavenumber corresponding to different values of a/b with $G = 1$, $h_1/h_2 = 0.25$ and $h_1/h_3 = 0.125$

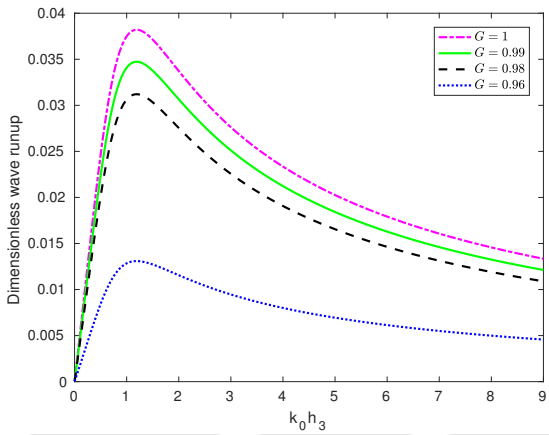

Figure 4.12: Dimensionless wave run-up $|\zeta_2(a,\theta)|/H$ against wavenumber corresponding to different values of G with $a/b = 0.5$, $h_1/h_2 = 0.25$ and $h_1/h_3 = 0.125$

Effect of porous parameter G on wave run-up ζ_2

In Figure 4.12 presents the maximum dimensionless wave run-up $|\zeta_2(a,\theta)|/H$ in the exterior region plotted against wavenumber corresponding to different values of G with $a/b = 0.5$, $h_1/h_2 = 0.25$ and $h_1/h_3 = 0.125$. It shows the occurrence of the highest value of the wave run-up in the neighbourhood of $k_0h_3 = 1.5$. Further, the wave run-up shows an upward trend corresponding to higher values of G.

Effect of radius ratio a/b at $z = -h_1$ on vertical force F_z^1

Figure 4.13 presents the dimensionless vertical force $|F_z^1|/\rho\pi gHa^2$ acting on the cylinder at $z = -h_1$ plotted against wavenumber corresponding to different values of radius ratio a/b with $G = 1$, $h_1/h_2 = 0.66$ and $h_1/h_3 = 0.33$. It is observed that all the graphs start from some non-zero value. Further, the figure shows the dimensionless vertical force at $z = -h_1$ of the cylinder taking increasing values when a/b decreases.

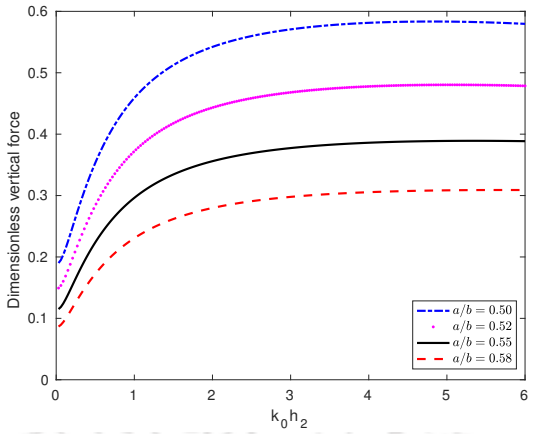

Figure 4.13: Dimensionless vertical force $|F_z^1|/\rho\pi gHa^2$ against wavenumber corresponding to various values of a/b with $G = 1$, $h_1/h_2 = 0.66$ and $h_1/h_3 = 0.33$

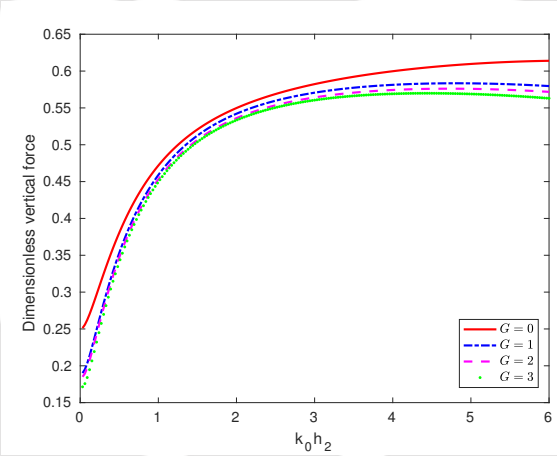

Figure 4.14: Variation of dimensionless vertical force $|F_z^1|/\rho\pi gHa^2$ against the wavenumber for various values of G corresponding to $a/b = 1/2$, $h_1/h_2 = 0.66$ and $h_1/h_3 = 0.33$

Effect of porous parameter G at $z = -h_1$ on vertical force F_z^1

Figure 4.14 presents the dimensionless vertical force $|F_z^1|/\rho\pi gHa^2$ acting on the cylinder at $z = -h_1$ plotted against wavenumber corresponding to different values of G with $a/b = 1/2$, $h_1/h_2 = 0.66$ and $h_1/h_3 = 0.33$. It is observed that the force attains peak value at $z = -h_1$ for $G = 0$, i.e., when the outer wall is assumed impermeable.

Effect of radius ratio a/b on vertical force F_z^2 at $z = -h_2$

Figure 4.15 shows the dimensionless vertical force $|F_z^2|/\rho\pi gHa^2$ at $z = -h_2$ plotted against wavenumber corresponding to radius ratio a/b with parameter values $G = 1$, $h_1/h_2 = 0.66$ and $h_1/h_3 = 0.33$. It is observed from the figure that the vertical force increases as the values of a/b decrease.

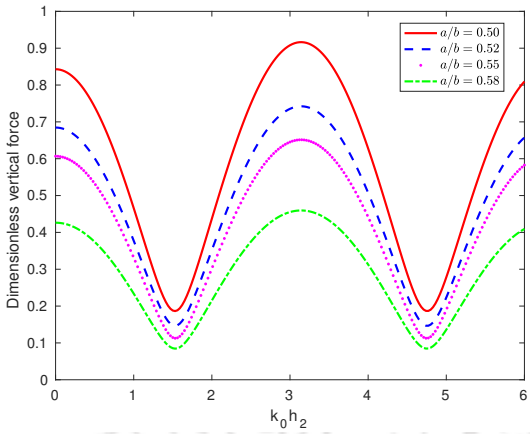

Figure 4.15: Dimensionless vertical force $|F_z^2|/\rho\pi gHa^2$ against wavenumber corresponding to different values of a/b with $G = 1$, $h_1/h_2 = 0.66$ and $h_1/h_3 = 0.33$

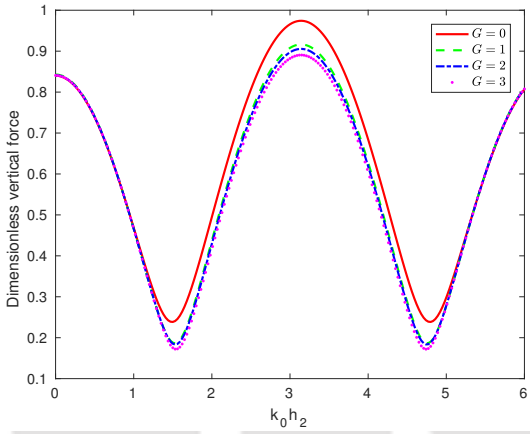

Figure 4.16: Dimensionless vertical force $|F_z^2|/\rho\pi gHa^2$ against wavenumber corresponding to various values of G with $a/b = 1/2$, $h_1/h_2 = 0.66$ and $h_1/h_3 = 0.33$

Effect of porous parameter G on vertical force F_z^2 at $z = -h_2$

Figure 4.16 presents the dimensionless vertical force $|F_z^2|/\rho\pi gHa^2$ at $z = -h_2$ plotted against wavenumber corresponding to different values of porous parameter G with parameter values $a/b = 1/2$, $h_1/h_2 = 0.66$ and $h_1/h_3 = 0.33$. In general, the maximum vertical force occurs at $z = -h_2$ of the cylinder as the porous parameter decreases. The peak value occurs for $G = 0$, i.e., when the cylinder is entirely impermeable.

Effect of radius ratio a/b on horizontal moment M_{y1}^1 at $r = b$

Figure 4.17 shows the variation of dimensionless horizontal moment $|M_{y1}^1|/\rho\pi gHa^3$ at the outer cylinder surface $r = b$ versus dimensionless wavenumber corresponding to different values of a/b for parameter values $G = 1$, $h_1/h_2 = 0.66$ and $h_1/h_3 = 0.33$. The moment center is considered to be at $(0, 0, 0)$. It is observed that the moment increases for decreasing values of radius ratio.

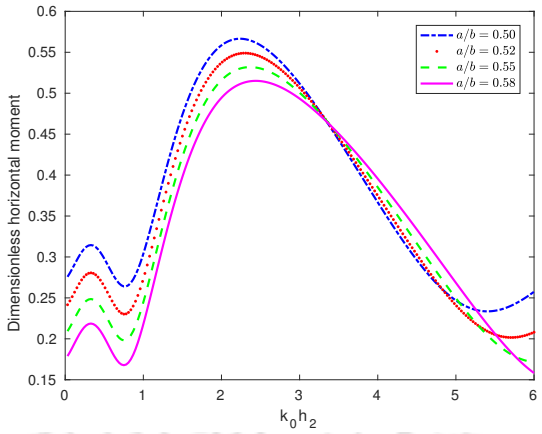

Figure 4.17: Dimensionless horizontal moment $|M^1_{y1}|/\rho\pi gHa^3$ at $r = b$ against wavenumber corresponding to different values of radius ration a/b with $G = 1$, $h_1/h_2 = 0.66$ and $h_1/h_3 = 0.33$

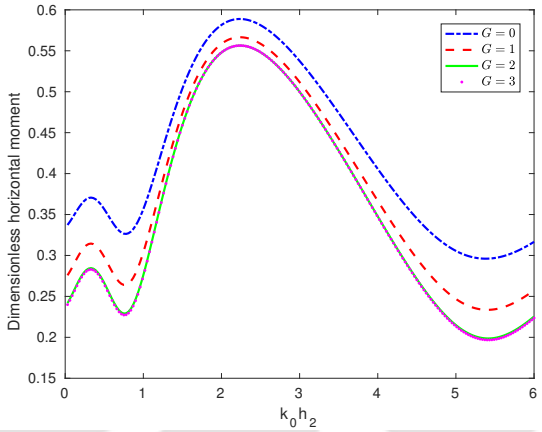

Figure 4.18: Dimensionless horizontal moment $|M^1_{y1}|/\rho\pi gHa^3$ at $r = b$ against wavenumber corresponding to different values of G with $a/b = 1/2$, $h_1/h_2 = 0.66$ and $h_1/h_3 = 0.33$

Effect of G at $r = b$ on horizontal moment M^1_{y1}

Figure 4.18 depicts the variation of dimensionless horizontal moment $|M^1_{y1}|/\rho\pi gHa^3$ at $r = b$ when plotted versus dimensionless wavenumber corresponding to different values of G for $a/b = 1/2$, $h_1/h_2 = 0.66$ and $h_1/h_3 = 0.33$. The peak moment occurs for $G = 0$, i.e., for the case when the cylinder is assumed impermeable. Therefore, the resonating pattern of the horizontal moment acting on the outer cylinder becomes more prominent for decreasing G.

Effect of radius ratio a/b on horizontal moment M^2_{y1} at $r = a$

Figure 4.19 presents the variation of dimensionless horizontal moment $|M^2_{y1}|/\rho\pi gHa^3$ at $r = a$ plotted against wavenumber corresponding to different values of radius ratio a/b for parameter values $G = 1$, $h_1/h_2 = 0.66$ and $h_1/h_3 = 0.33$. The moment profile shows a

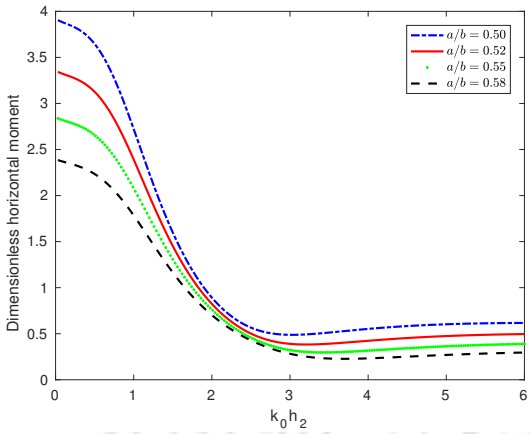

Figure 4.19: Dimensionless horizontal moment $|M^2_{y1}|/\rho\pi gHa^3$ at $r = a$ against wavenumber corresponding to different values of radius ratio a/b for $G = 1$, $h_1/h_2 = 0.66$ and $h_1/h_3 = 0.33$

similar trend. It is observed that the moment takes higher values corresponding to lower values of a/b. In other words, when the inner cylinder is much smaller than the outer cylinder, the moments are more significant.

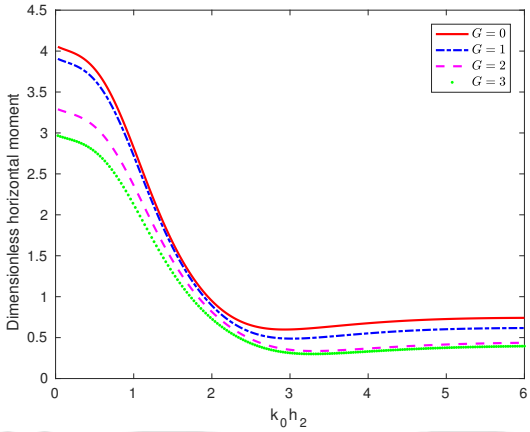

Figure 4.20: Dimensionless horizontal moment $|M^2_{y1}|/\rho\pi gHa^3$ at $r = a$ against wavenumber corresponding to different values of G for $a/b = 1/2$, $h_1/h_2 = 0.66$ and $h_1/h_3 = 0.33$

Effect of porous parameter G on horizontal moment M^2_{y1} at $r = a$

In Figure 4.20, the variation of dimensionless horizontal moment $|M^2_{y1}|/\rho\pi gHa^3$ at $r = a$ is shown against wavenumber corresponding to different values of porous parameter G for $a/b = 1/2$, $h_1/h_2 = 0.66$ and $h_1/h_3 = 0.33$. It is clear from the figure that the moment increases when $G = 0$, i.e., when the wall of the outer cylinder is assumed impermeable.

Effect of radius ratio a/b on vertical moment M^1_{y2} at $z = -h_1$

Figure 4.21 presents the variation of dimensionless vertical moment $|M^1_{y2}|/\rho\pi gHa^3$ at $z = -h_1$ plotted against wavenumber corresponding to different values of radius ratio a/b with

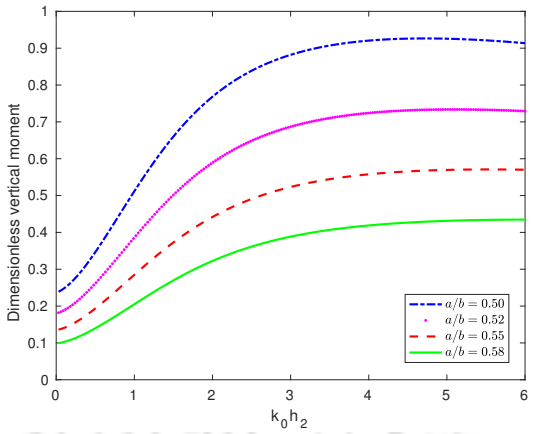

Figure 4.21: Dimensionless vertical moment $|M^1_{y2}|/\rho\pi gHa^3$ at $z = -h_1$ against wavenumber corresponding to different values of radius ratio a/b with $G = 1$, $h_1/h_2 = 0.66$ and $h_1/h_3 = 0.33$

$G = 1$, $h_1/h_2 = 0.66$ and $h_1/h_3 = 0.33$. The vertical moment becomes more significant at $z = -h_1$ corresponding to lower values of a/b, i.e., the moments are pronounced when the inner cylinder is much smaller than the outer cylinder.

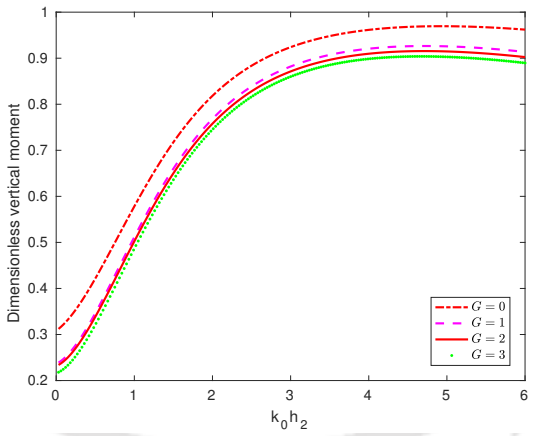

Figure 4.22: Dimensionless vertical moment $|M^1_{y2}|/\rho\pi gHa^3$ at $z = -h_1$ against wavenumber corresponding to different values of G for $a/b = 1/2$, $h_1/h_2 = 0.66$ and $h_1/h_3 = 0.33$

Effect of porous parameter G on vertical moment M^1_{y2} at $z = -h_1$

Figure 4.22 presents the variation of dimensionless vertical moment $|M^1_{y2}|/\rho\pi gHa^3$ at $z = -h_1$ plotted against wavenumber corresponding to different values of G for $a/b = 1/2$, $h_1/h_2 = 0.66$ and $h_1/h_3 = 0.33$. It is observed that the moment at $z = -h_1$ increases when the porosity of the outer cylinder decreases.

Effect of radius ratio a/b on vertical moment M^2_{y2} at $z = -h_2$

Figure 4.23 shows the variation of dimensionless vertical moment $|M^2_{y2}|/\rho\pi gHa^3$ at $z = -h_2$ versus dimensionless wavenumber corresponding to different values of radius ratio

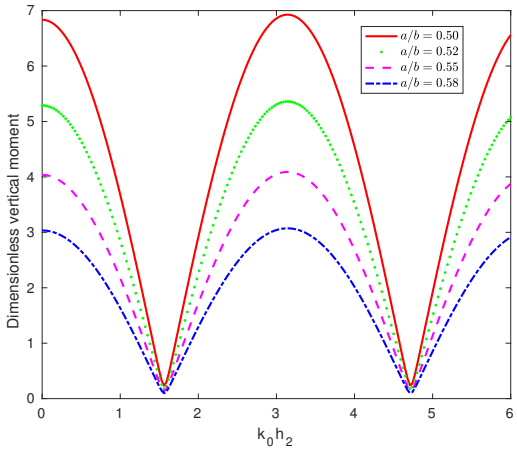

Figure 4.23: Dimensionless vertical moment $|M_{y2}^2|/\rho\pi gHa^3$ at $z = -h_2$ against wavenumber corresponding to different values of radius ratio a/b for $G = 1$, $h_1/h_2 = 0.66$ and $h_1/h_3 = 0.33$

a/b for $G = 1$, $h_1/h_2 = 0.66$ and $h_1/h_3 = 0.33$. It is observed that the moment increases for decreasing values of a/b.

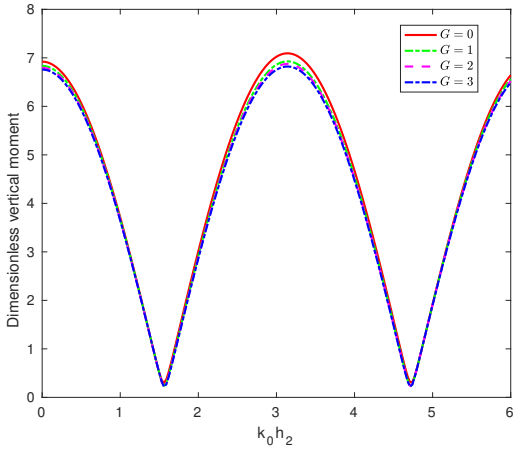

Figure 4.24: Dimensionless vertical moment $|M_{y2}^2|/\rho\pi gHa^3$ at $z = -h_2$ against wavenumber corresponding to different values of G for $a/b = 1/2$, $h_1/h_2 = 0.66$ and $h_1/h_3 = 0.33$

Effect of porous parameter G on vertical moment M_{y2}^2 at $z = -h_2$

Figure 4.24 shows the variation of dimensionless vertical moment $|M_{y2}^2|/\rho\pi gHa^3$ at $z = -h_2$ plotted against wavenumber corresponding to different values of G for $a/b = 1/2$, $h_1/h_2 = 0.66$ and $h_1/h_3 = 0.33$. It is observed that the moment takes higher values for the case $G = 0$, i.e., for an impermeable lower cylinder.

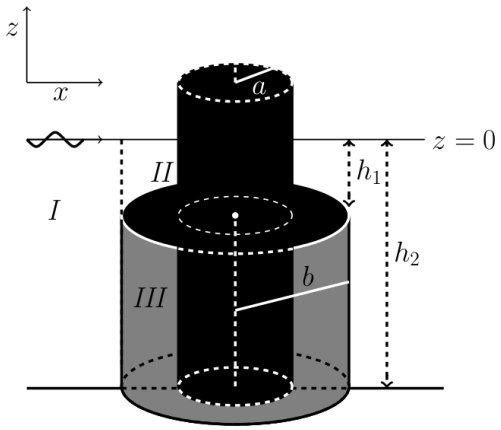

Figure 4.25: Surface-piercing partial-porous cylinder placed at sea bottom

4.2 Special case: bottom-mounted surface-piercing truncated partial-porous cylinder

As per the requirement for this problem with the bottom of the lower cylinder touching the sea-bed, the fluid domain is now divided into three regions (Figure 4.25) against four regions considered in the previous problem in Section 2: Region I $(r \geq b, -h_2 \leq z \leq 0)$; Region II $(a \leq r \leq b, -h_1 \leq z \leq 0)$ and Region III $(a \leq r \leq b, -h_2 \leq z \leq -h_1)$. Further, each potential satisfies Laplace's equation in respective regions as follows:

$$\nabla^2 \phi_j = 0, \quad j = 1, 2, 3, \tag{4.63}$$

with $\phi_j, \quad j = 1, 2, 3$ denoting the potentials in Regions I, II, and III, respectively. The free surface condition can be considered as equation (4.2) of our earlier problem along with the following modified sea-bed conditions:

$$\frac{\partial \phi_1}{\partial z} = 0; \quad z = -h_2, \quad r > b, \tag{4.64}$$

$$\frac{\partial \phi_3}{\partial z} = 0; \quad z = -h_2, \quad a < r < b. \tag{4.65}$$

The boundary conditions on the impermeable surface of cylinder remain the same as equations (4.5)-(4.8) of our earlier problem.

The boundary condition on the porous wall of the lower cylinder remains the same as equation (4.11).

Also, the Sommerfeld radiation condition for the exterior region remains the same as equation (2.15).

Similarly, the matching conditions are same as equations (4.12)-(4.14).

4.2.1 Diffracted potentials in sub-domains

In this case, the expressions for ϕ_1, ϕ_2 and ϕ_3 are same as equations (4.17)-(4.19), respectively. For Region I, wavenumbers k_j, $j = 0, 1, 2, 3, \ldots$, are derived from the following dispersion relation:

$$\omega^2 = \begin{cases} gk_j \tanh k_j h_2; & j = 0, \\ -gk_j \tan k_j h_2; & j \geq 1. \end{cases}$$

The vertical eigenfunctions $Z_j^{(1)}(k_j z)$ are defined as

$$Z_j^{(1)}(k_j z) = \begin{cases} \frac{\cosh k_j(z+h_2)}{\cosh k_j h_2}; & j = 0, \\ \frac{\cos k_j(z+h_2)}{\cos k_j h_2}; & j \geq 1. \end{cases}$$

4.2.2 Computation of unknown coefficients

In this case also we use the same technique as followed in the earlier case to calculate the unknown coefficients.

4.2.3 Hydrodynamic force and wave run-up

The expressions for hydrodynamic force and wave run-up can be taken as the same ones as in our earlier problem.

4.2.4 Results and discussion

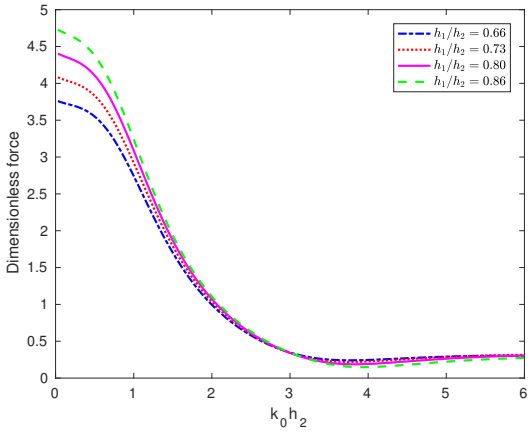

Figure 4.26: Dimensionless hydrodynamic force $\frac{|\tilde{F}_x^1|}{|\rho g a h_2 H|}$ on the inner cylinder against wavenumber corresponding to different values of h_1/h_2 with $G = 1$ and $a/b = 1/2$

Effect of h_1/h_2 on hydrodynamic force acting on the inner cylinder

Figure 4.26 presents the hydrodynamic force $\frac{|\tilde{F}_x^1|}{|\rho g a h_2 H|}$ for the inner cylinder plotted against wavenumber corresponding to different values of h_1/h_2 with $G = 1$ and $a/b = 1/2$. It is observed that all the graphs have the same pattern and the force takes higher values corresponding to higher values of h_1/h_2.

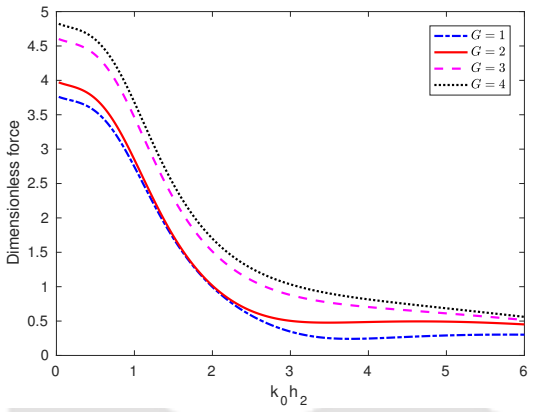

Figure 4.27: Dimensionless hydrodynamic force $\frac{|\tilde{F}_x^1|}{|\rho g a h_2 H|}$ on the inner cylinder against wavenumber corresponding to different values of G with $h_1/h_2 = 2/3$ and $a/b = 1/2$

Effect of porous parameter G on hydrodynamic force acting on the inner cylinder

In Figure 4.27, we plot hydrodynamic force $\frac{|\tilde{F}_x^1|}{|\rho g a h_2 H|}$ for the inner cylinder against wavenumber corresponding to different values of G for $a/b = 1/2$ and $h_1/h_2 = 2/3$. It is clear that G has a reasonably strong influence on the hydrodynamic force acting on the porous structures. It is observed that all curves have similar trend and the force takes higher values corresponding to higher values of porous coefficients.

Effect of radius ratio a/b on hydrodynamic force acting on the outer cylinder

In Figure 4.28, the hydrodynamic force $\frac{|\tilde{F}_x^2|}{|\rho g b h_2 H|}$ for the outer cylinder is plotted against wavenumber corresponding to different values of radius ratio a/b for $G = 1$ and $h_1/h_2 = 2/3$. It shows the shapes of all curves keeping a similar trend (i.e., initially increasing and then decreasing when the wavenumber increases). The maximum force occurs corresponding to lower values of the radius ratio. For the values of k_0h_2 in $0.8 < k_0h_2 < 1.2$, the force becomes higher. The wave energy acting at $r = b$ in Figure 4.28 is similar to the waveloads as discussed in Figure 4.5.

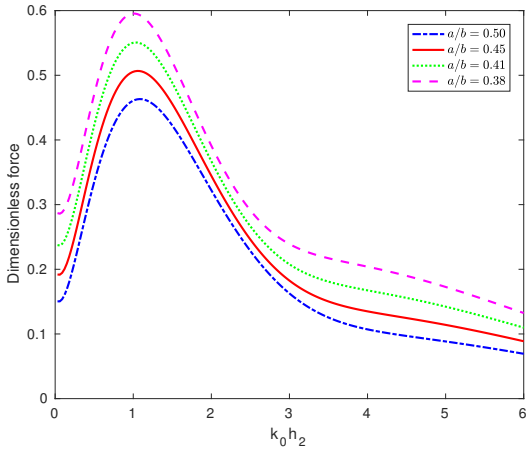

Figure 4.28: Dimensionless hydrodynamic force $\dfrac{|\tilde{F}_x^2|}{|\rho g b h_2 H|}$ on the outer cylinder against wavenumber corresponding to different values of a/b with $G = 1$ and $h_1/h_2 = 2/3$

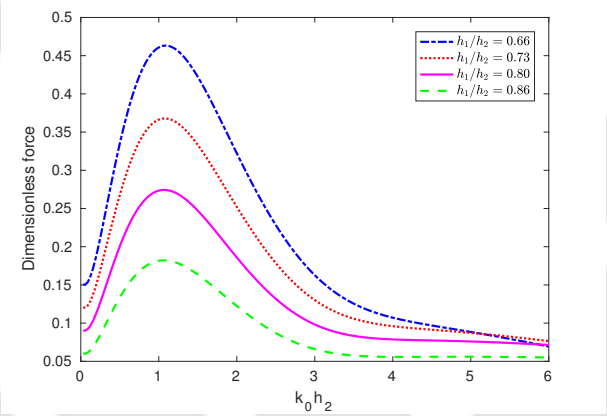

Figure 4.29: Dimensionless hydrodynamic force $\dfrac{|\tilde{F}_x^2|}{|\rho g b h_2 H|}$ on the outer cylinder against wavenumber corresponding to various values of h_1/h_2 with $G = 1$ and $a/b = 1/2$

Effect of h_1/h_2 on hydrodynamic force acting on the outer cylinder

Figure 4.29 presents the hydrodynamic force $\dfrac{|\tilde{F}_x^2|}{|\rho g b h_2 H|}$ for the outer cylinder plotted against wavenumber corresponding to different values of h_1/h_2 for $G = 1$ and $a/b = 1/2$. The same pattern of curves is observed. It starts from some non-zero value and is more pronounced only between $k_0h_2 = 0.5$ and $k_0h_2 = 1.8$. Beyond $k_0h_2 = 1.8$, the values decrease. Higher values of force occur corresponding to lower values of draft ratios.

Effect of radius ratio a/b on wave run-up ζ_1

Figure 4.30 presents the maximum dimensionless wave run-up $|\zeta_1(b,\theta)|/H$ in the exterior region by plotting it against wavenumber corresponding to different values of radius ratio a/b for $G = 1$ and $h_1/h_2 = 2/3$. Same trend of wave run-up as in the earlier case can

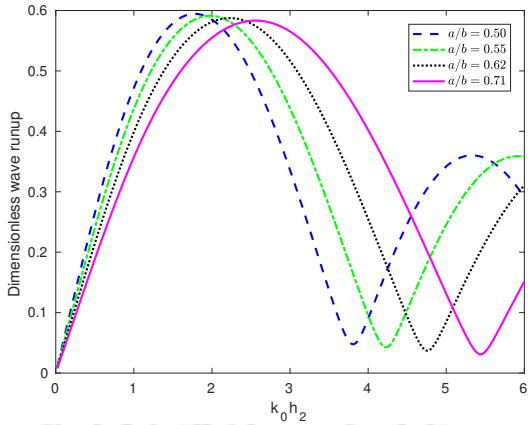

Figure 4.30: Dimensionless wave run-up $|\zeta_1(b,\theta)|/H$ against wavenumber corresponding to different values of a/b with $G = 1$ and $h_1/h_2 = 2/3$

be observed here too. The maximum value of run-up takes place in the range of values $2 < k_0h_2 < 3$.

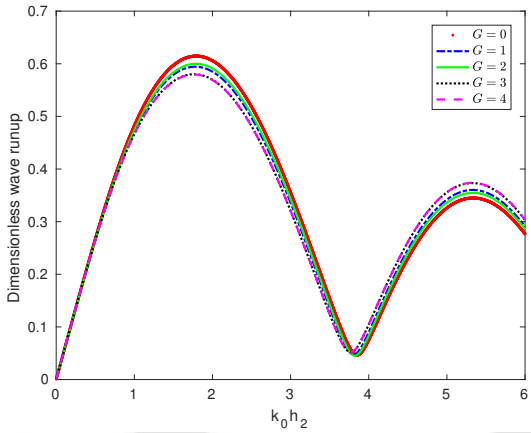

Figure 4.31: Dimensionless wave run-up $|\zeta_1(b,\theta)|/H$ against wavenumber corresponding to different values of G for $a/b = 1/2$ and $h_1/h_2 = 2/3$

Effect of porous parameter G on wave run-up ζ_1

In Figure 4.31, the maximum wave run-up $|\zeta_1(b,\theta)|/H$ in the exterior region is plotted against wavenumber corresponding to different values of G for $a/b = 1/2$ and $h_1/h_2 = 2/3$. Similar pattern of graph is observed here just as in Figure 4.30. It starts from zero and increases afterwards for increasing values of k_0h_2. Beyond $k_0h_2 = 2.1$, the graphs come downward. The observation is that for the case $G = 0$, i.e., for the impermeable case of the lower cylinder, the wave run-up becomes more pronounced.

Effect of radius ratio a/b on wave run-up ζ_2

Figure 4.32 presents the maximum dimensionless wave run-up $|\zeta_2(a,\theta)|/H$ in the exterior region plotted against wavenumber corresponding to different values of radius ratio a/b

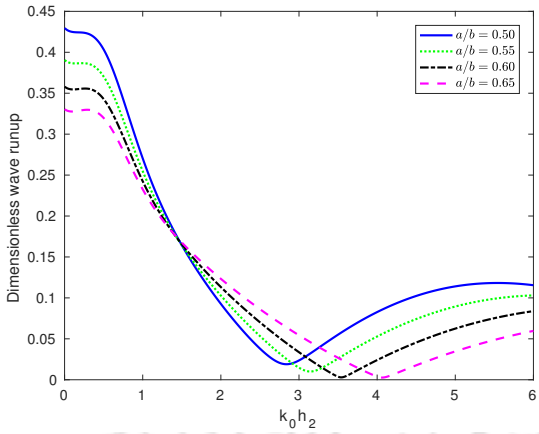

Figure 4.32: Dimensionless wave run-up $|\zeta_2(a,\theta)|/H$ against wavenumber corresponding to different values of a/b for $G = 1$, and $h_1/h_2 = 2/3$

for the values $G = 1$, and $h_1/h_2 = 2/3$. It is observed that the maximum value of the run-up occurs in the neighbourhood of $k_0h_2 = 0.5$. Another important observation here is that maximum run-up occurs corresponding to smaller values of radius ratio a/b, that is, the run-up takes higher values when the inner cylinder is much smaller than the outer cylinder.

4.3 Conclusion

The current chapter theoretically studies the interaction of linear water waves with partial-porous cylinders for two cases, namely, (i) a floating truncated partial-porous cylinder, and (ii) a bottom-mounted truncated partial-porous cylinder. By using eigenfunction expansion approach and the separation of variables technique, this diffraction problem governed by Laplace's equation is solved. It is observed through appropriate graphs that change of values for radii, draft and porosity has considerable effect on hydrodynamic loads. The behaviour of hydrodynamic load is found to be steady in the lower frequency range. We plot the wave run-up in the exterior regions. It is observed that as the distance from the surface of the cylinder increases in the exterior region, the amplitude of oscillation decreases. It is also demonstrated how the wave run-up behaves corresponding to different values of radii and the porous coefficient. It is also is found that for the impermeable cylinder case (Figures 4.8 and 4.31 for $G = 0$), hydrodynamic force and wave run-up become more prominent. The horizontal and vertical moment become more effective for $G = 0$ (Figures 4.20, 4.22 and 4.24).

Porosity plays a very crucial role in reducing/controlling the forces and moments on the system under consideration by dissipating maximum wave energy. The outer cylinder can be used not only for protection of inner impermeable rigid wall but also for developing an effective wave trapping system. For a floating surface-piercing cylinder, the force at the outer cylinder is higher in $1.8 < k_0h_3 < 2$, but diminishes for higher

values of k_0h_3. Further, the horizontal moment at the outer cylinder becomes higher in $2 < k_0h_3 < 3$. The peak moment occurs for $G = 0$, i.e., for the case when the cylinder is assumed impermeable. Similar type of behaviour of hydrodynamic force is observed for the bottom-mounted cylindrical system with the force at the outer cylinder higher in the range $1 < k_0h_3 < 1.5$.

As observed from various results, the following may be summed up:

1. With regard to the values of radius ratio a/b, greater value results in relatively smaller forces and less resonance - an ideal situation for reducing adverse hydrodynamic effect. In practical sense, the porous portion of the cylinder should be considered such that it is much larger than the inner impermeable cylinder, at least $a/b > 0.15$.

2. Porosity needs to be chosen so as to have the minimum impact on the outer cylinder in addition to affecting reduction of resonance effect. In our case, $G = 1$ is found to be ideal for all calculations.

3. Draft of the lower cylinder should not exceed the draft of the upper cylinder by a large amount. In other words, the ratio h_1/h_2 should be closer to unity so as to have the best effect.

CHAPTER 5

Interaction of Water Waves with a Semi-Porous Bottom-Mounted Cylindrical Storage Tank Containing a Cylindrical Pile

The objective of the present chapter is to investigate diffraction of water waves by a surface-piercing bottom-mounted cylindrical storage tank the inner part of which consists of an impermeable cylindrical pile and the outer part consists of a thin coaxial hollow porous cylinder. We intend to discuss two cases: (i) a thin hollow porous cylinder surrounding an impermeable coaxial inner cylinder with some space between them which stores water, and (ii) then the same structure placed on a bottom-mounted impermeable cylinder of equal radius. This type of structures are used for aquaculture around wind farm for multi-use and profits. For both cases, the hydrodynamic forces and wave run-up for different porosity, radii etc are studied. As far as the authors' knowledge is concerned, mathematical problems concerning such structures have not been taken up earlier by anyone else and it is expected that the results obtained here are going to benefit those working in designing and installing wind farm and/or aquaculture structure. Validation of the present model is carried out by comparing with an available one in the literature.

5.1 Mathematical formulation for outer thin hollow porous cylinder

We take up the problem of interaction of water waves with a surface-piercing bottom-mounted storage tank in the form of a vertical circular cylinder the outer part of which is a thin hollow porous cylinder of porosity G and the inner part an impermeable coaxial solid circular cylinder (i.e., a pile) of same height (Figure 5.1). The intermediate portion between these cylinders stores water. Considering a homogeneous, incompressible and inviscid fluid undergoing irrotational motion and the sea-bed to be flat and impermeable,

a cylindrical coordinate system in variables (r, θ, z) is taken with the origin considered at the undisturbed free surface and the z-axis vertically upward. Let a and b be the radii of the inner and outer cylinders, respectively. Employing linear theory, a train of small-amplitude waves is assumed to propagate from negative infinity towards the structure and subsequently, the potential $\Phi(r, \theta, z, t) = \mathrm{Re}[\phi(r, \theta, z) \exp(-\mathrm{i}\omega t)]$, with ω as the angular wave frequency, is considered.

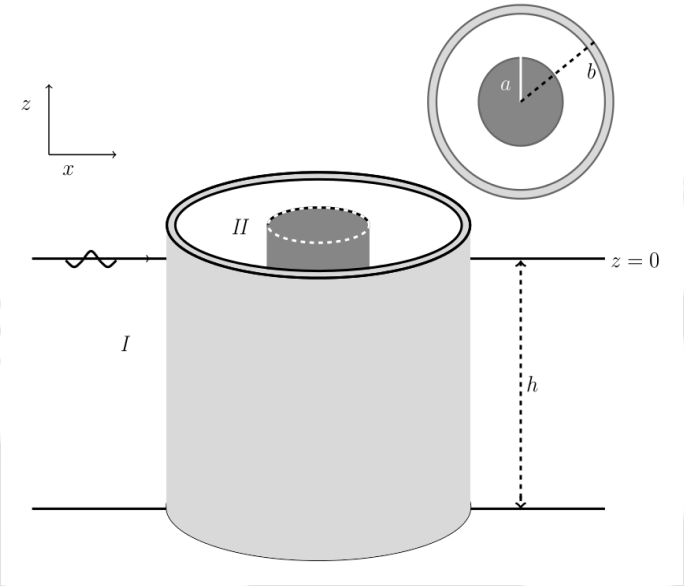

Figure 5.1: Schematic diagram of the structure

We split the fluid domain into two regions: Region I $(r \geq b, -h \leq z \leq 0)$ and Region II $(a \leq r \leq b, -h \leq z \leq 0)$. The velocity potentials in those regions are taken as Φ_j for $j = 1, 2$.

The free surface condition and the bottom boundary condition on the sea-bed are of the following form:

$$\frac{\partial \phi_j}{\partial z} - \frac{\omega^2}{g}\phi_j = 0; \quad z = 0, \quad j = 1, 2, \tag{5.1}$$

$$\frac{\partial \phi_1}{\partial z} = 0; \quad z = -h, \quad r > b, \tag{5.2}$$

$$\frac{\partial \phi_2}{\partial z} = 0; \quad z = -h, \quad a < r < b. \tag{5.3}$$

The boundary conditions to be satisfied on the surface of the porous cylinder are the following:

$$\frac{\partial \phi_2}{\partial r} = \mathrm{i}k_0 G(\phi_2 - \phi_1); \quad r = b, \quad -h < z < 0, \tag{5.4}$$

$$\frac{\partial \phi_1}{\partial r} = \frac{\partial \phi_2}{\partial r}; \quad r = b, \quad -h < z < 0, \tag{5.5}$$

where G and k_0 are complex porous coefficient and incident wavenumber, respectively.

Further, the boundary conditions on the impermeable surface of the inner cylinder is

$$\frac{\partial \phi_2}{\partial r} = 0; \quad r = a, \quad -h < z < 0. \tag{5.6}$$

The Sommerfeld radiation condition for the exterior region is same as equation (2.15). The velocity potential ϕ_1 in region I is found to be

$$\begin{aligned}\phi_1(r,\theta,z) &= -\frac{igH}{\omega}\Bigg[\sum_{m=0}^{\infty}\tau_m J_m(k_0 r)\cos m\theta Z_0(k_0 z) \\ &\quad + \sum_{m=0}^{\infty}\cos m\theta \sum_{j=0}^{\infty} A_{mj} Z_j(k_j z) U_m^{(1)}(k_j r)\Bigg],\end{aligned} \tag{5.7}$$

where A_{mj} are the unknown coefficients. The radial eigenfunctions $U_m^{(1)}(k_j r)$ are given as follows:

$$U_m^{(1)}(k_j r) = \begin{cases} \frac{H_m^{(1)}(k_j r)}{H_m^{(1)'}(k_j b)}; & j = 0, \\ \frac{K_m(k_j r)}{K_m'(k_j b)}; & j \geqslant 1. \end{cases}$$

Likewise ϕ_2, the scattered velocity potential, has the following expression:

$$\phi_2(r,\theta,z) = -\frac{igH}{\omega}\Bigg[\sum_{m=0}^{\infty}\cos m\theta \sum_{j=0}^{\infty}(B_{mj}U_m^{(2)}(k_j r) + C_{mj}U_m^{(3)}(k_j r))Z_j(k_j z)\Bigg], \tag{5.8}$$

with B_{mj} and C_{mj} being the unknown coefficients. The radial eigenfunctions $U_m^{(2)}(k_j r)$ and $U_m^{(3)}(k_j r)$ are as follows:

$$U_m^{(2)}(k_j r) = \begin{cases} \frac{H_m^{(1)}(k_j r)}{H_m^{(1)'}(k_j b)}; & j = 0, \\ \frac{I_m(k_j r)}{I_m'(k_j b)}; & j \geqslant 1, \end{cases} \qquad U_m^{(3)}(k_j r) = \begin{cases} \frac{H_m^{(2)}(k_j r)}{H_m^{(2)'}(k_j b)}; & j = 0, \\ \frac{K_m(k_j r)}{K_m'(k_j b)}; & j \geqslant 1. \end{cases}$$

5.2 Evaluation of unknown coefficients

The next foremost task is to determine the coefficients appearing in the expressions in the velocity potentials. The boundary condition (5.6) and the orthogonal property of the depth eigenfunctions give rise to the following for the coefficients $B_{m\alpha}$ and $C_{m\alpha}$ in ϕ_2:

$$\frac{H_m^{(1)'}(k_0 a)}{H_m^{(1)'}(k_0 b)}B_{m0} + \frac{H_m^{(2)'}(k_0 a)}{H_m^{(2)'}(k_0 b)}C_{m0} = 0, \tag{5.9}$$

$$\frac{I_m'(k_\alpha a)}{I_m'(k_\alpha b)}B_{m\alpha} + \frac{K_m'(k_\alpha a)}{K_m'(k_\alpha b)}C_{m\alpha} = 0, \quad \alpha \geqslant 1. \tag{5.10}$$

Use of the matching condition (5.5) for $-h < z < 0$, and the orthogonal property of the depth functions Z_j gives

$$A_{m0} - B_{m0} - C_{m0} = -\tau_m J'_m(k_0 b), \tag{5.11}$$

$$A_{m\alpha} - B_{m\alpha} - C_{m\alpha} = 0 \quad \alpha \geqslant 1. \tag{5.12}$$

Again applying boundary condition (5.4) for $-h < z < 0$ at $r = b$, and orthogonal property of the depth functions, the following are obtained:

$$B_{m0} + C_{m0} = \mathrm{i}k_0 G \left(B_{m0} \frac{H_m^{(1)}(k_0 b)}{H_m^{(1)'}(k_0 b)} + C_{m0} \frac{H_m^{(2)}(k_0 b)}{H_m^{(2)'}(k_0 b)} - \tau_m J_m(k_0 b) - A_{m0} \frac{H_m^{(1)}(k_0 b)}{H_m^{(1)'}(k_0 b)} \right), \tag{5.13}$$

$$B_{m\alpha} + C_{m\alpha} = \mathrm{i}k_0 G \left(B_{m\alpha} \frac{I_m(k_\alpha b)}{I'_m(k_\alpha b)} + C_{m\alpha} \frac{K_m(k_\alpha b)}{K'_m(k_\alpha b)} - A_{m\alpha} \frac{K_m(k_\alpha b)}{K'_m(k_\alpha b)} \right), \alpha \geqslant 1. \tag{5.14}$$

5.3 Wave run-up and hydrodynamic force

For various applications, the appropriate quantities are required to be calculated. Water wave run-up in both exterior and interior regions, given by $\eta_j(r, \theta, t) = \mathrm{Re}[\zeta_j(r, \theta) \exp(-\mathrm{i}\omega t)]$ for $j = 1, 2$, can be computed by using the dynamic free surface condition given by

$$\eta_j = -\frac{1}{g} \frac{\partial \Phi_j}{\partial t} \quad \text{on} \quad z = 0 \quad \text{for} \quad j = 1, 2. \tag{5.15}$$

Then we find

$$\zeta_1 = H \left[\sum_{m=0}^{\infty} \tau_m J_m(k_0 b) \cos m\theta Z_0(0) + \sum_{m=0}^{\infty} \cos m\theta \sum_{j=0}^{\infty} A_{mj} Z_j(0) U_m^{(1)}(k_j b) \right], \tag{5.16}$$

$$\zeta_2 = H \left[\sum_{m=0}^{\infty} \cos m\theta \sum_{j=0}^{\infty} \left[B_{mj} U_m^{(2)}(k_j a) + C_{mj} U_m^{(3)}(k_j a) \right] Z_j(0) \right]. \tag{5.17}$$

The total hydrodynamic force in the direction of wave propagation on the inner cylinder ($r = a$) and the outer cylinder ($r = b$) can be computed by carrying out integration on the pressure distribution at the surface of the structures. We define $\tilde{F}_x^j(t) = \mathrm{Re}[\tilde{F}_x^j \exp(-\mathrm{i}\omega t)]$ for $j = 1, 2$ as

$$\tilde{F}_x^1 = \mathrm{i}\omega\rho \int_{-h}^{0} \int_{0}^{2\pi} \phi_2(a, \theta, z) \cos\theta \, \mathrm{d}z\mathrm{d}\theta, \tag{5.18}$$

$$\tilde{F}_x^2 = \mathrm{i}\omega\rho \int_{-h}^{0} \int_{0}^{2\pi} \phi_2(b, \theta, z) \cos\theta \, \mathrm{d}z\mathrm{d}\theta - \mathrm{i}\omega\rho \int_{-h}^{0} \int_{0}^{2\pi} \phi_1(b, \theta, z) \cos\theta \, \mathrm{d}z\mathrm{d}\theta. \tag{5.19}$$

Truncating the infinite series appearing in (5.7) and (5.8) after some finite terms N,

here $N = 20$, as in Ning et al. [38] and our previous works, and then using equations $(5.9) - (5.14)$ lead to a system of matrix equations for the coefficients A_{mj}, B_{mj}, and C_{mj} appearing in the potentials ϕ_1 and ϕ_2. The convergence follows similarly as demonstrated in Chapter 2. Ultimately the following linear system of algebraic equations is derived:

$$\mathcal{A}_l \mathcal{X}_l = \mathcal{B}_l, \tag{5.20}$$

where, $\mathcal{X}_l = [A_{l1}, A_{l2}, ..., A_{lN}, B_{l1}, B_{l2}, ..., B_{lN}, C_{l1}, C_{l2}, ..., C_{lN}]^t$. $\mathcal{A}_l$ are coefficients matrices and $\mathcal{B}_l$ are the right hand vectors.

5.4 Results and discussion

MATLAB is used to develop a computer program in order to implement the above results, and thereby to study the diffraction characteristics for a number of configurations of the structure under consideration. Four values of porous coefficient G, viz., $0, 1 + \mathrm{i}, 2 + 2\mathrm{i}$ and $3 + 3\mathrm{i}$, are considered for the purpose. To realize the role of the porous structures in actual sense, the complex form of porous parameter $G = G_r + \mathrm{i}G_\mathrm{i}$ ($G_r = G_\mathrm{i}$ in each case), where G_r and G_i, respectively, denote the real and imaginary parts of G, is considered in carrying out the parametric study. Further, ocean depth is taken as $h = 3$ meter in the discussion throughout.

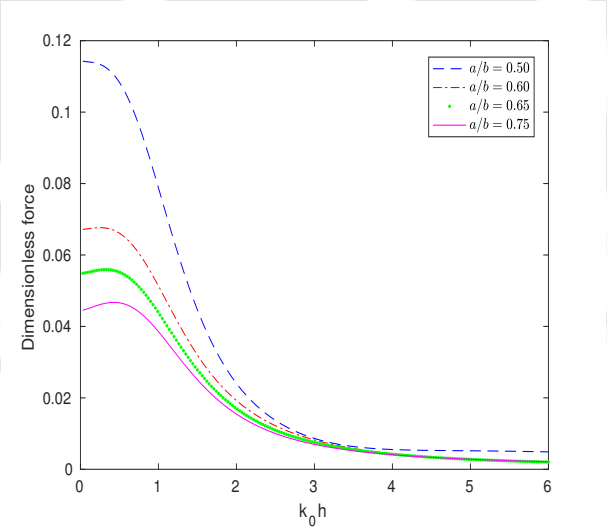

Figure 5.2: Dimensionless hydrodynamic force at $r = a$ against the wavenumber corresponding to different values of radius ratio a/b with $G = 1 + \mathrm{i}$

Figure 5.2 presents the plots of dimensionless hydrodynamic force $\dfrac{|\tilde{F}_x^1|}{|\rho g b h H|}$ acting on the inner cylinder at $r = a$ corresponding to different values of radius ratio a/b, for $G = 1 + \mathrm{i}$. It is observed that dimensionless hydrodynamic force takes higher values for lower radius ratio a/b within the lower range of wavenumbers, i.e., $(k_0 h < 0.5)$. It is clear that the forces diminish at higher $k_0 h$. This clearly indicates that for a larger annular

region and long waves, a force with reasonable higher intensity acts on the inner cylinder. However, short waves result in significant reduction in force values.

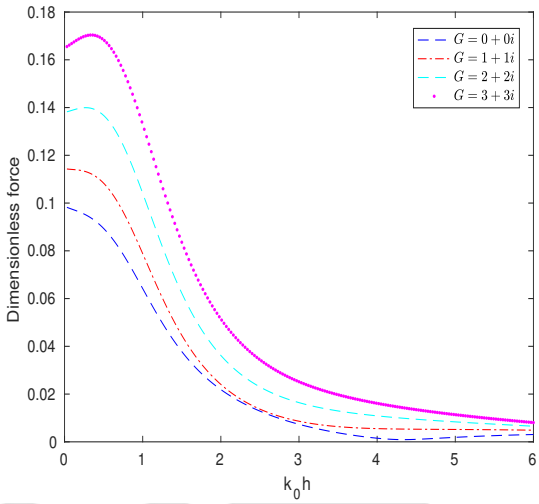

Figure 5.3: Dimensionless hydrodynamic force at $r = a$ against the wavenumber corresponding to different values of G for $a/b = 1/2$

In Figure 5.3, the dimensionless hydrodynamic force $\frac{|\tilde{F}_x^1|}{|\rho g b h H|}$ acting on the inner cylinder at $r = a$ is plotted corresponding to different values of porous coefficient G for $a/b = 1/2$. It shows that the wave force increases as the value of $|G|$ increases, i.e., the real and imaginary parts of G increase. All curves show a similar trend for different values of G. This implies that a highly porous cylinder admits higher force acting on the inner cylinder.

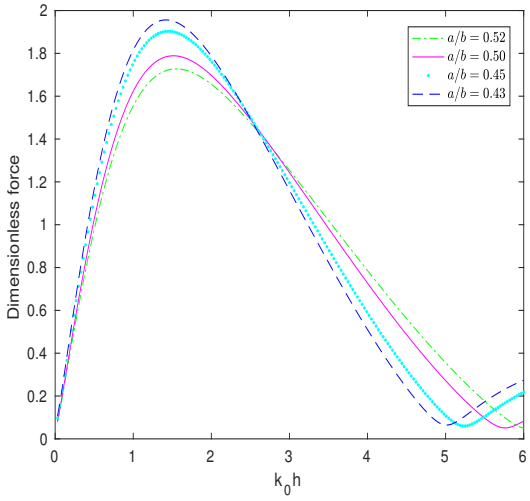

Figure 5.4: Dimensionless hydrodynamic force at $r = b$ against the wavenumber corresponding to different values of a/b for $G = 1 + \mathrm{i}$

Figure 5.4 shows the dimensionless hydrodynamic force $\frac{|\tilde{F}_x^2|}{|\rho g b h H|}$ acting on the outer

porous cylinder at $r = b$ for various values of radius ratio a/b for $G = 1 + \mathrm{i}$. For lower wavenumber range, higher values of a/b give higher dimensionless hydrodynamic force. It is observed that the force increases first and then decreases when $k_0 h$ increases.

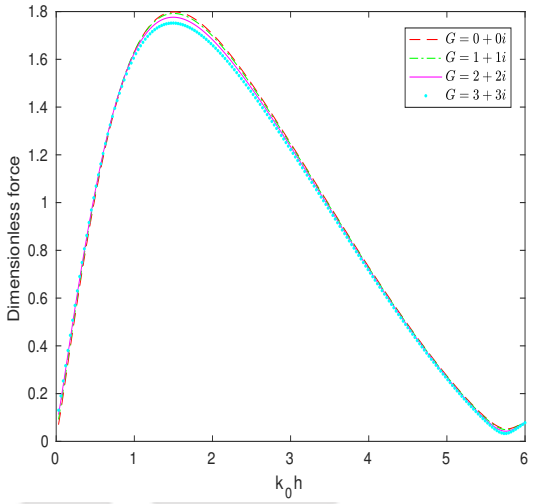

Figure 5.5: Dimensionless hydrodynamic force at $r = b$ against the wavenumber corresponding to different values of G for $a/b = 1/2$

In Figure 5.5, the dimensionless hydrodynamic force $\dfrac{|\tilde{F}_x^2|}{|\rho g b h H|}$ acting on the outer cylinder at $r = b$ are plotted corresponding to different values of G for $a/b = 1/2$. It shows that the wave force increases as the breakwater porosity (i.e., real and imaginary parts of porous coefficient) decreases.

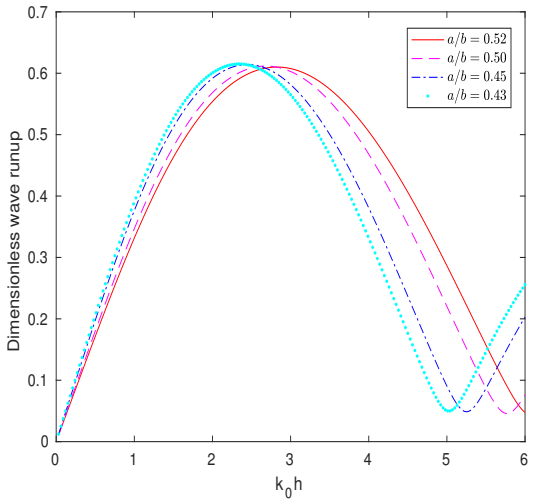

Figure 5.6: Dimensionless wave run-up at $r = b$ against the wavenumber corresponding to different values of a/b for $G = 1 + \mathrm{i}$

Figure 5.6 shows the plot of dimensionless wave run-up $|\zeta_1(b, \theta)|/H$ acting on the outer cylinder at $r = b$ corresponding to different values of a/b for $G = 1 + \mathrm{i}$. It is observed that

as the value of a/b increases, the peak value shifts towards right, i.e., for a bigger inner cylinder which though still follows $a < b$.

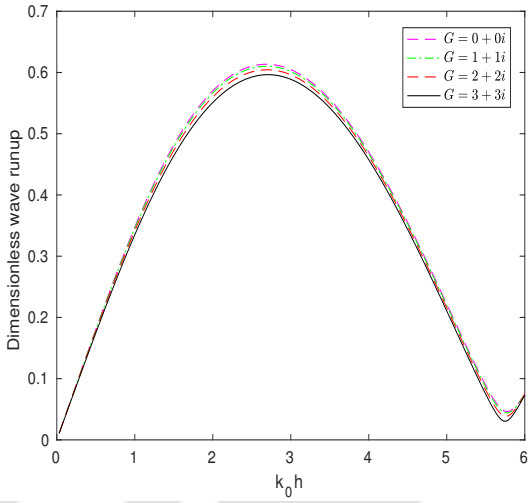

Figure 5.7: Dimensionless wave run-up at $r = b$ against the wavenumber corresponding to different values of G for $a/b = 1/2$

In Figure 5.7, the dimensionless wave run-up $|\zeta_1(b, \theta)|/H$ acting on the outer cylinder at $r = b$ is plotted corresponding to different values of porous coefficient G with $a/b = 1/2$. The maximum run-up occurs for $G = 0$, i.e., when the outer cylinder is assumed impermeable.

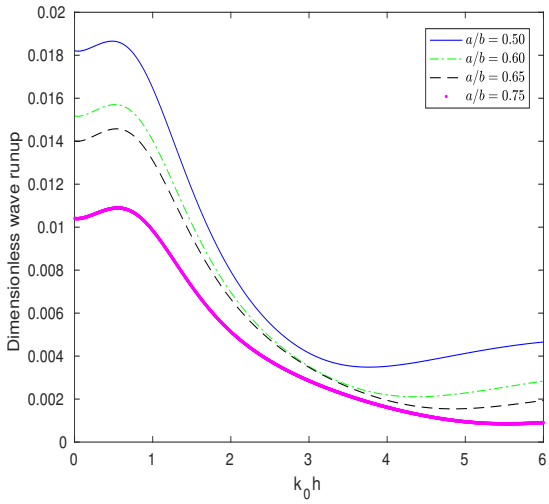

Figure 5.8: Dimensionless wave run-up at $r = a$ against the wavenumber corresponding to different values of a/b for $G = 1 + \mathrm{i}$

In Figure 5.8, the dimensionless wave run-up $|\zeta_2(a, \theta)|/H$ at $r = a$ is plotted against the wavenumber corresponding to different values of a/b for $G = 1 + \mathrm{i}$. The occurrence of the maximum run-up is noticed corresponding to smaller values of a/b. Further, it is

seen that for $k_0h < 1$, the wave run-up on the interior cylinder decreases for increasing values of a/b.

Figure 5.9 shows the plots of the dimensionless wave run-up $|\zeta_2(a,\theta)|/H$ at $r = a$ against the wavenumber corresponding to different values of G for $a/b = 1/2$. It is clear from the figure that the wave run-up increases as G increases. This shows that the porosity of the structure has reasonable impact on the wave run-up.

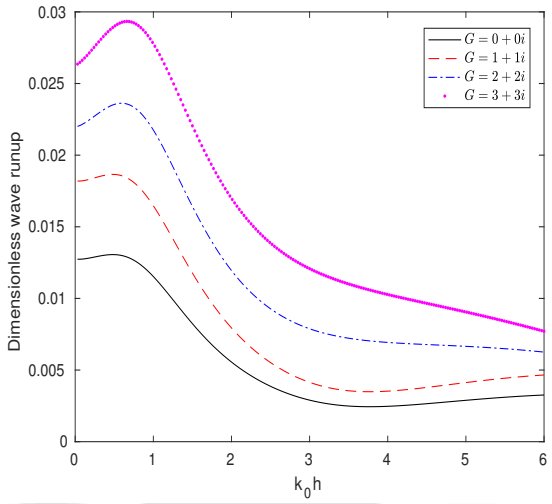

Figure 5.9: Dimensionless wave run-up at $r = a$ against the wavenumber corresponding to different values of G for $a/b = 1/2$

5.5 Mathematical formulation for a thin hollow porous cylinder with an impermeable cylinder at the bottom

It is clear that the model under consideration in the previous sections is based on consideration of a semi-porous storage tank of which the inner part contains an impermeable cylinder and the outer part contains a thin hollow porous cylinder with both being bottom-mounted. Now in this case, a similar structure is considered but it is now not bottom-mounted, and is placed on an impermeable solid coaxial cylinder of the same radius. Like our earlier problem, upon evaluation of the potentials, the hydrodynamic force and wave run-up acting on the inner part and outer part of the cylinder are computed. The effect of radius ratio a/b and porous coefficient G on hydrodynamic force and wave run-up is discussed. Further, the results of the earlier case and this case are compared. As per the requirement for this problem, the fluid domain is split into two regions as shown in Figure 5.10: Region I $(r \geq b, -h_2 \leq z \leq 0)$ and Region II $(a \leq r \leq b, -h_1 \leq z \leq 0)$.

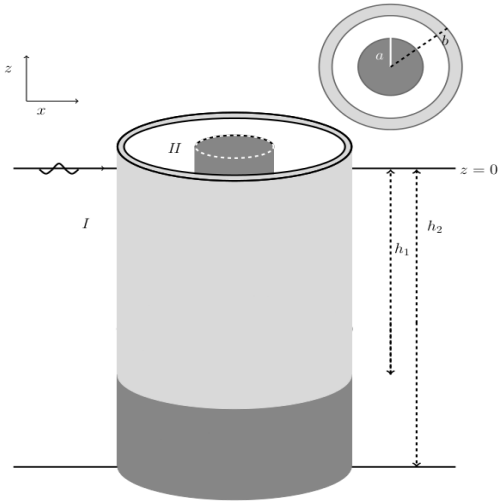

Figure 5.10: Schematic diagram of the structure mounted on a rigid cylinder

Further, following the properties of flow of potential kind, potentials for these regions satisfy Laplace's equation, namely,

$$\nabla^2\phi_j = 0, \quad j = 1, 2, \tag{5.21}$$

where $\phi_j, \quad j = 1, 2$ denotes the potentials in Regions I and II, respectively. The free surface condition can be considered as equation (5.1) of our earlier problem along with the following sea-bed condition:

$$\frac{\partial\phi_1}{\partial z} = 0; \quad z = -h_2, \quad r > b. \tag{5.22}$$

The body boundary conditions on the impermeable surfaces of both cylinders are

$$\frac{\partial\phi_2}{\partial r} = 0; \quad r = a, \quad -h_1 < z < 0, \tag{5.23}$$

$$\frac{\partial\phi_1}{\partial r} = 0; \quad r = b, \quad -h_2 < z < h_1, \tag{5.24}$$

$$\frac{\partial\phi_2}{\partial z} = 0; \quad z = -h_1, \quad a < r < b. \tag{5.25}$$

The boundary conditions for $r = b, -h_1 < z < 0$ on the porous cylindrical wall remain the same as equations (5.4) and (5.5).
Also, the Sommerfeld radiation condition for the exterior region is same as equation (2.15). The velocity potential in Region I takes the form

$$\phi_1(r,\theta,z) = -\frac{igH}{\omega}\left[\sum_{m=0}^{\infty}\tau_m J_m(k_0 r)\cos m\theta Z_0^{(1)}(k_0 z) + \sum_{m=0}^{\infty}\cos m\theta\sum_{j=0}^{\infty}D_{mj}Z_j^{(1)}(k_j z)U_m^{(4)}(k_j r)\right], \tag{5.26}$$

(5.27)

where D_{mj} are the unknown coefficients. Wavenumbers k_j $(j = 0, 1, 2, 3, \ldots)$ are found by solving the following dispersion relations:

$$\omega^2 = \begin{cases} gk_j \tanh k_j h_2; & j = 0, \\ -gk_j \tan k_j h_2; & j \geqslant 1. \end{cases}$$

$U_m^{(4)}(k_j r)$, the radial eigenfunctions, are given by

$$U_m^{(4)}(k_j r) = \begin{cases} \frac{H_m^{(1)}(k_j r)}{H_m^{(1)'}(k_j b)}; & j = 0, \\ \frac{K_m(k_j r)}{K_m'(k_j b)}; & j \geqslant 1. \end{cases}$$

The depth eigenfunctions $Z_j(k_j z)$ have the following form:

$$Z_j^{(1)}(k_j z) = \begin{cases} \frac{\cosh k_j(z+h_2)}{\cosh k_j h_2}; & j = 0, \\ \frac{\cos k_j(z+h_2)}{\cos k_j h_2}; & j \geqslant 1. \end{cases}$$

The scattered velocity potential ϕ_2 is found to be

$$\phi_2(r, \theta, z) = -\frac{igH}{\omega}\left[\sum_{m=0}^{\infty} \cos m\theta \sum_{j=0}^{\infty} (E_{mj} U_m^{(5)}(\lambda_j r) + F_{mj} U_m^{(6)}(\lambda_j r)) Z_j^{(2)}(\lambda_j z)\right], \quad (5.28)$$

where E_{mj} and F_{mj} are the unknown coefficients. The radial eigenfunctions $U_m^{(5)}(\lambda_j r)$ and $U_m^{(6)}(\lambda_j r)$ are as follows:

$$U_m^{(5)}(\lambda_j r) = \begin{cases} \frac{H_m^{(1)}(\lambda_j r)}{H_m^{(1)'}(\lambda_j b)}; & j = 0, \\ \frac{I_m(\lambda_j r)}{I_m'(\lambda_j b)}; & j \geqslant 1, \end{cases}$$

$$U_m^{(6)}(\lambda_j r) = \begin{cases} \frac{H_m^{(2)}(\lambda_j r)}{H_m^{(2)'}(\lambda_j b)}; & j = 0, \\ \frac{K_m(\lambda_j r)}{K_m'(\lambda_j b)}; & j \geqslant 1. \end{cases}$$

Wavenumbers λ_j, $j = 0, 1, 2, 3, \ldots$, are found by solving

$$\omega^2 = \begin{cases} gk_j \tanh \lambda_j h_1; & j = 0, \\ -gk_j \tan \lambda_j h_1; & j \geqslant 1. \end{cases}$$

The vertical eigenfunctions $Z_j^{(2)}(\lambda_j z)$ are defined as

$$Z_j^{(2)}(\lambda_j z) = \begin{cases} \frac{\cosh \lambda_j (z+h_1)}{\cosh \lambda_j h_1}; & j = 0, \\ \frac{\cos \lambda_j (z+h_1)}{\cos \lambda_j h_1}; & j \geqslant 1. \end{cases}$$

5.6 Evaluation of the unknown coefficients

Here we use the same technique as followed in the earlier case to calculate the unknown coefficients.

5.7 Validation

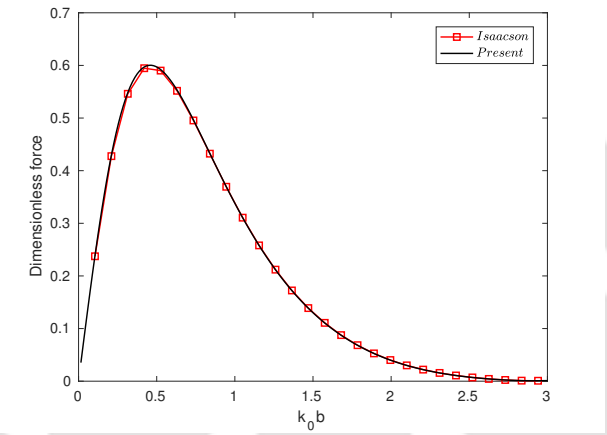

Figure 5.11: Comparison between present model and Isaacson's [19] model

A bottom-mounted compound cylinder is used to validate the present formulation, i.e., the porous parameter G is chosen as an infinite value in the present study, so that our model overlaps with that of Isaacson [19]. It may be noted that Ning et al. [38] also followed the same for comparison in their work. We consider a bottom-mounted compound cylinder corresponding to $G = 1 \times 10^{10} + \mathrm{i} \times 10^{10}, h_1/h_2 = 0.5, h_2/b = 2, a/b = 0.5$. Figure 5.11 depicts the hydrodynamic force acting on outer wall for both Isaacson's work and our work from which an excellent agreement is reached. In view of this, our model can be considered effective and hence can be utilized to study and analyze different aspects of various parameters for such problems.

5.8 Wave run-up and hydrodynamic force

Water wave run-up for both exterior and interior regions are the same as in the earlier case.

As usual, the total hydrodynamic forces in the direction of wave propagation for both the inner cylinder ($r = a$) and the outer cylinder ($r = b$) are be evaluated by carrying out integration of the pressure distribution on the structures. We define $\widehat{F}_x^j(t) = Re[\widehat{F}_x^j \exp(-\mathrm{i}\omega t)]$ for $j = 1, 2$ as

$$\widehat{F}_x^1 = \mathrm{i}\omega\rho \int_{-h_1}^{0} \int_{0}^{2\pi} \phi_2(a, \theta, z) \cos\theta \, \mathrm{d}z\mathrm{d}\theta, \tag{5.29}$$

$$\begin{aligned} \widehat{F}_x^2 &= \mathrm{i}\omega\rho \int_{-h_1}^{0} \int_{0}^{2\pi} \phi_2(b, \theta, z) \cos\theta \, \mathrm{d}z\mathrm{d}\theta \\ &- \mathrm{i}\omega\rho \int_{-h_1}^{0} \int_{0}^{2\pi} \phi_1(b, \theta, z) \cos\theta \, \mathrm{d}z\mathrm{d}\theta \\ &- \mathrm{i}\omega\rho \int_{-h_2}^{-h_1} \int_{0}^{2\pi} \phi_1(b, \theta, z) \cos\theta \, \mathrm{d}z\mathrm{d}\theta. \end{aligned} \tag{5.30}$$

5.9 Results and discussion

Here we discuss the effects of various parameters on the hydrodynamic force and wave run-up acting on the cylindrical structure. The results are presented graphically and the observations are analysed.

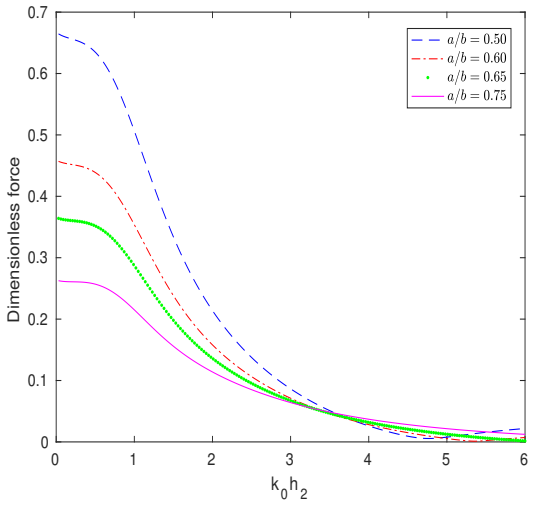

Figure 5.12: Dimensionless hydrodynamic force at $r = a$ against the wavenumber corresponding to different values of a/b for $G = 1 + \mathrm{i}$

In Figure 5.12, the dimensionless hydrodynamic force acting on the inner cylinder at $r = a$ is shown against the wavenumber corresponding to different values of radius ratio a/b for $G = 1 + \mathrm{i}$. The figure shows that the hydrodynamic force acting on the inner cylinder takes increasing values corresponding to a reduction in the values of the radius ratio. For decreasing values of a/b, more wave energy is concentrated in a confined region between the two cylinders. As a result, the force becomes higher which was also observed by Mandal et al. [26]. Figure 5.13 presents the hydrodynamic force acting on

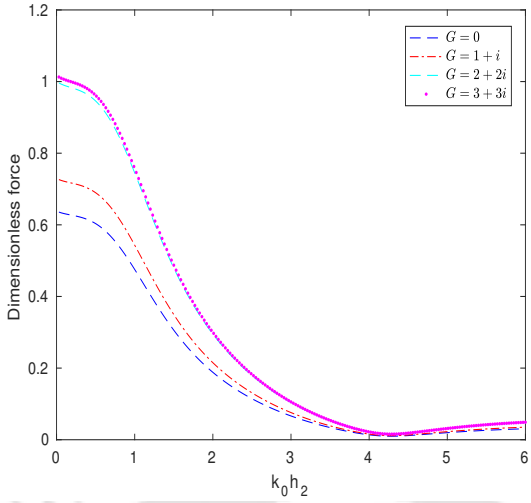

Figure 5.13: Dimensionless hydrodynamic force at $r = a$ against the wavenumber corresponding to different values of G for $a/b = 1/2$

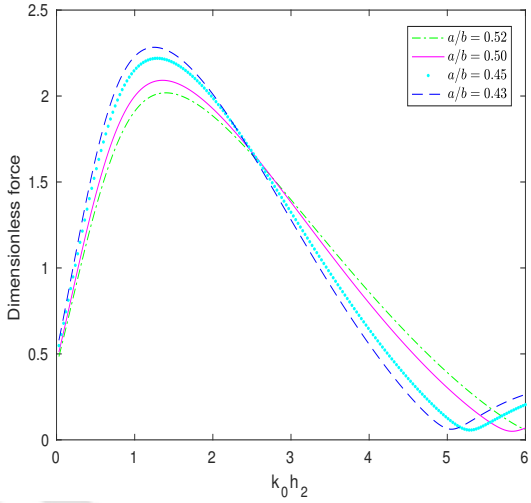

Figure 5.14: Dimensionless hydrodynamic force at $r = b$ against the wavenumber corresponding to different values of a/b for $G = 1 + \mathrm{i}$

the inner cylinder at $r = a$ against wavenumber corresponding to different values of G for $a/b = 1/2$. The figure shows that the wave force acting on the interior cylinder increases as the real and imaginary parts of G increase. As the value of $|G|$ increases, it allows more wave to pass through the structure. Therefore more amount of wave impinges on the inner cylindrical pile and the force becomes more pronounced. Comparing Figures 5.3 and 5.13, it is clearly noticed that the hydrodynamic force for this case (presence of impermeable cylinder at the bottom) is higher at $r = a$ than that in the earlier case. Figure 5.14 shows the dimensionless hydrodynamic force acting on the outer cylinder at $r = b$ corresponding to different values of radius ratio a/b for $G = 1+\mathrm{i}$. This force exhibits a monotonically increasing behaviour for wavenumber k_0h_2 and it attains a maximum in the range $1 < k_0h_2 < 2.3$, depending on the value of a/b. It is observed that the peak

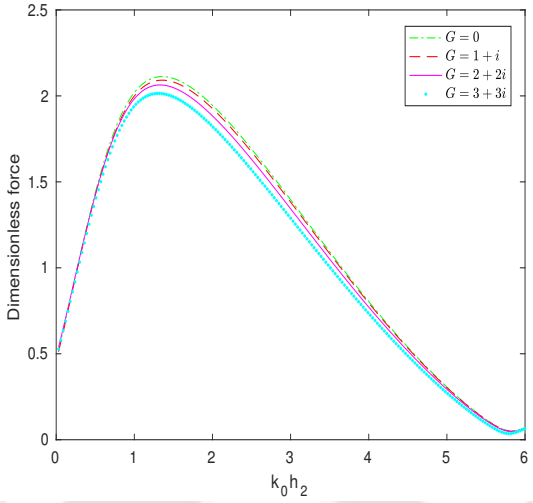

Figure 5.15: Dimensionless hydrodynamic force at $r = b$ against the wavenumber corresponding to different values of G for $a/b = 1/2$

value occurs for the lower values of radius ratio a/b. For certain values of k_0h_2, waveload on the outer cylinder becomes very low and it creates turning points. This may be due to the interaction of incoming and scattered waves leading to destructive interference near the outer cylinder. This means that at these turning points, destructive interference occurs. This type of turning points was observed in Mandal et al. [26] too. Similarly at the maximum points, constructive interference occurs. In the neighbourhood of $k_0h_2 = 1.6$, a spike of decreasing magnitude is observed in the amplitude of the wave force. This force spike is associated with the resonant frequencies of the wave. Similar observation in some of the latter figures in this work can also be attributed to the same phenomenon of resonance as observed in Darwiche et al. [10] too. It is already mentioned in Chapter 4 how the zeros of the derivatives of various kinds of Bessel functions correspond to the standing waves near the wall.

Figure 5.15 shows the plots of the dimensionless hydrodynamic force at $r = b$ against the wavenumber corresponding to different values of G for $a/b = 1/2$. The dimensionless hydrodynamic force acting on the outer cylinder attains the peak value for $G = 0$, i.e., when the outer wall is assumed to be impermeable. As the value of $|G|$ increases, though it allows more wave to pass through the structure, at the same time it reduces the outer porous cylinder resistance to the wave motion. Thus, with a reduction in the value of $|G|$, the force acting at $r = b$ increases. Figure 5.16 shows the dimensionless wave run-up at $r = b$ plotted against the wavenumber corresponding to different values of radius ratio a/b for a fixed depth with $G = 1 + \mathrm{i}$. The peak value of the wave run-up gets shifted towards the right which may be due to the phase shift of the wave as the radius ratio of the cylindrical system changes. Figure 5.17 shows the plots of wave run-up acting on the outer cylinder at $r = b$ against wavenumber corresponding to different values of G for $a/b = 1/2$. Similar type of wave pattern can be noticed here too (i.e., the wave run-up

first increases and then decreases). The run-up becomes higher for $G = 0$, that is, for the case when the outer wall is assumed to be impermeable. Figure 5.18 presents the wave run-up acting on the inner cylinder at $r = a$ corresponding to different values of G for $a/b = 1/2$. Turning points are visible in the neighborhood of $k_0h_2 = 4.2$, which corresponds to destructive interference. Comparing Figures 5.9 and 5.18, it is evident that for the earlier case, the wave run-up is not as pronounced as that in this case (presence of an impermeable cylinder at the bottom).

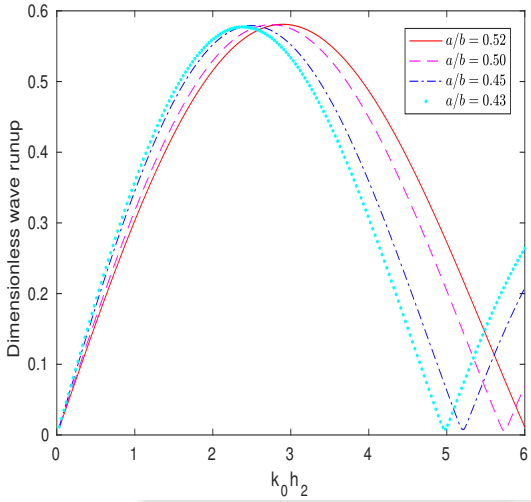

Figure 5.16: Dimensionless wave run-up at $r = b$ against the wavenumber corresponding to different values of a/b for $G = 1 + \mathrm{i}$

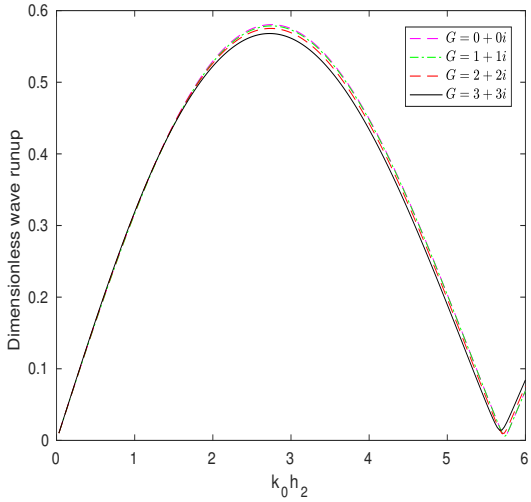

Figure 5.17: Dimensionless wave run-up at $r = b$ against the wavenumber corresponding to different values of G corresponding to $a/b = 1/2$

From Figures 5.19 and 5.20, it is observed that the hydrodynamic force experienced by the second model is higher than the first model for the same depth. This may be due to the presence of an impermeable solid coaxial cylinder of the same radius for which the

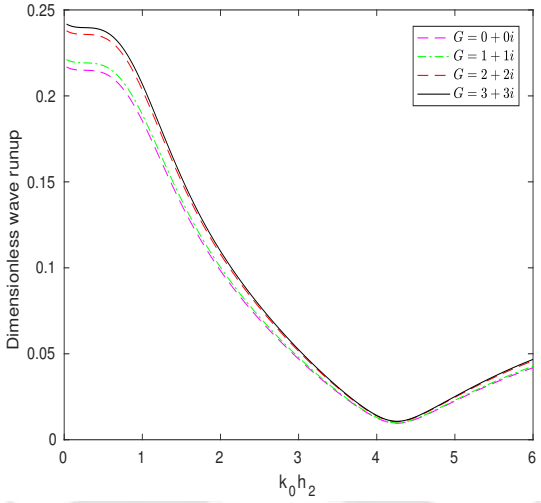

Figure 5.18: Dimensionless wave run-up at $r = a$ against the wavenumber corresponding to different values of G corresponding to $a/b = 1/2$

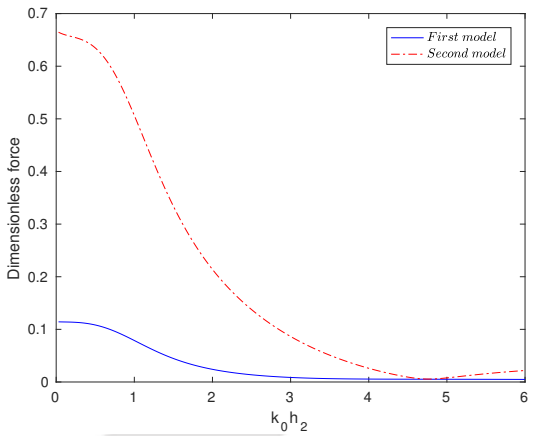

Figure 5.19: Comparison of first model and second model for dimensionless hydrodynamic force at $r = a$ ($G = 1$, $a/b = 0.50$ and same depth)

wave force concentration is more on the free surface for the second model than that for the first model.

An important and interesting observation for both works is that the wave force on the inner cylinder does not approach zero even when the wavenumber approaches zero. For a fixed frequency, $k = 0$ physically means that the wavelength is so large that the water surface would apparently seem to breathe which means that it will rise up and go down according to the given frequency. High frequency implies that the up-and-down movement will be quick while it is the opposite for low frequency. This subsequent motion does not affect much in the open sea (corresponding to high frequency it may show some positive values of the wave force on the outer cylinder but very unlikely for low frequency) implying zero wave force on the outer cylinder. However, in a confined region, it affects just like sloshing and hence the up-and-down motion surely has a significant effect on the

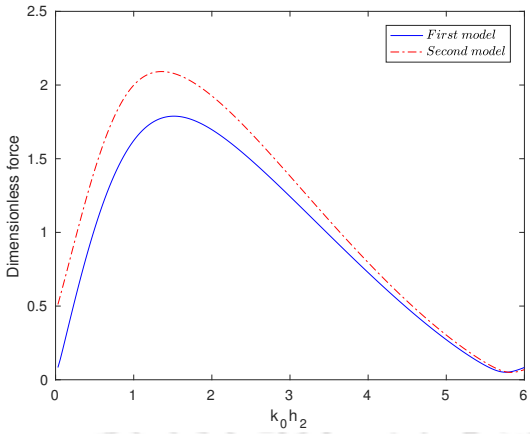

Figure 5.20: Comparison of first model and second model for dimensionless hydrodynamic force at $r = b$ ($G = 1$, $a/b = 0.50$ and same depth)

inner region and, consequently, on the wall of the inner cylinder.

5.10 Conclusion

In this chapter, we discuss diffraction of linear waves around a semi-porous cylindrical storage tank in finite depth. The tank consists of an inner solid cylindrical pile and a coaxial thin hollow porous cylinder of greater radius. Here we discuss two cases: (i) the storage tank being bottom-mounted, and (ii) the storage tank placed on an impermeable bottom-mounted coaxial solid cylinder. The problem is solved through a simple model based on the linear theory of wave propagation over a flat impermeable bottom. An eigenfunction expansion method and separation of variables technique are employed for solving these problems. These works are mainly based on the idea and information obtained from the projects "Mar de Trafalgar" in Spain and "A Pioneer Project of Aquaculture-Wind Farm Multi-Uses" in German North Sea, the aim of which includes a plan to integrate aquaculture, i.e., construction of multi-use sites in the open ocean. The objective of constructing and erecting such structures in oceans is to utilize a storage tank surrounding the cylindrical pile of the aerogenerators for aquaculture. In this work, by solving the appropriate problem, the dimensionless hydrodynamic force and wave run-up are calculated. Thereafter the effects of the various useful parameters on the hydrodynamic forces and wave run-up are investigated. This is likely to give some useful and important information for designing of appropriate and efficient structure. It is found that the porous parameter G has a very dominating effect on the hydrodynamic loads acting on such porous structures. When compared with an impermeable cylinder (that is for $G = 0$), the wave run-up on the outer part of the cylinder (Figures 5.7 and 5.17) gets reduced significantly for both the cases. From Figure 5.6 it is clear that for certain values of k_0h maximum and minimum wave run-up occur. These happen due to the constructive and destructive interference, respectively. It is observed that for the storage tank containing

an impermeable cylinder at the bottom, the hydrodynamic force acting at $r = b$ increases (Figures 5.5 and 5.15) for decreasing values of the porous coefficient, i.e., for a reduction in the values of the real and imaginary parts of G. Overall, by comparing Figures 5.3 and 5.13, it is observed that the hydrodynamic force for the first case is less at $r = a$ than that for the second case. Validation of current result obtained by comparing with that of Isaacson [19] shows a similar pattern from which it may be concluded that it will be worthwhile to consider the current model. Taking into consideration the hydrodynamic force and wave run-up obtained for both the cases under different conditions, it is expected that the results derived here can be utilized in getting reasonable benefit from a practically designed structure.

CHAPTER 6

Hydrodynamic Coefficients for a Floating Semi-Porous Compound Cylinder in Finite Ocean Depth

This chapter describes an investigation carried out on radiation of a floating surface-piercing semi-porous compound cylinder in water of finite depth. Since all motions are not very significant, we discuss only two translational motions in the x- and z-directions, i.e., surge and heave motions, respectively. We split the region into four and find the respective potentials by utilizing the given conditions. For accomplishing this, suitable matching conditions, due to continuity of pressure and velocity, along the vertical boundaries are applied to derive and solve a system of linear equations. Evaluation of those radiated potentials allows us to calculate the hydrodynamic coefficients, namely, added mass and damping coefficients, due to the motion of the structure. These coefficients play a crucial role for a structure in motion, however small it may be. Added mass and damping coefficient for surge and heave motions are obtained for different values of radii, draft, porosity and depth ratios. This work can be considered as an extension of the work carried out in Chapter 4 in which only diffraction for the same configuration was discussed. Further, the present model is validated against an available result in the literature and an excellent agreement is observed.

6.1 Mathematical formulation

It is known that a rigid floating structure in ocean can undergo six degrees of freedom: three translational motions in the x-, y- and z-directions, known as surge, sway and heave, respectively, and three rotational motions about the x-, y- and z-axes, known as roll, pitch and yaw, respectively. Considering the fluid to be incompressible, homogenous and inviscid, and the motion irrotational, a train of waves of small amplitude is assumed

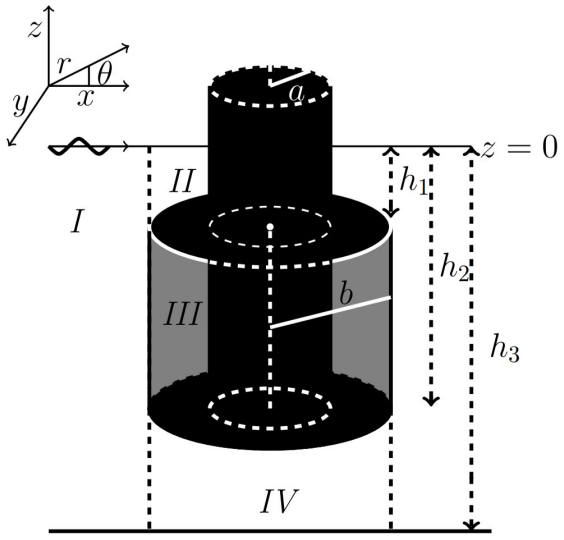

Figure 6.1: Floating surface-piercing semi-porous compound cylinder

to be incident on a vertical floating surface-piercing semi-porous compound cylinder with its porous region having a porous coefficient G. The upper surface and the lower surface of the lower cylinder are located at $z = -h_1$ and $z = -h_2$, respectively, where the z-axis is considered vertically upwards (Figure 6.1). Here we plan to discuss surge and heave radiation by the cylinder for a wave of amplitude H incident on it where the finite depth of water is h_3. Let a and $b(> a)$ be, respectively, the radii of inner and outer cylinders. Taking cylindrical coordinate system (r, θ, z) and due to physical considerations and convenience, we consider the following four regions: Region I $(r \geq b, -h_3 \leq z \leq 0)$; Region II $(a \leq r \leq b, -h_1 \leq z \leq 0)$; Region III $(a \leq r \leq b, -h_2 \leq z \leq -h_1)$ and Region IV $(0 \leq r \leq b, -h_3 \leq z \leq -h_2)$. Further, we introduce the velocity potentials $\Phi_j(r, \theta, z, t)$ as $\Phi_j(r, \theta, z, t) = \mathrm{Re}[\phi_j(r, \theta, z) \exp(-\mathrm{i}\omega t)]$ with $\phi_j,\ j = 1, 2, 3, 4$ referring to the potentials in Regions I, II, III and IV, respectively.

Each potential $\phi_j,\ j = 1, 2, 3, 4$, satisfies Laplace's equation in respective flow regions:

$$\nabla^2 \phi_j = 0, \quad j = 1, 2, 3, 4. \tag{6.1}$$

Subsequently, the boundary conditions on the free surface $z = 0$ and the sea-bed $z = -h_3$ can be written as

$$\frac{\partial \phi_j}{\partial z} - \frac{\omega^2}{g}\phi_j = 0; \quad z = 0, \quad j = 1, 2, \tag{6.2}$$

$$\frac{\partial \phi_1}{\partial z} = 0; \quad z = -h_3, \quad r > b, \tag{6.3}$$

$$\frac{\partial \phi_4}{\partial z} = 0; \quad z = -h_3, \quad 0 < r < b. \tag{6.4}$$

The boundary conditions on the moving solid surface (S_s) and porous surface (S_p) of the

structure are given by Williams et al. [60] as

$$\frac{\partial \phi}{\partial n} = \vec{v}.\vec{n} \quad \text{on} \quad S_s, \tag{6.5}$$

$$\frac{\partial \phi}{\partial n} = \vec{v}.\vec{n} - w(r,\theta,z) \quad \text{on} \quad S_p, \tag{6.6}$$

where $\vec{v}$ is the structural velocity, $\vec{n}$ is the outward normal to the surface (S_s or S_p), and $w(r,\theta,z)$ is the spatial component of the normal velocity $W(r,\theta,z,t)$ of the fluid passing through the semi-porous cylinder from the exterior region to the interior region with $W(r,\theta,z,t)$ given by

$$W(r,\theta,z,t) = \mathrm{Re}[w(r,\theta,z)\exp(-\mathrm{i}\omega t)]. \tag{6.7}$$

The fluid flow through the porous walls obeys Darcy's law. Therefore, the flow velocity is linearly proportional to the pressure difference across the boundary of the porous cylinder as can be seen from Taylor [52]. The hydrodynamic pressure

$$P(r,\theta,z,t) = \mathrm{Re}[p(r,\theta,z)\exp(-\mathrm{i}\omega t)]$$

at any point in the fluid domain can be deduced from the linearized Bernoulli's equation as $p = \mathrm{i}\rho\omega\phi$, where ρ is the fluid density. Therefore, the boundary condition at the porous wall $r = b$ can be written as

$$w(r,\theta,z) = \frac{L\mathrm{i}\rho\omega}{\varepsilon}(\phi_1 - \phi_3) = \mathrm{i}k_0 G(\phi_1 - \phi_3), \tag{6.8}$$

where ε is the coefficient of dynamic viscosity, k_0 the incident wavenumber, L a coefficient having the dimension of length, and ϕ_1 and ϕ_3, respectively, are the velocity potentials in the fluid region $r > b$ and porous region $b < r < a$.

Furthermore, the radiated velocity potential in the exterior region satisfies the Sommerfeld radiation condition in the following form:

$$\lim_{r\to\infty} \sqrt{r}\left[\frac{\partial \Psi^m_{\mathrm{rad},1}}{\partial r} - \mathrm{i}k_0 \Psi^m_{\mathrm{rad},1}\right] = 0, \text{ for } m = 1, 2, \tag{6.9}$$

where $\Psi^m_{\mathrm{rad},1}$ is the radiated potential in the m-th mode in Region I. On the porous cylinder surface $r = b$, the potentials satisfy the following matching conditions:

$$\phi_1 = \phi_2; \quad r = b, \quad -h_1 < z < 0, \tag{6.10}$$

$$\frac{\partial \phi_1}{\partial r} = \frac{\partial \phi_2}{\partial r}; \quad r = b, \quad -h_1 < z < 0, \tag{6.11}$$

$$\frac{\partial \phi_1}{\partial r} = \frac{\partial \phi_3}{\partial r}; \quad r = b, \quad -h_2 < z < -h_1, \tag{6.12}$$

$$\phi_1 = \phi_4; \quad r = b, \quad -h_3 < z < -h_2, \tag{6.13}$$

$$\frac{\partial \phi_1}{\partial r} = \frac{\partial \phi_4}{\partial r}; \quad r = b, \quad -h_3 < z < -h_2. \tag{6.14}$$

6.2 Radiated potentials in the sub-domains

The total velocity potential can be decomposed into incident and radiated components as follows:

$$\phi_j = \delta_j \phi_{\text{inc}} + \sum_{m=1}^{2} \beta_m \Psi^m_{\text{rad},j}, \tag{6.15}$$

where $\delta_1 = 1$ and $\delta_j = 0$, for $j = 2, 3, 4$, β_m is the structural displacement in the m-th mode and $\Psi^m_{\text{rad},j}$ is the radiation potential in the m-th mode in the j-th region. The radiation modes are numbered in such a way that $m = 1, 2$ correspond to surge and heave motions, respectively. The incident potential is given by

$$\phi_{\text{inc}} = -\frac{igH}{\omega} \frac{\cosh k_0(z + h_3)}{\cosh k_0 h_3} \sum_{n=0}^{\infty} \tau_n J_n(k_0 r) \cos n\theta, \tag{6.16}$$

with

$$\tau_n = \begin{cases} 1 & n = 0, \\ 2\mathrm{i}^n & n \geq 1. \end{cases}$$

Using eigenfunction expansion method, as in Calisal and Subancu [5], the radiated velocity potential in Region I takes the following form:

$$\Psi^m_{\text{rad},1}(r, \theta, z) = \sum_{j=0}^{\infty} A^m_j \cos k_j(z + h_3) T^m_j(k_j r) \cos \nu\theta, \tag{6.17}$$

where $\nu = 1$ for $m = 1$ and $\nu = 0$ for $m = 2$, and A^m_j are the undetermined coefficients. The wavenumbers k_j $(j = 0, 1, 2, 3, \ldots)$ can be derived from the following dispersion relation by using the technique devised by Chamberlain and Porter [6]:

$$\sigma^2 = \begin{cases} gk_j \tanh k_j h_3; & j = 0, \\ -gk_j \tan k_j h_3; & j \geq 1. \end{cases}$$

The radial eigenfunctions $T^m_j(k_j r)$ have the following form:

$$T^m_j(k_j r) = \begin{cases} \frac{H^{(1)}_\nu(k_j r)}{H^{(1)'}_\nu(k_j b)}; & j = 0, \\ \frac{K_\nu(k_j r)}{K'_\nu(k_j b)}; & j \geq 1. \end{cases}$$

The radiated velocity potential in Region II satisfying the structural boundary conditions is given by (Wu et al. [61])

$$\Psi^m_{\text{rad},2}(r, \theta, z) = \sum_{j=0}^{\infty} [\{(B^m_j S^m_j(\lambda_j r) + C^m_j R^m_j(\lambda_j r)) \cos \lambda_j(z + h_1)\} + \Pi^m_2] \cos \nu\theta, \tag{6.18}$$

where B_j^m and C_j^m are the undetermined coefficients and Π_2^m represents the particular solution due to the dependent-mode. λ_j are obtained from the following expression:

$$\omega^2 = \begin{cases} g\lambda_j \tanh \lambda_j h_1; & j = 0, \\ -g\lambda_j \tan \lambda_j h_1; & j \geq 1. \end{cases}$$

The radial eigenfunctions $S_j^m(\lambda_j r)$ and $R_j^m(\lambda_j r)$ have the following forms:

$$S_j^m(\lambda_j r) = \begin{cases} \frac{H_\nu^{(1)}(\lambda_j r)}{H_\nu^{(1)'}(\lambda_j b)}; & j = 0, \\ \frac{I_\nu(\lambda_j r)}{I'_\nu(\lambda_j b)}; & j \geq 1, \end{cases} \qquad R_j^m(\lambda_j r) = \begin{cases} \frac{H_\nu^{(2)}(\lambda_j r)}{H_\nu^{(2)'}(\lambda_j b)}; & j = 0, \\ \frac{K_\nu(\lambda_j r)}{K'_\nu(\lambda_j b)}; & j \geq 1, \end{cases}$$

for $m = 1, 2$.

The term Π_2^m appearing in equation (6.18) has a very important role in permitting the radiated potentials to satisfy the otherwise difficult non-homogeneous boundary conditions on the body surface. In Region II, the particular solutions Π_2^m are as follows:

$$\Pi_2^1 = 0, \tag{6.19}$$

$$\Pi_2^2 = z + \frac{g}{\omega^2}. \tag{6.20}$$

The suitable expression for the radiated potential in Region III satisfying structural boundary conditions is (Wu et al. [61])

$$\Psi^m_{\text{rad},3}(r, \theta, z) = \sum_{j=0}^{\infty} [\{(D_j^m V_j^m(\mu_j r) + E_j^m W_j^m(\mu_j r)) \cos \mu_j (z + h_2)\} + \Pi_3^m] \cos \nu\theta, \tag{6.21}$$

where D_j^m and E_j^m are the undetermined coefficients, and μ_j can be obtained from the following:

$$\mu_j = \frac{\pi j}{h_2 - h_1}, \quad j = 0, 1, 2, \ldots.$$

The radial eigenfunctions $V_j^m(\mu_j r)$ and $W_j^m(\mu_j r)$ have the following forms:

$$V_j^m(\mu_j r) = \begin{cases} \frac{r^{-\nu}}{b^{-\nu-1}}; & j = 0, \\ \frac{K_\nu(\mu_j r)}{K'_\nu(\mu_j b)}; & j \geq 1, \end{cases} \qquad W_j^m(\mu_j r) = \begin{cases} \frac{r^{\nu}}{b^{\nu-1}}; & j = 0, \\ \frac{I_\nu(\mu_j r)}{I'_\nu(\mu_j b)}; & j \geq 1. \end{cases}$$

The particular solutions for Region III are as follows:

$$\Pi_3^1 = 0, \tag{6.22}$$

$$\Pi_3^2 = z. \tag{6.23}$$

The radiated velocity potential for Region IV is (Wu et al. [61])

$$\Psi^m_{\text{rad},4}(r,\theta,z) = \sum_{j=0}^{\infty}[F^m_j \cos\gamma_j(z+h_3)U^m_j(\gamma_j r) + \Pi^m_4]\cos\nu\theta, \tag{6.24}$$

where F^m_j are the undetermined coefficients and γ_j are obtained from the following expression:

$$\gamma_j = \frac{\pi j}{h_3 - h_2}, \quad j = 0, 1, 2, \ldots.$$

The radial eigenfunctions $U^m_j(\gamma_j r)$ have the following form:

$$U^m_j(\gamma_j r) = \begin{cases} \frac{r^\nu}{b^{\nu-1}}; & j = 0, \\ \frac{I_\nu(\gamma_j r)}{I'_\nu(\gamma_j b)}; & j \geq 1. \end{cases}$$

The particular solutions for Region IV are given by

$$\Pi^1_4 = 0, \tag{6.25}$$

$$\Pi^2_4 = \left[(z+h_3)^2 - \frac{r^2}{2}\right]\frac{1}{2(h_3-h_2)}. \tag{6.26}$$

6.3 Added mass and damping coefficient

The solution to the radiation problem for structures in motion in ocean yields the important hydrodynamic coefficients, i.e., added mass and damping coefficients. They are connected to the real and imaginary parts of the hydrodynamic reaction loads on the body arising due to prescribed body motions. The hydrodynamic force in the x- and z-directions (i.e., surge and heave) due to the motion of a cylinder in mode $m = 1, 2$ can be found out by carrying out integration of the corresponding pressure distribution over the cylinder surface. Non-dimensional surge added mass and damping coefficients can be obtained from the following (Calisal and Subancu [5]):

$$\begin{aligned} \chi_{11} + \mathrm{i}\frac{\Lambda_{11}}{\omega} &= \rho\int_{-h_1}^{0}\int_0^{2\pi}\Psi^m_2(a,\theta,z)a\cos\theta\,\mathrm{d}z\mathrm{d}\theta \\ &+ \rho\int_{-h_2}^{-h_1}\int_0^{2\pi}\Psi^m_3(a,\theta,z)a\cos\theta\,\mathrm{d}z\mathrm{d}\theta \\ &+ \rho\int_{-h_2}^{-h_1}\int_0^{2\pi}\Psi^m_1(b,\theta,z)b\cos\theta\,\mathrm{d}z\mathrm{d}\theta \\ &- \rho\int_{-h_2}^{-h_1}\int_0^{2\pi}\Psi^m_3(b,\theta,z)b\cos\theta\,\mathrm{d}z\mathrm{d}\theta. \end{aligned} \tag{6.27}$$

Similarly, non-dimensional heave added mass and damping coefficients are given by

(Calisal and Subancu [5]) as

$$\begin{aligned}\chi_{33}+\mathrm{i}\frac{\Lambda_{33}}{\omega} &= \rho\int_0^b\int_0^{2\pi}\Psi_4^m(-h_2,\theta,z)r\ \mathrm{d}r\mathrm{d}\theta\\ &- \rho\int_a^b\int_0^{2\pi}\Psi_3^m(-h_2,\theta,z)r\ \mathrm{d}r\mathrm{d}\theta\\ &- \rho\int_a^b\int_0^{2\pi}\Psi_2^m(-h_1,\theta,z)r\ \mathrm{d}r\mathrm{d}\theta\\ &+ \rho\int_a^b\int_0^{2\pi}\Psi_3^m(-h_1,\theta,z)r\ \mathrm{d}r\mathrm{d}\theta. \end{aligned}\tag{6.28}$$

6.4 Surge motion

6.4.1 Calculation of unknown coefficients

By applying the boundary condition for the surge motion ($m=1$) at $r=a$ for $-h_1<z<0$ and the orthogonality of the eigenfunctions, we get the following relationship between the potential coefficients B_α^1 and C_α^1 appearing in ϕ_2:

$$\left(S_\alpha^1(\lambda_j a)B_\alpha^1+R_\alpha^1(\lambda_j a)C_\alpha^1\right)\mathcal{R}_{\alpha\alpha} = \mathcal{A}_\alpha,\quad \alpha\geq 0.\tag{6.29}$$

Applying the matching conditions given by equations (6.10) and (6.11) for the depth $-h_1<z<0$, along with the orthogonality of the eigenfunctions, we obtain

$$\sum_{j=0}^{\infty}A_j^1T_j^1(k_jb)\mathcal{Q}_{\alpha j}-\left(B_\alpha^1S_\alpha^1(\lambda_\alpha b)+C_\alpha^1R_\alpha^1(\lambda_\alpha b)\right)\mathcal{R}_{\alpha\alpha} = \frac{\mathrm{i}gH}{\omega\cos k_0h_3}\tau_1J_1(k_0b)\mathcal{Q}_{\alpha0},\quad \alpha\geq 0,\tag{6.30}$$

$$\sum_{j=0}^{\infty}A_j^1T_j^{1'}(k_jb)\mathcal{Q}_{\alpha j}-\left(B_\alpha^1S_\alpha^{1'}(\lambda_\alpha b)+C_\alpha^1R_\alpha^{1'}(\lambda_\alpha b)\right)\mathcal{R}_{\alpha\alpha} = \frac{\mathrm{i}gH}{\omega\cos k_0h_3}\tau_1J_1'(k_0b)\mathcal{Q}_{\alpha0},\quad \alpha\geq 0.\tag{6.31}$$

Next, using equations (6.6) for the depth $-h_2<z<-h_1$, the matching condition (6.12) and the orthogonality of the eigenfunctions, we get

$$\begin{aligned}&\left(V_\alpha^{1'}(\mu_\alpha b)-\mathrm{i}k_0GV_\alpha^1(\mu_\alpha b)\right)D_\alpha^1\mathcal{N}_{\alpha\alpha}+\left(W_\alpha^{1'}(\mu_\alpha b)-\mathrm{i}k_0GW_\alpha^1(\mu_\alpha b)\right)E_\alpha^1\mathcal{N}\alpha\alpha\\ &+\ \mathrm{i}k_0G\sum_{j=0}^{\infty}A_j^1T_j^1(k_jb)\mathcal{P}_{\alpha j}=-\frac{\mathrm{i}gH}{\omega\cos k_0h_3}\tau_1J_1(k_0b)\mathcal{P}_{\alpha0}+\mathcal{B}_\alpha\quad \alpha\geq 0,\end{aligned}\tag{6.32}$$

$$\left(D_\alpha^1V_0^{1'}(\mu_\alpha b)+E_\alpha^1W_\alpha^{1'}(\mu_\alpha b)\right)\mathcal{N}_{\alpha\alpha}-\sum_{j=0}^{\infty}A_j^1T_j^{1'}(k_jb)\mathcal{P}_{\alpha j} = -\frac{\mathrm{i}gH}{\omega\cos k_0h_3}\tau_1\mathcal{P}_{\alpha0}J_1'(k_0b),$$

$$\alpha \geq 0. \tag{6.33}$$

Further, from the matching condition given by equation (6.14) across the boundary $r = b$ in the interval $-h_3 < z < -h_2$, and using the orthogonality of the eigenfunctions, we get

$$\sum_{j=0}^{\infty} A_j^1 T_j^{1'}(k_j b)\mathcal{S}_{\alpha j} - F_\alpha^1 U_0^{1'}(\gamma_\alpha b)\mathcal{L}_{\alpha\alpha} = \frac{\mathrm{i}gH}{\omega \cos k_0 h_3}\tau_1 J_1'(k_0 b)\mathcal{S}_{\alpha 0}, \quad \alpha \geq 0, \tag{6.34}$$

where,

$$\mathcal{Q}_{\alpha,j} = \int_{-h_1}^{0} \cos\lambda_\alpha(z+h_1)\cos k_j(z+h_3)\mathrm{d}z, \tag{6.35}$$

$$\mathcal{R}_{\alpha,\alpha} = \int_{-h_1}^{0} \cos\lambda_\alpha(z+h_1)\cos\lambda_\alpha(z+h_1)\mathrm{d}z, \tag{6.36}$$

$$\mathcal{T}_{\alpha,\alpha} = \int_{-h_2}^{-h_1} \cos\mu_\alpha(z+h_2)\cos\mu_\alpha(z+h_2)\mathrm{d}z, \tag{6.37}$$

$$\mathcal{P}_{\alpha,j} = \int_{-h_2}^{-h_1} \cos\mu_\alpha(z+h_2)\cos k_j(z+h_3)\mathrm{d}z, \tag{6.38}$$

$$\mathcal{S}_{\alpha,j} = \int_{-h_3}^{-h_2} \cos\gamma_\alpha(z+h_3)\cos k_j(z+h_3)\mathrm{d}z, \tag{6.39}$$

$$\mathcal{L}_{\alpha,\alpha} = \int_{-h_3}^{-h_2} \cos\gamma_\alpha(z+h_3)\cos\gamma_\alpha(z+h_3)\mathrm{d}z, \tag{6.40}$$

$$\mathcal{A}_{\alpha} = \int_{-h_1}^{0} \cos\lambda_\alpha(z+h_1)\mathrm{d}z, \tag{6.41}$$

$$\mathcal{B}_{\alpha} = \int_{-h_2}^{-h_1} \cos\mu_\alpha(z+h_2)\mathrm{d}z. \tag{6.42}$$

In order to evaluate the hydrodynamic coefficients, it is required to find the unknown coefficients A_j^m, B_j^m, C_j^m, D_j^m, E_j^m and F_j^m. Truncating the infinite series given by equations (6.29)-(6.34) after some terms $N = 20$, the values of the coefficients are computed. As a consequence, the following linear system of algebraic equations is found for determining the unknown coefficients:

$$\mathcal{T}^d\mathcal{X}^d = \mathcal{Y}^d, \tag{6.43}$$

where,
$\mathcal{X}^d = [A_1^d, A_2^d, ..., A_N^d, B_1^d, B_2^d, ..., B_N^d, C_1^d, C_2^d, ..., C_N^d, D_1^d, D_2^d, ..., D_N^d, E_1^d, E_2^d, ..., E_N^d,$
$F_1^d, F_2^d, ..., F_N^d]^t$,
$\mathcal{T}^d$ are coefficient matrices and
$\mathcal{Y}^d$ are the right-hand vectors.

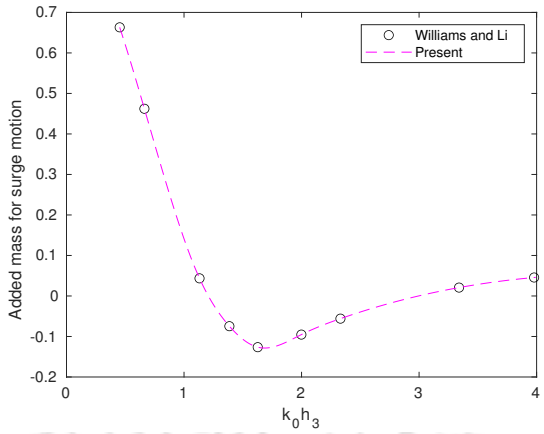

Figure 6.2: Comparison of surge added mass of present work with that of Williams and Li [58]

6.4.2 Validation of present model

To validate our present analytical model developed for solving the problem, we deem it suitable to compare one of the results with that of Williams and Li [58], i.e., when the cylinder is considered to be a floating compound cylinder (the curved surface of the bottom cylinder is considered impermeable). The relevant parameters in our problem are reconsidered conforming to the work of Williams and Li in order to convert to the same physical problem. Here we consider the values $G = 0$, $h_1/h_2 = 0.50$, $h_2/h_3 = 0.67$, $b/h_3 = 1$ and $a/b = 0.60$. Figure 6.2 presents an excellent agreement between both results for the dimensionless added mass for the surge motion of the cylinder. In view of this validation, our model can be considered to be efficient and hence can be utilized to study and analyze different aspects of various parameters for our subsequent experiments and also for such problems in general.

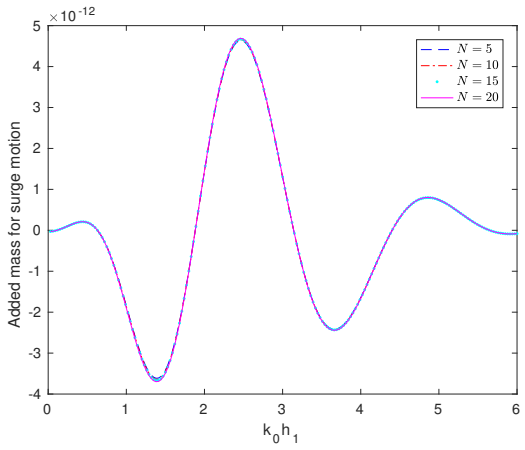

Figure 6.3: Convergence of added mass for surge motion against wavenumber corresponding to different values of N for $a/b = 1/2$, $h_1/h_2 = 1/2$, $h_2/h_3 = 1/2$ and $G = 1$

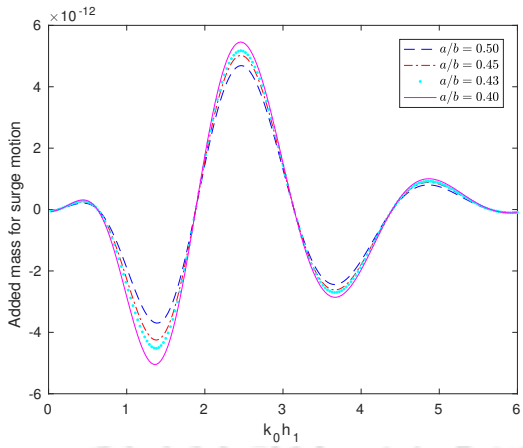

Figure 6.4: Added mass for surge motion against wavenumber corresponding to different values of a/b for $h_1/h_2 = 1/2$, $h_2/h_3 = 1/2$ and $G = 1$

6.4.3 Results and discussion

Here we discuss the effects of various parameters on the surge hydrodynamic coefficients acting on the cylindrical structure. The results are presented graphically and relevant observations are presented.

Figure 6.3 presents the convergence of added mass for surge motion with respect to N against wavenumber corresponding to different values of N for $a/b = 1/2$, $h_1/h_2 = 1/2$, $h_2/h_3 = 1/2$ and $G = 1$. It can easily be concluded from this figure that consideration of $N = 20$ provides satisfactory accuracy of evaluation of hydrodynamic coefficients and therefore, for all subsequent figures, $N = 20$ is to be considered whenever the requirement arises.

In Figure 6.4, the non-dimensionalized added mass χ_{11} for surge motion against wavenumber is discussed corresponding to different values of radius ratio a/b corresponding to $h_1/h_2 = 1/2$, $h_2/h_3 = 1/2$ and $G = 1$. It is observed that added mass oscillates alternately between negative and positive values for increasing values of k_0h_1. This type of added mass is also observed in the works of McIver and Evans [32] and Wu et al. [61]. The amplitudes of the oscillation are higher in the range $2 < k_0h_1 < 3$. It is also observed that for decreasing a/b, i.e., when the radius of the inner cylinder tends to be much smaller compared to that of the outer porous cylinder, the added mass increases. It may have happened due to more energy concentration near the inner cylinder and thus resulting in an increase in added mass. Figure 6.5 shows the non-dimensionalized added mass χ_{11} for surge motion against wavenumber corresponding to different values of porous coefficient G for $h_1/h_2 = 1/2$, $h_2/h_3 = 1/2$ and $a/b = 1/2$. The observation is that the added mass are not significantly affected by G. One important observation is that added mass does not vary much for different smaller values of G, say, when we take $G = 0, 1, 2$. This is due to the fact that the added mass for the semi-porous cylinder depends on the potential coefficients A_j^m, B_j^m, C_j^m, D_j^m, E_j^m and F_j^m which do not change appreciably.

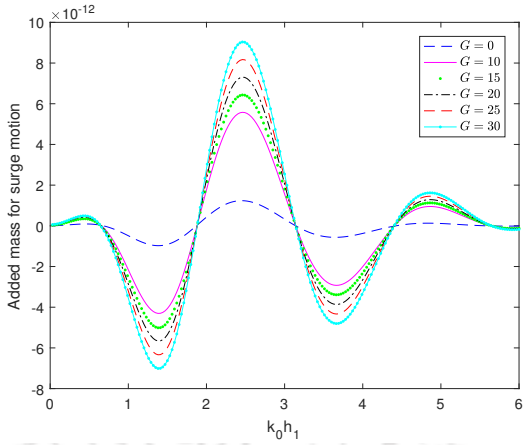

Figure 6.5: Added mass for surge motion against wavenumber corresponding to different values of G for $h_1/h_2 = 1/2$, $h_2/h_3 = 1/2$ and $a/b = 1/2$

Subsequently, this is the reason added mass do not get changed for such smaller values of porosity coefficient G. However, if we consider a large range of values of G from 0 to 30, then it is observed that, for increasing values of G, the oscillating behaviour of the graph becomes more pronounced. In Figure 6.6, the non-dimensionalized added mass χ_{11} for

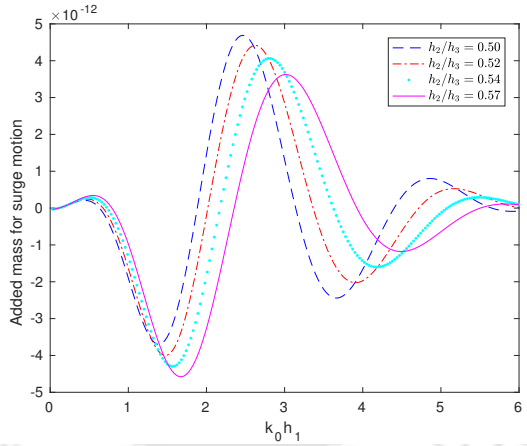

Figure 6.6: Added mass for surge motion against wavenumber corresponding to different values of h_2/h_3 for $h_1/h_2 = 1/2$, $a/b = 1/2$ and $G = 1$

surge motion against wavenumber is analyzed corresponding to different values of h_2/h_3 for $h_1/h_2 = 1/2$, $a/b = 1/2$ and $G = 1$. Similar pattern of graph is observed here just as in Figure 5.9. The amplitude of added mass becomes higher in $2 < k_0h_1 < 3$. The oscillation gets shifted towards left for decreasing values of h_2/h_3. There is a shift observed in the maxima of these curves which may be due to the phase shift of the wave when the draft of the cylindrical system changes. The non-dimensionalized added mass χ_{11} for surge motion against wavenumber corresponding to different values of h_1/h_2 for $h_2/h_3 = 1/2$, $a/b = 1/2$ and $G = 1$ are shown in Figure 6.7. The oscillation is observed to get shifted towards right for decreasing values of h_1/h_2. Figure 6.8 illustrates the non-dimensionalized

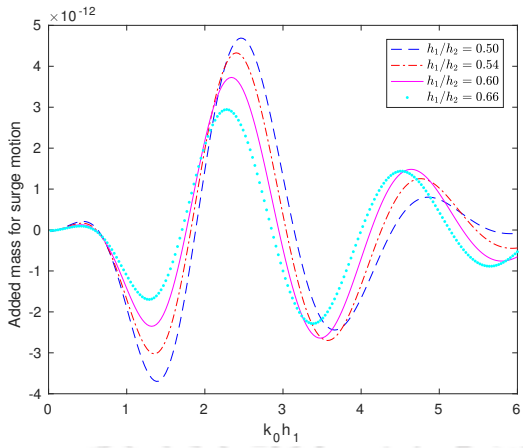

Figure 6.7: Added mass for surge motion against wavenumber corresponding to different values of h_1/h_2 for $h_2/h_3 = 1/2$, $a/b = 1/2$ and $G = 1$

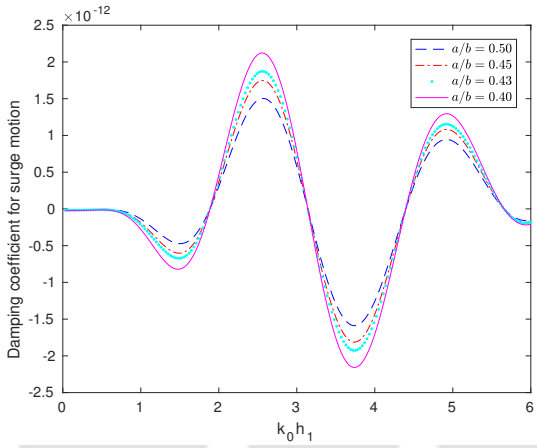

Figure 6.8: Damping coefficient for surge motion against wavenumber corresponding to different values of a/b for $h_1/h_2 = 1/2$, $h_2/h_3 = 1/2$ and $G = 1$

damping coefficient $\frac{\Lambda_{11}}{\omega}$ for surge motion against wavenumber corresponding to different values of radius ratio a/b for $h_1/h_2 = 1/2$, $h_2/h_3 = 1/2$ and $G = 1$. If a floating body is in motion in waves, then the motion in general involves six degrees of freedom. Negative damping coefficient usually appears in the so-called coupled terms. The motion in surge and yaw directions are always coupled which means that the surge motion is going to get influenced by the yaw motion. Therefore in the results, the yaw induced surge damping is negative which implies that it is not only added mass that can be negative, the occurrence of which is a quite familiar phenomenon, but damping coefficients can also take negative values under certain conditions. This type of phenomenon happens due to the coupled behaviour between different motions. Similarly the motion in heave and pitch are always coupled. In that case also, the added mass and damping coefficient may be negative. Here the damping coefficient oscillates alternately between negative and positive values. This type of behaviour of damping coefficient is also observed in the works of Wu et al. [61], Zheng and Zhang [66] and Zheng et al. [67]. The value of the damping coefficient be-

comes higher in $2 < k_0h_1 < 3$ and lower in $3.5 < k_0h_1 < 4$. Non-dimensionalized damping coefficient increases with decreasing radius ratio a/b, i.e., when the radius of the inner cylinder gets much smaller than that of the outer porous cylinder in $2 < k_0h_1 < 3$. The occurrence of maxima and minima for added mass for the structure may be due to the constructive and destructive interference between the incident and reflected waves.

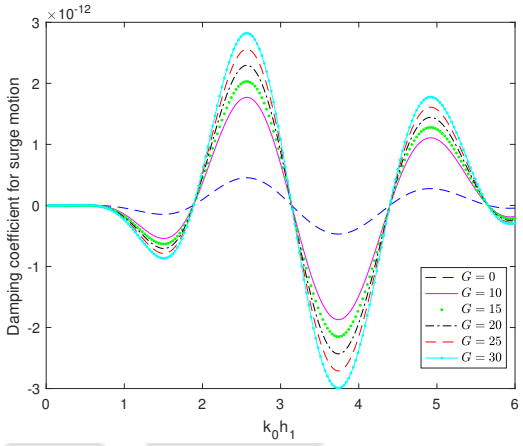

Figure 6.9: Damping coefficient for surge motion against wavenumber corresponding to different values of G for $h_1/h_2 = 1/2$, $h_2/h_3 = 1/2$ and $a/b = 1/2$

Figure 6.9 presents the non-dimensionalized damping coefficient $\frac{\Lambda_{11}}{\omega}$ for surge motion against wavenumber corresponding to different range of values of G for $h_1/h_2 = 1/2$, $h_2/h_3 = 1/2$ and $a/b = 1/2$. The behaviour of those curves is similar even when G takes different values. However, the variation is observed to be more pronounced for higher values of G. Similar type of behaviour as observed in Figure 6.5 for added mass is observed here too. Next, Figure 6.10 shows the non-dimensionalized damping coefficient

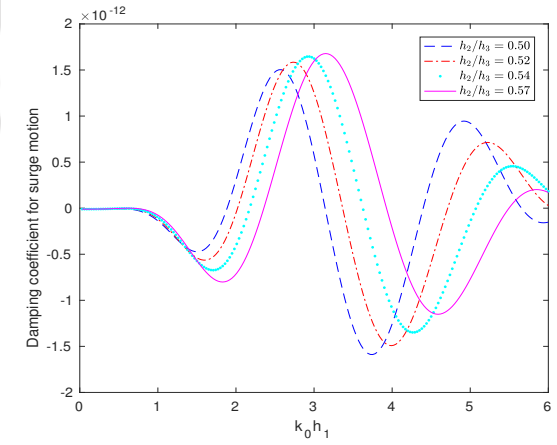

Figure 6.10: Damping coefficient for surge motion against wavenumber corresponding to different values of h_2/h_3 for $h_1/h_2 = 1/2$, $a/b = 1/2$ and $G = 1$

$\frac{\Lambda_{11}}{\omega}$ for surge motion against wavenumber corresponding to different values of h_2/h_3 for $h_1/h_2 = 1/2$, $a/b = 1/2$ and $G = 1$. In the lower wavenumber range for decreasing

values of h_2/h_3, amplitude of the damping coefficient is observed to get shifted towards left. In other words, this happens when the draft of the lower cylinder with respect to its lower surface is reduced which implies a position of the cylinder further away from the sea-bed. Figure 6.11 shows damping coefficient $\frac{\Lambda_{11}}{\omega}$ for surge motion against wavenumber

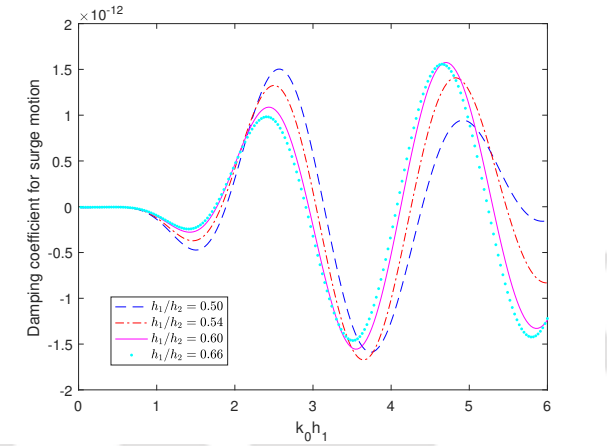

Figure 6.11: Damping coefficient for surge motion against wavenumber corresponding to different values of h_1/h_2 for $h_2/h_3 = 1/2$, $a/b = 1/2$ and $G = 1$

corresponding to different values of h_1/h_2 for $h_2/h_3 = 1/2$, $a/b = 1/2$ and $G = 1$. The oscillation is observed to get shifted towards right for decreasing values of h_1/h_2. In other words, this happens when the draft of the lower cylinder with respect to its upper surface is reduced which makes the cylinder closer to the free surface.

6.5 Heave motion

6.5.1 Calculation of unknown coefficients

Using the boundary condition for the heave motion ($m = 2$) at $r = a$ for $-h_1 < z < 0$ and the orthogonal property of the eigenfunctions, we get the following relationship between the potential coefficients B_α^2 and C_α^2 appearing in ϕ_2:

$$\left(S_\alpha^2(\lambda_j a)B_\alpha^2 + R_\alpha^2(\lambda_j a)C_\alpha^2\right)\mathcal{R}_{\alpha\alpha} = 0, \quad \alpha \geq 0. \tag{6.44}$$

Applying the matching conditions given by equations (6.10) and (6.11) for the depth $-h_1 < z < 0$, along with the orthogonality of the eigenfunctions, we obtain

$$\sum_{j=0}^{\infty} A_j^2 T_j^2(k_j b)\mathcal{Q}_{\alpha j} - \left(B_\alpha^2 S_\alpha^2(\lambda_\alpha b) + C_\alpha^2 R_\alpha^2(\lambda_\alpha b)\right)\mathcal{R}_{\alpha\alpha} = \frac{\mathrm{i}gH}{\omega \cos k_0 h_3}\tau_1 J_1(k_0 b)\mathcal{Q}_{\alpha 0} - \mathcal{C}_\alpha, \ \alpha \geq 0, \tag{6.45}$$

$$\sum_{j=0}^{\infty} A_j^2 T_j^{2'}(k_j b)\mathcal{Q}_{\alpha j} - \left(B_\alpha^2 S_\alpha^{2'}(\lambda_\alpha b) + C_\alpha^2 R_\alpha^{2'}(\lambda_\alpha b)\right)\mathcal{R}_{\alpha\alpha} = \frac{\mathrm{i}gH}{\omega\cos k_0 h_3}\tau_1 J_1'(k_0 b)\mathcal{Q}_{\alpha 0},\ \alpha \geq 0. \tag{6.46}$$

From equations (6.6) for the depth $-h_2 < z < -h_1$ and the matching condition (6.12), along with the orthogonality of the eigenfunctions, we get

$$\left(V_\alpha^{2'}(\mu_\alpha b) - \mathrm{i}k_0 G V_\alpha^2(\mu_\alpha b)\right)D_\alpha^2\mathcal{N}_{\alpha\alpha} + \left(W_\alpha^{2'}(\mu_\alpha b) - \mathrm{i}k_0 G W_\alpha^2(\mu_\alpha b)\right)E_\alpha^2\mathcal{N}\alpha\alpha + \mathrm{i}k_0 G\sum_{j=0}^{\infty} A_j^2 T_j^2(k_j b)\mathcal{P}_{\alpha j} = -\frac{\mathrm{i}gH}{\omega\cos k_0 h_3}\tau_1 J_1(k_0 b)\mathcal{P}_{\alpha 0} + \mathcal{D}_\alpha \quad \alpha \geq 0, \tag{6.47}$$

$$\left(D_\alpha^2 V_0^{2'}(\mu_\alpha b) + E_\alpha^2 W_\alpha^{2'}(\mu_\alpha b)\right)\mathcal{N}_{\alpha\alpha} - \sum_{j=0}^{\infty} A_j^2 T_j^{2'}(k_j b)\mathcal{P}_{\alpha j} = -\frac{\mathrm{i}gH}{\omega\cos k_0 h_3}\tau_1 \mathcal{P}_{\alpha 0} J_1'(k_0 b), \alpha \geq 0. \tag{6.48}$$

Further, from the matching condition given by equation (6.14) at $r = b$ in the interval $-h_3 < z < -h_2$, and using the orthogonality of the eigenfunctions, we get

$$\sum_{j=0}^{\infty} A_j^2 T_j^{2'}(k_j b)\mathcal{S}_{\alpha j} - F_\alpha^2 U_0^{2'}(\gamma_\alpha b)\mathcal{L}_{\alpha\alpha} = \frac{\mathrm{i}gH}{\omega\cos k_0 h_3}\tau_1 J_1'(k_0 b)\mathcal{S}_{\alpha 0} + \mathcal{E}_\alpha,\ \alpha \geq 0, \tag{6.49}$$

where, $\mathcal{Q}_{\alpha j}, \mathcal{R}_{\alpha\alpha}, \mathcal{T}_{\alpha\alpha}, \mathcal{P}_{\alpha j}, \mathcal{S}_{\alpha j}, \mathcal{L}_{\alpha\alpha}$ are given by equations (6.35)-(6.40) and

$$\mathcal{C}_\alpha = \int_{-h_1}^{0}\left(z + \frac{g}{\omega^2}\right)\cos\lambda_\alpha(z + h_1)\mathrm{d}z, \tag{6.50}$$

$$\mathcal{D}_\alpha = \mathrm{i}k_0 G\int_{-h_2}^{-h_1} z\cos\mu_\alpha(z + h_2)\mathrm{d}z, \tag{6.51}$$

$$\mathcal{E}_\alpha = \frac{-b}{2(h_3 - h_2)}\int_{-h_3}^{-h_2}\cos\gamma_\alpha(z + h_3)\mathrm{d}z. \tag{6.52}$$

6.5.2 Results and discussion

Here we discuss the effects of various parameters on the heave hydrodynamic coefficients acting on the cylindrical structure. The results are presented graphically and the observations are analysed.

Figures 6.12-6.14 show the added mass for heave motion against the wavenumber for different values of radius ratio a/b, porous coefficient G and draft h_2/h_3, respectively. For all the cases, an oscillating nature is observed. Both minimum and maximum values of χ_{33} are attained at specific values of $k_0 h_1$ for all values of $a/b, G$ and h_2/h_3. The value of added mass χ_{33} increases with an increase in the value of a/b, i.e., for the situation of increasing radius of the inner cylinder or decreasing radius of the outer cylinder. Also the presence of the porous region influences the impacts faced by the compound cylinder. It

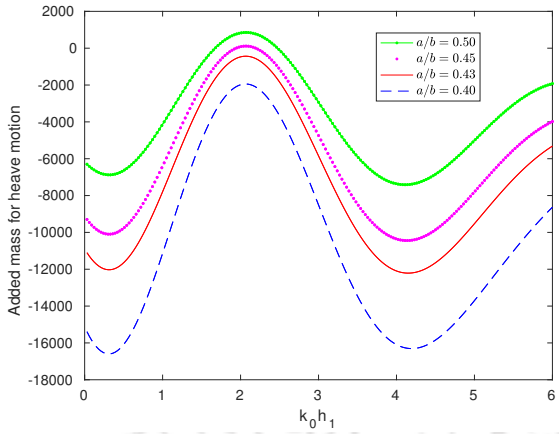

Figure 6.12: Added mass for heave motion against wavenumber corresponding to different values of a/b for $h_1/h_2 = 0.37$, $h_2/h_3 = 0.66$ and $G = 1$

can be seen from Figure 6.13 that with an increase in the value of the porous coefficient G, the added mass decreases. As the value of G increases, it allows more wave to pass through the structure but reduces the resistance of the structure to the wave motion. Thus, with a reduction in the value of G, the added mass acting on the cylinder increases. The added mass is also observed to be affected by the draft ratios. It is observed from Figure 6.14 that the maximum value of the added mass get reduced for higher values of h_2/h_3.

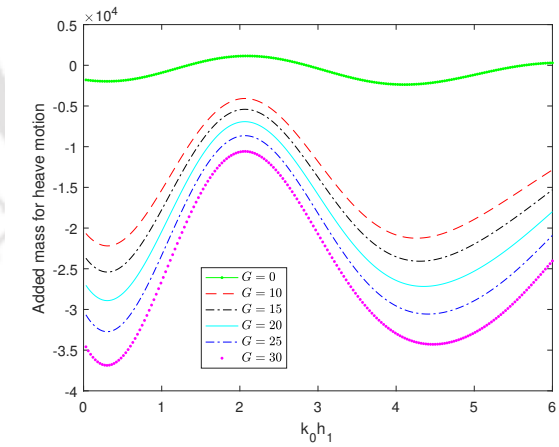

Figure 6.13: Added mass for heave motion against wavenumber corresponding to different values of G for $h_1/h_2 = 0.37$, $h_2/h_3 = 0.66$ and $a/b = 0.50$

Figures 6.15-6.17 show the damping coefficient $\frac{\Lambda_{33}}{\omega}$ for heave motion against the wavenumber for different values of $a/b, G$ and h_2/h_3, respectively. In this case also, an oscillating behaviour is observed. At low frequencies (wavenumbers), the component of the damping coefficient increases as a/b increases, i.e., when the radius of the upper cylinder gets closer to that of the lower cylinder. The heave damping coefficient is remarkably influenced by the porosity of the structure. It can be observed from Figure 6.16

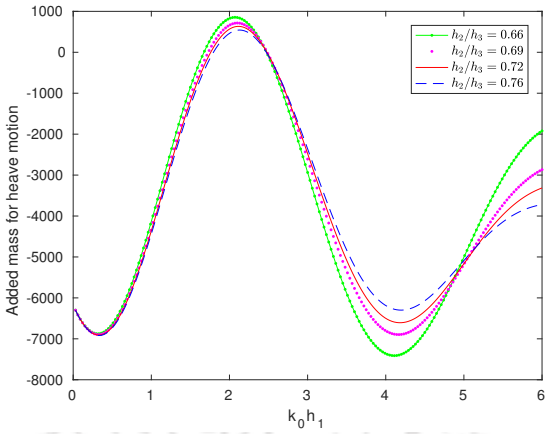

Figure 6.14: Added mass for heave motion against wavenumber corresponding to different values of h_2/h_3 for $h_1/h_2 = 0.37$, $G = 1$ and $a/b = 0.50$

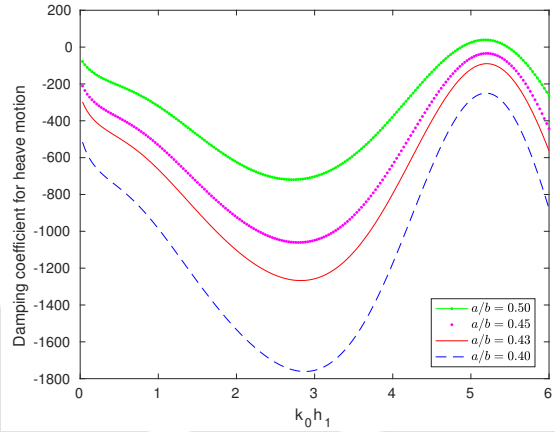

Figure 6.15: Damping coefficient for heave motion against wavenumber corresponding to different values of a/b for $h_1/h_2 = 0.37$, $h_2/h_3 = 0.66$ and $G = 1$

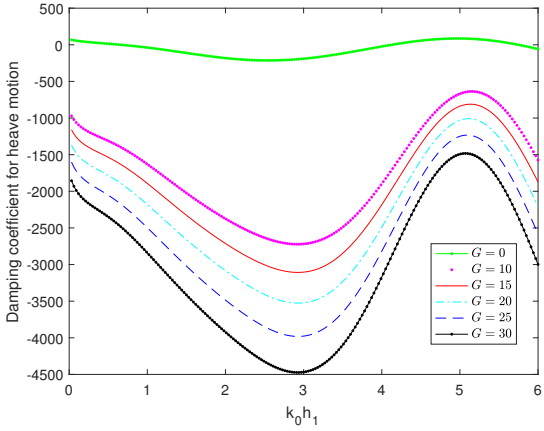

Figure 6.16: Damping coefficient for heave motion against wavenumber corresponding to different values of G for $h_1/h_2 = 0.37$, $h_2/h_3 = 0.66$ and $a/b = 0.50$

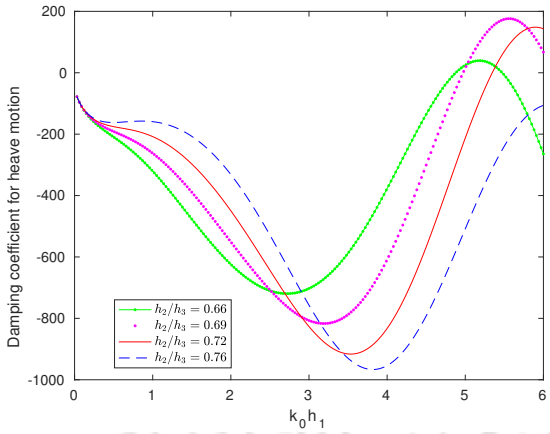

Figure 6.17: Damping coefficient for heave motion against wave number corresponding to different values of h_2/h_3 for $h_1/h_2 = 0.37$, $G = 1$ and $a/b = 0.50$

that an increase in damping coefficient is associated with a reduction in the values of the porous coefficient. Figure 6.17 presents damping coefficient $\frac{\Lambda_{33}}{\omega}$ for heave motion against wavenumber corresponding to different values of h_2/h_3 for $h_1/h_2 = 0.37$, $a/b = 0.50$ and $G = 1$. The oscillation is observed to get shifted towards right for increasing values of h_2/h_3. In other words, this happens when the draft of the lower cylinder with respect to its lower surface is increased which means the cylinder gets further away from the free surface or getting closer to the sea-bed.

6.6 Conclusion

Employing linear water wave theory, radiated potentials are derived for each sub-domain by taking into account the presence of a floating surface-piercing semi-porous compound cylinder in finite ocean depth. Eigenfunction expansion approach and separation of variables technique are utilized in solving this radiation problem governed by Laplace's equation. Various matching conditions are applied to derive a system of linear equations for determining the unknown coefficients. Nondimensionalized added mass and damping coefficients due to surge and heave motions are evaluated. Further, the effect of radius, depth and porosity on the added mass and damping coefficient are examined. For surge motion, as the radius ratio a/b of the cylinder decreases, added mass and damping coefficient both increase. It is observed that added mass oscillates between positive and negative values before converging corresponding to higher values of k_0h_1. Such type of peculiar behaviour of added mass is also observed in the works of McIver and Evans [32] and Wu et al. [61].

It is observed that the yaw induced surge damping is negative which implies that it is not only added mass that can be negative, the occurrence of which is a quite familiar phenomenon, but damping coefficients can also take negative values under certain conditions. This type of phenomenon can be attributed to the coupled behaviour between different

motions. The damping coefficients are found to oscillate alternately between negative and positive values. A similar phenomenon was also observed by Wu et al. [61], Zheng et al. [67] and Zheng and Zhang [66]. It is also noticed from Figure 6.9 that for surge motion, the added mass is not sufficiently affected by lower values of porous coefficient G. On the other hand, consideration of a large range of values of G shows added mass exhibiting variation for higher G. But for the heave motion, added mass is influenced by the porous coefficient G (Figure 6.13) − it decreases as G increases. With respect to the effect of the gap between the cylinder and depth, it is clearly observed from Figure 6.14 that for fixed values of the radii and porous coefficient, the added mass for heave motion increases as h_2/h_3, i.e., the submergence of the lower face of the outer (porous) cylinder, decreases. Then, with respect to the heave motion, keeping h_2/h_3 and G fixed, the damping coefficient increases as the value of radius ratio a/b increases. For fixed values of porous coefficient and radii, it is observed that the oscillation of damping coefficient for surge motion gets shifted towards right for decreasing values of h_1/h_2. It is expected that the results obtained in this work will provide necessary background for designing appropriate and efficient structures for reducing waveloads on such type of structures installed for various marine applications.

The obtained results are validated by comparing one result with an available result (Williams and Li [58]) and a satisfactory agreement is noticed thereby implying the effectiveness of the current mathematical model and subsequent results of the present chapter.

CHAPTER 7

Hydrodynamic Force and Wave run-up due to Diffraction of Ocean Water Waves by a Surface-Piercing Bottom-Mounted Compound Partial-Porous Cylinder

In this chapter, we carry out a theoretical study on the interaction of linear surface waves with a bottom-mounted compound partial-porous cylinder which consists of two coaxial cylinders with a hollow upper cylinder with a thin porous wall, and a rigid lower cylinder placed on the sea-bed. The fluid region is split into three subregions. By employing linear water wave theory and eigenfunction expansion, the problem is solved analytically in each fluid region by an appropriate use of the conditions on and across the boundaries. The hydrodynamic forces due to diffraction of waves acting on the structure are computed. The impacts of various parameters due to the wave and the structure on the hydrodynamic forces exerted on the upper and lower part of the cylinder are illustrated graphically. The accuracy of the present model is validated against an available result in the literature.

7.1 Theoretical formulation

In this section we set up the boundary value problem with suitable boundary conditions and matching conditions. We also calculate diffracted potentials in each sub-domain. There may be equations, conditions and expressions same or similar to those earlier chapters. Instead of eliminating them here and referring them from earlier, some of them are kept so as to have a free flow in reading this chapter.

A compound partial-porous cylinder consisting of two coaxial cylinders is considered such that the upper cylinder piercing the free surface is hollow with a thin porous side wall and the lower one is rigid and bottom-mounted. Conforming to the geometry, a cylindrical coordinate system (r, θ, z) is considered with the origin located on $z = 0$ along the axis of

the cylinders with the z-axis in vertical upward direction. a and b, with $b > a$, are taken to be the radii of the upper and lower cylinders, respectively. The lower cylinder has its upper surface and bottom surface, respectively, located at $z = -h_1$ and$z = -h_2$ (Figure 7.1). For convenience and practical point of view, the whole fluid region is split into three regions as follows: Region I $(r \geq b, -h_2 \leq z \leq 0)$; Region II $(a \leq r \leq b, -h_1 \leq z \leq 0)$ and Region III $(0 \leq r \leq a, -h_1 \leq z \leq 0)$. In each of these regions, the velocity potentials are defined by Φ_j for $j = 1, 2, 3$ as $\Phi(r, \theta, z, t) = \mathrm{Re}[\phi(r, \theta, z) \exp(-\mathrm{i}\omega t)]$, where $j = 1, 2, 3$, respectively, refers to Regions I, II and III. Subsequently, the incident velocity poten-

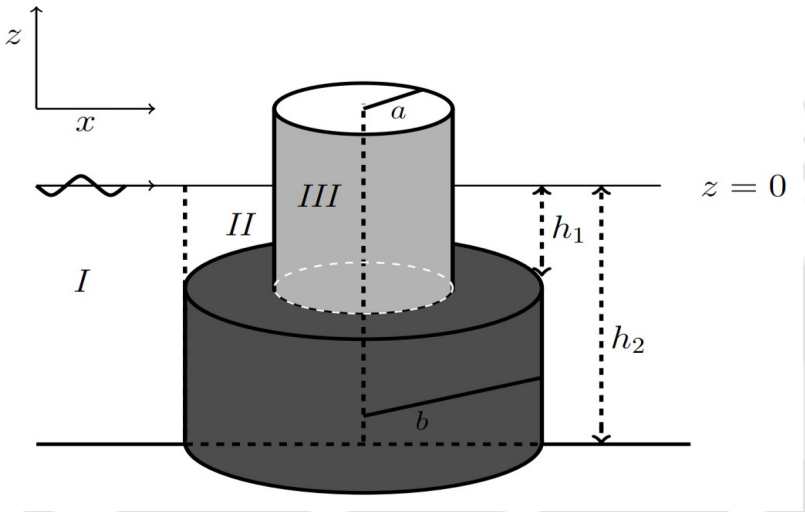

Figure 7.1: Schematic diagram of the compound partial-porous cylinder

tial due to a wave of amplitude H and angular wave frequency ω that propagates in the positive x-direction takes the following form (MacCamy and Fuchs [23]):

$$\phi_{inc} = -\frac{\mathrm{i}gH}{\omega} \frac{\cosh k_0(z + h_2)}{\cosh k_0 h_2} \sum_{m=0}^{\infty} \tau_m J_m(k_0 r) \cos m\theta, \tag{7.1}$$

where

$$\tau_m = \begin{cases} 1, & m = 0, \\ 2\mathrm{i}^m, & m \geq 1. \end{cases}$$

For such a flow, each potential ϕ_j satisfies the Laplace's equation as follows:

$$\nabla^2 \phi_j = 0; \quad j = 1, 2, 3, \tag{7.2}$$

with $\phi_j, j = 1, 2, 3$ representing the velocity potentials in Regions I, II and III, respectively.

The boundary value problems for each ϕ_j are formulated with the boundary conditions

on the free surface, sea-bed and the surface of the lower cylinder as follows:

$$\frac{\partial \phi_j}{\partial z} - \frac{\omega^2}{g}\phi_j = 0; \quad \text{at} \quad z = 0, \quad j = 1, 2, 3, \tag{7.3}$$

$$\frac{\partial \phi_1}{\partial z} = 0; \quad \text{at} \quad z = -h_2, \quad r > b, \tag{7.4}$$

$$\frac{\partial \phi_2}{\partial z} = 0; \quad \text{at} \quad z = -h_1, \quad a < r < b, \tag{7.5}$$

$$\frac{\partial \phi_1}{\partial r} = 0; \quad \text{at} \quad r = b, \quad -h_2 < z < -h_1, \tag{7.6}$$

$$\frac{\partial \phi_3}{\partial z} = 0; \quad \text{at} \quad z = -h_1, \quad 0 < r < a. \tag{7.7}$$

The important condition on the porous surface of the structure has the following form (Williams et al. [60]):

$$\frac{\partial \phi_3}{\partial r} = \mathrm{i}k_0 G(\phi_3 - \phi_2) \quad \text{on} \quad r = a, \quad -h_1 < z < 0. \tag{7.8}$$

The parameter G denotes the dimensionless porous parameter as used by Chwang [7] with k_0 as the incident wavenumber. Further, G can be expressed in the from $G_r + \mathrm{i}G_\mathrm{i}$ as used by Yu [64], where G_r and G_i, respectively, denote the real part and the imaginary part. The dimensionless porous parameter G is given by

$$G = \frac{L\rho\omega}{\varepsilon k_0}, \tag{7.9}$$

where ρ is the fluid density, ε is the coefficient of dynamic viscosity and L is a coefficient which has the dimension of length.

Also, the Sommerfeld radiation condition for the exterior region remains the same as equation (2.15).

At the boundary $r = b$, the relevant potentials ϕ_1 and ϕ_2 must satisfy the following matching conditions to ensure the continuity of velocity and pressure across the boundary:

$$\phi_1 = \phi_2; \quad \text{at} \quad r = b, \quad -h_1 < z < 0, \tag{7.10}$$

$$\frac{\partial \phi_1}{\partial r} = \frac{\partial \phi_2}{\partial r}; \quad \text{at} \quad r = b, \quad -h_1 < z < 0. \tag{7.11}$$

Similarly, at the boundary $r = a$, the relevant potentials ϕ_2 and ϕ_3 must satisfy following matching conditions:

$$\frac{\partial \phi_2}{\partial r} = \frac{\partial \phi_3}{\partial r}; \quad \text{at} \quad r = a, \quad -h_1 < z < 0. \tag{7.12}$$

Using eigenfunction expansion method, expressions for each potential $\phi_j, j = 1, 2, 3$ can be expressed as infinite series of orthogonal functions having validity in its respective fluid region. As a consequence, the diffracted velocity potential ϕ_1 for Region I takes the

following form (Ning et al. [38]):

$$\phi_1(r,\theta,z) = -\frac{igH}{\omega}\left[\sum_{m=0}^{\infty}\tau_m J_m(k_0 r)\frac{\cosh k_0(z+h_2)}{\cosh k_0 h_2}\cos m\theta + \sum_{m=0}^{\infty}\cos m\theta\sum_{j=0}^{\infty}\mathcal{A}_{mj}\mathcal{Z}_j^{(1)}(k_j z)\mathcal{T}_m^{(1)}(k_j r)\right], \tag{7.13}$$

where the unknown coefficients $\mathcal{A}_{mj}$ are to be determined. The wavenumbers k_j ($j = 0, 1, 2, 3, \ldots$) are calculated from the following dispersion relation:

$$\omega^2 = \begin{cases} gk_j \tanh k_j h_2; & j = 0, \\ -gk_j \tan k_j h_2; & j \geq 1. \end{cases}$$

For this purpose, the method devised by Chamberlain and Porter [6] is utilized. $\mathcal{T}_m^{(1)}(k_j r)$, the radial eigenfunctions in (7.13), are as follows:

$$\mathcal{T}_m^{(1)}(k_j r) = \begin{cases} \frac{H_m^{(1)}(k_j r)}{H_m^{(1)'}(k_j b)}; & j = 0, \\ \frac{K_m(k_j r)}{K_m'(k_j b)}; & j \geqslant 1. \end{cases}$$

For this case, the vertical eigenfunctions $\mathcal{Z}_j^{(1)}(k_j z)$ are given by

$$\mathcal{Z}_j^{(1)}(k_j z) = \begin{cases} \frac{\cosh k_j(z+h_2)}{\cosh k_j h_2}; & j = 0, \\ \frac{\cos k_j(z+h_2)}{\cos k_j h_2}; & j \geqslant 1. \end{cases}$$

The velocity potential ϕ_2 in Region II satisfies the relevant surface boundary conditions and has the following form (Ning et al. [38]):

$$\phi_2(r,\theta,z) = -\frac{igH}{\omega}\left[\sum_{m=0}^{\infty}\sum_{j=0}^{\infty}\left\{\mathcal{B}_{mj}\mathcal{S}_m^{(1)}(\lambda_j r) + \mathcal{C}_{mj}\mathcal{R}_m^{(1)}(\lambda_j r)\right\}\mathcal{Z}_j^{(2)}(\lambda_j z)\cos m\theta\right], \tag{7.14}$$

where the unknowns $\mathcal{B}_{mj}$ and $\mathcal{C}_{mj}$ are to be determined. The eigenvalues λ_j are derived from

$$\omega^2 = \begin{cases} g\lambda_j \tanh \lambda_j h_1; & j = 0, \\ -g\lambda_j \tan \lambda_j h_1; & j \geq 1. \end{cases}$$

The pair of radial eigenfunctions $\mathcal{S}_m^{(1)}(\lambda_j r)$ and $\mathcal{R}_m^{(1)}(\lambda_j r)$ appearing in (7.14) have the following forms:

$$\mathcal{S}_m^{(1)}(\lambda_j r) = \begin{cases} \frac{H_m^{(1)}(\lambda_j r)}{H_m^{(1)'}(\lambda_j b)}; & j = 0, \\ \frac{I_m(\lambda_j r)}{I_m'(\lambda_j b)}; & j \geq 1, \end{cases} \qquad \mathcal{R}_m^{(1)}(\lambda_j r) = \begin{cases} \frac{H_m^{(2)}(\lambda_j r)}{H_m^{(2)'}(\lambda_j b)}; & j = 0, \\ \frac{K_m(\lambda_j r)}{K_m'(\lambda_j b)}; & j \geq 1. \end{cases}$$

In this case, the relevant vertical eigenfunctions $\mathcal{Z}_j^{(2)}(\lambda_j z)$ are given by

$$\mathcal{Z}_j^{(2)}(\lambda_j z) = \begin{cases} \frac{\cosh\lambda_j(z+h_1)}{\cosh\lambda_j h_1}; & j=0, \\ \frac{\cos\lambda_j(z+h_1)}{\cos\lambda_j h_1}; & j\geqslant 1. \end{cases}$$

Now the velocity potential ϕ_3 in Region III has the following form:

$$\phi_3(r,\theta,z) = -\frac{\mathrm{i}gH}{\omega}\left[\sum_{m=0}^{\infty}\cos m\theta\sum_{j=0}^{\infty}\mathcal{D}_{mj}\mathcal{Z}_j^{(2)}(\lambda_j z)\mathcal{U}_m^{(1)}(\lambda_j r)\right], \tag{7.15}$$

where $\mathcal{D}_{mj}$ are coefficients to be determined. The radial eigenfunctions $\mathcal{U}_m^{(1)}(\lambda_j r)$ appearing in (7.15) are as follows:

$$\mathcal{U}_m^{(1)}(\lambda_j r) = \begin{cases} \frac{J_m(\lambda_j r)}{J_m'(\lambda_j a)}; & j=0, \\ \frac{I_m(\lambda_j r)}{I_m'(\lambda_j a)}; & j\geqslant 1. \end{cases}$$

7.2 Determination of unknown coefficients

Utilization of matching conditions (7.10)-(7.11) for $-h_1 < z < 0$, and then application of orthogonal property of the eigenfunctions gives

$$\sum_{j=0}^{\infty}\mathcal{A}_{mj}\mathcal{T}_m^{(1)}(k_j b)Q_{0j} - \left\{\mathcal{B}_{m0}\mathcal{S}_m^{(1)}(\lambda_0 b) + \mathcal{C}_{m0}\mathcal{R}_m^{(1)}(\lambda_0 b)\right\}V_{00} = -\beta_m J_m(k_0 b)Q_{00}, \tag{7.16}$$

$$\sum_{j=0}^{\infty}\mathcal{A}_{mj}\mathcal{T}_m^{(1)}(k_j b)Q_{\alpha j} - \left\{\mathcal{B}_{m\alpha}\mathcal{S}_m^{(1)}(\lambda_\alpha b) + \mathcal{C}_{m\alpha}\mathcal{R}_m^{(1)}(\lambda_\alpha b)\right\}V_{\alpha\alpha} = -\beta_m J_m(k_0 b)Q_{\alpha 0}, \quad \alpha\geqslant 1, \tag{7.17}$$

$$\sum_{j=0}^{\infty}\mathcal{A}_{mj}\mathcal{T}_m^{(1)'}(k_j b)Q_{0j} - \left\{\mathcal{B}_{m0}\mathcal{S}_m^{(1)'}(\lambda_0 b) + \mathcal{C}_{m0}\mathcal{R}_m^{(1)'}(\lambda_0 b)\right\}V_{00} = -\beta_m J_m'(k_0 b)Q_{00}, \tag{7.18}$$

$$\sum_{j=0}^{\infty}\mathcal{A}_{mj}\mathcal{T}_m^{(1)'}(k_j b)Q_{\alpha j} - \left\{\mathcal{B}_{m\alpha}\mathcal{S}_m^{(1)'}(\lambda_\alpha b) + \mathcal{C}_{m\alpha}\mathcal{R}_m^{(1)'}(\lambda_\alpha b)\right\}V_{\alpha\alpha} = -\beta_m J_m'(k_0 b)Q_{\alpha 0}, \quad \alpha\geqslant 1. \tag{7.19}$$

Again using the condition (7.12), along with the orthogonality of eigenfunctions, we obtain

$$\mathcal{D}_{m0}\mathcal{U}_m^{(1)'}(\lambda_0 a) - \left(\mathcal{B}_{m0}\mathcal{S}_m^{(1)'}(\lambda_0 a) + \mathcal{C}_{m0}\mathcal{R}_m^{(1)'}(\lambda_0 a)\right) = 0, \tag{7.20}$$

$$\mathcal{D}_{m\alpha}\mathcal{U}_m^{(1)'}(\lambda_\alpha a) - \left(\mathcal{B}_{m\alpha}\mathcal{S}_m^{(1)'}(\lambda_\alpha a) + \mathcal{C}_{m\alpha}\mathcal{R}_m^{(1)'}(\lambda_\alpha a)\right) = 0, \quad \alpha\geqslant 1. \tag{7.21}$$

Now application of the porous wall condition (7.8) for the depth $-h_1 < z < 0$ and the orthogonality of the eigenfunctions gives the following:

$$\left(1 - \mathrm{i}k_0 G\mathcal{U}_m^{(1)}(\lambda_0 a)\right)\mathcal{D}_{m0} + \mathrm{i}k_0 G\left(\mathcal{B}_{m0}\mathcal{S}_m^{(1)}(\lambda_0 a) + \mathcal{C}_{m0}\mathcal{R}_m^{(1)}(\lambda_0 a)\right) = 0, \tag{7.22}$$

$$\left(1 - \mathrm{i}k_0 G\mathcal{U}_m^{(1)}(\lambda_\alpha a)\right)\mathcal{D}_{m\alpha} + \mathrm{i}k_0 G\left(\mathcal{B}_{m\alpha}\mathcal{S}_m^{(1)}(\lambda_\alpha a) + \mathcal{C}_{m\alpha}\mathcal{R}_m^{(1)}(\lambda_\alpha a)\right) = 0, \quad \alpha \geq 1, \tag{7.23}$$

where

$$Q_{\alpha,j} = \int_{-h_1}^{0} \mathcal{Z}_\alpha^{(2)}(\lambda_\alpha z)\mathcal{Z}_j^{(1)}(k_j z)\mathrm{d}z, \tag{7.24}$$

$$V_{\alpha,\alpha} = \int_{-h_1}^{0} \mathcal{Z}_\alpha^{(2)}(\lambda_\alpha z)\mathcal{Z}_\alpha^{(2)}(\lambda_\alpha z)\mathrm{d}z. \tag{7.25}$$

For evaluating hydrodynamic forces and wave run-up, first the unknown coefficients are required to be computed. By truncating each of the infinite series appearing in equations (7.16) – (7.23) after some terms $N = 20$, the values of the coefficients $\mathcal{A}_{mj}$, $\mathcal{B}_{mj}$, $\mathcal{C}_{mj}$ and $\mathcal{D}_{mj}$ are computed. This results in the following linear system of algebraic equations:

$$\mathcal{H}_l\mathcal{X}_l = \mathcal{Y}_l, \tag{7.26}$$

with
$\mathcal{X}_l = [\mathcal{A}_{l1}, \mathcal{A}_{l2}, \ldots, \mathcal{A}_{lN}, \mathcal{B}_{l1}, \mathcal{B}_{l2}, ..., \mathcal{B}_{lN}, \mathcal{C}_{l1}, \mathcal{C}_{l2}, ..., \mathcal{C}_{lN}, \mathcal{D}_{l1}, \mathcal{D}_{l2}, \ldots, \mathcal{D}_{lN}]^t$: the unknown vectors,
$\mathcal{H}_l$: the coefficient matrices, and
$\mathcal{Y}_l$: the right-hand vectors.

7.3 Hydrodynamic forces and wave run-up

The hydrodynamic forces acting on both constituents of the compound partial-porous cylinder in the direction of wave propagation can be computed by integration of the pressure at the surface of the structure. The forces $\tilde{F}_x^j(t) = \mathrm{Re}[\tilde{F}_x^j \exp(-\mathrm{i}\omega t)]$ for $j = 1, 2$ ($j = 1$ refers to upper cylinder and $j = 2$ to lower cylinder) are defined as follows:

$$\tilde{F}_x^1 = \mathrm{i}\omega\rho \int_{-h_1}^{0}\int_{0}^{2\pi} \phi_3(a,\theta,z)\cos\theta \,\mathrm{d}z\mathrm{d}\theta - \mathrm{i}\omega\rho \int_{-h_1}^{0}\int_{0}^{2\pi} \phi_2(a,\theta,z)\cos\theta \,\mathrm{d}z\mathrm{d}\theta, \tag{7.27}$$

$$\tilde{F}_x^2 = -\mathrm{i}\omega\rho \int_{-h_2}^{-h_1}\int_{0}^{2\pi} \phi_1(b,\theta,z)\cos\theta \,\mathrm{d}z\mathrm{d}\theta. \tag{7.28}$$

The wave run-up for both exterior and interior regions, expressed as
$\eta_j(r,\theta,t) = Re[\zeta_j(r,\theta)\exp(-\mathrm{i}\omega t)]$ for $j = 1, 2, 3$, is calculated by applying the following dynamic free surface condition:

$$\eta_j = -\frac{1}{g}\frac{\partial \Phi_j}{\partial t}, \quad z = 0, \quad j = 1, 2, 3. \tag{7.29}$$

7.4 Validation of present model

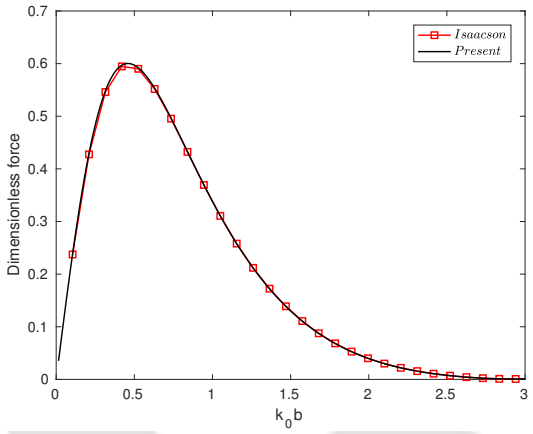

Figure 7.2: Comparison of hydrodynamic force of present work with that of Isaacson [19]

For validating the present analytical model, a comparison of our result with that of Isaacson [19] is carried out, i.e., when the compound partial-porous cylinder is considered to be an impermeable compound cylinder (in other words, $G = 0$). All the parameters in our problem are reconsidered conforming to Isaacson's work so that our problem can be converted to the same physical problem of Isaacson. For this comparison, the following values are considered: $G = 0$, $h_1/h_2 = 0.5$, $h_2/b = 2$, $a/b = 0.5$. Figure 7.2 depicts the hydrodynamic force acting on the base of the cylinder for both Isaacson's work and our work from which an excellent agreement is reached. In view of this, our model can be considered as an efficient one and hence more investigations follow in this work by adopting this model.

7.5 Results and discussion

Here we discuss how various parameters affect the hydrodynamic forces and wave run-up acting on the cylindrical structure. The results are presented graphically and relevant observations are presented.

Figure 7.3 presents the hydrodynamic force $\frac{|\tilde{F}_x^2|}{|\rho g b h_2 H|}$ acting on the lower cylinder plotted versus wavenumber for four values of radius ratio a/b with fixed values $G = 1$, $h_1/h_2 = 0.66$. It is observed that all curves show a similar trend (i.e., start from non-zero value and then take increasing values as the value of the wavenumber increases). That the higher values of force correspond to the lower values of radius ratio a/b means that for a

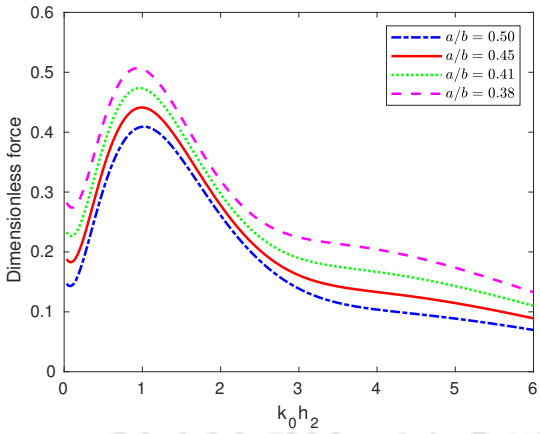

Figure 7.3: Hydrodynamic force for the lower cylinder against wavenumber corresponding to different values of a/b for $h_1/h_2 = 0.66$ and $G = 1$

much smaller upper cylinder or much bigger lower cylinder, an increase in hydrodynamic force takes place. It is observed that in the neighbourhood of $k_0h_2 = 1$, the wave force exhibits a large value irrespective of values of a/b which is associated with the resonant frequencies of the wave. Similar phenomenon is observed in some latter figures attributed to resonance as observed by Darwiche et al. [10] too. A detailed explanation of such occurrences was presented in Chapter 4. Figure 7.4 presents the hydrodynamic force

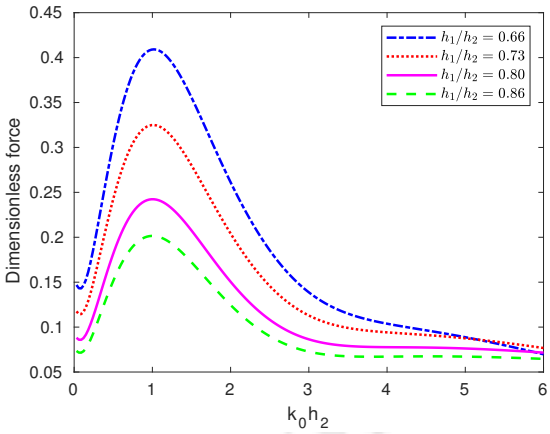

Figure 7.4: Hydrodynamic force for the lower cylinder against wavenumber corresponding to different values of h_1/h_2 for $a/b = 0.50$ and $G = 1$

$\frac{|\tilde{F}_x^2|}{|\rho g b h_2 H|}$ acting on the lower cylinder plotted versus wavenumber for various values of h_1/h_2 with $G = 1$ and $a/b = 0.50$. The force is observed to take higher values for lower values of h_1/h_2. This implies that when the draft of the upper cylinder is less, then the force on the lower cylinder increases due to a larger fluid region between the cylinders. Figure 7.5 presents the hydrodynamic force $\frac{|\tilde{F}_x^2|}{|\rho g b h_2 H|}$ acting on the lower cylinder plotted against wavenumber corresponding to various values of porous coefficient

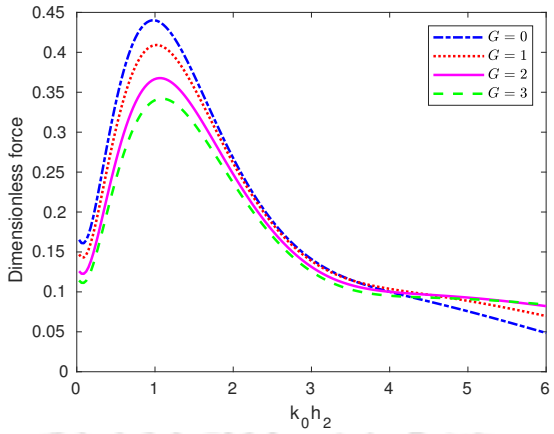

Figure 7.5: Hydrodynamic force acting on the lower cylinder plotted against wavenumber for various values of porous coefficient G with fixed values $a/b = 0.50$ and $h_1/h_2 = 0.66$

G with $a/b = 0.50$ and $h_1/h_2 = 0.66$. It is clearly visible that G has a reasonable influence on the exciting forces and each curve exhibits the same type of behaviour as seen earlier. Also lower values of porous coefficient results in higher values of wave force. As the porous coefficient G takes increasing values, more waves pass through the structure, but this brings reduction of the resistance of the cylinder to the wave motion.

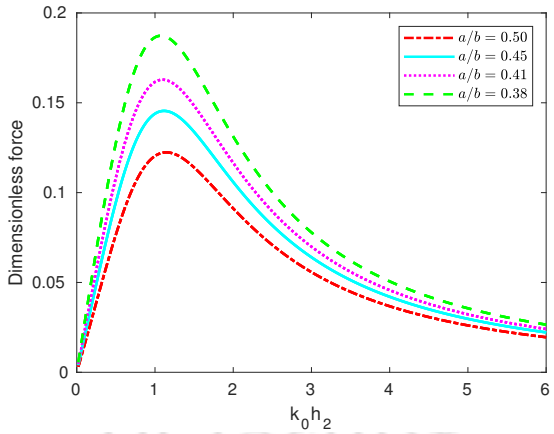

Figure 7.6: Hydrodynamic force acting on the upper cylinder plotted against wavenumber for various values of radius ratio a/b with $h_1/h_2 = 0.66$ and $G = 1$

Figure 7.6 presents the hydrodynamic force $\dfrac{|\tilde{F}_x^1|}{|\rho g a h_2 H|}$ acting on the upper cylinder plotted versus wavenumber for various values of radius ratio a/b with $G = 1$ and $h_1/h_2 = 0.66$. The initial value of the force is observed to be zero. In general, the force takes higher values in the range $0.8 < k_0 h_2 < 1.5$. A clear observation is that the higher forces occur for lower values of a/b. This happens as more energy gets concentrated near the upper cylinder which results in an increase of the hydrodynamic force. It establishes that the size of the cylinder needs to be adjusted for getting higher or lower force on the cylinder

surface. Figure 7.7 presents hydrodynamic force $\frac{|\tilde{F}_x^1|}{|\rho g a h_2 H|}$ on the upper cylinder against

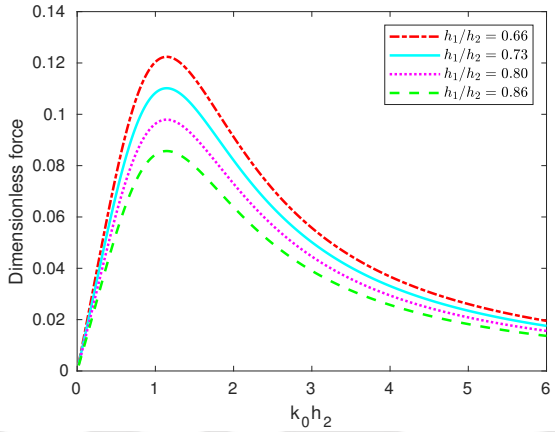

Figure 7.7: Hydrodynamic force for the upper cylinder against wavenumber corresponding to different values of h_1/h_2 for $a/b = 0.50$ and $G = 1$

wavenumber for different values of h_1/h_2 with fixed values $G = 1$ and $a/b = 0.50$. Here also, the same graph pattern as in Figure 7.6 is observed. Figure 7.8 depicts the variation

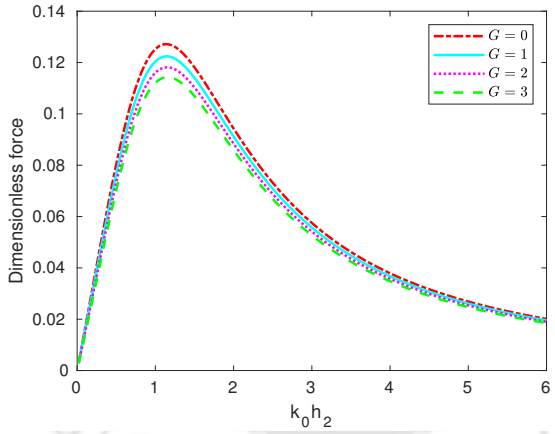

Figure 7.8: Hydrodynamic force on the upper cylinder plotted against wavenumber for different values of porous coefficient G with $h_1/h_2 = 0.66$ and $a/b = 0.50$

of dimensionless hydrodynamic force at $r = a$ plotted versus dimensionless wavenumber corresponding to various values of G for $h_1/h_2 = 0.66$ and $a/b = 0.50$. The hydrodynamic force on the upper cylinder attains the peak value for $G = 0$, i.e., for the case when its outer wall is assumed to be impermeable. In general, the force on the upper cylinder reduces when G takes increasing values for which more waves pass through the structure, but this brings reduction of the resistance of the cylinder to the wave motion. This establishes the influence of the porosity of the upper cylinder on the hydrodynamic forces.

Figures 7.9 and 7.10 present contour plots of the wave run-up nearer the free surface corresponding to two different values of frequency. They illustrate that when the wave

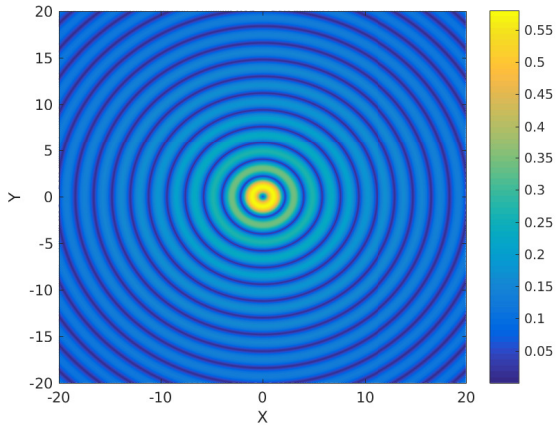

Figure 7.9: Contour plot for the wave run-up $|\zeta_1(r,\theta)|/H$ at free surface for $k_0 b = 3.5$, $a/b = 0.50$, $h_1/h_2 = 0.66$ and $G = 1$

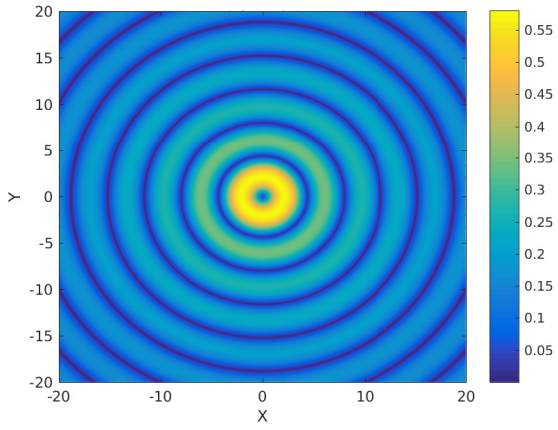

Figure 7.10: Contour plot for the wave run-up $|\zeta_1(r,\theta)|/H$ at free surface for $k_0 b = 1.75$, $a/b = 0.50$, $h_1/h_2 = 0.66$ and $G = 1$

gets scattered by the cylinder, the elevation gets reduced. By comparison of these two figures, it is clearly noticed that corresponding to higher frequency incident waves, the pattern of the diffracted wave becomes more assertive in addition to the observation of appearance of more number of wave ripples in the annular region.

Figures 7.11 - 7.14 present the wave run-up $|\zeta_1(r,\theta)|/H$ for Region I and $|\zeta_2(r,\theta)|/H$ for Region II against wavenumber corresponding to different values of a/b and G, respectively. It is observed that the dimensionless wave run-up acting on the upper and lower cylinder attains the peak values for $G = 0$, i.e., when the outer wall is assumed to be impermeable. Also higher values of wave run-up are observed to occur for lower values of a/b. For certain values of $k_0 h_2$, wave run-up becomes very low or very high. This may be due to the interaction of incoming and scattered waves leading to destructive or constructive interference near the cylinder. The case of higher value is attributed to constructive interference while the case of lower value is attributed to destructive interference.

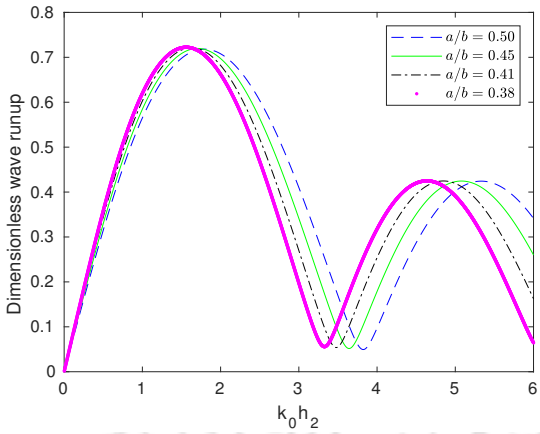

Figure 7.11: Wave run-up $|\zeta_1(r,\theta)|/H$ plotted against wavenumber for various values of radius ratio a/b with $h_1/h_2 = 0.66$ and $G = 1$

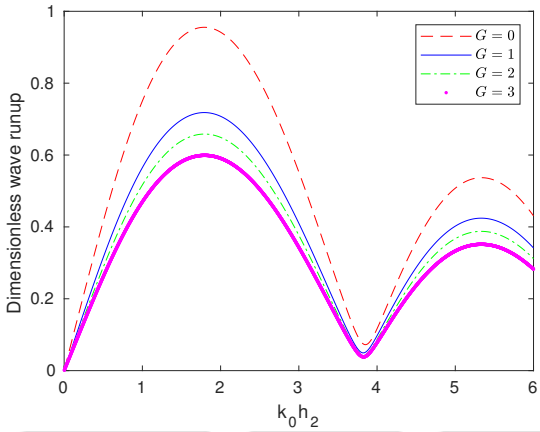

Figure 7.12: Wave run-up $|\zeta_1(r,\theta)|/H$ plotted against wavenumber for various values of porous coefficient G with $h_1/h_2 = 0.66$ and $a/b = 0.50$

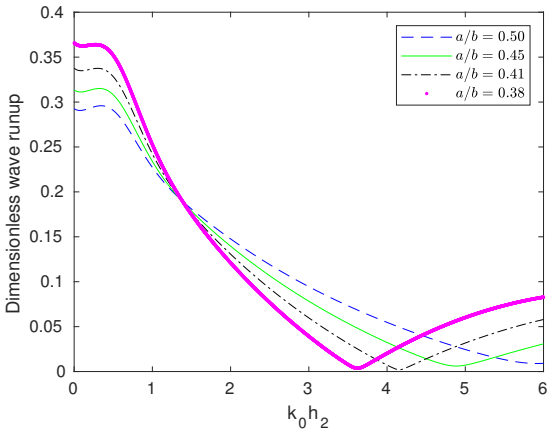

Figure 7.13: Wave run-up $|\zeta_2(r,\theta)|/H$ plotted against wavenumber for various values of radius ratio a/b with $h_1/h_2 = 0.66$ and $G = 1$

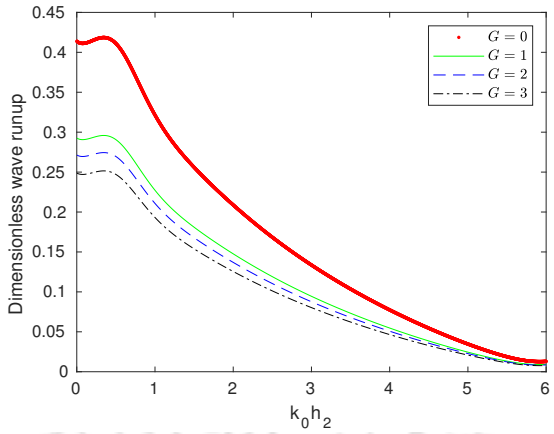

Figure 7.14: Wave run-up $|\zeta_2(r,\theta)|/H$ plotted against wavenumber for various values of porous coefficients G with $h_1/h_2 = 0.66$ and $a/b = 0.50$

7.6 Conclusion

This chapter carries out a theoretical study on diffraction of linear water waves by a bottom-mounted surface-piercing compound partial-porous cylinder comprising of an upper hollow cylinder with a porous wall and a lower rigid bottom-mounted cylinder having radius bigger than that of the upper cylinder. By using the familiar methods of eigenfunction expansion and separation of variables, the diffraction problem governed by Laplace's equation is solved. The main objective here is to study the hydrodynamic force and wave run-up due to the cylindrical system interacting with the water waves. Subsequently, graphical representation of the results allow to conclude that variation of values of parameters such as radii, draft and porosity has a significant impact on the exciting force and wave run-up. It is found that the force acting on the upper cylinder takes increasing values for lower values of radius ratio. Further, the force becomes higher when draft h_1/h_2 takes lower values. There is a clear observation that higher force occurs corresponding to lower porous coefficients. Comparison of current result with that of Isaacson [19] shows similar pattern from which it may be concluded that it will be worthwhile to consider the current model. It is also observed that for fixed radius, porosity and depth, the wave run-up is more visible corresponding to increasing values of wavenumber. The expectation here is that the configuration and formulations suggested and results obtained in the present work will be able to provide essential information for designing suitable and effective porous structures that may be installed in oceans to cater to various activities such as capturing wind energy and wave energy.

CHAPTER 8

Exciting Force for a Coaxial Configuration of a Floating Porous Cylinder and a Bottom-Mounted Rigid Cylinder in Finite Ocean Depth

In this chapter, the interaction of linear surface waves with a cylindrical system consisting of two coaxial vertical cylinders is theoretically investigated. Here we discuss two cases: (i) a system consisting of a hollow porous cylinder at the top and a rigid solid cylinder at the bottom, (ii) a solid porous cylinder at the top with a rigid solid cylinder considered at the bottom. Such a structure can be considered to represent of a wave energy device utilized for harnessing energy from ocean waves. The entire fluid region is split into a number of subregions. By employing linear water wave theory and eigenfunction expansion, the problem is solved analytically in each fluid region with appropriate use of the conditions on and across the boundaries. The impacts of various parameters due to the wave and the structure on the exciting forces exerted on the upper and lower cylinders are illustrated graphically. We calculate the forces on the cylinders induced by diffraction and the expectation is that the outcomes may be appropriately utilized in designing effective devices.

8.1 Two coaxial cylinders: an upper hollow porous cylinder and a lower rigid solid cylinder

8.1.1 Theoretical formulation

Two coaxial cylinders, a hollow upper cylinder with porous side-wall and a solid rigid lower cylinder, are considered such that the upper one floats and the lower one is placed

at the ocean bottom. A cylindrical coordinate system (r, θ, z) is considered with the origin on $z = 0$ along the axis of the cylinders and the z- axis pointing vertically upwards. a and b are the radii of the upper and lower cylinders, respectively, and h_1 is the draft of the upper cylinder. The bottom of lower cylinder is located at ocean depth $z = -h_3$ with its upper surface at $z = -h_2$ (Figure 8.1). For convenience and practical point of

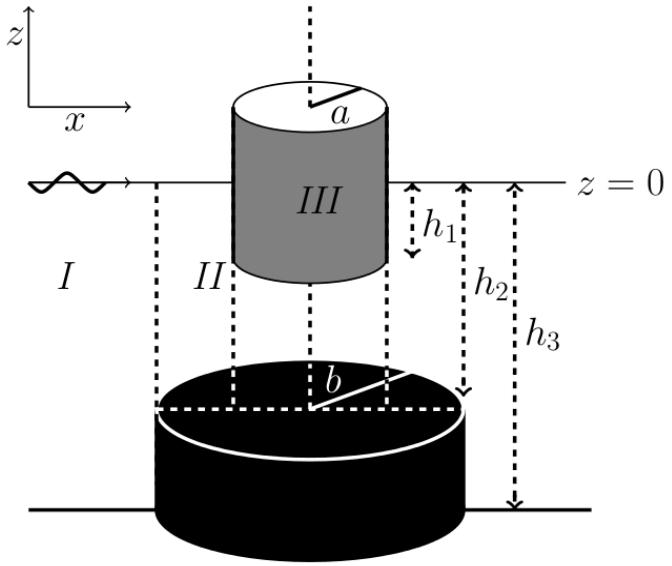

Figure 8.1: Schematic diagram of the configuration

view, the whole fluid domain is split into three regions: Region I $(r \geq b, -h_3 \leq z \leq 0)$; Region II $(a \leq r \leq b, -h_2 \leq z \leq 0)$ and Region III $(0 \leq r \leq a, -h_2 \leq z \leq 0)$ in each of which the velocity potentials are defined by Φ_j for $j = 1, 2, 3$ as $\Phi(r, \theta, z, t) = \mathrm{Re}[\phi(r, \theta, z) \exp(-\mathrm{i}\omega t)]$. Subsequently, the incident velocity potential due to a wave of amplitude H and angular wave frequency ω that propagates in the positive x-direction takes the following form [23]:

$$\phi_{inc} = -\frac{\mathrm{i}gH}{\omega} \frac{\cosh k_0(z + h_3)}{\cosh k_0 h_3} \sum_{m=0}^{\infty} \tau_m J_m(k_0 r) \cos m\theta, \tag{8.1}$$

where

$$\tau_m = \begin{cases} 1, & \text{for} \quad m = 0, \\ 2\mathrm{i}^m, & \text{for} \quad m \geq 1. \end{cases}$$

For such a flow, Laplace's equation is satisfied by each potential ϕ_j:

$$\nabla^2 \phi_j = 0; \quad j = 1, 2, 3, \tag{8.2}$$

where $\phi_j, j = 1, 2, 3$ represent the potentials in regions I, II and III, respectively.
To construct the boundary value problems for ϕ_j, the boundary conditions on the free surface, sea-bed and the surface of the lower cylinder can be written in the following form:

$$\frac{\partial \phi_j}{\partial z} - \frac{\omega^2}{g}\phi_j = 0; \quad \text{at} \quad z = 0, \quad j = 1, 2, 3, \tag{8.3}$$

$$\frac{\partial \phi_1}{\partial z} = 0; \quad \text{at} \quad z = -h_3, \quad r > b, \tag{8.4}$$

$$\frac{\partial \phi_2}{\partial z} = 0; \quad \text{at} \quad z = -h_2, \quad a < r < b, \tag{8.5}$$

$$\frac{\partial \phi_1}{\partial r} = 0; \quad \text{at} \quad r = b, \quad -h_3 < z < -h_2, \tag{8.6}$$

$$\frac{\partial \phi_3}{\partial z} = 0; \quad \text{at} \quad z = -h_2, \quad 0 < r < a. \tag{8.7}$$

The important condition on the porous surface of the structure is (Williams et al. [60])

$$\frac{\partial \phi_3}{\partial r} = \mathrm{i}k_0 G(\phi_2 - \phi_3) \quad \text{on} \quad r = a, \quad -h_1 < z < 0. \tag{8.8}$$

Also, the Sommerfeld radiation condition for the exterior region remains the same as equation (2.15).
On the boundary $r = b$, the relevant potentials ϕ_1 and ϕ_2 must satisfy the following matching conditions to ensure continuity of velocity and pressure across the boundary:

$$\frac{\partial \phi_1}{\partial r} = \frac{\partial \phi_2}{\partial r}; \qquad -h_2 < z < 0, \tag{8.9}$$

$$\phi_1 = \phi_2; \quad -h_2 < z < 0. \tag{8.10}$$

Similarly, at the boundary $r = a$, the relevant potentials ϕ_2 and ϕ_3 must satisfy following matching conditions:

$$\frac{\partial \phi_2}{\partial r} = \frac{\partial \phi_3}{\partial r}; \quad -h_2 < z < -h_1, \tag{8.11}$$

$$\phi_2 = \phi_3; \quad -h_2 < z < -h_1. \tag{8.12}$$

Using eigenfunction expansion method, expressions for each potential $\phi_j, j = 1, 2, 3$ can be obtained as infinite series of orthogonal functions valid in the respective fluid region. The diffracted velocity potential for Region I takes the following form:

$$\begin{aligned}\phi_1(r, \theta, z) = -\frac{\mathrm{i}gH}{\omega}\Bigg[&\sum_{m=0}^{\infty} \tau_m J_m(k_0 r)\frac{\cosh k_0(z + h_3)}{\cosh k_0 h_3}\cos m\theta \\ &+ \sum_{m=0}^{\infty}\cos m\theta \sum_{j=0}^{\infty} \mathcal{A}_{mj}\mathcal{Z}_j^{(1)}(k_j z)\mathcal{T}_m^{(1)}(k_j r)\Bigg],\end{aligned} \tag{8.13}$$

where the unknown coefficients $\mathcal{A}_{mj}$ are to be determined. The wavenumbers k_j ($j =$

$0, 1, 2, 3, \ldots$) are derived from the following dispersion relation:

$$\omega^2 = \begin{cases} gk_j \tanh k_j h_3; & j = 0, \\ -gk_j \tan k_j h_3; & j \geq 1. \end{cases}$$

The vertical eigenfunctions $\mathcal{Z}_j^{(1)}(k_j z)$ are defined as

$$\mathcal{Z}_j^{(1)}(k_j z) = \begin{cases} \frac{\cosh k_j(z+h_3)}{\cosh k_j h_3}; & j = 0, \\ \frac{\cos k_j(z+h_3)}{\cos k_j h_3}; & j \geqslant 1. \end{cases}$$

$\mathcal{T}_m^{(1)}(k_j r)$, the radial eigenfunctions in (8.13), are as follows:

$$\mathcal{T}_m^{(1)}(k_j r) = \begin{cases} \frac{H_m^{(1)}(k_j r)}{H_m^{(1)'}(k_j b)}; & j = 0, \\ \frac{K_m(k_j r)}{K_m'(k_j b)}; & j \geqslant 1, \end{cases}$$

with $H_m^{(1)}(k_j r)$ and $K_m(k_j r)$, respectively, denoting Hankel function of first kind and modified Bessel function of second kind of order m. Velocity potential ϕ_2 in Region II satisfies the structural boundary conditions and has the following form:

$$\phi_2(r, \theta, z) = -\frac{igH}{\omega} \left[\sum_{m=0}^{\infty} \sum_{j=0}^{\infty} \left\{ \mathcal{B}_{mj} \mathcal{S}_m^{(1)}(\lambda_j r) + \mathcal{C}_{mj} \mathcal{R}_m^{(1)}(\lambda_j r) \right\} \mathcal{Z}_j^{(2)}(\lambda_j z) \cos m\theta \right], \quad (8.14)$$

where the unknowns $\mathcal{B}_{mj}$ and $\mathcal{C}_{mj}$ are to be determined. The eigenvalues λ_j are derived from

$$\omega^2 = \begin{cases} g\lambda_j \tanh \lambda_j h_2; & j = 0, \\ -g\lambda_j \tan \lambda_j h_2; & j \geq 1. \end{cases}$$

The vertical eigenfunctions $\mathcal{Z}_j^{(2)}(\lambda_j z)$ are found as

$$\mathcal{Z}_j^{(2)}(\lambda_j z) = \begin{cases} \frac{\cosh \lambda_j(z+h_2)}{\cosh \lambda_j h_2}; & j = 0, \\ \frac{\cos \lambda_j(z+h_2)}{\cos \lambda_j h_2}; & j \geqslant 1. \end{cases}$$

The pair of radial eigenfunctions $\mathcal{S}_m^{(1)}(\lambda_j r)$ and $\mathcal{R}_m^{(1)}(\lambda_j r)$ appearing in (8.14) have the following forms:

$$\mathcal{S}_m^{(1)}(\lambda_j r) = \begin{cases} \frac{H_m^{(1)}(\lambda_j r)}{H_m^{(1)'}(\lambda_j b)}; & j = 0, \\ \frac{I_m(\lambda_j r)}{I_m'(\lambda_j b)}; & j \geq 1, \end{cases} \qquad \mathcal{R}_m^{(1)}(\lambda_j r) = \begin{cases} \frac{H_m^{(2)}(\lambda_j r)}{H_m^{(2)'}(\lambda_j b)}; & j = 0, \\ \frac{K_m(\lambda_j r)}{K_m'(\lambda_j b)}; & j \geq 1, \end{cases}$$

where $H_m^{(2)}(\lambda_j r)$ and $I_m(\lambda_j r)$, respectively, denote Hankel function of second kind and modified Bessel function of first kind of order m.

Now the potential ϕ_3 in region III takes the following form:

$$\phi_3(r,\theta,z) = -\frac{\mathrm{i}gH}{\omega}\left[\sum_{m=0}^{\infty}\cos m\theta\sum_{j=0}^{\infty}\mathcal{D}_{mj}\mathcal{Z}_j^{(2)}(\lambda_j z)\mathcal{U}_m^{(1)}(\lambda_j r)\right], \tag{8.15}$$

where $\mathcal{D}_{mj}$ are the unknown coefficients to be determined. The radial eigenfunctions $\mathcal{U}_m^{(1)}(\lambda_j r)$ are as follows:

$$\mathcal{U}_m^{(1)}(\lambda_j r) = \begin{cases} \frac{J_m(\lambda_j r)}{J'_m(\lambda_j a)}; & j=0, \\ \frac{I_m(\lambda_j r)}{I'_m(\lambda_j a)}; & j\geqslant 1. \end{cases}$$

8.1.2 Determination of unknown coefficients

Applying the matching conditions (8.9) and (8.10) for $-h_2 < z < 0$ and the orthogonality of the eigenfunctions, the following are obtained:

$$\begin{aligned}&\sum_{j=0}^{\infty}\mathcal{A}_{mj}\mathcal{T}_j^{(1)'}(k_j b)\mathcal{Q}_{\alpha j} - \left(\mathcal{B}_{m\alpha}\mathcal{S}_m^{(1)'}(\lambda_\alpha b) + \mathcal{C}_{m\alpha}\mathcal{R}_m^{(1)'}(\lambda_\alpha b)\right)\mathcal{V}_{\alpha\alpha} \\ &= -\beta_m J'_m(k_0 b)\mathcal{Q}_{\alpha 0},\ \alpha \geq 0, \end{aligned} \tag{8.16}$$

$$\begin{aligned}&\sum_{j=0}^{\infty}\mathcal{A}_{mj}\mathcal{T}_j^{(1)}(k_j b)\mathcal{Q}_{\alpha j} - \left(\mathcal{B}_{m\alpha}\mathcal{S}_m^{(1)}(\lambda_\alpha b) + \mathcal{C}_{m\alpha}\mathcal{R}_m^{(1)}(\lambda_\alpha b)\right)\mathcal{V}_{\alpha\alpha} \\ &= -\beta_m J_m(k_0 b)\mathcal{Q}_{\alpha 0},\ \alpha \geq 0. \end{aligned} \tag{8.17}$$

Again using the condition (8.11), along with the orthogonality of eigenfunctions $\cos\lambda_\alpha(z+h_2)$, we obtain

$$\sum_{j=0}^{\infty}\mathcal{D}_{m\alpha}\mathcal{U}_m^{(1)'}(\lambda_\alpha a)\mathcal{L}_{\alpha j} - \sum_{j=0}^{\infty}\left(\mathcal{B}_{m\alpha}\mathcal{S}_m^{(1)'}(\lambda_\alpha a) + \mathcal{C}_{m\alpha}\mathcal{R}_m^{(1)'}(\lambda_\alpha a)\right)\mathcal{L}_{\alpha j} = 0, \quad \alpha \geq 0. \tag{8.18}$$

Now application of the porous wall condition for the depth $-h_1 < z < 0$ and the eigenfunctions
$\cos\lambda_\alpha(z+h_2)$ gives the following:

$$\begin{aligned}&\sum_{j=0}^{\infty}\left(\mathcal{U}_m^{(1)'}(\lambda_j a) + \mathrm{i}k_0 G\mathcal{U}_m^{(1)}(\lambda_j a)\right)\mathcal{D}_{mj}\mathcal{W}_{\alpha j} \\ &+\mathrm{i}k_0 G\sum_{j=0}^{\infty}\left(\mathcal{B}_{mj}\mathcal{S}_j^{(1)}(\lambda_j a) + \mathcal{C}_{mj}\mathcal{R}_j^{(1)}(\lambda_j a)\right)\mathcal{W}_{\alpha j} = 0, \alpha \geq 0, \end{aligned} \tag{8.19}$$

where

$$\mathcal{Q}_{\alpha,j} = \int_{-h_2}^{0}\mathcal{Z}_\alpha^{(2)}(\lambda_\alpha z)\mathcal{Z}_j^{(1)}(k_j z)\mathrm{d}z, \tag{8.20}$$

$$\mathcal{V}_{\alpha,\alpha} = \int_{-h_2}^{0} \mathcal{Z}_{\alpha}^{(2)}(\lambda_\alpha z)\mathcal{Z}_{\alpha}^{(2)}(\lambda_\alpha z)\mathrm{d}z, \tag{8.21}$$

$$\mathcal{L}_{\alpha,j} = \int_{-h_2}^{-h_1} \mathcal{Z}_{\alpha}^{(2)}(\lambda_\alpha z)\mathcal{Z}_{j}^{(2)}(\lambda_j z)\mathrm{d}z, \tag{8.22}$$

$$\mathcal{W}_{\alpha,j} = \int_{-h_1}^{0} \mathcal{Z}_{\alpha}^{(2)}(\lambda_\alpha z)\mathcal{Z}_{j}^{(2)}(\lambda_j z)\mathrm{d}z. \tag{8.23}$$

In order to obtain the exciting forces and wave run-up, the unknown coefficients are required to be computed. By truncating each of the infinite series appearing in equations (8.16) – (8.19) after some terms $N = 20$, the values of the coefficients $\mathcal{A}_{mj}$, $\mathcal{B}_{mj}$, $\mathcal{C}_{mj}$ and $\mathcal{D}_{mj}$ are computed. As a consequence, the following linear system of algebraic equations is obtained for determining the unknowns:

$$\mathcal{H}_l\mathcal{X}_l = \mathcal{E}_l, \tag{8.24}$$

with
$\mathcal{X}_l = [\mathcal{A}_{l1}, \mathcal{A}_{l2}, \ldots, \mathcal{A}_{lN}, \mathcal{B}_{l1}, \mathcal{B}_{l2}, ..., \mathcal{B}_{lN}, \mathcal{C}_{l1}, \mathcal{C}_{l2}, ..., \mathcal{C}_{lN}, \mathcal{D}_{l1}, \mathcal{D}_{l2}, \ldots, \mathcal{D}_{lN}]^t$,
$\mathcal{H}_l$ the coefficient matrices,
$\mathcal{E}_l$ the right-hand vectors.

8.1.3 Horizontal exciting forces and wave run-up

The exciting forces acting on the upper and the lower cylinders in the direction of wave propagation can be computed by integrating the pressure at the surface of the structure. The forces $\tilde{F}_x^j(t) = \mathrm{Re}[\tilde{F}_x^j \exp(-\mathrm{i}\omega t)]$ for $j = 1, 2$ ($j = 1$ refers to upper cylinder and $j = 2$ to lower cylinder) are defined as follows:

$$\tilde{F}_x^1 = \mathrm{i}\omega\rho \int_{-h_1}^{0}\int_{0}^{2\pi} \phi_3(a,\theta,z)\cos\theta \,\mathrm{d}z\mathrm{d}\theta - \mathrm{i}\omega\rho \int_{-h_1}^{0}\int_{0}^{2\pi} \phi_2(a,\theta,z)\cos\theta \,\mathrm{d}z\mathrm{d}\theta, \tag{8.25}$$

$$\tilde{F}_x^2 = -\mathrm{i}\omega\rho \int_{-h_3}^{-h_2}\int_{0}^{2\pi} \phi_1(b,\theta,z)\cos\theta \,\mathrm{d}z\mathrm{d}\theta. \tag{8.26}$$

The wave run-up for the exterior and interior regions, as given by
$\eta_j(r,\theta,t) = \mathrm{Re}[\zeta_j(r,\theta)\exp(-\mathrm{i}\omega t)]$ for $j = 1, 2, 3$ (j denoting regions I, II and III), is calculated by applying the following dynamic free surface condition:

$$\eta_j = -\frac{1}{g}\frac{\partial\Phi_j}{\partial t}, \quad z = 0, \quad j = 1, 2, 3. \tag{8.27}$$

8.1.4 Results and discussion

In practice, G always possesses positive real and imaginary parts but when the resistance effect against the flow dominates the inertial effect of the fluid inside the porous material,

then G takes real values. Conforming to our problem, we discuss only real part of G, that means when resistance effect dominates inertial effect. Further, it is observed that even if G is imaginary or a mix of real and imaginary, there is no significant deviation at all from present results.

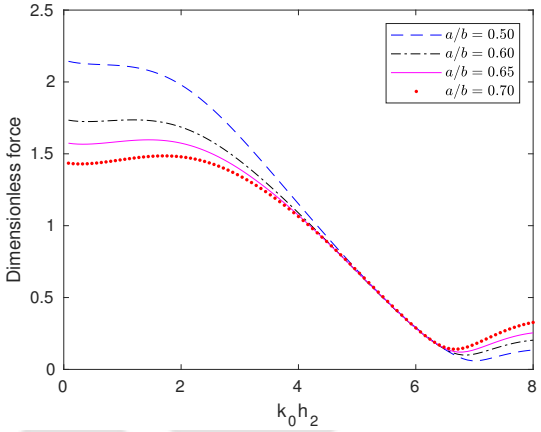

Figure 8.2: Exciting force acting on the upper cylinder plotted against wavenumber for various values of radius ratio a/b with $h_1/h_2 = 0.37$, $h_2/h_3 = 0.66$ and $G = 1$

Figure 8.2 presents the exciting force $\frac{|\tilde{F}_x^1|}{|\rho g a h_2 H|}$ acting on the upper cylinder plotted against wavenumber for various values of radius ratio a/b with $G = 1$, $h_1/h_2 = 0.37$ and $h_1/h_3 = 0.66$. It is observed that the initial value of the force is initially nonzero. For certain values of k_0h_2, waveload on the upper cylinder becomes very low and it creates turning points. This may be due to the interaction of incoming and scattered waves leading to destructive interference near the upper cylinder. The clear observation is that the higher forces occur for lower values of a/b. This is due to more energy getting concentrated near the upper cylinder and consequently resulting in an increase of exciting force. It establishes that the size of the cylinder needs to be adjusted for getting higher or lower force on the cylinder surface.

The exciting force $\frac{|\tilde{F}_x^1|}{|\rho g a h_2 H|}$ acting on the upper cylinder corresponding to different values of h_1/h_2 with fixed values $G = 1$, $h_2/h_3 = 0.66$ and $a/b = 0.50$ is plotted against wavenumber in Figure 8.3. The same trend of graph pattern as observed in Figure 8.2 is observed here too. The oscillation is observed to get shifted towards left for increasing values of h_1/h_2. The occurrence of shift in these curves may be due to the phase shift of the wave with the change of the drafts of the porous cylindrical system.

In Figure 8.4, the exciting force $\frac{|\tilde{F}_x^1|}{|\rho g a h_2 H|}$ acting on the upper cylinder is examined by plotting it against wavenumber corresponding to various values of porous coefficient G for the fixed values $a/b = 0.5$, $h_2/h_3 = 0.66$ and $h_1/h_2 = 0.37$. It is clearly visible that G has a reasonable influence on the exciting forces and all curves exhibit similar

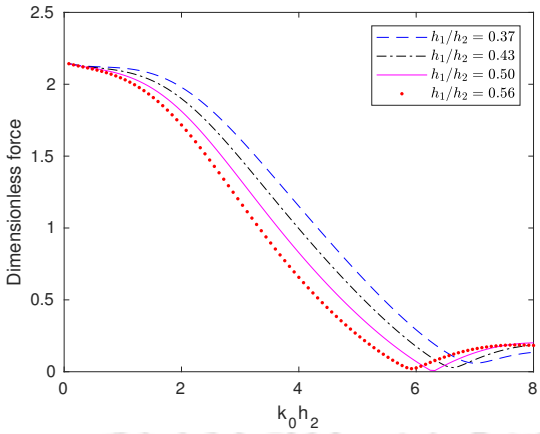

Figure 8.3: Exciting force for the upper cylinder against wavenumber corresponding to different values of h_1/h_2 for $a/b = 0.50$, $h_2/h_3 = 0.66$ and $G = 1$

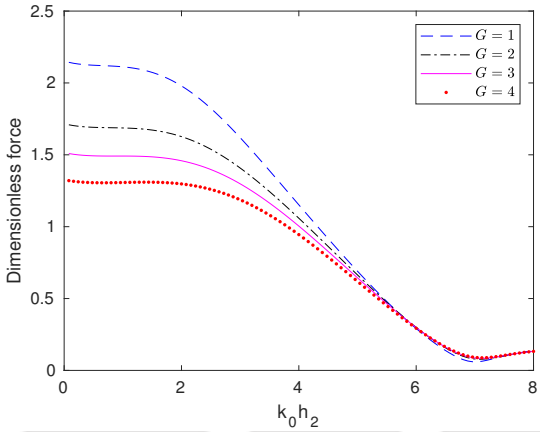

Figure 8.4: Exciting force acting on the upper cylinder plotted against wavenumber for different values of porous parameter G with fixed values $a/b = 0.50$, $h_2/h_3 = 0.66$ and $h_1/h_2 = 0.37$

behaviour as observed in the earlier cases. Also lower values of porous coefficient gives rise to higher values of force. As the porous coefficient G takes increasing values, more waves pass through the structure which brings reduction of the resistance of the cylinder to the wave motion.

Figure 8.5 presents the exciting force $\dfrac{|\tilde{F}_x^2|}{|\rho g b h_2 H|}$ acting on the lower cylinder plotted against wavenumber corresponding to four values of radius ratio a/b with fixed parameter values $G = 1$, $h_1/h_2 = 0.37$ and $h_2/h_3 = 0.66$. It is observed that all curves maintain a similar trend (i.e., start from zero and then take increasing values as the values of the wavenumber increase). That the higher values of force correspond to the lower values of radius ratio a/b means that for a much smaller upper cylinder or a much bigger lower cylinder, the increase in exciting force occurs.

Figure 8.6 shows the exciting force $\dfrac{|\tilde{F}_x^2|}{|\rho g b h_2 H|}$ acting on the lower cylinder plotted

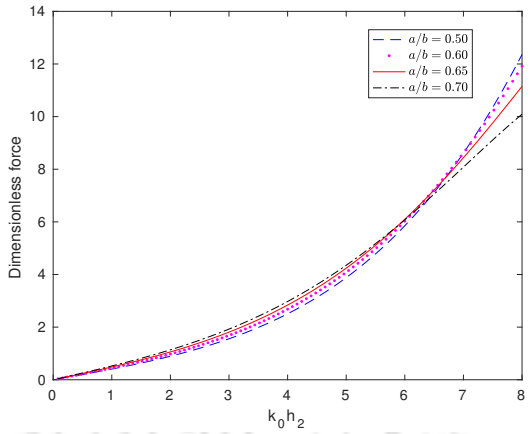

Figure 8.5: Exciting force acting on the lower cylinder plotted against wavenumber for various values of radius ratio a/b with fixed values $h_1/h_2 = 0.37$, $h_2/h_3 = 0.66$ and $G = 1$

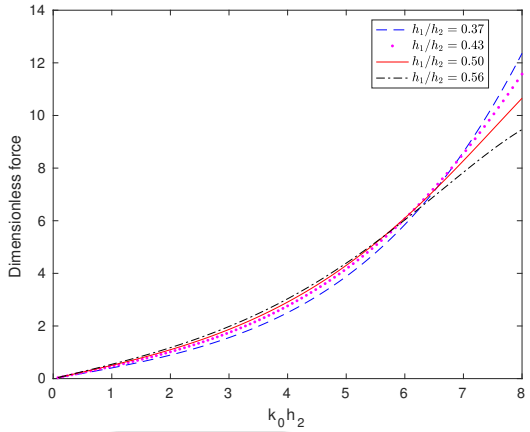

Figure 8.6: Exciting force for the lower cylinder against wavenumber corresponding to different values of h_1/h_2 for $a/b = 0.50$, $h_2/h_3 = 0.66$ and $G = 1$

against wavenumber for various values of h_1/h_2 with fixed values $G = 1$, $h_2/h_3 = 0.66$ and $a/b = 0.5$. The force takes higher values corresponding to lower values of h_1/h_2. This implies that when the draft of the upper cylinder is less, then the force acting on the lower cylinder increases due to a larger fluid region between the cylinders.

Figures 8.7 and 8.8 present contour plots of the wave run-up nearer the free surface corresponding to two different values of frequency. They illustrate that when the wave gets scattered by the cylinder, the elevation gets reduced. By comparison of these two figures, it is clearly noticed that corresponding to higher frequency incident waves, the pattern of the diffracted wave becomes more assertive in addition to the observation of appearance of more number of wave ripples in the annular region.

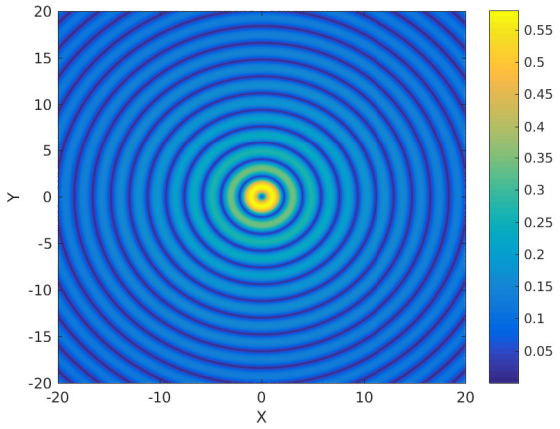

Figure 8.7: Contour plot for the wave run up $|\zeta_1(r,\theta)|/H$ at free surface for $k_0 b = 3.5$, $a/b = 0.50$, $h_1/h_2 = 0.37$, $h_2/h_3 = 0.66$ and $G = 1$

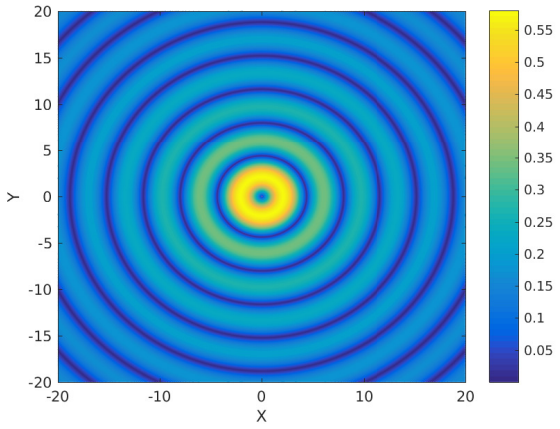

Figure 8.8: Contour plot for the wave run up $|\zeta_1(r,\theta)|/H$ at free surface for $k_0 b = 1.75$, $a/b = 0.50$, $h_1/h_2 = 0.37$, $h_2/h_3 = 0.66$ and $G = 1$

8.2 Two coaxial cylinders: an upper porous cylinder and a lower rigid cylinder

8.2.1 Theoretical formulation

In this case we take up two coaxial cylinders such that the upper cylinder of radius a is fully porous with an impermeable bottom and the lower cylinder of radius b is rigid. There are four fluid regions considered: Region I $(r \geq b, -h_3 \leq z \leq 0)$; Region II $(a \leq r \leq b, -h_2 \leq z \leq 0)$; Region III $(0 \leq r \leq a, -h_2 \leq z \leq -h_1)$ and Region IV $(0 \leq r \leq a, -h_1 \leq z \leq 0)$ (Figure 8.9). In each of these regions, the velocity potentials are defined by $\Phi_j(r,\theta,z,t) = \mathrm{Re}(\phi_j(r,\theta,z)\exp(-\mathrm{i}\omega t))$ for $j = 1,2,3,4$. In this case also, each potential satisfies Laplace's equation in the respective region as defined above. The boundary conditions on the free surface, sea-bed and the surface of the bottom cylinder are same as equations (8.3)-(8.6) from the first problem along with the following additional

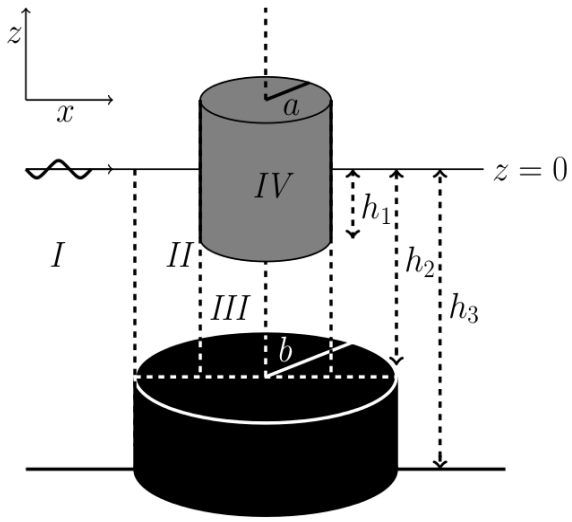

Figure 8.9: Schematic diagram of the second problem

conditions with respect to ϕ_3 and ϕ_4:

$$\frac{\partial \phi_4}{\partial z} = 0; \quad \text{at} \quad z = -h_1, \quad 0 < r < a, \tag{8.28}$$

$$\frac{\partial \phi_3}{\partial z} = 0; \quad \text{at} \quad z = -h_2, \quad 0 < r < a, \tag{8.29}$$

$$\frac{\partial \phi_3}{\partial z} = 0; \quad \text{at} \quad z = -h_1, \quad 0 < r < a. \tag{8.30}$$

The condition on the porous boundary wall has the following form [52]:

$$\frac{\partial \phi_4}{\partial r} = \mathrm{i}k_0 G(\phi_2 - \phi_4) \quad \text{on} \quad r = a, \quad -h_1 < z < 0. \tag{8.31}$$

The matching conditions are expressed by equations (8.9) and (8.10) along with the following additional conditions:

$$\frac{\partial \phi_4}{\partial r} = \frac{\partial \phi_2}{\partial r}; \quad \text{at} \quad r = a, \quad -h_1 < z < 0, \tag{8.32}$$

$$\frac{\partial \phi_3}{\partial r} = \frac{\partial \phi_2}{\partial r}; \quad \text{at} \quad r = a, \quad -h_2 < z < -h_1, \tag{8.33}$$

$$\phi_3 = \phi_2; \quad \text{at} \quad r = a, \quad -h_2 < z < -h_1. \tag{8.34}$$

The potentials ϕ_1 and ϕ_2 are given by (8.13) and (8.14), respectively. Further ϕ_3 has the following form:

$$\phi_3(r, \theta, z) = -\frac{\mathrm{i}gH}{\omega} \left[\sum_{m=0}^{\infty} \cos m\theta \sum_{j=0}^{\infty} \left[\mathcal{F}_{mj} \mathcal{N}_m^{(1)}(\mu_j r) \right] \mathcal{Z}_j^{(3)}(\mu_j z) \right], \tag{8.35}$$

where $\mathcal{F}_{mj}$ are the coefficients to be determined.
The vertical eigenfunctions $\mathcal{Z}_j^{(3)}(\mu_j z)$ are found as

$$\mathcal{Z}_j^{(3)}(\mu_j z) = \begin{cases} \frac{1}{\sqrt{2}}; & j = 0, \\ \cos \mu_j (z + h_2); & j \geqslant 1, \end{cases}$$

where μ_j can be found from

$$\mu_j = \frac{\pi j}{h_2 - h_1}, \quad j = 0, 1, 2, ...$$

The radial eigenfunctions $\mathcal{N}_m^{(1)}$ appearing in (8.35) are as follows:

$$\mathcal{N}_m^{(1)} = \begin{cases} \frac{r^m}{a^{m-1}}; & j = 0, \\ \frac{I_m(\mu_j r)}{I'_m(\mu_j a)}; & j \geqslant 1. \end{cases}$$

Now potential ϕ_4 in Region IV takes the form

$$\phi_4(r, \theta, z) = -\frac{igH}{\omega} \left[\sum_{m=0}^{\infty} \cos m\theta \sum_{j=0}^{\infty} \mathcal{G}_{mj} \mathcal{Z}_j^{(4)}(\sigma_j z) \mathcal{O}_m^{(1)}(\sigma_j r) \right], \tag{8.36}$$

where $\mathcal{G}_{mj}$ are unknown coefficients.
The vertical eigenfunctions $\mathcal{Z}_j^{(4)}(\sigma_j z)$ here are found as

$$\mathcal{Z}_j^{(4)}(\sigma_j z) = \begin{cases} \frac{\cosh \sigma_j (z + h_1)}{\cosh \sigma_j h_1}; & j = 0, \\ \frac{\cos \sigma_j (z + h_1)}{\cos \sigma_j h_1}; & j \geqslant 1. \end{cases}$$

The wavenumbers σ_j $(j = 0, 1, 2, 3, \ldots)$ are derived from the following dispersion relation:

$$\omega^2 = \begin{cases} g\sigma_j \tanh \sigma_j h_1; & j = 0, \\ -g\sigma_j \tan \sigma_j h_1; & j \geq 1. \end{cases}$$

The radial eigenfunctions $\mathcal{O}_m^{(1)}(\sigma_j r)$ are as follows:

$$\mathcal{O}_m^{(1)}(\sigma_j r) = \begin{cases} \frac{J_m(\sigma_j r)}{J'_m(\sigma_j a)}; & j = 0, \\ \frac{I_m(\sigma_j r)}{I'_m(\sigma_j a)}; & j \geqslant 1. \end{cases}$$

8.2.2 Determination of unknown coefficients

Applying the matching conditions (8.9) and (8.10) for $-h_2 < z < 0$ and also the orthogonality of the eigenfunctions, we get the first two equations (8.16) and (8.17). Then using matching condition (8.32) for the depth $-h_1 < z < 0$, along with the orthogonality of the

eigenfunctions, we get

$$\mathcal{G}_{m\alpha}\mathcal{O}_m^{(1)'}(\sigma_\alpha a)\mathcal{X}_{\alpha\alpha} - \sum_{j=0}^{\infty}\left(\mathcal{B}_{mj}\mathcal{S}_j^{(1)'}(\lambda_j a) + \mathcal{C}_{mj}\mathcal{R}_j^{(1)'}(\lambda_j a)\right)\mathcal{P}_{\alpha j} = 0, \quad \alpha \geq 0. \tag{8.37}$$

Again using the condition (8.33) for the depth $-h_2 < z < -h_1$, along with the orthogonality of eigenfunctions $\cos\mu_\alpha(z+h_2)$, we obtain

$$\left(\mathcal{F}_{m\alpha}\mathcal{N}_m^{(1)'}(\mu_\alpha a)\right)\mathcal{K}_{\alpha\alpha} - \sum_{j=0}^{\infty}\left(\mathcal{B}_{mj}\mathcal{S}_j^{(1)'}(\lambda_j a) + \mathcal{C}_{mj}\mathcal{R}_j^{(1)'}(\lambda_j a)\right)\mathcal{Y}_{\alpha j} = 0, \quad \alpha \geq 0. \tag{8.38}$$

Similarly, with the help of matching condition (8.31) for the depth $-h_1 < z < 0$, along with orthogonality of the eigenfunctions, we get

$$\begin{aligned} &\mathcal{G}_{m\alpha}(1 + \mathrm{i}k_0 G\mathcal{O}_m^{(1)}(\sigma_\alpha a))\mathcal{X}_{\alpha\alpha} \\ -\ &\mathrm{i}k_0 G\sum_{j=0}^{\infty}\left(\mathcal{B}_{mj}\mathcal{S}_j^{(1)}(\lambda_j a) + \mathcal{C}_{mj}\mathcal{R}_j^{(1)}(\lambda_j a)\right)\mathcal{P}_{\alpha j} = 0, \alpha \geq 0 \end{aligned} \tag{8.39}$$

where

$$\mathcal{P}_{\alpha,j} = \int_{-h_1}^{0}\mathcal{Z}_\alpha^{(4)}(\sigma_\alpha z)\mathcal{Z}_j^{(2)}(\lambda_j z)\mathrm{d}z, \tag{8.40}$$

$$\mathcal{X}_{\alpha,\alpha} = \int_{-h_1}^{0}\mathcal{Z}_\alpha^{(4)}(\sigma_\alpha z)\mathcal{Z}_\alpha^{(4)}(\sigma_\alpha z)\mathrm{d}z, \tag{8.41}$$

$$\mathcal{Y}_{\alpha,j} = \int_{-h_2}^{-h_1}\mathcal{Z}_\alpha^{(3)}(\mu_\alpha z)\mathcal{Z}_j^{(2)}(\lambda_j z)\mathrm{d}z, \tag{8.42}$$

$$\mathcal{K}_{\alpha,\alpha} = \int_{-h_2}^{-h_1}\mathcal{Z}_\alpha^{(3)}(\mu_\alpha z)\mathcal{Z}_\alpha^{(3)}(\mu_\alpha z)\mathrm{d}z. \tag{8.43}$$

To calculate the unknown coefficients, the same technique as used in the earlier problem is followed here too.

8.2.3 Validation of present model

To validate our present analytical model for solving the problem, we compare one result with that of Garrett [16], i.e., when the upper cylinder is considered to be a solid impermeable cylinder ($G = 0$) and the height of the lower cylinder is taken to be zero, i.e., the lower cylinder is not present at all in this comparison case. All the parameters in our problem are reconsidered conforming to Garrett's work so that our problem can be converted to the same physical problem considered by Garrett. We consider a floating cylinder corresponding to $G = 0, h_3/a = 0.75, (h_1 - h_3)/a = 0.50$. Figure 8.10 depicts the hydrodynamic force acting on outer wall for both Garrett's work and our work from which

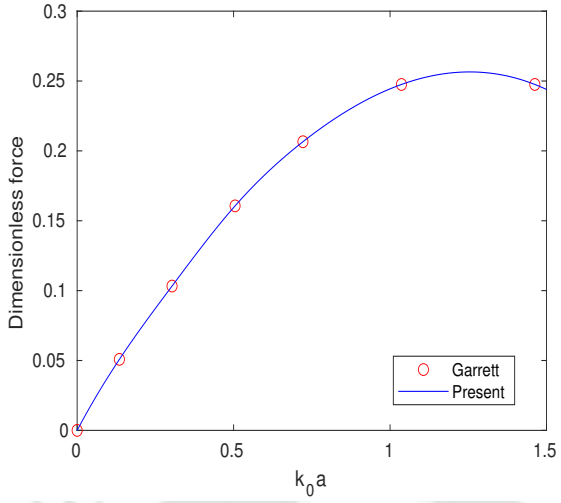

Figure 8.10: Comparison of hydrodynamic force of present work with that of Garrett

an excellent agreement is reached. In view of this, our model can be considered effective and hence can be utilized to study and analyze different aspects of various parameters for such problems.

8.2.4 Results and discussion

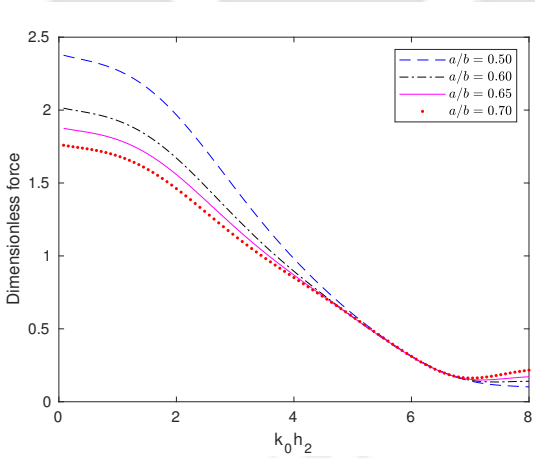

Figure 8.11: Dimensionless exciting force on the upper cylinder plotted against wavenumber for different values of radius ratio a/b with $G = 1$, $h_1/h_2 = 0.37$ and $h_2/h_3 = 0.66$

In Figure 8.11, the dimensionless exciting force acting on the upper cylinder at its surface $r = a$ is plotted against the wavenumber for various values of radius ratio a/b with fixed values $G = 1$, $h_1/h_2 = 0.37$ and $h_2/h_3 = 0.66$. This figure shows that the exciting force acting on the upper cylinder increases corresponding to a reduction in the value of the radius ratio. Comparing Figures 8.2 and 8.11, it is clearly visible that the exciting force for this case (presence of solid porous cylinder at the top) is higher at $r = a$ than that in the earlier case (presence of hollow porous cylinder at the top).

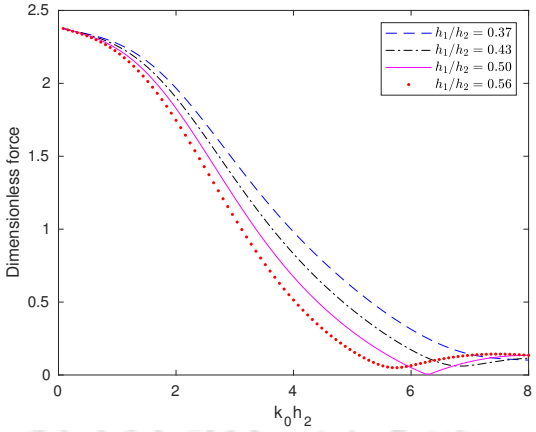

Figure 8.12: Dimensionless exciting forces on the upper cylinder plotted against wavenumber for various values of h_1/h_2 with $G = 1$, $h_2/h_3 = 0.66$ and $a/b = 0.50$

Figure 8.12 presents the exciting force acting on the upper cylinder plotted against wavenumber corresponding to various values of draft h_1/h_2 with $G = 1$, $h_2/h_3 = 0.66$ and $a/b = 0.50$. This figure shows that force increases when h_1/h_2 decreases. This implies that the draft of the upper cylinder has a significant effect on the exciting force. Further, the exciting force acting at the cylinder surface $r = a$ in Figure 8.12 is found to be similar to that observed in Figure 8.3.

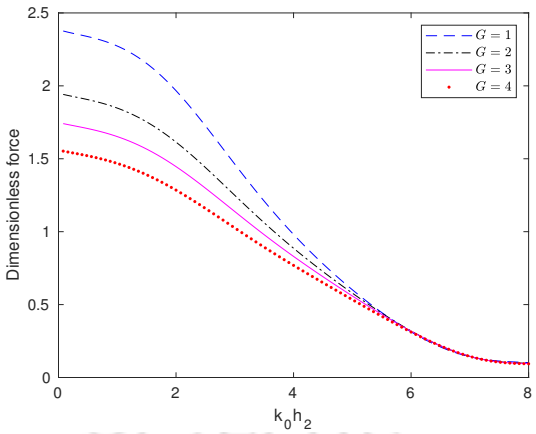

Figure 8.13: Dimensionless exciting force on the upper cylinder plotted against wavenumber for different values of porous coefficient G with $h_1/h_2 = 0.37$, $h_2/h_3 = 0.66$ and $a/b = 0.50$

Figure 8.13 depicts the variation of dimensionless exciting force at $r = a$ plotted against dimensionless wavenumber for various values of G corresponding to the fixed values $h_1/h_2 = 0.37$, $h_2/h_3 = 0.66$ and $a/b = 0.50$. Comparing Figures 8.4 and 8.13, it is evident that for the earlier case (presence of hollow porous cylinder at the top), the exciting force is not as pronounced as is observed in this case (presence of solid porous cylinder at the top). The peak value of the force occurs for $G = 1$ and the force on the upper cylinder, in general, reduces corresponding to increasing values of G. This

establishes the influence of the porosity of the upper cylinder on the exciting forces.

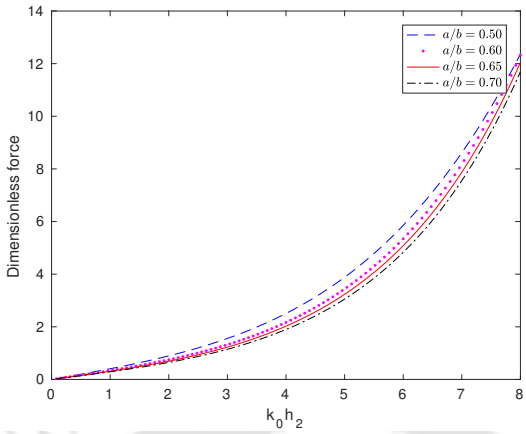

Figure 8.14: Dimensionless exciting force on the lower cylinder plotted against wavenumber for various values of radius ratio a/b with $G = 1$, $h_1/h_2 = 0.37$ and $h_2/h_3 = 0.66$

Figure 8.14 shows the dimensionless exciting force acting on the lower cylinder at its surface $r = b$ for various values of radius ratio a/b with $G = 1$, $h_1/h_2 = 0.37$ and $h_2/h_3 = 0.66$. This figure indicates that the wave force acting on the lower cylinder increases as the radius ratio a/b decreases. This implies that in order to achieve lower forces, the configuration is to be made such that the sizes of the lower and the upper cylinder must not differ much from each other with the restriction $a < b$.

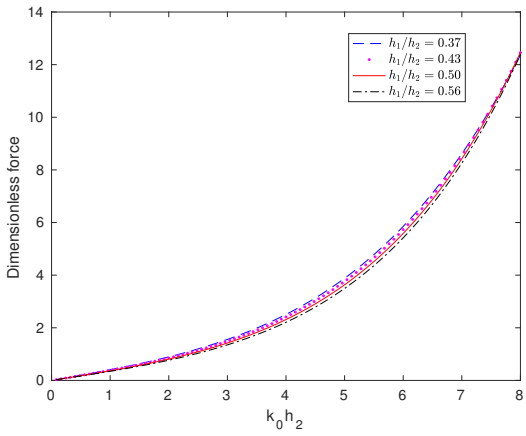

Figure 8.15: Dimensionless exciting forces on the lower cylinder plotted against wavenumber for various values of h_1/h_2 with $G = 1$, $h_2/h_3 = 0.66$ and $a/b = 0.50$

Figure 8.15 shows the variation of dimensionless exciting force on the lower cylinder versus dimensionless wavenumber corresponding to different values of h_1/h_2 with $G = 1$, $h_2/h_3 = 0.66$ and $a/b = 0.50$. The observation here is that the force increases corresponding to decreasing values of h_1/h_2. This shows that a lower value of the draft of the upper cylinder, which results in a larger fluid region between the cylinders, is responsible for the occurrence of higher force on the lower cylinder.

Comparing the results of both the cases of keeping a hollow porous or a solid porous cylinder at the top, it can be seen that corresponding to the same set of values of radius ratio a/b, draft h_1/h_2 and porous coefficient G, the exciting force is higher for the solid porous cylinder case than the hollow porous cylinder case.

8.3 Conclusion

The current chapter caries out a theoretical study on the interaction of linear water waves with a system consisting of two coaxial vertical cylinders in the form of a riding hollow or a solid porous cylinder at the top and a bottom-mounted solid rigid cylinder. The radius of the lower cylinder is taken to be greater than the radius of the upper cylinder. By using the familiar methods of eigenfunction expansion and separation of variables, this diffraction problem governed by Laplace's equation is solved. The main objective here is to study the exciting force and wave run-up due to the system interacting with the water waves. Subsequently, it is concluded through appropriate graphical representation that variation of values in radii, draft and porosity has significant impact on the exciting force and wave run-up. It is found that for the first case (i.e., a riding hollow porous cylinder at the top), the force acting on the upper cylinder takes increasing values corresponding to lower values of radius ratio a/b. Further, for this case, the force also becomes higher corresponding to lower values of draft h_1/h_2. It is observed from Figure 8.4 that higher force occurs corresponding to lower porous coefficients. It is also observed that for fixed radius, porosity and depth, the wave run-up is more visible corresponding to increasing values of wavenumber. Analysing Figures 8.2 and 8.11, it is observed that the exciting force for the second case (i.e., a solid porous cylinder at the top) is higher at the surface of the upper cylinder than that in the first case (i.e., a hollow porous cylinder at the top). A successful validation shows that the current model will be effective for such problems. The expectation here is that the configuration and formulations suggested and results obtained in this work will provide essential information to design suitable and effective porous structures that may be installed in ocean and that these structures will efficiently serve as wave energy devices and also for other meaningful purposes.

CHAPTER 9

Hydrodynamic Coefficients Due to Surge and Heave Motions of a Combination of a Porous and a Rigid Cylinder

This chapter describes an investigation carried out on radiation of porous cylindrical structure consisting of two coaxial vertical cylinders of the same type as in Chapter 8 in water of finite depth. In other words, this chapter is an extension of Chapter 8. By keeping a rigid solid cylinder at the bottom, we separately study two configurations: (i) a hollow porous cylinder at the top, (ii) a solid porous cylinder at the top. Since all motions are not very significant, we discuss only two translational motions in the x- and z-directions, i.e., surge and heave motions, respectively. For convenience, the total fluid region is split into three and four regions, respectively, for case (i) and case (ii). By employing linear water wave theory and eigenfunction expansion, the radiation problem is solved analytically in each fluid region with appropriate use of the boundary and matching conditions. The impacts of various parameters related to the wave and the structure on hydrodynamic coefficients, namely, added mass and damping coefficients for surge and heave motions, are illustrated graphically. The forces induced by radiation are also evaluated and analyzed. It is expected that the outcomes for the hydrodynamic coefficients (as well as the exciting force from Chapter 8) can be appropriately utilized in designing an effective device.

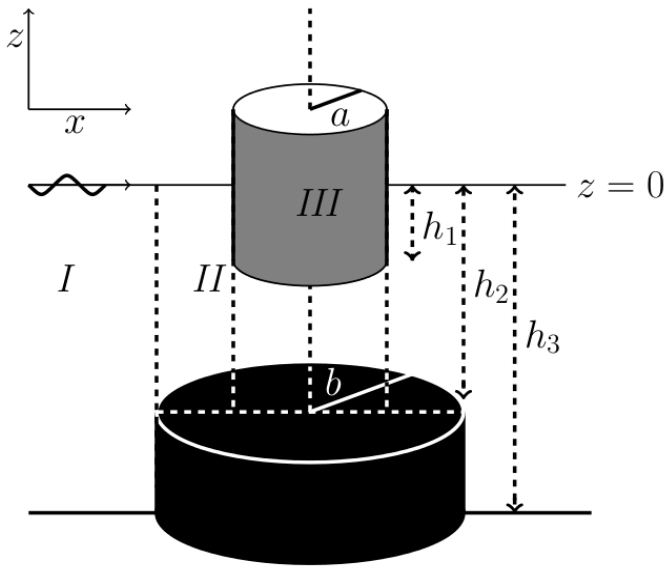

Figure 9.1: Schematic diagram of the model

9.1 Two coaxial cylinders: an upper hollow porous cylinder and a lower rigid solid cylinder

9.1.1 Theoretical formulation

A system consisting of two coaxial cylinders is considered: a hollow upper cylinder with porous side wall and a solid rigid lower cylinder. This structure is same as the one considered in Chapter 8. Three regions are considered in each of which the velocity potentials are defined by Φ_j for $j = 1, 2, 3$. A portion of the upper cylinder rises above the free surface as shown in Figure 9.1. A cylindrical coordinate system is considered with the origin on $z = 0$ along the axis of the cylinders and the z-axis pointing vertically upwards. Here a, b are, respectively, the radii of the upper and lower cylinders, and h_1 is the draft of the upper cylinder. The lower cylinder is placed at a depth $z = -h_3$ with its upper surface located at $z = -h_2$. For convenience and practical point of view, the whole fluid domain is considered to consist of three fluid regions: Region I in $r \geq b, -h_3 \leq z \leq 0$; Region II in $a \leq r \leq b, -h_2 \leq z \leq 0$ and Region III in $0 \leq r \leq a, -h_2 \leq z \leq 0$. A train of linear waves is incident on the structure which is assumed to be in motion due to surge and heave modes along x- and z-directions, respectively. The fluid flow is described by a velocity potential $\Phi(r, \theta, z, t) = \mathrm{Re}[\phi(r, \theta, z) \exp(-\mathrm{i}\omega t)]$. For such a potential flow, Laplace's equation is the governing equation satisfied by each potential ϕ_j:

$$\nabla^2 \phi_j = 0; \quad j = 1, 2, 3, \tag{9.1}$$

where $\phi_j, j = 1, 2, 3$ represent the velocity potentials in regions I, II and III, respectively. To constitute the boundary value problem in ϕ_j, the following boundary conditions at the free surface $z = 0$, sea-bed $z = -h_3$ and the surface $z = -h_2$ of the lower solid cylinder are satisfied:

$$\frac{\partial \phi_j}{\partial z} - \frac{\omega^2}{g}\phi_j = 0; \quad \text{at} \quad z = 0, \quad j = 1, 2, 3, \tag{9.2}$$

$$\frac{\partial \phi_1}{\partial z} = 0; \quad \text{at} \quad z = -h_3, \quad r > b, \tag{9.3}$$

$$\frac{\partial \phi_2}{\partial z} = 0; \quad \text{at} \quad z = -h_2, \quad a < r < b, \tag{9.4}$$

$$\frac{\partial \phi_1}{\partial r} = 0; \quad \text{at} \quad r = b, \quad -h_3 < z < -h_2, \tag{9.5}$$

$$\frac{\partial \phi_3}{\partial z} = 0; \quad \text{at} \quad z = -h_2, \quad 0 < r < a. \tag{9.6}$$

The boundary conditions on the constituents solid surface (S_s) and porous surface (S_p) of the structure are given by Williams et al. [60] as

$$\frac{\partial \phi}{\partial n} = \vec{v}.\vec{n} \quad \text{on} \quad S_s, \tag{9.7}$$

$$\frac{\partial \phi}{\partial n} = \vec{v}.\vec{n} - w(r, \theta, z) \quad \text{on} \quad S_p, \tag{9.8}$$

where $\vec{v}$ is the velocity of the structure and $\vec{n}$ is the outward normal to the surface (S_s or S_p). Here $w(r, \theta, z)$ is assumed to be the spatial component of the normal velocity $W(r, \theta, z, t)$ of the fluid passing from the exterior region to the interior region of the porous cylinder. On the boundary $r = b$, the relevant potentials ϕ_1 and ϕ_2 obey the continuity of velocity and pressure and subsequently the following matching conditions arise:

$$\frac{\partial \phi_1}{\partial r} = \frac{\partial \phi_2}{\partial r}; \quad \text{at} \quad r = b, \quad -h_2 < z < 0, \tag{9.9}$$

$$\phi_1 = \phi_2; \quad \text{at} \quad r = b, \quad -h_2 < z < 0. \tag{9.10}$$

Similarly, the relevant potentials ϕ_2 and ϕ_3 satisfy following matching conditions at $r = a$:

$$\frac{\partial \phi_2}{\partial r} = \frac{\partial \phi_3}{\partial r}; \quad \text{at} \quad r = a, \quad -h_2 < z < -h_1, \tag{9.11}$$

$$\phi_2 = \phi_3; \quad \text{at} \quad r = a, \quad -h_2 < z < -h_1. \tag{9.12}$$

9.1.2 Incident potential and radiated potentials in sub-domains

After radiation of wave takes place, the total velocity potential can be decomposed into incident and radiated components for surge and heave motions as follows [60]:

$$\phi_j = \delta_j \phi_{\text{inc}} + \sum_{m=1}^{2} \beta_m \Psi^m_{\text{rad},j}, \tag{9.13}$$

where $\delta_1 = 1$ and $\delta_j = 0$, for $j = 2, 3, 4$, β_m is the displacement of the structure in the m-th mode and $\Psi^m_{\text{rad},j}$ is the radiation potential in the m-th mode and the j-th region. Further, $m = 1, 2$ correspond to surge and heave radiation mode, respectively. The incident potential can be written as

$$\phi_{\text{inc}} = -\frac{\mathrm{i}gH}{\omega}\frac{\cosh k_0(z+h_3)}{\cosh k_0 h_3}\sum_{n=0}^{\infty}\tau_n J_n(k_0 r)\cos n\theta, \tag{9.14}$$

with

$$\tau_n = \begin{cases} 1 & n = 0, \\ 2\mathrm{i}^n & n \geq 1. \end{cases}$$

Using eigenfunction expansion method, as in Calisal and Subancu [5], the radiated velocity potential in Region I can be written as follows:

$$\Psi^m_{\text{rad},1}(r,\theta,z) = \sum_{j=0}^{\infty} A^m_j \cos k_j(z+h_3) T^m_j(k_j r)\cos\nu\theta, \tag{9.15}$$

where A^m_j are the undetermined coefficients. The wavenumbers k_j $(j = 0, 1, 2, 3, \ldots)$ can be computed from the following by adopting the method in [6]:

$$\omega^2 = \begin{cases} gk_j \tanh k_j h_3; & \text{for} \quad j = 0, \\ -gk_j \tan k_j h_3; & \text{for} \quad j \geq 1. \end{cases}$$

The radial eigenfunctions $T^m_j(k_j r)$ have the following form:

$$T^m_j(k_j r) = \begin{cases} \frac{H^{(1)}_\nu(k_j r)}{H^{(1)'}_\nu(k_j b)}; & j = 0, \\ \frac{K_\nu(k_j r)}{K'_\nu(k_j b)}; & j \geq 1, \end{cases}$$

where $\nu = 1$ for $m = 1$ and $\nu = 0$ for $m = 2$. The radiated velocity potential in Region II satisfying the relevant structural boundary condition is as follows (Wu et al. [61]):

$$\Psi^m_{\text{rad},2}(r,\theta,z) = \sum_{j=0}^{\infty}[\{(B^m_j S^m_j(\lambda_j r) + C^m_j R^m_j(\lambda_j r))\cos\lambda_j(z+h_2)\} + \Pi^m_2]\cos\nu\theta, \tag{9.16}$$

where B^m_j and C^m_j are the undetermined coefficients and the wavenumbers λ_j are obtained from

$$\omega^2 = \begin{cases} g\lambda_j \tanh \lambda_j h_2; & \text{for} \quad j = 0, \\ -g\lambda_j \tan \lambda_j h_2; & \text{for} \quad j \geq 1. \end{cases}$$

$S_j^m(\lambda_j r)$ and $R_j^m(\lambda_j r)$ appearing in (9.16) have the following forms:

$$S_j^m(\lambda_j r) = \begin{cases} \frac{H_\nu^{(1)}(\lambda_j r)}{H_\nu^{(1)'}(\lambda_j b)}; & j = 0, \\ \frac{I_\nu(\lambda_j r)}{I_\nu'(\lambda_j b)}; & j \geq 1, \end{cases} \qquad R_j^m(\lambda_j r) = \begin{cases} \frac{H_\nu^{(2)}(\lambda_j r)}{H_\nu^{(2)'}(\lambda_j b)}; & j = 0, \\ \frac{K_\nu(\lambda_j r)}{K_\nu'(\lambda_j b)}; & j \geq 1, \end{cases}$$

for $m = 1, 2$. Further the term Π_2^m appearing in equation (9.16) is the particular solution due to the dependent-mode. It has a very important role in the radiated potentials satisfying the otherwise difficult non-homogeneous boundary conditions prescribed on the body surface. In Region II, $\Pi_2^m, m = 1, 2$, are given as follows:

$$\Pi_2^1 = 0, \tag{9.17}$$

$$\Pi_2^2 = z + \frac{g}{\omega^2}. \tag{9.18}$$

The radiated velocity potential for region III is (Mavrakos [30])

$$\Psi_{\text{rad},3}^m(r, \theta, z) = \sum_{j=0}^{\infty} [D_j^m \cos \lambda_j (z + h_2) U_j^m(\lambda_j r)] \cos \nu\theta, \tag{9.19}$$

where D_j^m are the undetermined coefficients. The radial eigenfunctions $U_j^m(\lambda_j r)$ have the following form:

$$U_j^m(\lambda_j r) = \begin{cases} \frac{J_m(\lambda_j r)}{J_m'(\lambda_j a)}; & j = 0, \\ \frac{I_m(\lambda_j r)}{I_m'(\lambda_j a)}; & j \geqslant 1. \end{cases} \tag{9.20}$$

9.1.3 Determination of unknown coefficients

Here we use the same technique as followed in earlier chapters to calculate the unknown coefficients.

Added mass and damping coefficients

Upon solving radiation problems in ocean waves yields the important hydrodynamic coefficients, namely, added mass and damping coefficients. These coefficients arise as the real and imaginary parts of the hydrodynamic reaction loads on the body due to the prescribed body motions. The hydrodynamic forces in the x- and z-directions (i.e., for surge and heave motions) due to the motion of the cylinder in modes $m = 1, 2$ can be found out by integrating the corresponding pressure over the cylinder. The non-dimensional added mass χ_{11} and damping coefficients $\frac{\Lambda_{11}}{\omega}$ due to surge motion have the following form (Calisal and Subancu [5]):

$$\chi_{11} + \mathrm{i}\frac{\Lambda_{11}}{\omega} = \rho \int_{-h_1}^{0} \int_{0}^{2\pi} \Psi_2^1(a, \theta, z) a \cos\theta \, \mathrm{d}z\mathrm{d}\theta$$

$$- \rho \int_{-h_1}^{0} \int_{0}^{2\pi} \Psi_3^1(a, \theta, z) a \cos\theta \, \mathrm{d}z\mathrm{d}\theta. \tag{9.21}$$

For this configuration, only surge motion is considered. The following explains why heave motion is not considered for this problem:

The upper cylinder under consideration being hollow, the waves interact with it from the z-direction in a very insignificant way. Usually waves interact with such vertical floating cylinders only if they have a reasonable solid base. Keeping this in view, heave motion for this cylinder is not accounted for since its contribution would have been minimal.

9.1.4 Validation of present model

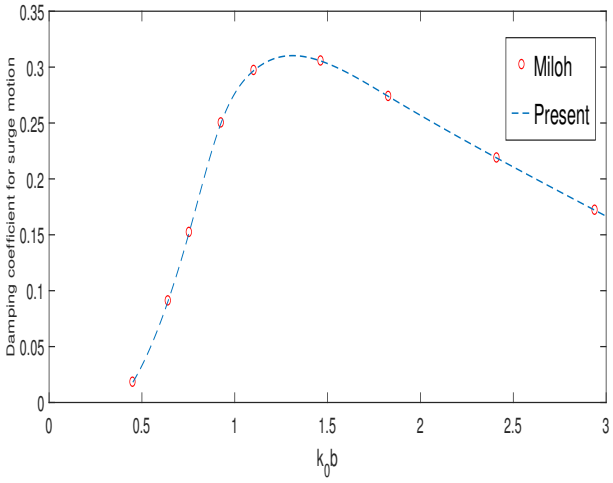

Figure 9.2: Comparison of surge damping coefficient of present work with that of Miloh (1983)

To validate our present analytical model for solving the problem, we compare one result with that of Miloh [34], i.e., when the upper cylinder is considered to be a hollow impermeable cylinder (i.e., $G = 0$) and the height of the lower cylinder is taken to be zero, i.e., the lower cylinder is not present at all in this comparison case. All the parameters in our problem are reconsidered conforming to Miloh's work so that our problem can be converted to the same physical problem as Miloh's. Here we consider $a = 15$ cm, $h_1 = 8$ cm, $h_3 = 60$ cm, $G = 0$. Figure 9.2 depicts the damping coefficient for surge motion acting on hollow cylinder for both Miloh's work and our work from which an excellent agreement is reached. In view of this, our model can be considered effective and hence can be utilized to study and analyze different aspects of various parameters for such problems.

9.1.5 Results and discussion

In Figure 9.3, the non-dimensionalized added mass for surge motion is discussed corresponding to various values of radius ratio a/b, for $h_1/h_2 = 0.38$, $h_2/h_3 = 0.66$ and $G = 1$,

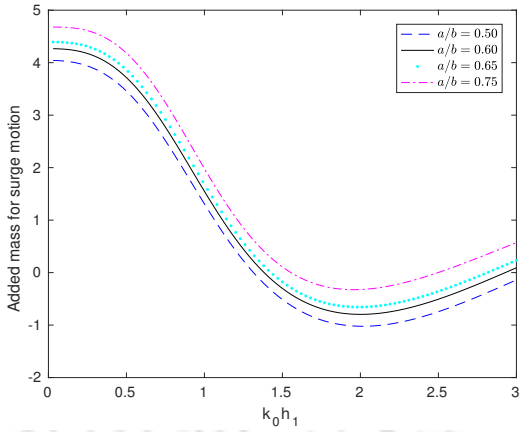

Figure 9.3: Effect of radius ratio a/b of upper hollow porous cylinder on surge added mass against wavenumber with $h_1/h_2 = 0.38$, $h_2/h_3 = 0.66$ and $G = 1$

by plotting it against wavenumber. It is found that the added mass starts from nonzero values and becomes negative for increasing values of k_0h_1. This type of added mass is also observed in the works of McIver and Evans [32] and Wu et al. [61]. It is also noticed that for increasing a/b, the added mass increases which is due to a substantial amount of energy getting concentrated near the upper cylinder. Figure 9.4 shows the non-dimensionalized

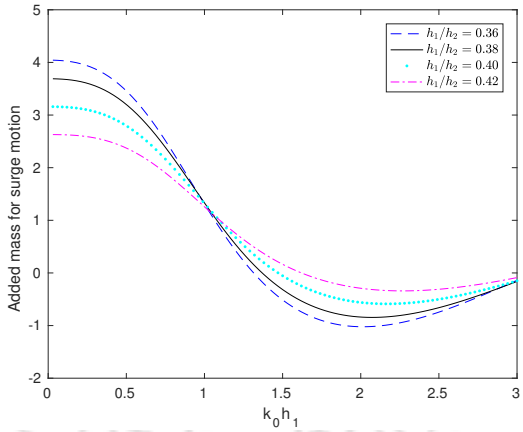

Figure 9.4: Effect of draft h_1/h_2 of upper hollow porous cylinder on surge added mass against wavenumber with $h_1/h_3 = 0.75$, $a/b = 0.50$ and $G = 1$

added mass for surge motion corresponding to various values of draft h_1/h_2 of the upper hollow cylinder for $h_1/h_3 = 0.75$, $a/b = 0.50$ and $G = 1$, plotted against wavenumber. This type of added mass is also observed in the works of Calisal and Subancu [5] and Yeung [62]. The value of added mass becomes higher in the range $0 < k_0h_1 < 0.5$. It is observed that added mass takes maximum value for decreasing values of h_1/h_2. In other words, added mass becomes higher when the draft of the upper cylinder is reduced. Figure 9.5 shows the non-dimensionalized added mass for surge motion corresponding to various values of porous parameter G for $h_1/h_2 = 0.38$, $h_2/h_3 = 0.66$ and $a/b = 0.50$, plotted

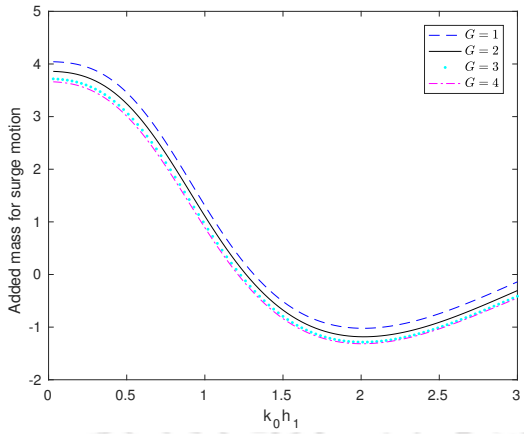

Figure 9.5: Effect of porous parameter G of upper hollow porous cylinder on surge added mass for surge motion against wavenumber with $h_1/h_2 = 0.38$, $h_2/h_3 = 0.66$ and $a/b = 0.50$

against wavenumber. The observation is that the added mass are significantly affected by G. Pattern of graph is found to be similar here like in Figure 9.3: added mass takes higher values for decreasing values of G. Increasing G makes it possible that more waves pass through the structure, but at the same time it brings reduction in the resistance of the cylinder to the wave propagation.

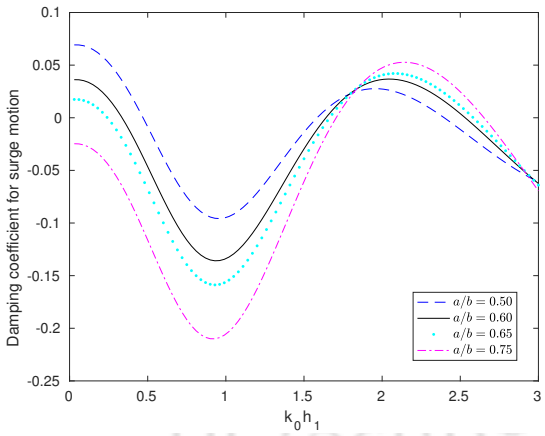

Figure 9.6: Effect of radius ratio a/b of upper hollow porous cylinder on surge damping coefficient against wavenumber with $h_1/h_2 = 0.38$, $h_2/h_3 = 0.66$ and $G = 1$

Figure 9.6 illustrates the non-dimensionalized damping coefficient for surge motion corresponding to various values of radius ratio a/b for $h_1/h_2 = 0.38$, $h_2/h_3 = 0.66$ and $G = 1$, plotted against wavenumber. Similar pattern of graph was also observed in the works of Wu et al. [61]. It is found that the damping coefficient oscillates alternately between negative and positive values for increasing values of k_0h_1. In the neighbourhood of $k_0h = 0.2$, with a decrease in the value of a/b, the damping coefficient increases. In Figure 9.7, the non-dimensionalized damping coefficient for surge motion is analyzed by plotting it against wavenumber for various values of draft h_1/h_2 for $h_1/h_3 = 0.75$, $a/b = 0.50$ and

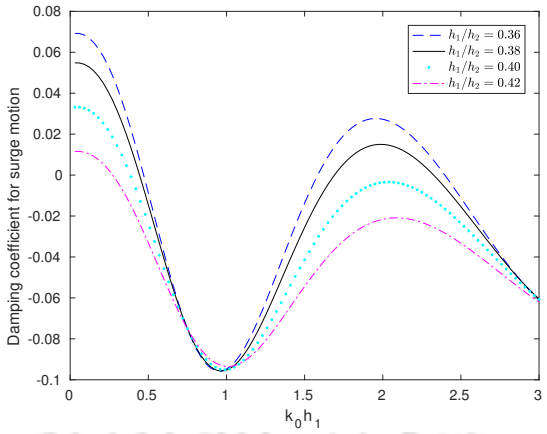

Figure 9.7: Effect of draft h_1/h_2 of upper hollow porous cylinder on surge damping coefficient against wavenumber with $h_1/h_3 = 0.75$, $a/b = 0.50$ and $G = 1$

$G = 1$. Similar type of graphs is observed here like in Figure 9.6. The oscillation gets shifted towards left corresponding to decreasing values of h_1/h_2. The observed shift in the curves of this figure happens very likely due to the occurrence of phase shift in the wave corresponding to values of the draft. Figure 9.8 shows the non-dimensionalized damping

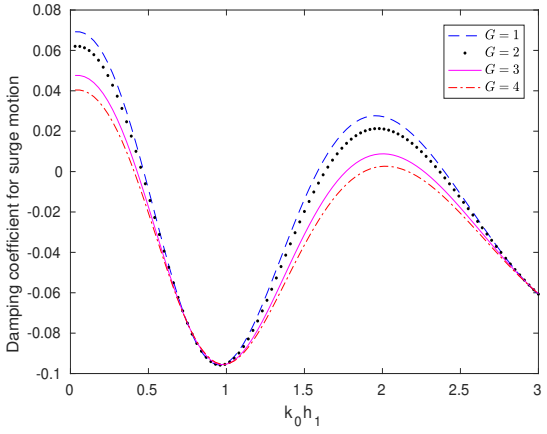

Figure 9.8: Effect of porous parameter G of upper hollow porous cylinder on surge damping coefficient against wavenumber with $h_1/h_2 = 0.38$, $h_2/h_3 = 0.66$ and $a/b = 0.50$

coefficient for surge motion plotted against wavenumber corresponding to various values of porous parameter G for $h_1/h_2 = 0.38$, $h_2/h_3 = 0.66$ and $a/b = 0.50$. The damping coefficient takes higher values corresponding to decreasing values of G.

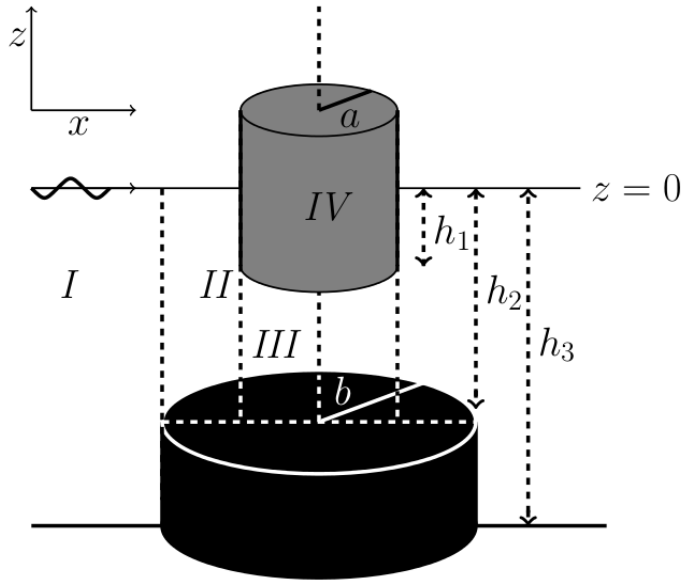

Figure 9.9: Schematic diagram of the second model

9.2 Two coaxial cylinders: an upper solid porous cylinder and a lower rigid cylinder

9.2.1 Theoretical formulation

In Figure 9.9, the geometrical configuration and fluid characteristics are considered to be same as in earlier problem. Each velocity potential Φ_j for $j = 1, 2, 3, 4$ defined in these regions satisfies Laplace's equation. The boundary conditions on the free surface, sea-bed and the surface of the lower cylinder are given by already defined equations (9.2)-(9.5). Similarly, equations (9.7)-(9.8) represent the boundary conditions on the porous and the impermeable wall of the upper cylinder whereas equations (9.9)-(9.12) represent the matching conditions.

(9.15) and (9.16), respectively, give the potentials ϕ_1 and ϕ_2. Further, the radiated velocity potential ϕ_3 for region III can be written as (Wu et al. [61])

$$\Psi^m_{\text{rad},3}(r,\theta,z) = \sum_{j=0}^{\infty}[E^m_j \cos\gamma_j(z+h_2)V^m_j(\gamma_j r) + \Pi^m_3]\cos\nu\theta, \tag{9.22}$$

where E^m_j are the undetermined coefficients and γ_j are obtained from the following expression (Wu et al. [61]):

$$\gamma_j = \frac{\pi j}{h_2 - h_1}, \quad j = 0, 1, 2, ...$$

The radial eigenfunctions $V_j^m(\gamma_j r)$ have the following form:

$$V_j^m(\gamma_j r) = \begin{cases} \frac{r^\nu}{a^{\nu-1}}; & j = 0, \\ \frac{I_\nu(\gamma_j r)}{I'_\nu(\gamma_j a)}; & j \geq 1. \end{cases}$$

The particular solutions for Region III are given by

$$\Pi_3^1 = 0, \tag{9.23}$$

$$\Pi_3^2 = \left[(z+h_2)^2 - \frac{r^2}{2}\right] \frac{1}{2(h_2 - h_1)}. \tag{9.24}$$

The radiated velocity potential for Region IV is (Mavrakos [30])

$$\Psi^m_{\text{rad},4}(r,\theta,z) = \sum_{j=0}^{\infty} [F_j^m \cos \mu_j(z+h_1) W_j^m(\mu_j r)] \cos \nu\theta, \tag{9.25}$$

where F_j^m are the undetermined coefficients. The radial eigenfunctions $U_j^m(\mu_j r)$ have the following form:

$$W_j^m(\mu_j r) = \begin{cases} \frac{J_\nu(\mu_j r)}{J'_\nu(\mu_j a)}; & j = 0, \\ \frac{I_\nu(\mu_j r)}{I'_\nu(\mu_j a)}; & j \geqslant 1. \end{cases} \tag{9.26}$$

Wavenumbers μ_j are obtained from

$$\omega^2 = \begin{cases} g\mu_j \tanh \mu_j h_1; & \text{for} \quad j = 0, \\ -g\mu_j \tan \mu_j h_1; & \text{for} \quad j \geq 1. \end{cases}$$

9.2.2 Determination of unknown coefficients related to hydrodynamic coefficients of heave motion

Here we use the same technique as followed in earlier chapters to calculate the unknown coefficients.

Added mass and damping coefficient for surge and heave motions

Unlike the earlier problem when an upper hollow porous cylinder was considered and subsequently heave motion was not taken into account, here both surge and heave motions are to be taken into account since the upper porous cylinder is no more hollow.

The non-dimensional added mass χ_{11} and damping coefficients $\frac{\Lambda_{11}}{\omega}$ due to surge motion have the following form (Calisal and Subancu [5]):

$$\chi_{11} + \mathrm{i}\frac{\Lambda_{11}}{\omega} = \rho \int_{-h_1}^{0} \int_{0}^{2\pi} \Psi_2^1(a,\theta,z) a \cos\theta \, \mathrm{d}z\mathrm{d}\theta$$

$$- \quad \rho \int_{-h_1}^{0} \int_{0}^{2\pi} \Psi_4^1(a,\theta,z) a \cos\theta \, \mathrm{d}z\mathrm{d}\theta. \tag{9.27}$$

The non-dimensional added mass χ_{33} and damping coefficients $\dfrac{\Lambda_{33}}{\omega}$ due to heave motion can be written as follows (Calisal and Subancu [5]):

$$\begin{aligned} \chi_{33} + \mathrm{i}\frac{\Lambda_{33}}{\omega} &= \rho \int_{0}^{a} \int_{0}^{2\pi} \Psi_4^2(-h_1,\theta,z) r \, \mathrm{d}r\mathrm{d}\theta \\ &- \rho \int_{0}^{a} \int_{0}^{2\pi} \Psi_3^2(-h_1,\theta,z) r \, \mathrm{d}r\mathrm{d}\theta. \end{aligned} \tag{9.28}$$

The same procedure as in the previous problem is used for evaluating the unknown coefficients.

9.2.3 Results and discussion

Here we describe the effects of various parameters on the heave hydrodynamic coefficients acting on the cylindrical structure. The results are presented graphically and the observations are analyzed.

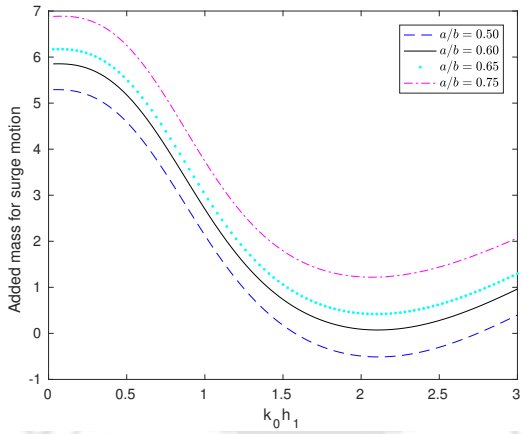

Figure 9.10: Effect of radius ratio a/b of upper solid porous cylinder on surge added mass against wavenumber with $h_1/h_2 = 0.38$, $h_2/h_3 = 0.66$ and $G = 1$

First, we discuss the added mass and damping coefficient for surge motion for the current problem. Figures 9.10 – 9.12 illustrate the non-dimensionalized added mass of upper solid porous cylinder for surge motion corresponding to different values of parameters (radius ratio, draft and porous coefficient) against wavenumber. Similar type of graph pattern is observed as in Figures 9.3 – 9.5. Comparing the added mass for hollow porous cylinder (earlier case) and solid porous cylinder (present case), it is observed that added mass becomes higher for the solid porous cylinder.

In Figures 9.13 – 9.15, the non-dimensionalized damping coefficient of upper solid porous cylinder for surge motion is plotted against wavenumber corresponding to various

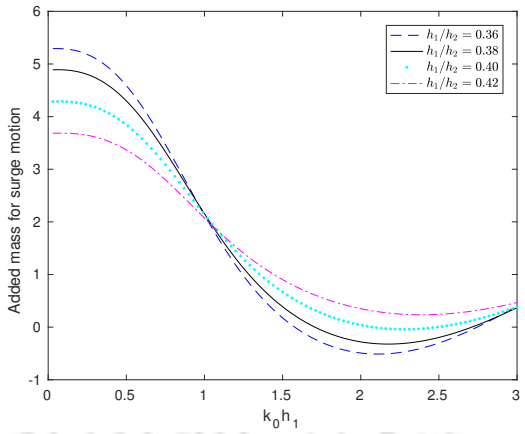

Figure 9.11: Effect of draft h_1/h_2 of upper solid porous cylinder on surge added mass against wavenumber with $h_1/h_3 = 0.75$, $a/b = 0.50$ and $G = 1$

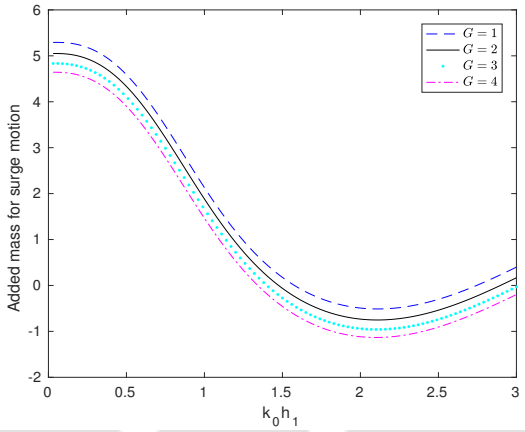

Figure 9.12: Effect of porous parameter G of upper solid porous cylinder on surge added mass for surge motion against wavenumber with $h_1/h_2 = 0.38$, $h_2/h_3 = 0.66$ and $a/b = 0.50$

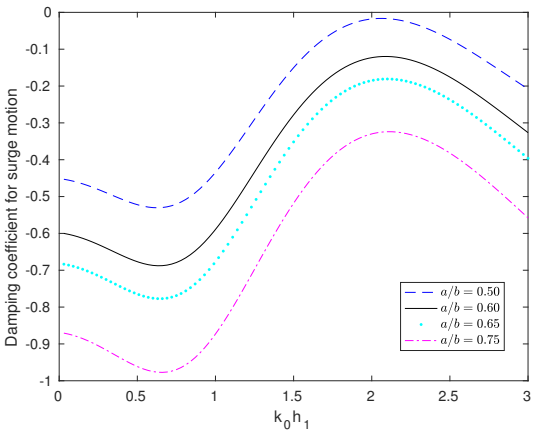

Figure 9.13: Effect of radius ratio a/b of upper solid porous cylinder on surge damping coefficient against wavenumber with $h_1/h_2 = 0.38$, $h_2/h_3 = 0.66$ and $G = 1$

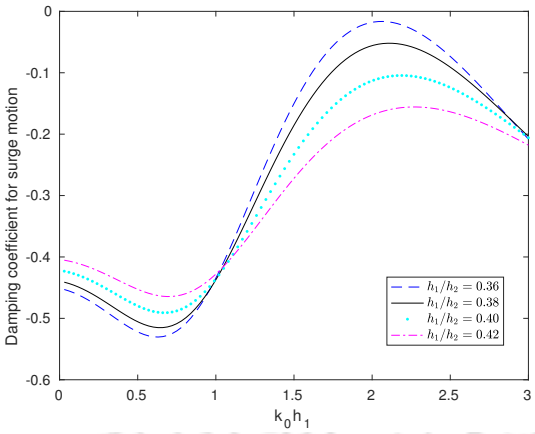

Figure 9.14: Effect of draft h_1/h_2 of upper solid porous cylinder on surge damping coefficient against wavenumber with $h_1/h_3 = 0.75$, $a/b = 0.50$ and $G = 1$

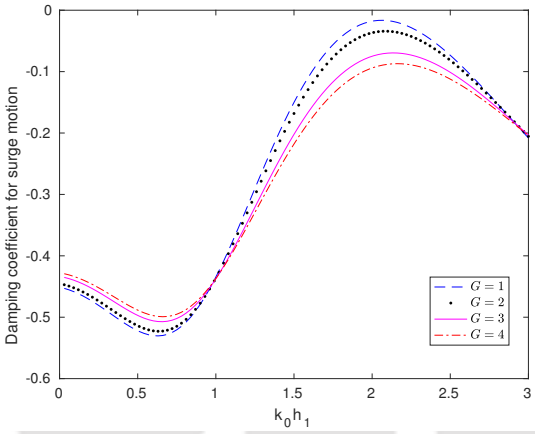

Figure 9.15: Effect of porous parameter G of upper solid porous cylinder on surge damping coefficient against wavenumber with $h_1/h_2 = 0.38$, $h_2/h_3 = 0.66$ and $a/b = 0.50$

parameters (radius ratio, draft and porous coefficient). Analysing the damping coefficients for hollow porous and solid porous cylinders, it is observed that the damping coefficient takes lower values for the solid porous cylinder case. Similar damping coefficients are discussed in Figures 9.6 – 9.8.

Now added mass and damping coefficient due to heave motion are considered. In Figure 9.16, the non-dimensionalized added mass for heave motion is plotted against wavenumber corresponding to four values of radius ratio a/b for $h_1/h_2 = 0.38$, $h_2/h_3 = 0.66$ and $G = 1$. This type of added mass can be seen in the works of Williams et al. [60]. The added mass starts from some negative values and takes increasing positive values corresponding to increasing values of k_0h_1. That is, the added mass seems more pronounced and effective for increasing values of a/b. In other words, reasonable larger radius of the upper porous cylinder results in higher added mass. Figure 9.17 shows the non-dimensionalized added mass for heave motion against wavenumber corresponding to four values of draft h_1/h_2 for $h_1/h_3 = 0.75$, $a/b = 0.50$ and $G = 1$. The behaviour of

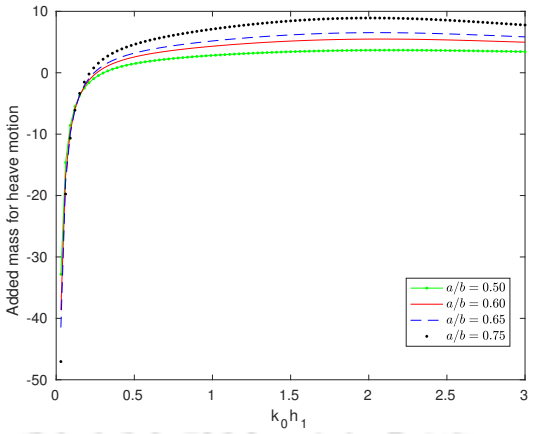

Figure 9.16: Effect of radius ratio a/b of upper solid porous cylinder on heave added mass against wavenumber with $h_1/h_2 = 0.38$, $h_2/h_3 = 0.66$ and $G = 1$

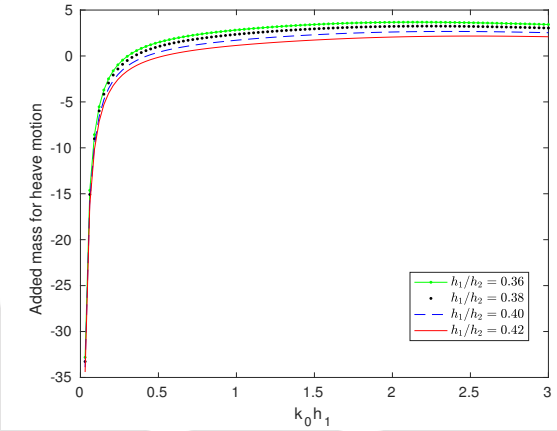

Figure 9.17: Effect of draft h_1/h_2 of upper solid porous cylinder on heave added mass against wavenumber with $h_1/h_3 = 0.75$, $a/b = 0.50$ and $G = 1$.

those curves is similar to those in Figure 9.16. This means added mass takes higher values corresponding to lower draft values. Figure 9.18 presents the non-dimensionalized heave added mass against wavenumber corresponding to four different values of porous parameter G for $h_1/h_2 = 0.38$, $h_2/h_3 = 0.66$ and $a/b = 0.50$. From this figure, the influence of the porous parameter on the added mass can be observed to be significant. It is observed that if G is assigned lower porosity, the added mass takes higher values.

In Figure 9.19, the non-dimensionalized heave damping coefficient is plotted against wavenumber for various values of radius ratio a/b for $h_1/h_2 = 0.38$, $h_2/h_3 = 0.66$ and $G = 1$ and it is observed that these dimensionless radiation damping coefficients decrease corresponding to decreasing a/b. The dimensionless radiation damping coefficient tends to be steady after $k_0h_1 = 1$. The observations will allow to choose the radii of the cylinders appropriately.

Figures 9.20 and 9.21 present the non-dimensionalized heave damping coefficients against wavenumber corresponding to various values of draft h_1/h_2 and porous coeffi-

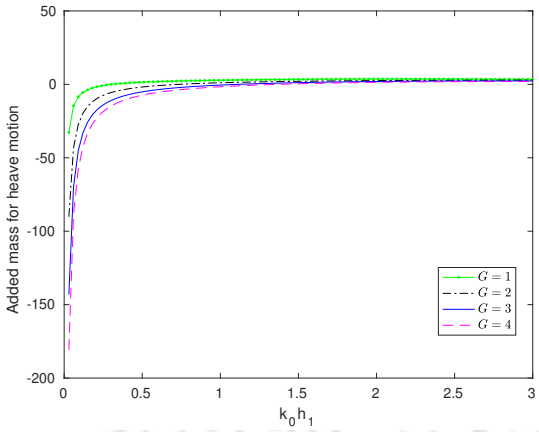

Figure 9.18: Effect of porous parameter G of upper solid porous cylinder on heave added mass against wavenumber with $h_1/h_2 = 0.38$, $h_2/h_3 = 0.66$ and $a/b = 0.50$

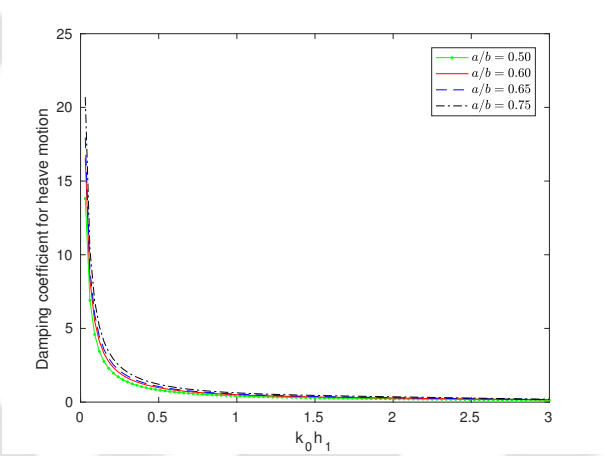

Figure 9.19: Effect of radius ratio a/b of upper solid porous cylinder on heave damping coefficient against wavenumber with $h_1/h_2 = 0.38$, $h_2/h_3 = 0.66$ and $G = 1$

cient G, respectively. It is observed that the dimensionless radiation damping coefficient decreases corresponding to decreasing radius ratio a/b. The damping coefficient for heave motion is significantly affected by the porous coefficient. Moreover, the damping coefficients take reduced values when the porous parameter G is assigned higher values.

In the problems considered in this work, surge motion is considered for both types of configurations: an upper hollow porous cylinder and an upper solid porous cylinder. Figures 9.22 and 9.23, respectively, illustrate the comparison of added mass and damping coefficients due to surge motion for both cases of hollow porous cylinder and solid porous cylinder. It is obviously clear that added mass take lower values and damping coefficients take higher values for the former case than those for the latter case. Accordingly, a suitable configuration may be selected as per requirement of the situation.

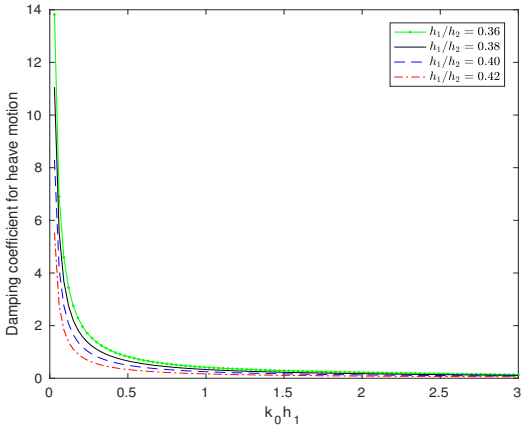

Figure 9.20: Effect of draft h_1/h_2 of upper solid porous cylinder on heave damping coefficient against wavenumber with $h_1/h_3 = 0.75$, $a/b = 0.50$ and $G = 1$

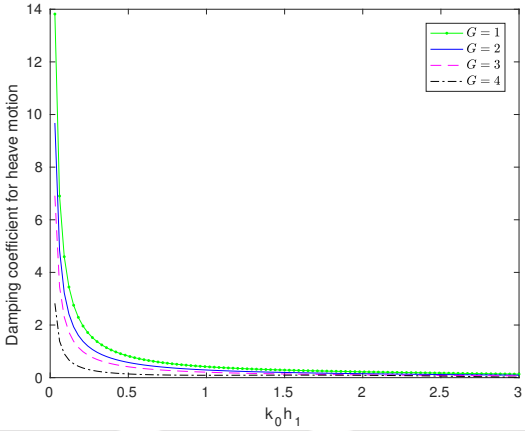

Figure 9.21: Effect of porous parameter G of upper solid porous cylinder on heave damping coefficient against wavenumber with $h_1/h_2 = 0.38$, $h_2/h_3 = 0.66$ and $a/b = 0.50$

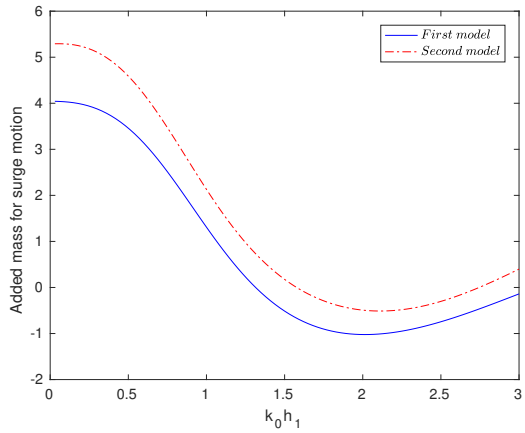

Figure 9.22: Comparison of first model (hollow porous cyilnder) and second model (solid porous cylinder) for surge added mass ($G = 1$, $h_1/h_2 = 0.38$, $h_2/h_3 = 0.66$ and $a/b = 0.50$)

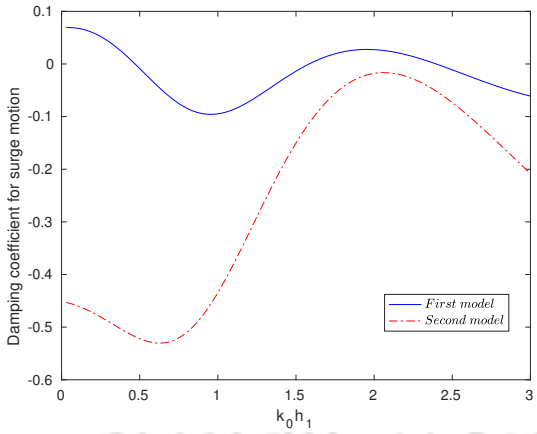

Figure 9.23: Comparison of first model and second model for surge damping coefficient ($G = 1$, $h_1/h_2 = 0.38$, $h_2/h_3 = 0.66$ and $a/b = 0.50$)

9.3 Conclusion

Utilizing linear water wave theory, radiation problem is solved for two coaxial vertical cylinders in water of finite depth. The investigation takes up two cases: (i) a structure consisting of a hollow porous cylinder at the top, (ii) a structure consisting of a solid porous cylinder at the top; with a rigid solid cylinder considered at the bottom for both cases. By using eigenfunction expansion method and separation of variables technique, these radiation problems are solved. Nondimensionalized added mass and damping coefficients due to surge and heave motions are evaluated and analysed. Further, the effect of radius, depth and porosity on the added mass and damping coefficient are thoroughly examined. For validating effectiveness of our model, one present result is compared with the result of Miloh [34] by considering same parameters for both. This comparison brings an excellent agreement between the results. With this validation, various other issues related to radiation are discussed. Figure 9.3 shows that the added mass starts from nonzero values and becomes negative for increasing values of k_0h_1. This type of negative added mass can also be found in the works of McIver and Evans [32] and Wu et al. [61]. It is found that the added mass for surge motion takes higher values corresponding to decreasing values of G. The added mass for heave motion starts from some negative values and taking increasing positive values for increasing values of k_0h_1. This type of added mass is also observed in the works of Williams et al. [60]. The dimensionless radiation damping coefficients for heave motion decrease with decreasing radius ratio of the cylinders a/b. Two figures, namely, Figures 9.22 and 9.23, respectively, illustrate the comparison of added mass and damping coefficients due to surge motion for both a hollow porous cylinder and a solid porous cylinder. It is clearly noticed that added mass takes lower values and damping coefficient takes higher values for the former case than those for the latter case.

From the derived results, it is clear that the added mass and damping coefficient are

affected very significantly by parameters such as the radii of the cylinders, the gap between them and and the porous coefficient of the structure. While designing such structures, it is pertinent that a proper location is chosen, along with all other appropriate parameters, so that it becomes feasible to extract as much ocean energy as possible. From this point of view, it is expected that configuration of the structure, along with formulation, results and observations, for the present problems will be beneficial to a large extent.

CHAPTER 10

Summary and Future Directions

This chapter is devoted to a brief summary of the results highlighting the contributions made by this thesis along with the techniques used in deriving these. It also provides information for the scope of possible extensions of the present work and future investigations in related problems.

10.1 Chapter-wise summary

In Chapter 2, we consider a bottom-mounted surface-piercing compound porous cylinder in finite water depth. The condition on the porous boundary is defined by applying Darcy's law as in [60]. The hydrodynamic force and wave run-up are investigated for different radii, different porosity and different depth. For the upper cylinder, the behaviour of hydrodynamic load is found to be steady in the lower frequency. However, a peculiar behaviour occurs due to the resonance situation in the neighbourhood of a specific frequency range. We compare our result with the result of Isaacson [19], when the lower potion of the cylinder is impermeable, shows good agreement.

Chapter 3 is concerned with a floating surface-piercing compound porous cylinder in finite water depth. Using the same method as in Chapter 2, the analytical expression for diffracted potential in the corresponding regions are obtained. It is observed that for the upper cylinder, force spikes become steeper for increasing values of h_1/h_2. Also for the lower cylinder, higher values of the force occur for lower values of a/b. We observe that for the lower cylinder, the higher values of the force occur within higher values of h_1/h_3. For validating our result, we compare our result with that of Kokkinowrachos et al. [21] when the side wall of the lower cylinder is impermeable. Suitable agreement can be observed between both results.

Chapter 4 deals with the diffraction in an ocean due to the presence of a specific type

of cylinders. In this current work, two models are studied: (i) a floating surface-piercing truncated partial-porous cylinder, (ii) a surface-piercing truncated partial-porous cylinder placed at the bottom. Hydrodynamic force, moment and wave run-up are calculated by using the velocity potentials. Through numerical tests, various experiments are carried out to investigate the impact of various parameters, such as porous coefficients, draft ratio, the ratio of inner and outer radii, the water depth etc., on hydrodynamic force, moment and wave run-up. It is found that the force initially starts from non-zero values. In general, the force decreases for increasing values of k_0h_3. It is clear that occurrence of higher values of force happens corresponding to lower values of a/b. Also the moment increases when $G = 0$, i.e., when the wall of the outer cylinder is assumed impermeable.

In Chapter 5, we discuss diffraction of linear waves by a cylindrical storage tank, the inner part of which contains a cylindrical pile and the outer part contains a coaxial thin hollow porous cylinder, in finite depth. Here we consider two cases: (i) an impermeable solid circular cylinder surrounded by an outer coaxial thin hollow porous cylinder of same height extending from free surface to sea-bed, (ii) a similar structure fully placed atop an impermeable solid circular cylinder of same radius. It is found that the hydrodynamic force at the outer cylinder take peak value for the lower values of radius ratio a/b. For certain values of k_0h_2, waveload on the outer cylinder becomes very low and it creates turning points. This may be due to the interaction of incoming and scattered waves leading to destructive interference near the outer cylinder. Also the wave run-up becomes higher for $G = 0$, that is, for the case when the outer wall is assumed to be impermeable.

Chapter 6 is concerned with the radiation in an ocean due to the presence of a floating surface-piercing truncated partial-porous cylinder in small motion (or in oscillation). This work is an extension of Chapter 4. Numerical investigation is taken up here in order to examine the influence of submerged depth, radii, porous coefficient and water depth on added mass and radiation damping, two most important entities in radiation problems, with respect to surge and heave motions. It is found that the variation of porous coefficient, radii and depth has a significant influence on the added mass and damping coefficients for the semi-porous compound cylinder. The added mass is found not sufficiently affected by lower values of porous coefficient G but exhibits significant variation corresponding to higher values of G. Another important observation is that the damping coefficients oscillate alternately between negative and positive values which can be attributed to coupled behaviour between different modes of motion.

Chapter 7 deals with linear water wave interaction with a bottom-mounted surface-piercing compound partial-porous cylinder consisting of two coaxial cylinders of which the upper cylinder is hollow with a thin porous side wall and the lower impermeable cylinder, with radius greater than that of the upper one, is rigid and subsequently, we examine the associated hydrodynamic forces. The problem is developed in terms of suitable velocity potentials. The important boundary condition on the porous boundary is defined with the aid of Darcy's law. The matching conditions across the linear interface between successive

fluid domains arising due the continuity of pressure and velocity are suitably used. Various numerical experiments show the effect of different parameters, such as porosity of the upper cylinder, draft ratio, the ratio of radii of the upper and lower cylinders and the depth of water on hydrodynamic force and wave run-up. It is found that the force acting on the upper cylinder takes increasing values for lower values of radius ratio, i.e., when the radius of the upper cylinder tends to be much smaller compared to that of the lower cylinder. Further, the force becomes higher when draft h_1/h_2 takes lower values, i.e., when the draft of the lower cylinder with respect to its upper surface is reduced which makes the cylinder closer to the free surface.

In Chapter 8, we discuss exciting forces for an arrangement of two coaxial vertical cylinders – a riding porous cylinder and a submerged bottom-mounted solid rigid cylinder. We take up two cases: first, we consider a hollow porous cylinder at the top and secondly, a solid porous cylinder at the top, and for both the cases, there is a solid rigid cylinder placed at the bottom. The present configuration may be observed as a wave energy device which can tap and transfer ocean wave energy to be used as non-conventional energy. The matching conditions across the linear interface between the adjacent fluid domains can be obtained through the continuity of pressure and velocity. Subsequently, after solving a system of linear equations, exciting force and wave run-up for the upper and lower cylinders are calculated through the velocity potentials evaluated. The exciting force acting on the upper cylinder increases corresponding to a reduction in the value of the radius ratio. It is clearly visible that the exciting force for the second case (presence of solid porous cylinder at the top) is higher at $r = a$ than that in the earlier case (presence of hollow porous cylinder at the top).

Chapter 9 is concerned with the radiation problems for ocean water waves due to a specific type of cylinders in finite depth. The problems are formulated and solved for (i) a system consisting of a hollow porous cylinder at the top, (ii) another system comprising a solid porous cylinder at the top; with a rigid solid cylinder considered at the bottom for both cases. Two translational motions in the x- and z-directions due to radiation of waves are considered, namely, surge and heave motions, respectively, and the added mass and damping coefficients due to these two motions are investigated. It is observed that added mass takes maximum value for decreasing values of h_1/h_2, i.e., when the draft of the lower cylinder with respect to its upper surface is reduced which makes the cylinder closer to the free surface. It is obviously clear that for added mass takes lower values for the hollow porous case than the solid porous cylinder case. The damping coefficient takes higher values corresponding to decreasing values of a/b, i.e., when the radius of the upper cylinder tends to be much smaller compared to that of the lower cylinder.

10.2 Overall summary

1. Problems are presented for a composite porous cylinder for either diffraction or radiation.

2. Hydrodynamic forces, wave run-up and hydrodynamic coefficients (added mass and damping coefficient) are evaluated as per requirement of the individual problem.

3. Separation of variables and eigenfunction techniques are the main mathematical tools used.

4. The computational component of the work is carried out by using various in-built functions of MATLAB.

5. The effect of various parameters on diffraction and radiation are analysed through numerical experiments.

6. The objective of the thesis was to suggest appropriate values of various parameters for getting the desired output for selecting a suitable porous structure for a number of activities in ocean.

7. The outcomes of the works carried out in this thesis is expected to be beneficial to the designers and engineers of different types of ocean structures.

10.3 Future directions

We now present some informal observations pertaining to the possible extensions of our results to different problems. We briefly outline some interesting problems which can be taken up in future. Therefore, the possible extensions of this type of problems with the compound porous cylinder can be as follows:

- the problem of diffraction and radiation for similar type of structures in a two-layer fluid.

- the problem of diffraction and radiation for similar type of structures in water of infinite depth.

- the problem of diffraction and radiation for similar type of structures in water of elastic/porous/poroelastic sea-bed.

- the problem of diffraction and radiation for similar type of structures in water with a rigid or an elastic lid at the free surface for an impermeable sea-bed.

- the problem of diffraction and radiation of the same structure fully submerged in water of finite depth.

Further, we note the following:

- In the cases of wave diffraction problems, surface tension is negligible, while it is not for other cases. The present problems may be reformulated and solved by considering surface tension at the free surface.
- Different type of porous structures like porous barrier, porous box, porous lid etc. can also be studied with respect to diffraction and radiation.
- Flexural gravity wave problem can be incorporated suitably by considering a floating ice-sheet or an elastic sea-floor.
- Multiple porous cylindrical structures, i.e., an array of porous cylinders can be studied with respect to diffraction and radiation. Such works will give a new impetus to such studies. Such an extension will not be too difficult since we can still use the Darcy's porous wall condition, matching conditions and standard matrix technique as used in the problems in this thesis. Only change that will occur will be the velocity potential in different regions due to the location of different structures.
- The time history or transient analysis of the added masses on the structural integrity (for the radiation problems) can be studied. This will give some idea about the wear and tear of the structure.

Bibliography

[1] H. Behera, S. Mandal, and T. Sahoo. Oblique wave trapping by porous and flexible structures in a two-layer fluid. *Physics of Fluids*, 25:112110, 2013.

[2] D. D. Bhatta. Computations of hydrodynamic coefficients, displacement-amplitude ratios and forces for a floating cylinder due to wave diffraction and radiation. *International Journal of Non-Linear Mechanics*, 46:1027–1041, 2011.

[3] D. D. Bhatta and M. Rahman. On scattering and radiation problem for a cylinder in water of finite depth. *International Journal of Engineering Science*, 41(9):931–967, 2003.

[4] B. H. Buck and R. Langan. Aquaculture perspective of multi-use sites in the open ocean: The untapped potential for marine resources in the anthropocene. *Springer International Publishing*, 2018.

[5] S. M. Calisal and T. Sabuncu. Hydrodynamic coefficients for vertical composite cylinders. *Ocean Engineering*, 11:529–542, 1984.

[6] P. G. Chamberlain and D. Porter. On the solution of the dispersion relation for water waves. *Applied Ocean Research*, 21:161–166, 1999.

[7] A. T. Chwang and W. Li. A porous wave-maker theory. *Journal of Fluid Mechanics*, 132:395–406, 1983.

[8] A. Craik. The origins of water wave theory. *Annual Review of Fluid Mechanics*, 36:1–28, 2004.

[9] R. A. Dalrymple, I. J. Losada, and O. A. Martin. Reflection and transmission from porous structures under oblique wave attack. *Journal of Fluid Mechanics*, 224:625–644, 1991.

[10] M. K. D. Darwiche, A. N. Williams, and K. H. Wang. Wave interaction with a semi-porous cylindrical breakwater. *Journal of Waterway, Port, Coastal and Ocean Engineering*, 120:382–402, 1994.

[11] S. Das and S. N. Bora. Damping of oblique ocean waves by a vertical porous structure placed on a multi-step bottom. *Journal of Marine Science and Applications*, 13:362–376, 2014.

[12] S. Das and S. N. Bora. Reflection of oblique ocean water waves by a vertical rectangular porous structure placed on an elevated horizontal bottom. *Ocean Engineering*, 82:135–143, 2014.

[13] S. Das and S. N. Bora. Oblique water wave damping by two fully submerged thin vertical porous plates of different heights. *Computational and Applied Mathematics*, 37:3759–3779, 2018.

[14] S. Earnshaw. The mathematical theory of the two great solitary waves of the first order. *Transactions of the Cambridge Philosophical Society*, 8:326–341, 1847.

[15] C. J. R. Garrett. Bottomless harbours. *Journal of Fluid Mechanics*, 43:433–449, 1970.

[16] C. J. R. Garrett. Wave forces on a circular dock. *Journal of Fluid Mechanics*, 46:129–139, 1971.

[17] G. Green. On the motion of waves in a variable canal of small depth and width. *Transactions of the Cambridge Philosophical Society*, 6:457–462, 1838.

[18] M. Hassan and S. N. Bora. Hydrodynamic coefficients in surge for a radiating hollow cylinder placed above a coaxial cylinder at finite ocean depth. *Journal of Marine Science and Technology*, 19:450–461, 2014.

[19] M. Isaacson. Wave forces on compound cylinders. *In: Proceedings of Civil Engineering in the Oceans IV, ASCE, San Francisco*, pages 518–530, 1979.

[20] P. Kelland. On the theory of waves. *Report of the British Association for the Advanced of Science*, pages 50–52, 1840.

[21] K. Kokkinowrachos, S. Mavrakos, and S. Asorakos. Behaviour of vertical bodies of revolution in waves. *Ocean Engineering*, 13:505–538, 1986.

[22] C. M. Linton and D. V. Evans. The interaction of waves with arrays of vertical circular cylinders. *Journal of Fluid Mechanics*, 215:549–569, 1990.

[23] R. C. MacCamy and R. A. Fuchs. Wave forces on piles: a diffraction theory. *US Army Beach Erosion Board, Technology Memo*, 69:17, 1954.

[24] S. Manam and T. Sahoo. Waves past porous structures in a two-layer fluid. *Journal of Engineering Mathematics*, 52:355–377, 2005.

[25] S. Mandal, H. Behera, and T. Sahoo. Oblique wave interaction with porous, flexible barriers in a two-layer fluid. *Journal of Engineering Mathematics*, 100:1–31, 2015.

[26] S. Mandal, N. Datta, and T. Sahoo. Hydroelastic analysis of surface wave interaction with concentric porous and flexible cylinder systems. *Journal of Fluids and Structures*, 42:437–455, 2013.

[27] S. Mandal and T. Sahoo. Axisymmetric gravity wave diffraction by flexible porous cylinder system in two-layer fluid. *Ocean Engineering*, 106:87–101, 2015.

[28] S. Mandal and T. Sahoo. Gravity wave interaction with a flexible circular cage system. *Applied Ocean Research*, 58:37–48, 2016.

[29] S. A. Mavrakos. Wave loads on a stationary floating bottomless cylindrical body with finite wall thickness. *Applied Ocean Research*, 7:213–224, 1985.

[30] S. A. Mavrakos. Hydrodynamic coefficients for a thick walled bottomless cylindrical body floating in water of finite depth. *Ocean Engineering*, 15:213–229, 1988.

[31] P. McIver. Complex resonances in the water-wave problem for a floating structure. *Journal of Fluid Mechanics*, 546:423–443, 2005.

[32] P. McIver and D. V. Evans. The occurrence of negative added mass in free-surface problems involving submerged oscillating bodies. *Journal of Fluid Mechanics*, 18:7–12, 1984.

[33] Q. R. Meng and D. Q. Lu. Scattering of gravity waves by a porous rectangular barrier on a sea-bed. *Journal of Hydrodynamics*, 28:519–522, 2016.

[34] T. Miloh. Wave loads on a floating solar pond. *In: Proceedings of the international workshop on ship and platform motions. Department of Naval Architecture and Ocean Engineering, Berkeley*, 1983.

[35] R. Mondal, S. Mandal, and T. Sahoo. Surface gravity wave interaction with circular flexible structures. *Ocean Engineering*, 88:446–462, 2014.

[36] M. A. Mustapa, O. B. Yaakoba, M. A. Yasser, K. R. Chang, K. K. Kohb, and A. A. Faizul. Wave energy device and breakwater integration: A review. *Renewable and Sustainable Energy Reviews*, 77:43–58, 2017.

[37] J. N. Newman. Marine Hydrodynamics. *MIT Press, Cambridge, Massachussetts, USA*, 1977.

[38] D. Z. Ning, X. L. Zhao, B. Teng, and L. Johanning. Wave diffraction from a truncated cylinder with an upper porous sidewall and an inner column. *Ocean Engineering*, 130:471–481, 2017.

[39] T. F. Ogilvie. First and second order forces on a cylinder submerged under a free surface. *Journal of Fluid Mechanics*, 16:451–472, 1963.

[40] M. S. Park, Y. J. Jeong, Y. J. You, D. H. Lee, and B. C. Kim. Numerical analysis of a gravity substructure for 5mw offshore wind turbines due to soil conditions. *ASME 34th International Conference on Ocean, Offshore and Arctic Engineering, Newfoundland, Canada.*, 2015.

[41] M. Rahman. Water Waves: Relating Modern Theory to Advanced Engineering Applications. *Clarendon Press, Oxford, UK*, 1995.

[42] M. Rahman and D. D. Bhatta. Second order wave forces on a pair of cylinders. *Canadian Applied Mathematics Quarterly*, 1:343–382, 1993.

[43] B. Rayleigh. On waves. *Philosophical Magazine*, 5:257–279, 1876.

[44] J. S. Russell and S. J. Robinson. Report on waves. *Report of the British Association for the Advanced of Science*, pages 417–496, 1837.

[45] T. Sahoo. On the generation of water waves by cylindrical porous wave-maker. *Acta Mechanica*, 126:231–239, 1998.

[46] T. Sahoo, A. T. Chan, and A. T. Chwang. Scattering of oblique surface waves by permeable barriers. *Journal of Waterway, Port, Coastal and Ocean Engineering*, 126:196–205, 2000.

[47] K. Sankarbabu, S. A. Sannasiraj, and V. Sundar. Interaction of regular waves with a group of dual porous circular cylinders. *Applied Ocean Research*, 29:180–190, 2007.

[48] H. Sherief, M. Faltas, and E. Saad. Forced gravity waves in two-layered fluids with the upper fluid having a free surface. *Canadian Journal of Physics*, 81:675–689, 2003.

[49] C. K. Sollitt and R. H. Cross. Wave transmission through permeable breakwaters. *Proceedings 13th Coastal Engineering Conference of American Society for Civil Engineers, Vancouver, Canada*, pages 1827–1846, 1972.

[50] B. H. Spring and P. L. Monkmeyer. Interaction of plane waves with vertical cylinders. *In Proc. the Fourteenth International Conference on Coastal Engineering, Copenhagen, Denmark*, 107:1828–1845, 1974.

[51] G. G. Stokes. On the theory of oscillatory waves. *Transactions of the Cambridge Philosophical Society*, 8:441–455, 1847.

[52] G. I. Taylor. Fluid flow in regions bounded by porous surfaces. *Proceeding of the Royal Society London A*, 234:456–575, 1956.

[53] F. Ursell. On the heaving motion of a circular cylinder on the surface of a fluid. *The Quarterly Journal of Mechanics and Applied Mathematics*, 2:218–231, 1949.

[54] A. M. Viselli, A. J. Goupee, and H. J. Dagher. Model test of a 1:8-scale floating wind turbine offshore in the gulf of maine. *Journal of Offshore Mechanics and Arctic Engneering*, 137:041901, 2015.

[55] K. H. Wang and X. Ren. Wave interaction with a concentric porous cylinder system. *Ocean Engineering*, 21:343–360, 1994.

[56] G. N. Watson. A Treatise on the Theory of Bessel Functions. *Cambridge Mathematical Library*, 1944.

[57] A. N. Williams and W. Li. Wave interaction with a semi-porous cylindrical breakwater mounted on a storage tank. *Ocean Engineering*, 25:195–219, 1998.

[58] A. N. Williams and W. Li. The hydrodynamics of floating compound cylinders. *Journal of Offshore Mechanics and Arctic Engineering*, 121:213–218, 1999.

[59] A. N. Williams and W. Li. Water wave interaction with an array of bottom-mounted surface- piercing porous cylinders. *Ocean Engineering*, 27:841–866, 2000.

[60] A. N. Williams, W. Li, and K. H. Wang. Water wave interaction with a floating porous cylinder. *Ocean Engineering*, 27:1–28, 2000.

[61] B. Wu, Y. Zheng, and Y. You. On diffraction and radiation problem for two cylinders in water of finite depth. *Ocean Engineering*, 33:679–704, 2006.

[62] R. W. Yeung. Added mass and damping of a vertical cylinder in finite-depth waters. *Applied Ocean Research*, 3:119–133, 1981.

[63] Y. L. Young, M. R. Motley, and R. W. Yeung. Three-dimensional numerical modeling of the transient fluid-structural interaction response of tidal turbines. *Journal of Offshore Mechanics and Arctic Engneering*, 132:011101, 2015.

[64] X. P. Yu. Diffraction of water waves by porous breakwaters. *Journal of Waterway, Port, Coastal and Ocean Engineering*, 121:275–282, 1995.

[65] C. Y. Yueh and S. H. Chuang. A piston-type porous wave energy converter theory. *Journal of Marine Science and Technology*, 21:309–317, 2013.

[66] S. Zheng and Y. Zhang. Wave radiation from a truncated cylinder in front of a vertical wall. *Ocean Engineering*, 111:602–614, 2016.

[67] Y. H. Zheng, Y. M. Shen, Y. G. You, B. J. Wu, and R. Liu. Hydrodynamic properties of two vertical truncated cylinders in waves. *Ocean Engineering*, 32:241–271, 2005.

List of published and communicated papers

Based on the work in this thesis, the following published and communicated papers have resulted:

1. Abhijit Sarkar and Swaroop Nandan Bora, Hydrodynamic forces due to water wave interaction with a bottom-mounted surface-piercing compound porous cylinder, *Ocean Engineering*, 171, 59-70, **2019**.

2. Abhijit Sarkar and Swaroop Nandan Bora, Water wave diffraction by a surface-piercing floating compound porous cylinder in finite depth, *Geophysical & Astrophysical Fluid Dynamics*, 113 (4), 348-376, **2019**.

3. Abhijit Sarkar and Swaroop Nandan Bora, Hydrodynamic forces and moments due to interaction of linear water waves with truncated partial-porous cylinders in finite depth, *Journal of Fluids and Structures*. 94, Paper ID 102898, 29 pages, **2020**.

4. Abhijit Sarkar and Swaroop Nandan Bora, Hydrodynamic coefficients for a floating semi-porous compound cylinder in finite ocean depth *Marine Systems & Ocean Technology*, Published online since September 15, 2020, 16 pages, **2020**.

5. Abhijit Sarkar and Swaroop Nandan Bora, Hydrodynamic force and wave run-up due to diffraction of ocean water waves by a surface-piercing bottom-mounted compound partial-porous cylinder *Fluid Dynamics Research*, Published online since January 13, 2021, DOI: 10.1088/1873-7005/abdb3d, **2021**.

6. Abhijit Sarkar and Swaroop Nandan Bora, Interaction of water waves with a semi-porous bottom-mounted cylindrical storage tank containing a cylindrical pile. (Communicated)

7. Abhijit Sarkar and Swaroop Nandan Bora, Hydrodynamic coefficients due to surge and heave motions of a combination of a porous and a rigid cylinder acting as an energy device. (Communicated)

8. Abhijit Sarkar and Swaroop Nandan Bora, Exciting force for a coaxial configuration of a floating porous cylinder and a bottom-mounted rigid cylinder in finite ocean depth. (Communicated)